Monitoring the Integrated Deep Meridional Flow in the Tropical North Atlantic

Dissertation

zur Erlangung des Doktorgrades

der Mathematisch-Naturwissenschaftlichen Fakultät

der Christian-Albrechts-Universität

zu Kiel

vorgelegt von

Torsten Kanzow

2004

Referent/in:	Prof. Dr. U. Send
Korreferent/in:	Prof. Dr. M. Visbeck
Tag der mündlichen Prüfung:	28.10.2004

Zum Druck genehmigt: Kiel, ...

Der Dekan

Abstract

Meridional transport of heat is accomplished by fundamentally different mechanisms in the atmosphere and the ocean. While in the atmosphere eddies exhibit a dominant role, the largest fraction of northern hemisphere poleward heat transport in the ocean is related to the Atlantic meridional overturning circulation (MOC). The evolution of the MOC and its impact on climate have been subject to intensive theoretical and numerical studies, however continuous measurements of MOC variability have not been carried out.

In this study results from an observational pilot project to monitor fluctuations of the deep southward branch of the MOC across a latitude circle in the tropical North Atlantic are presented. Within the framework of the Meridional Overturning Variability Experiment (MOVE) a four year long time series of deep meridional volume transport fluctuations has been recorded. The backbone of the experiment design is an end point measurement method, which makes use of the fact that the deep ocean flow field is to first order in geostrophic balance: Fluctuations of deep zonally integrated meridional transports in the western trough[1] of the Atlantic are efficiently monitored by continuous moored measurements of the evolution of the zonal density and bottom pressure difference between the eastern and western end point of the section.

One main aspect of this study comprises data calibration and processing as well as a thorough technical performance assessment of the different measurement components of the monitoring array. It is found that two components (density and current meter measurements) provide robust estimates of transport fluctuations. As a consequence of sensor characteristics and data processing the third element (bottom pressure) is found to suppress low frequency variability. Simulations suggest that changes in the deployment scheme might help to overcome these problems to a large extent. Bottom pressure fluctuations derived from space-borne gravity field measurements at 16°N deviate substantially from the in-situ observations and thus do not provide robust estimates of the evolution of deep transports.

For the interpretation of the observed mean and time variable velocities and volume transports and the verification of the monitoring design comparisons to independent observational data and numerical model output have been carried out and spectral analysis as well as basic theoretical aspects of fluid dynamics have been applied. Since only the western trough of the Atlantic is covered by the array, westward propagating Rossby waves from the eastern trough represent a major source of noise, which may mask the MOC signal. An extension of the zonal integration scale from the western boundary from 400 to 1000 km leads to a substantial suppression of the wave signal, thus confirming the monitoring strategy. The best estimate of mean southward transport of North Atlantic Deep Water is 14.9 ± 3.0 Sv[2], its inter-annual variability amounts to 2.4 Sv.

A verification of the experiment design using model simulations attest the transport signal observed by MOVE to be moderately representative for MOC and meridional heat transport fluctuations at 16°N at inter-annual time scales. An eastward extension of the array into the eastern trough might lead to a drastic increase in the signal-to-noise ratio. However it is found that only at longer than decadal time scales coherent MOC fluctuation over the entire meridional extent of the Atlantic can be found. To separate locally and remotely forced MOC fluctuations on shorter time scales, it is suggested to operate two end point monitoring systems simultaneously at different latitude circles of the North Atlantic. Additional monitoring elements specifically designed to quantify the impact of different mechanisms responsible for MOC fluctuations should be added.

[1] area west of the Mid-Atlantic Ridge
[2] 1 Sv = $10^6 m^3 s^{-1}$

Contents

1 Introduction

1.1 Motivation

Motivation In the recent years more and more reliable observational evidence for substantial climate changes has been reported. This includes an increase in global average surface temperature and sea level over the last century by 0.6°C and 15 cm, respectively, and a decrease in snow cover and ice extent of at least 10% since the 1950s, according to the latest assessment of Intergovernmental Panel on Climate Change (IPCC, 2001). Also, high and mid-latitude continental precipitation is likely to have increased over the Northern Hemisphere by 0.5-1.0% per decade over the last century. Large parts of these sustained changes are thought to be attributable to human activity, mainly to an increased emission of greenhouse gases. Very recent observational evidence for a substantial and rapid change in the ocean circulation has been presented by Häkkinen and Rhines (2004): Satellite altimetry suggests a slowdown of the subpolar gyre in the North Atlantic of up to 25% during the 1990s, which might affect the evolution of the Atlantic meridional overturning circulation (MOC) and therefore might reflect a substantial and possibly irreversible climate change. Even if such a change may possibly be unpreventable already, it is of general interest to humanity observe it in order to be able to predict and attenuate its socio-economic consequences.

As a result of the presently ongoing changes in boundary conditions most future projections from climate models forced by realistic greenhouse gas emission scenarios predict a strong decrease in volume transport of the MOC (Fig. 1.1). From the classical view, the MOC consists of a near surface branch carrying warm waters northward and a deep ocean branch returning cold waters southward, which are linked by convective activity restricted to high latitudes of the North Atlantic and broad upwelling in the world ocean interior, as highlighted in Fig. 1.2. The MOC is thought to be responsible for the moderate climate over the Northeast Atlantic sector, whose temperatures may exceed those of the Northeast Pacific by up to 4°C. At subtropical latitudes in the North Atlantic the MOC is associated with more than 60% of the total northward oceanic heat transport (e.g. Bryden and Imawaki, 2001), and even in the South Atlantic the heat transport is directed northward against the sea surface temperature (SST) gradient, which suggests an impact of the MOC not only on the North Atlantic but also on the global climate. There is evidence in paleoclimate records, such as the famous GRIP ice core (GRIP, 1993), that during the last glacial period changes in the mean climate state over Greenland of up to 10°C could have taken place within few decades (Johnson et al., 1992). Adkins et al. (1997) concluded from sediment cores from the Bermuda Rise that the last interglacial period began and ended rather abruptly and that these transitions where linked to changes in the deep oceanic flow field. Several numerical climate model simulations have attributed these abrupt changes to fluctuations in the strength of the MOC (Ganopolski et al., 1998; Ganopolski and Rahmsdorf, 2001). To demonstrate the relevance of the MOC for the global climate exemplarily, surface temperature changes resulting from a breakdown of the MOC as simulated by Vellinga and Wood (2002) are highlighted in Fig. 1.3. The strongest change is observed in the mid-latitude and northern North Atlantic showing a temperature decrease of 3 - 6 °C. But the consequences of a MOC shutdown are not only confined to this area: a temperature decrease is observed throughout the Northern Hemisphere, including the Eurasian continent. Instead, the entire South Atlantic and several locations in the South Pacific and the Southern Ocean exhibit a

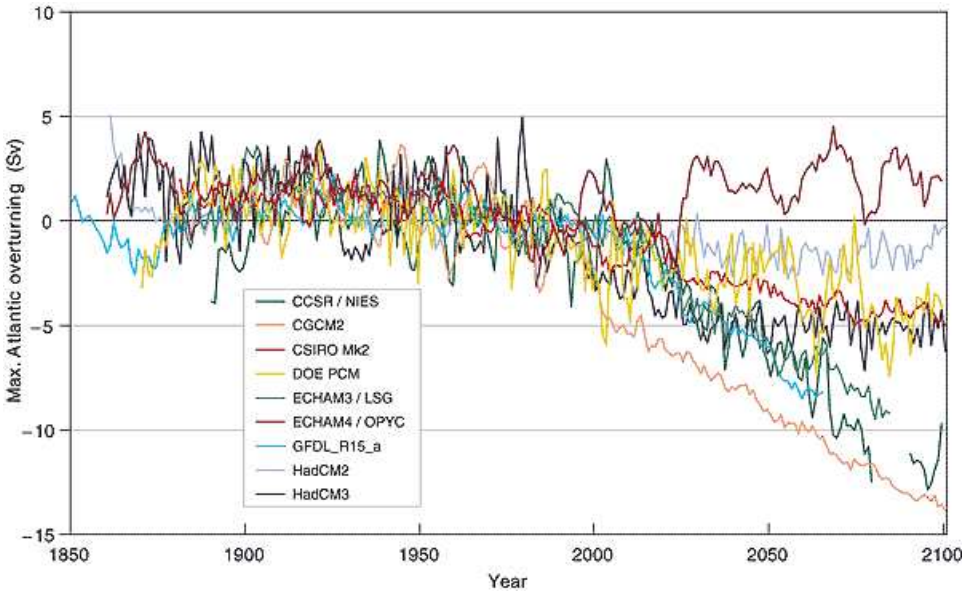

Figure 1.1: *Evolution of maximum strength of the MOC (in Sv) in a range of global warming scenarios. Shown is the annual mean relative to the mean of 1961-1990. Past forcings with greenhouse gas and aerosol only, future forcing scenario is the IS92a (IPCC, 2001).*

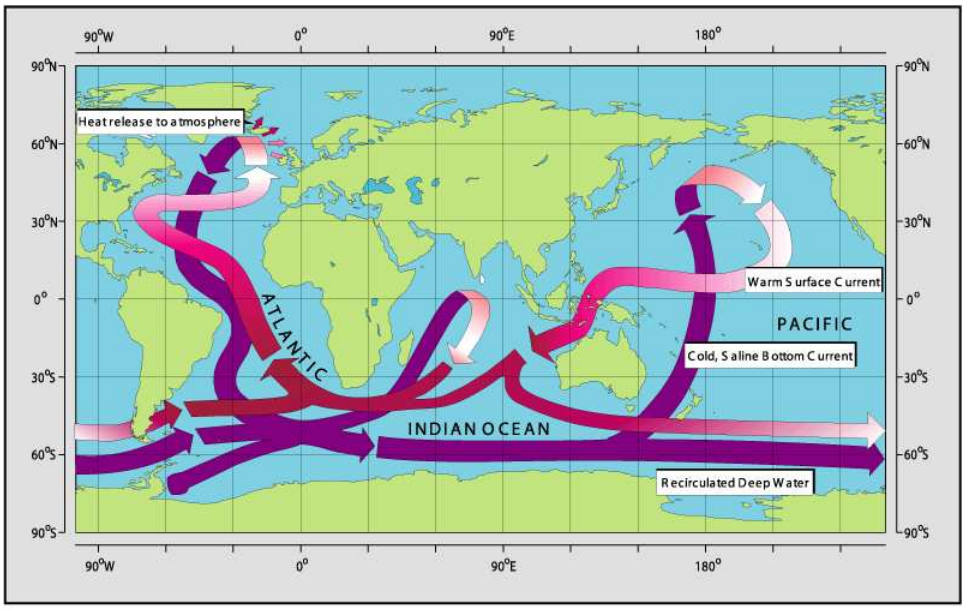

Figure 1.2: *Schematics of the circulation pathways involved in the MOC after W. Broecker (modified by E. Maier-Reimer). The graphics has been obtained from the home page of the Climate Variability and Predictability (CLIVAR) program (www.clivar.org).*

weak but significant temperature rise in this climate simulation. In a greenhouse scenario the Northern Hemisphere cooling would be superimposed by global warming.

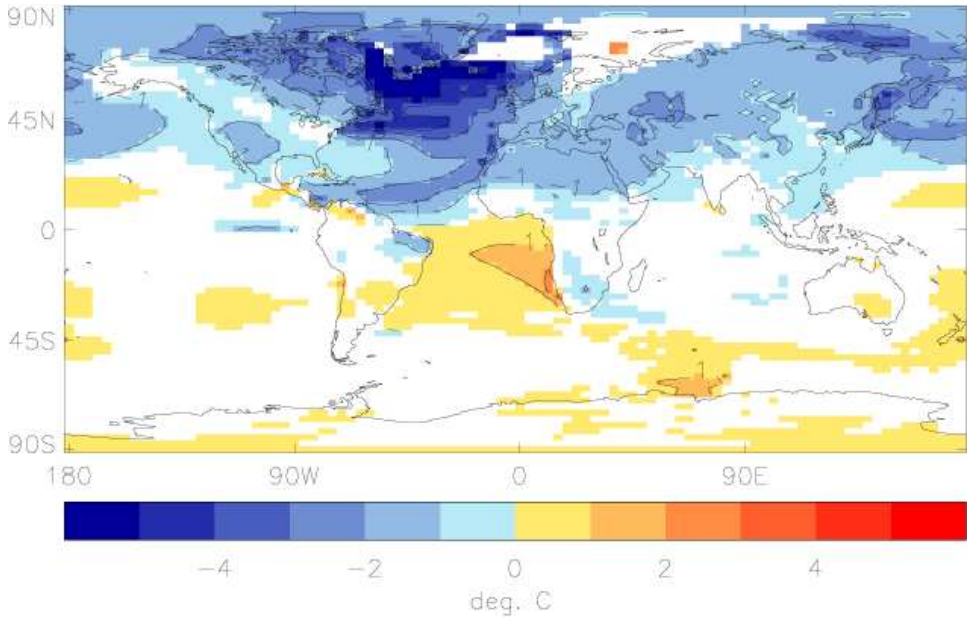

Figure 1.3: *Average SST change 50-100 years after the breakdown of the MOC in a pre-industrial climate simulation using the HadCM3 model (Vellinga and Wood, 2002). Areas that fall within the level of natural variability of the control run appear as white.*

As can be concluded from the spread in the ensemble of climate model MOC future projections in Fig. 1.1, ranging between a decrease in volume transport of 14 Sv and an increase of 2 Sv over the 21st century, the predictions exhibit a high degree of uncertainty. This, however, is not only true for long-term trends, but also for shorter-term variability. Since direct transport measurements of the MOC have been difficult to carry out, hardly any observational information on its present-day fluctuations on annual and longer timescales exists. One exception is the hydrography based study on MOC variability of Koltermann et al. (1999). They find decadal transport changes of 2.5 - 6.3 Sv at different latitudes of the North Atlantic, but the errors of their estimates are of the same order of magnitude. Thus, a robust monitoring system has to be developed to allow for continuous observations of changes in the MOC.

Target of this study In order to contribute to close this apparent gap in the observations, the potential of an efficient measurement technique to quantify MOC fluctuations is investigated. A four year long time series (from February 2000 to February 2004) of deep meridional transport fluctuations integrated across the western trough of the tropical North Atlantic - acquired within the framework of the Meridional Overturning Variability Experiment (MOVE) - is analyzed. The ultimate target of this experiment is to provide estimates of inter-annual and longer term changes of the MOC and relate these its forcing mechanisms. The key elements of MOVE are so-called "end point" moorings, equipped with bottom pressure sensors and with instruments that allow to derive continuously profiles of water density. This allows for an efficient monitoring of geostrophic transport fluctuations zonally integrated over almost the entire trough with only two moorings. One major aspect in this study is an assessment of the accuracy and consistency of the different measurement components that can be achieved, if careful calibration and subsequent data processing are applied. Of equal importance is the physical interpretation of the velocity and volume transport records, which requires comparisons to independent observational and model data and takes into account the experiment design and the deployment schedule. Based on these findings, advantages as well as disadvantages of the

measurement design are discussed and possible improvements are proposed. Finally, the experiment is incorporated into a comprehensive approach to study MOC fluctuations, consisting of different observational as well as modeling elements. As an outlook, the potential of space-borne measurements of the Earth's gravity field to provide estimates of deep-ocean transport fluctuations is investigated.

1.2 Status of Science

The MOC in the Steady State Before the MOVE experiment is described in detail, background information on the current knowledge of the MOC is given. Covering a much smaller area than the Pacific, the special role of the Atlantic in terms of heat transport arises from the fact, that the global deep-water formation is confined to certain high-latitude North Atlantic regions, such as the Labrador Sea or the Seas north of the Greenland-Iceland-Faroe-Scotland Ridges (Iceland/Greenland/Norwegian Sea). The different contributions of this deep water mass, which spreads southward, are summarized by the term North Atlantic Deep Water (NADW). To account for the "loss" of surface waters to the deep ocean, these areas are supplied by northward flow of near-surface waters. The circulation is closed by upwelling of deep water over the entire word ocean. A simple schematics of the essentially 3-dimensional circulation is presented in Fig. 1.2. It also has been referred to as the thermohaline circulation (THC). However, since various definitions of the THC can be found in literature, the use of this term may be misleading (Wunsch, 2002). This is even more true since buoyancy appears not to be the dominating source of energy required to sustain the MOC (see below). The current estimates of the strength of the MOC range between 11 and 18 Sv. (Schmitz, 1995; Ganachaud and Wunsch, 2000; Bryden and Imawaki, 2001).

The source regions of the different contributions to the NADW are well-established (see above). However there is ongoing scientific debate about where and how the deep water is returned to the surface. Munk (1966) and Munk and Wunsch (1966) calculated that a vertical mixing rate of $10^{-4}\mathrm{m}^2\mathrm{s}^{-1}$ in the ocean interior is required to sustain the MOC. Until recently ocean mixing has been estimated to amount to one order of magnitude less than that. However, recent studies indicate the existence of regions of enhanced vertical mixing (with diapycnal diffusivities exceeding $10^{-4}\mathrm{m}^2\mathrm{s}^{-1}$) over rough topography such as the mid-oceanic ridges (Polzin et al., 1997; Mauritzen et al., 2002), rather than a uniform diffusivity over the the entire sub-surface ocean. Another line of argumentation assumes that more than half of the diapycnal mixing takes place near the surface in the Southern Ocean (Döös, K. and Webb, D.J., 1994; Toggweiler and Samuels, 1998; Webb and Suginohara, 2001b), which would explain why apart from areas exhibiting rough topography, deep ocean mixing rates are rather small. It is argued that in the Southern Ocean deep-water is transported towards the surface not by mixing but owing to the strong Ekman suction. Near the surface the energy required for mixing is supplied by wind forcing (in fact 70% of the global wind energy input occurs south of 40 ° S).

Forcing and Energetics For simplicity, the ocean circulation has often been decomposed into a wind-driven and a buoyancy-driven component. However, Pasquero and Tziperman (2004) point out that both may interact. Some authors claim that the MOC is driven by the difference of heating and cooling at low and high latitudes, respectively. This argumentation goes back to the box model of Stommel (1961), where the strength of the MOC has been linked explicitly to the meridional density gradient. Interestingly, the same behavior has been found in coarse resolution three dimensional numerical models, where this relationship had not been prescribed. This is true for steady state (Rahmstorf, 1996) as well as transient experiments (Thorpe et al., 2001). However, since essentially a diagnostic rather than a prognostic relationship between both

variables is observed in these models, it is problematic to conclude, that the density gradient actually drives the MOC. Also, Straub (1996) points out a fundamental difference between the Stommel box model and the model of deep-ocean flow developed by Stommel and Aarons (1960), which is considered fundamental until today: In the Stommel-Aarons theory the strength and structure of the MOC is prescribed and the model solves for the horizontal circulation. In this case the zonally averaged density field is independent of the sense and structure of the MOC. Greatbatch and Lu (2003) argue that in a week damping regime of the Kawase (1987) model the MOC resembles the Stommel-Aarons case whereas for strong damping (which is the case for coarse resolution models) the Stommel-box behavior is found. In which regime the real ocean resides is unclear.

There are two lines of argumentation that question the dominant role of buoyancy forcing for the strength of the MOC. The first line follows purely energetic arguments. Sandström (1908) argues on the basis of a perfect fluid undergoing a Carnot cycle, that hardly any mechanical work (to drive the MOC with) could be extracted, if the heating does not take place at a higher pressure level than the cooling. In the real ocean heating at lower latitudes by the incoming short-wave radiation and cooling associated with outgoing long-wavelength radiation both are confined to the sea surface. Huang (1999) has confirmed these findings in a simple tube model. He points out that if the heat source is located at lower pressure than the heat sink, the strength of the overturing circulation is limited by friction whereas in the opposite case the mechanical energy available for mixing is of controlling influence. The latter follows from the model proposed by Osborn (1980), which relates the turbulent mixing rate to the energy dissipation. By means of scaling analysis Huang (1999) argues that the real ocean cannot be regarded as a heat engine but that it works as a "heat conveyor belt" with an amplification ratio of O(100): The meridional heat energy transport is by a factor of 100 larger than the input rate of mechanical energy.

The second strong argument is based on the observation that the deep ocean exhibits a stable stratification. In the absence of additional mechanical energy input, the oceans below the surface layer would fill with cold water exhibiting no stratification. In order to return the waters vertically across the isopycnals, turbulent mixing is required, which cannot be generated by buoyancy forcing (Paparella and Young, 2002).

On the global scale the sources of mechanical energy to sustain the mixing are mainly wind forcing and tidal dissipation, whereas geothermal heating, buoyancy forcing and atmospheric pressure loading appear to be of almost negligible importance (Wunsch and Ferrari, 2004). According to where one thinks the mixing occurs (deep ocean or near-surface Southern Ocean) different amounts of energy input are required: Munk and Wunsch (1966) argue that an energy input of 2.1 TW (1TW = 10^{12}W) is required to upwell the 30 Sv of deep and bottom waters, which corresponds to an average mixing rate of $10^{-4}\mathrm{m}^2\mathrm{s}^{-1}$ (exceeding the actually observed mixing rates). According to Wunsch and Ferrari (2004) about 1.5 TW are available from wind forcing, whereas another 1 TW of energy supply in the deep ocean may be due to tidal dissipation (Egbert and Ray, 2003a). Model findings of Toggweiler and Samuels (1998) suggest that the largest fraction (9 Sv) of deep to intermediate water conversion takes place in near surface regions of the Southern Ocean, brought to the surface by Ekman suction. For this case Webb and Suginohara (2001b) argue that an energy supply of only 0.6 TW would be needed to account for deep ocean mixing of the remaining less than 8 Sv. This would correspond to a mixing rate of O($3 \times 10^{-5}\mathrm{m}^2\mathrm{s}^{-1}$), which is much closer to the observed values. It should be added that in contrast to Munk and Wunsch (1966), the estimate of Webb and Suginohara (2001b) emanates from the assumption of only up to 17 Sv of NADW that have to be mixed, since in the near-surface water formation regions around Antarctica the density corresponds to that in the NADW. Therefore the bottom waters only have to be mixed up to the NADW level and not through the whole water column.

Mechanisms and Timescales of Variability So far the steady state of the MOC has been described. However the main focus of MOVE is directed on its temporal evolution. From ocean and climate models indications for various mechanisms of MOC variability exists, associated with different time scales.

Inter-annual and higher frequency MOC fluctuations seem to be dominated by direct wind forcing (Dong and Sutton, 2001; Jayne and Marotzke, 2001; Beismann et al., 2002). Typical amplitudes of inter-annual MOC fluctuations amount to 2 Sv. Moreover, NADW formation by high latitude convection is of fundamental importance for the Atlantic MOC. The formation rate of the Labrador Sea Water (LSW), which is the uppermost constituent of the NADW, has been shown to vary substantially on inter-annual to decadal time scale (Curry et al., 1998). Their results indicate a positive correlation between the formation rate and wintertime heat flux anomalies related to the North Atlantic Oscillation (NAO) index. The latter describes simultaneous fluctuations of weakening and strengthening of the Azores high and Iceland low (Wallace and Gutzler, 1981). Based on hydrographic observations at 26.5 ° N Molinari et al. (1998) suggested, that these convection related water mass anomalies would arrive in the subtropics only about 10 years later, advected by the Deep Western Boundary Current (DWBC). This corresponds to estimates of LSW ages at 16 ° N and the equator of 15-22 and 21-31 years, respectively (Steinfeldt and Rhein, 2004). However, whether the advective changes are associated with changes in the MOC is presently unclear, since they appear to exhibit a large degree of density compensation. In a numerical study Eden and Willebrand (2001) investigate the MOC response to NAO variability. They find that a phase of increased heat loss in the Labrador Sea due to high NAO results in an increased subpolar and subtropical MOC with a time lag of 2 - 3 and 6 years, respectively. The response of the MOC to wind stress related to a high NAO is two-fold: Changes in Ekman transport result in instantaneous negative (positive) MOC anomalies in subpolar (subtropical) regions, whereas a delayed baroclinic response of reversed signs with few years time lag is observed (Eden and Willebrand, 2001).

A different class of fast MOC response goes back to the deep ocean circulation spin-up problem originally investigated by Kawase (1987) in a highly idealized model, but has subsequently also been found in eddy-permitting models using realistic topography (e.g. Döscher et al., 1994): Within some months high-latitude perturbations in deep-water formation are communicated towards the tropics by western boundary Kelvin waves. Subsequently the signals travel eastward as equatorial Kelvin waves. Having arrived at the eastern boundary, coastal Kelvin waves are generated that head poleward in both hemispheres, radiating westward propagating Rossby waves into the ocean interior. Johnson and Marshall (2002, 2004) specifically point out the special role of the equator, that tends to act like a "buffer", restricting MOC changes of decadal and shorter time scales to the hemisphere where they are generated: In order to balance a certain transport anomaly, the corresponding pressure anomaly associated with the initial southward moving Kelvin wave becomes smaller and smaller on its way to the tropics (as a consequence of the geostrophic relationship, see Eq. 1.1). Due to the energy loss related to shedding of Rossby waves, transport anomalies associated with the eastern boundary Kelvin waves are increasingly weakend towards higher latitudes.

Whereas the inter-hemispheric oceanic response to the Kelvin wave mechanism may be small on periods smaller than decades, evidence from a coupled ocean-atmosphere model for an associated atmospheric teleconnection exists, that communicates the MOC perturbation globally (Dong and Sutton, 2002): 5-6 years after the arrival of the Kelvin wave in the tropics, a significant tropical SST anomaly associated with a shift of the inter-tropical convergence zone (ITCZ) is observed, which eventually triggers an El Nino event in the tropical Pacific one year later, possibly due to atmospheric Rossby waves. In fact, the static unstable tropical atmosphere is particularly susceptible to oceanic temperature forcing. Yang (1999) has pointed out observational evidence for a 5 year time lag between LSW formation and the strength of an equatorial sea surface

temperature (SST) dipole and speculated about the role of the MOC in accomplishing the linkage. In a very idealized model setup, prescribing MOC fluctuations with a period of 15 years, they are able to simulate the 5 year lag between both variables, proposing anomalous advection of temperatures as a possible mechanism.

Another location affecting the strength of the MOC is thought to be the Southern Ocean, since a large fraction of the conversion from deep to intermediate water may take place here. Results of Toggweiler and Samuels (1995, 1998) and Gnanadesikan (1999) indicate the wind stress driving the Antarctic Circumpolar Current and not the vertical mixing is of dominating influence for the large scale oceanic stratification and therefore for the strength of the MOC. According to Toggweiler and Samuels (1998) buoyancy forcing at high latitudes of the North Atlantic act mainly as a "trigger", making available the mechanical energy to the MOC, which is put into the system by the wind field over the Southern Ocean.

Inter-decadal to millenial time scales of variability are inherent of the MOC. Delworth et al. (1993) find inter-decadal peak to peak oscillations of O(2Sv) in a coupled climate model. (Weaver et al., 1993) performed studies on the importance of freshwater relative to thermal forcing in an ocean circulation model. Besides inter-decadal oscillations they find states without deep-water formations alternating with MOC "flushes" of more than 100 Sv on centennial time scales. Such fluctuations are related to the forcing as well as positive and negative feedback mechanisms involving either the oceanic component alone or the different components of the coupled climate system (see Paul and Schulz (2002) for a summary). Ocean only feedbacks include the advective feedback of the mean circulation (negative) as well as the haline (positive) and the thermal (negative) feedback (Willebrand, 1993; Rahmstorf and Willebrand, 1995). The latter feedbacks are displayed schematically in Fig. 1.4. Examples in the coupled system are the temperature-evaporation (positive), atmospheric moisture transport (positive) and the ice-albedo (negative) feedback (Marotzke, 1996; Jayne and Marotzke, 1999).

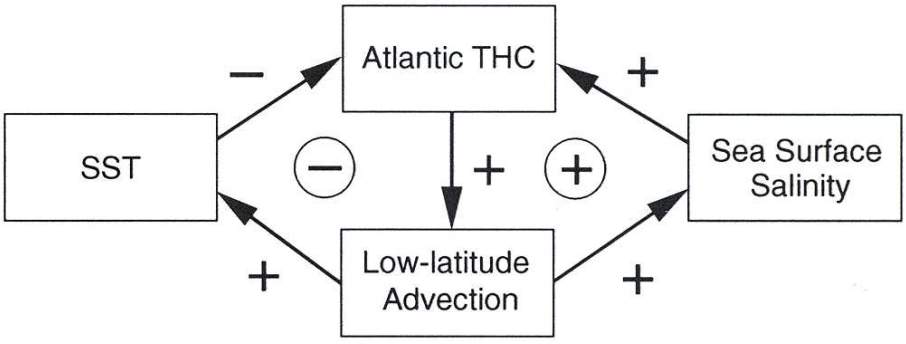

Figure 1.4: *Schematics of two ocean internal feedbacks of heat and salt advection after IPCC (2001). The signs attached to the arrows indicated the correlation between changes of the outgoing box with that of the ingoing box. Negative and positive feedbacks have a stabilizing or destabilizing effect on the MOC, respectively.*

The last aspect of MOC variability described here is that related to human activity. How does the MOC behave in a greenhouse scenario (i.e., under increasing CO_2 input into the atmosphere, as can be expected for the 21st century)? Most future projections from climate models display a substantial decrease of up to 14 Sv in magnitude as a result of global warming, but none of them exhibits a complete shutdown (Fig. 1.1). Two of the models that do not show a strong decrease in overturning strength, exhibit different stabilizing mechanisms, which are either due to increased evaporation in the subpolar North Atlantic (Gent, 2001) or due to El Nino related increased evaporation in the subtropics followed by reduced poleward freshwater transport (Latif et al., 2000).

The stability of the MOC could be analyzed systematically in more idealized (steady state) experiments for both greenhouse and freshwater forcing In certain configurations multiple stable states have been found (e.g. Stommel, 1961; Weaver et al., 1993; Rahmstorf and Willebrand, 1995; Manabe and Stouffer, 1994), however evidence for these from high-resolution models under present-day conditions is still lacking. No uniform answer to the question exists, how close today's forcing conditions are to a possible instability threshold, but Tziperman (2000) points out that a 25% weaker and less dominated by thermal forcing ocean may enter an unstable state, which may go along with either an increased, a strongly oscillating or a closed down MOC.

Heat Transport The strength of the Atlantic MOC is directly associated with the meridional heat transport (MHT). The latter is directed northward not only in the North but also in the South Atlantic, what can be demonstrated by summarizing a suite of analyzes of transoceanic hydrographic sections (e.g. Bryden and Imawaki, 2001). According those direct estimates at 24°N the Atlantic MOC is thought carry about 1.2 PW (1 PW = 10^{15} W) northward and thus is responsible for more than 60% of total oceanic MHT across this latitude circle (which is close to the latitude of maximum oceanic MHT).

The strength of the NADW cell at 24°N in the Atlantic appears to be almost linearly related to the amount of heat carried northward across that latitude, as analyzes of an ensemble of model experiments indicate: Böning and Semtner (2001) find that an increase in overturning strength of 4 Sv is associated with an increase in MHT of 0.2 PW. In contrast, the wind-driven horizontal circulation (the subtropical gyre varied by a factor of 2 in these realizations) was found to be of negligible influence. At seasonal to inter-annual time scales changes in MHT seem to be related to first order to changes in meridional surface Ekman transports and its rather barotropic compensation at depth (Jayne and Marotzke, 2001; Dong and Sutton, 2001), whereas on longer time scales the associated MOC fluctuations display much more baroclinic response. However, it is important to note that the fraction of the total MHT accomplished by the ocean is presumably rather small compared to that of the atmosphere: Trenberth and Caron (2001) find that at the latitude of maximum total poleward MHT in the Northern Hemisphere (35°N) only 22% of the 5 PW are carried by the ocean. The global MHT can be considered rather stable, since typical inter-annual variability amounts to only 1-3% of the mean. Even if the atmosphere strongly dominates the MHT, it should be reminded that the ocean exhibits a possible mechanism for abrupt changes of MHT, namely an MOC shutdown.

1.3 Integral Measurements of Mass Transports

The transport of NADW carried southward by the Deep Western Boundary Current (DWBC) in the Atlantic has been estimated at several locations along its pathway using current meter and hydrographic measurements. These have been summarized by Hogg (2001), see also Fig. 1.5. The strength of the DWBC at the entry of the subtropical North Atlantic is about 13.3 Sv (Pickard and Smethie, 1998), comparing well with the new estimate of 12.2 Sv just upstream at the exit of the subpolar North Atlantic by Schott et al. (2004b), which is not displayed in Fig. 1.5. At 26°N Lee et al. (1996) find a southward DWBC flow of 40 Sv, whereas in the northequatorial Atlantic estimates range between 19 and 29 Sv (Johns et al., 1993; Schott et al., 1993; Rhein et al., 1995; Fischer and Schott, 1997).

Hogg (2001) emphasizes that the meridional DWBC transport distribution contradicts the classical theory of deep-ocean horizontal flow suggested by Stommel and Aarons (1960), according to which the transport should steadily decrease towards the South owing to mass supply of the broad interior flow. To account for this discrepancy, the investigators have speculated about possible interior recirculations, but observational evidence is still missing. However, this implies

that observations limited to the DWBC give no reliable estimates of the strength and the variability of the MOC. Instead one would have to extend the measurements sufficiently far into the basin interior to account for these recirculations. However, there is another caveat: Using a classical coherent current meter array for this purpose is rather impractical, since it requires the resolution of the horizontal scales of the flow to provide reliable estimates of net cross section transport fluctuations. This in turn makes it necessary to set the horizontal mooring spacing less wide than the local baroclinic Rossby radius R_i, which is a measure of a typical de-correlation length scale of geostrophic motions. According to Chelton et al. (1998) R_i takes values in the North Atlantic of about 70, 40 and 20 km at 16°, 26° and 45°N, respectively.

When investigating the MOC, the focus lies on the zonally integrated meridional flow rather than the exact zonal velocity distribution. In this case one might consider applying a much more efficient transport monitoring scheme, which makes use of the integral nature of the horizontal pressure field. The latter property can be derived from the geostrophic balance, which is commonly regarded to hold to first order in the ocean away from its boundaries:

$$P(r_1) - P(r_0) = -\int_{r_0}^{r_1} \mathbf{k} \cdot (\rho f \mathbf{v} \times \mathrm{d}\mathbf{r}) \tag{1.1}$$

with P, ρ and f denoting pressure, density and Coriolis parameter, respectively, $\mathbf{k}$ the vertical unit vector, and $\mathbf{v}$ and $\mathbf{r}$ stand for the horizontal velocity and distance, respectively. The simple and meaningful message from this integral representation of the geostrophic balance is that the pressure difference between two end-points r_0 and r_1 lying on an equi-geopotential surface yields the integrated geostrophic flow normal to the section bounded by these end points. In applying this relationship there is no need to resolve the complicated horizontal structure of the velocity field to recover the net flow. This makes it advantageous compared to classic direct point measurements in climate monitoring applications, where transports through up to basin-scale sections are to be observed (Kanzow, 2000; Send et al., 2002; Hirschi et al., 2003; Johns et al., 2004).

Due to the inability to determine absolute horizontal[1] pressure gradients with sufficient accuracy, for a long time oceanographers have only partly exploited this powerful relationship. It is a standard procedure to determine the horizontal internal geostrophic flow field (i.e., relative to some depth level) from lowered measurements of temperature T and salinity S during hydrographic surveys (e.g. Defant, 1941). From these quantities the water density $\rho(S,T,P)$ can be derived (with P denoting pressure), which allows for the computation of the relative pressure field. In practice profiles of specific volume anomaly $\delta(S,T,P) = \frac{1}{\rho(S,T,P)} - \frac{1}{\rho(35,0,P)}$ are computed, from which geopotential (or dynamic) height $\Delta\Phi$ is obtained

$$\Delta\Phi(P,t) = \int_{P_{ref}}^{P} \delta(P,t) dP \tag{1.2}$$

defined by the pressure integral of δ. The difference of dynamic height (relative to some reference pressure P_{ref}) yields the internal geostrophic velocity v_{int} horizontally integrated between two sites A and B for a constant f (constant latitude)

$$v_{int}(P,t) = \frac{1}{fL} \int_{P_{ref}}^{P} \left[\delta(P,t)^A - \delta(P,t)^B\right] dP \tag{1.3}$$

where t denotes time and L the horizontal separation between A and B. A disadvantage lies in the low temporal repeat sampling rate when applied during hydrographic surveys, as ship time is expensive and hydrographic sections are mostly repeated at long and often irregular intervals.

[1] The underlying coordinate system is oriented such that horizontal planes are defined as equi-geopotential surfaces.

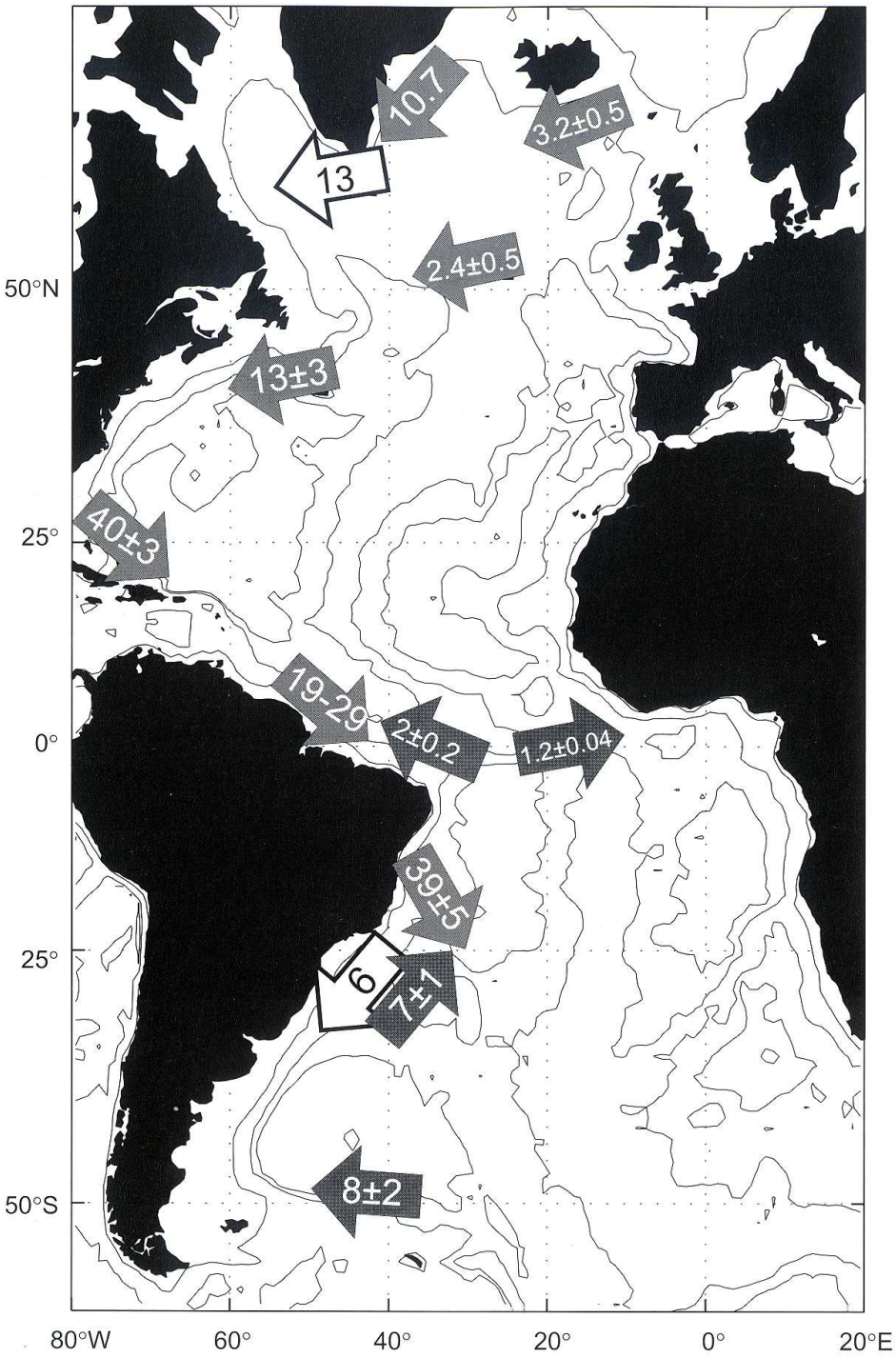

Figure 1.5: *Estimates of NADW and AABW transports [Sv] in the Atlantic from current meter arrays (filled arrows) as well as hydrographic data (open arrows). Arrows with a northward (southward) component denote AABW (NADW) estimates. After Hogg (2001).*

On the other hand this concept can applied to moored density measurements as well, which can be carried out continuously.

However those measurements lack the "external" velocity (i.e., the velocity at the reference level). As stated before, absolute horizontal pressure gradients cannot be obtained with sufficient accuracy. In moored applications there is a way to compute at least near-bottom external velocity *fluctuations* v'_{ext} (i.e., with time mean substracted). These are obtained from measurements of bottom pressure fluctuations P'_{bot}, which in turn can be acquired with high precision (e.g. Whitworth, 1983; Kanzow, 2000; Johns et al., 2004):

$$v'_{ext}(t) = \frac{1}{\rho f L}\left[{P'_{bot}}^{A}(t) - {P'_{bot}}^{B}(t)\right] \tag{1.4}$$

Generally the water depth at any two sites A and B will differ from each other. Strictly speaking, at the deeper location pressure anomalies arising from density variations in the depth range between the bottom and the water depth of the shallower location would have to be subtracted from the bottom pressure anomalies. In practice when applied in the deep ocean with the depth difference between the two sites not exceeding much more than several hundred meters, this contribution generally turns out to be negligible (Wahr et al., 2002; Johns et al., 2004). When simultaneous density measurements are available in the vertical, it is possible to account for this contribution explicitly, by vertically integrating the hydrostatic equation $\mathrm{d}P = -g\rho(z)\mathrm{d}z$, with g, ρ, z denoting gravity acceleration, water density and the vertical coordinate, respectively.

Volume transports M from v_{int} and v'_{ext} in a depth interval $z_1 < z < z_2$ are computed as follows:

$$M_{int}(t) = L\int_{z_1}^{z_2} v_{int}(z(P), t)\mathrm{d}z \tag{1.5}$$

$$M'_{ext}(t) = v'_{ext}(t)[z_2 - z1]L \tag{1.6}$$

Some examples in literature refer to v_{int} and v_{ext} as baroclinic and barotropic velocities, respectively. A separation of vertical profiles of horizontal geostrophic velocity into barotropic and baroclinic modes shows that amplitudes of baroclinic modes are generally not zero at the bottom (see also Fig. 4.12). This means that baroclinic dynamics does have an impact on bottom pressure (and thus on external transports). However, it is argued on a theoretical basis by Luther and Chave (1993) that bottom pressure fluctuations are dominated by barotropic motions. This is demonstrated exemplarily from observations from the ACCP-3 by Johns, Kanzow and Zantopp (2004), hereafter referred to as JKZ2004 (Fig. 2.5). Nevertheless, in this study the expressions internal and external for Eq. 1.3 and 1.4 are used to avoid ambiguities with conflicting definitions.

Geostrophic (internal plus external) velocities are then obtained (except for a time independent offset) by adding the contributions from equations 1.3 and 1.4. In theory the minimum requirement for the correction of the offset is a measurement of the (geostrophic) velocity at one depth level and one point of time, which has to resolve the horizontal scales of the flow (e.g. Whitworth, 1983).

Interestingly, except for the early DRAKE79 experiment in Drake Passage (Whitworth, 1983) only recently moored end point measurements have been used to determine the temporal evolution of geostrophic flow using a combination of bottom pressure and density measurements. Time series from geostrophic transports have been compared with simultaneous current meter measurements in the narrowly-spaced ACCP3 array located in the Deep Western Boundary Current in the subtropical North-Atlantic (JKZ2004).

The MOVE experiment in the tropical Northwest-Atlantic represents the first continuous multi-annual moored geostrophic experiment that the author is aware of. Operating since February 2000, the array is maintained at approximately annual intervals, which offers a unique basis for the analysis of the long-term performance of this experiment. Another important new aspect is that in contrast to previously described geostrophic arrays (Whitworth, 1983; Johns et al., 2004), where vertical density profiles were determined from temperature measurements only (with salinities derived via an empirical $\theta - S$ relationship), during MOVE along with temperatures also the salinities are acquired. Both quantities jointly with pressure levels of the moored devices allows to infer in-situ densities directly and with higher accuracy.

Within the framework of the U.K. RAPID program a new end point MOC monitoring system (Hirschi et al., 2003) has been deployed in March 2004 at 26°N in the Atlantic.

1.4 Structure

Here a short description of the structure of this manuscript is given. In chapter 2 the design of the MOVE experiment is described in detail and it is investigated whether the end point monitoring technique yields reliable estimates of fluctuations of the deep integrated flow. Chapter 3 gives an overview over the data acquisition and processing. Additionally the quality of the sensors' long-term performance is thoroughly assessed. Estimates of the degree of accuracy of continuous temperature, conductivity and pressure measurements that can be achieved carrying out careful sensor calibration and data processing are presented. First consistency checks of the density data are provided. The processing and deployment scheme of the bottom pressure records is critically reviewed and suggestions for an enhanced signal recovery are made. In chapter 4 the hydrographic background field is analyzed with a focus on density fluctuations as well the mean vertical distribution of the meridional velocities. A statistical description of principle vertical patterns of time varying internal velocities is given and finally time series of external and directly measured velocities are presented.

Chapter 5 deals with the observed volume transport fluctuations: After consistency checks of the different transport contributions and a basic statistical description of these, different regimes of variability are identified using spectral analysis. The underlying dynamics is unraveled by comparison with numerical model output and independent observations as well as by theoretical arguments. These findings allow to verify aspects of the monitoring design. Finally a comparison of transport fluctuations at the MOVE site with those observed at the already mentioned ACCP-3 site reveals interesting similarities as well as differences. In chapter 6 different techniques to reference the geostrophic transport fluctuations are described and a "best" estimate of the mean southward NADW transport across 16°N is presented. A verification of the MOVE design based on simulations using output from a numerical model is carried out in chapter 7. Also, meridional coherence scales of MOC fluctuations are investigated with a focus on implications for a comprehensive monitoring design of the MOC. Chapter 8 treats the potential of satellite measurements of the time varying gravity field to allow for robust estimates of bottom pressure and external velocity fluctuations. Finally conclusions are drawn and a short outlook is given.

The appendices A, B and C contain detailed information on additional data and numerical model output used in this study. Finally a glossary can be found, explaining the abbreviations used this manuscript. Regarding nomenclature, variables printed in bold letters denote vectors whereas others represent scalars.

2 Experiment Design

2.1 Introduction

This study is mainly focused on the analysis of the MOVE experiment, whose design will be described in the following. Subsequently the technically similar ACCP-3 (Atlantic Climate Change) experiment, whose results will also be discussed, is briefly introduced. The basic principle of the experiments' transport monitoring approach is the validity of the geostrophic balance, which will be verified at the of this chapter.

2.2 MOVE Experiment

The MOVE experiment located at 16°N in the western basin of the Atlantic (Fig, 2.1,top) has been designed to monitor fluctuations of the deep meridional flow on up to inter-annual time scales by means of horizontally integrating end point moorings. They are complemented by direct current measurements. MOVE consists of three long "geostrophic" moorings (M3, M2, M1, see Fig. 2.1), originally covering the depth range of about 1200 - 5000 m. Each of these was originally equipped with 15 MicroCAT temperature and conductivity recorders at the beginning of the project. Their data allow the calculation of time dependent profiles of dynamic height $\Delta\Phi$ according to Eq. 1.2. In addition about 5 temperature and pressure loggers (MTP) are attached to each mooring to observe vertical mooring motions induced by ocean currents in order to determine precisely the MicroCATs' depths. MicroCAT conductivities (C) and temperatures (T) can thus be allocated with high accuracy to the correct depths and the corresponding salinities can be derived. From these δ is computed and finally the internal geostrophic velocities (horizontally integrated between two sites A and B) are derived as defined in Eq. 1.3. From the third deployment period onwards (Feb. 2002) the measurements at M3 and M1 have been extended up to the surface using now 22 MicroCATs in each of these moorings.

At the base of each of the geostrophic moorings M3, M2 and M1 a bottom pressure sensor combined with an inverted echosounder (PIES) is deployed. These allow for the computation of near-bottom "external" velocity *fluctuations* v'_{ext} according to Eq. 1.4 As mentioned above geostrophic (internal plus external) velocity fluctuations are then obtained by adding the contributions from equations 1.3 and 1.4. Different approaches to derive absolute velocity (transports) are demonstrated in chapter 6.

The flow that passes the geostrophic array M3-M1 inshore of M3 over the continental slope has to be determined by direct current meter measurements from M4 and M3 which are moored at the base of and right in the middle of the continental slope, respectively (Fig. 2.1, bottom). The horizontal distance between M3 and M4 amounts to 10 km. From the third deployment period onwards (after February 2002) an additional current meter mooring (M5) has been deployed even further up the slope (9 km west of M4). In addition to density measuring devices, moorings M3-M1 are also equipped with current meters, covering 6 depth levels below 1600m (Fig. 2.1, bottom).

Furthermore, MOVE initially had been merged with the Guyana Abyssal Gyre Experiment

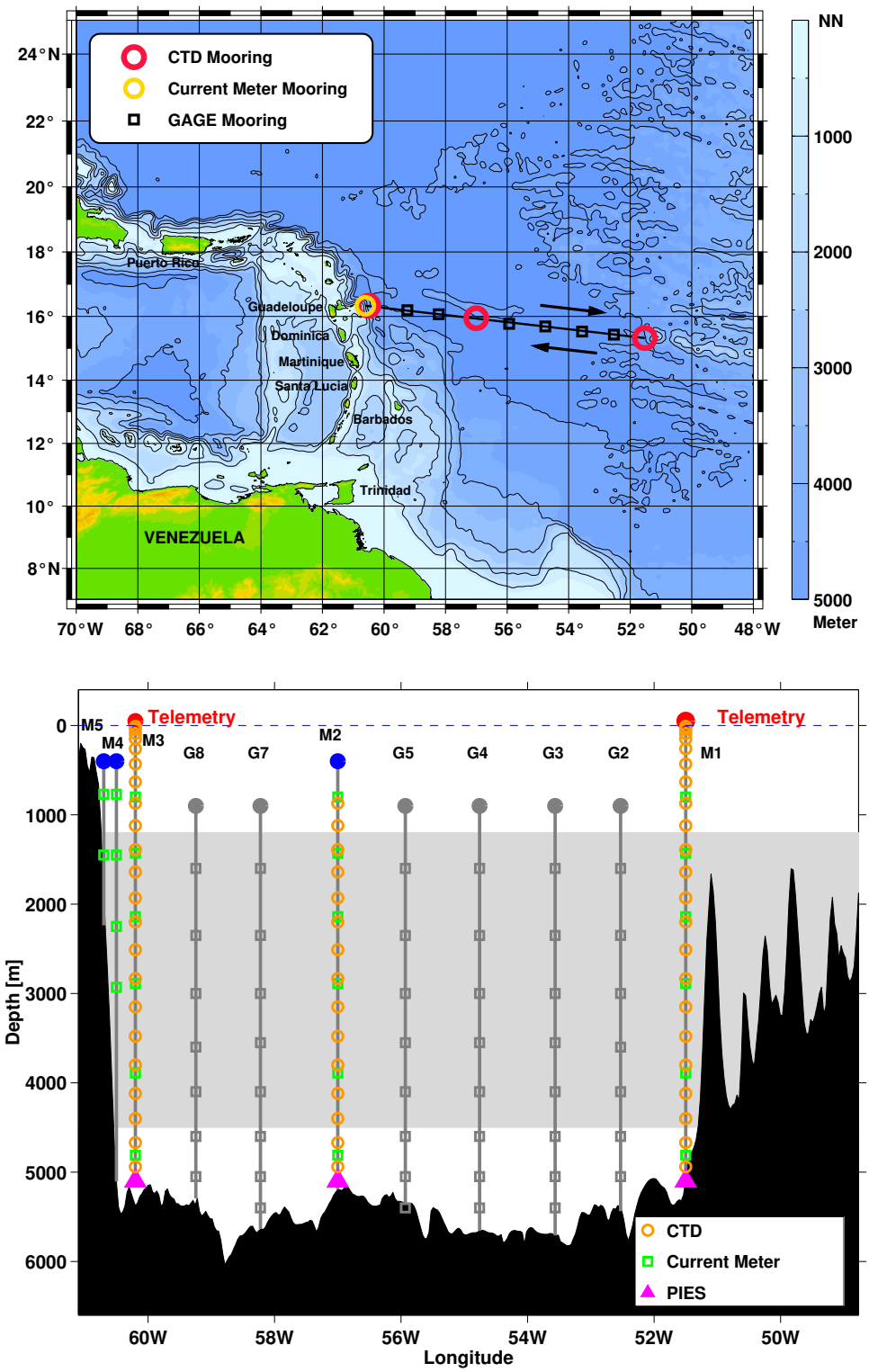

Figure 2.1: *Top: The MOVE, located at 16° N in the tropical North Atlantic consists of 3 "geostrophic" moorings (M1-M3) equipped with density sensors and current meters in the vertical as well as combined bottom pressure recorders/ inverted echosounders (PIES). A further current meter only mooring (M4) is located on the western continental rise. The locations of the 6 GAGE current meter moorings are displayed as well. The main target of MOVE are transport fluctuations in the NADW layer (gray shading). Courtesy of C. Begler. Bottom: The MOVE array (M1-M5) is bounded by the Lesser Antilles Arc (Guadeloupe) in the west and the Mid-Atlantic Ridge (Researcher Rise) in the east. Also shown are the current meter moorings of the GAGE experiment. The triangular area between the western continental rise west and mooring M3 is subsequently referred to as western boundary triangle.*

(GAGE, operated by M. McCartney and C. Mauritzen). GAGE has its focus on the abyssal offshore northward recirculation of deep NADW and Antarctic Bottom Water (AABW) (McCartney, 1993; Lux et al., 2001). By merging and mutually complementing the MOVE and GAGE moorings, current meter measurements at 6 depth levels below 1600 m were obtained from February 2000 and April 2002 (final recovery of the GAGE array) from the 10 moorings at the 16°N section (Fig.2.1, bottom). With a baroclinic Rossby radius in the order of 70 km in this region (Chelton et al., 1998) this combined array with a horizontal mooring spacing of about 120 km was not designed to resolve completely the horizontal scales of the flow (especially in the DWBC) on subinertial time scales. However, the joint current meter array can guide the referencing of the geostrophic velocities (see chapter 6).

The experiment location was selected such that it has to fulfill several "geometric" requirements: In the west the continental slope ought to be steep such that only a small fraction of the southward DWBC would pass inshore of the geostrophic array (M3-M1) through the western boundary triangle (west of M3) over the continental slope. That way the number of current meter moorings required west of M3 was kept reasonably small. To make the geostrophic monitoring approach feasible, the topography between M1 and M3 should preferably be flat and at least not rise above the levels of the end points (i.e. 5000 m). Also, to reduce transport errors from geostrophy, the array should be deployed sufficiently far from the equator and have little meridional extent to avoid ambiguities from the latitudinal dependence of f (equation 1.1). Furthermore the zonal extension of the array should cover the whole western basin of the Atlantic to capture potential interior recirculations (McCartney, 1993; Lee et al., 1996; Lux et al., 2001) and still preferably be small. The location at approximately 16°N (Fig. 2.1, top) meets these requirements in an optimal manner. In the west the array is bounded by the Lesser Antilles arc and in the east by the Researcher Rise (a westward extension of the Mid-Atlantic ridge).

Furthermore, dynamic requirements had to be met, for which this location seems suitable: As transport fluctuations on up to inter-annual timescales are this study's target, seasonal and higher frequency variability should be sufficiently small. On the one hand this requirement necessitates an adequate distance from North Brazil Current (NBC) rings, which very rarely make their way up to 16°N (e.g. Glicksen et al., 2000). On the other hand numerical simulations based on the FLAME 1/3° model (see Appendix A.1) suggest an increase in seasonal transport variability towards the subtropics. Also, the deep southward flow in the North-Atlantic only becomes focused on the western boundary somewhere in the subtropics according to various numerical models (pers. communication D. Stammer). Accordingly, a too northward location of the experiment would have required additional measurements in the eastern basin of the Atlantic, involving much more instrumentation and ship time. Based on the above constraints the 16°N section thus appears to be a good choice.

2.3 ACCP-3 Experiment

During October 1995 and June 1997 an experiment was carried out within the framework of U.S. WOCE (Word Ocean Circulation Experiment) to monitor the strength and variability of the DWBC in the subtropical North Atlantic, off Abaco (26.5°N). The design of the ACCP-3 array (Atlantic Climate Change Program) resembles that of MOVE in many aspects (see Figs. 2.2 and 2.3 for an overview). The interested reader is referred to JKZ2004 for a detailed description. The experiences the author gained from analyzing the ACCP-3 data set (together with W.E. Johns and R. Zantopp) were invaluable for the interpretation of the MOVE data. Most importantly, the design of the ACCP-3 array allowed for the verification of measuring current velocities with the endpoint monitoring approach (used in MOVE) by means of direct current measurements:

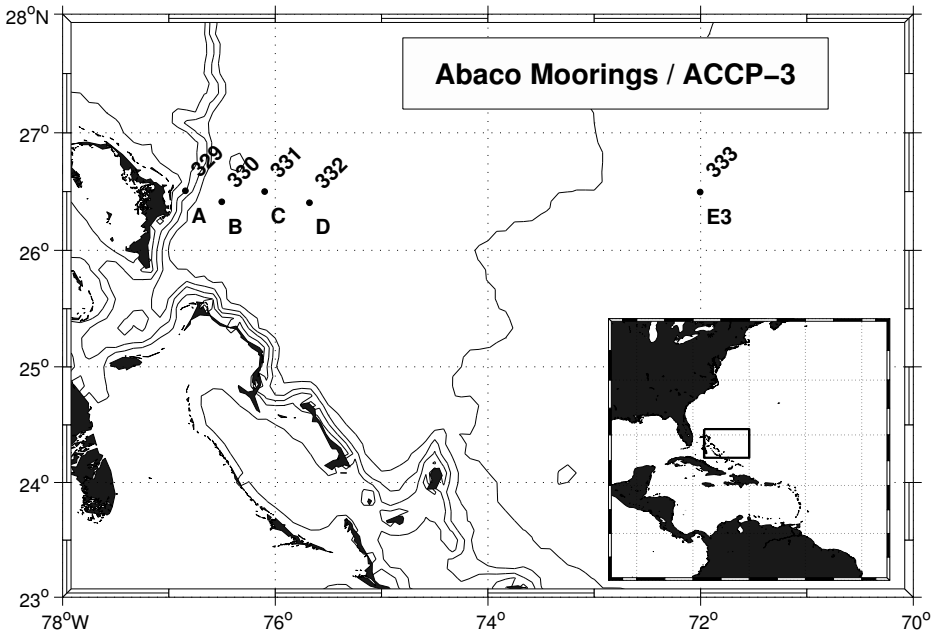

Figure 2.2: *Location of ACCP-3 mooring array on the western continental margin of the North Atlantic. Moorings A-D form a coherent array near the western boundary while mooring E is located approximately 500 km offshore. Bottom contour interval is 1000 km.*

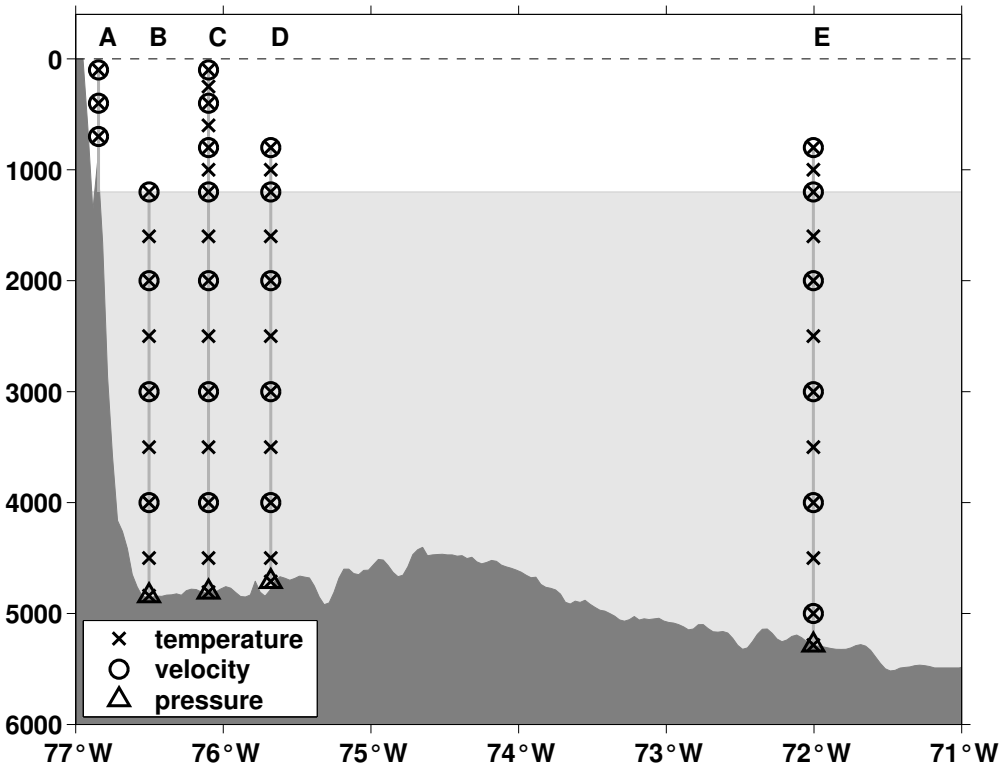

Figure 2.3: *Moored instrumentation during ACCP-3.*

The moorings B,C and D in Fig. 2.3 form a coherent array with a horizontal spacing of only 40 km, which corresponds to the baroclinic Rossby radius in this region (Emery et al., 1984). Current meters were deployed at 4 levels between 1200m and the sea-floor. Additionally each mooring was equipped with a bottom pressure sensor and 9 temperature sensors (below 1200m) to allow for a computation of geostrophic velocities. One important difference to MOVE is that ACCP-3 lacked conductivity sensors. Thus, salinities needed for the computation of internal velocities were estimated from temperatures using an empirical $\theta - S$ relationship. This and other differences as well as their consequences will be addressed in this study. Even though exhibiting a technically simpler design, the ACCP-3 experiment can be regarded as a prototype for MOVE and it will be referred to frequently.

2.4 Verification of the End Point Approach

The success of the end-point monitoring strategy used in MOVE depends on the degree to which the geostrophic balance holds. Therefore its validity will be verified in the following by theoretical arguments, model simulations as well as observations. A recent citation from Condi and Wunsch (2004) says that "on time scales longer than about 1 day, on spatial scales greater than about 10 km, and at latitudes farther from the equator than a few degrees, the ocean tends, to a very high degree of accuracy, to be in hydrographic, geostrophic balance" (away from its boundaries). Similar statements can be found frequently in literature and these are usually supported by scaling analysis of the equations of motion (e.g. Pond and Pickard, 1978). Indeed, much of today's knowledge of large scale ocean circulation has been obtained by computing internal velocities from hydrographic data that oceanographers have acquired for many decades (e.g. Defant, 1941). It should be added that near the ocean surface in the so called Ekman layer currents driven by wind stress are superimposed on the geostrophic flow.

As the MOVE current measurements show, velocities in the DWBC at times exceed 50 cm/s (Fischer and Schott, 1997) and thus, frictional and non-linear terms might corrupt the assumption of a purely geostrophically balanced flow. For example, when flow paths are curved, as is the situation in eddies and meandering currents, the centripetal force exerted on the water parcels might upset the geostrophic balance (e.g. Apel, 1995). The importance of non-linearity can be estimated from Rossby number $Ro = \frac{U}{fL}$, which is the ratio of advective to geostrophic velocities, with U and L denoting a characteristic velocity and spatial scale of the flow, respectively. It is shown in chapter 4.3 that an integration of the flow over several hundreds of kilometers using the MOVE end-point moorings (say, $L = 500km$) yields net velocities < 5cm/s. The corresponding Rossby number (with $f = 4 \cdot 10^{-5} s^{-1}$) does not exceed 0.04 at 16°N. Following this scaling argument, the flow can be considered geostrophically balanced "to a very high degree of accuracy".

Further convincing evidence for the validity of the geostrophic balance comes from a simulation using a high-resolution FLAME 1/12° model (see Appendix A). Its high resolution allows to resolve eddy dynamics to a large extent, which might possibly upset the geostrophic balance. In Fig. 2.4 true model transports between 60.5° and 51.5°W across 16°N are contrasted to those derived from model dynamic height from the section's endpoints. This simulation mimics the MOVE measurements at M3 and M1. A good agreement between the two transport curves can be observed, with small deviations visible only on very short time periods of < 10 days. This can be taken as a confirmation that on longer time scales the geostrophic relationship represents a rather accurate approximation for the zonally integrated flow. On the other hand, it does not mean, that the current variability in the band between the period of inertia $\frac{1}{f}$ and 10 days displays significant departures from the geostrophic balance, since the time series in Fig. 2.4 are composed of 3-day snapshots. If for example 3-day averaged values would have been available

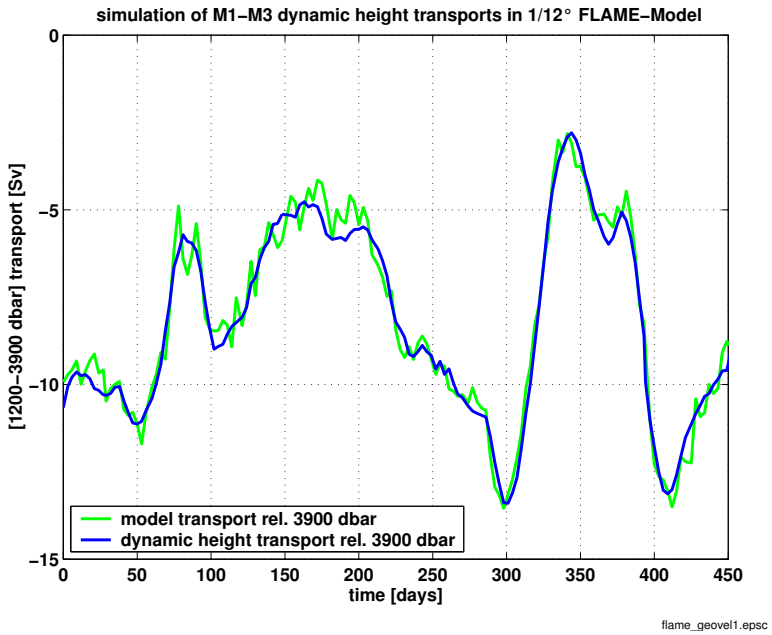

Figure 2.4: *Simulation of the MOVE monitoring approach in the FLAME 1/12° model: Meridional transports across 16° N in the 1200-3900 dbar range (rel. 3900 dbar) are displayed, integrated between 60.5° W and 51.5° W, the endpoints of the MOVE array. The blue and green lines indicate transports from the model's true velocity output and computed from the dynamic height at the endpoints at 60.5° and 51.5° W (corresponding to the positions of the MOVE moorings M3 and M1), respectively.*

instead, the blue curve representing the true model transport, would most likely have displayed much less variability on these short time scales, such that the agreement between the two curves would have been better in the high frequency limit as well.

Observational evidence for the validity of the geostrophic balance is obtained from the ACCP-3 experiment (Fig. 2.5, lower panel). Here geostrophic and directly measured flow below 1200m in the DWBC between the sites B and D are compared (see Fig. 2.3 for nomenclature). Both graphs display a reasonable agreement in amplitude as well as phase over most of the time series, which means that the geostrophic balance is thus found to hold in the DWBC as well. Deviations are largest before day 30 and after day 480 (i.e. near both endpoints of the time series) and are most likely caused by measurement problems and not by departures from geostrophy, since both measurement techniques suffer specific errors. While on the one hand the horizontal scales of the flow were not fully resolved by the current meter measurements, residual instrumental drift of the bottom pressure sensors contaminated the external velocities (see discussion from JKZ2004 and chapter 3.6 of this study). Moreover, internal transports should be regarded with particular caution after day 470 (see caption of Fig. 2.5 for a detailed explanation). The r.m.s difference between the two records amounts to 8.9 Sv. Apart from measurement uncertainties, also the dynamical environment, in which these observations were carried out, represents per se a bigger challenge for the geostrophic balance to hold. With a zonal integration scale (between moorings B and D) of only 80 km (unlike up to 1000 km in the MOVE case) and measurements having taken place in a regime exhibiting horizontally averaged flow speeds of up to 25 cm/s, Rossby numbers may reach 0.2. But nonetheless, with error estimates of each of the two techniques being O(5 Sv), both records agree within their error bars (JKZ2004), such that the geostrophic balance can be regarded a good approximation. In conclusion, theoretical arguments, simulations using an eddy resolving model as well as observations in a challenging environment suggests no significant departures from the geostrophic balance in the deep ocean, when integrating over sufficiently large spatial scales. Therefore the MOVE endpoint mooring design can be regarded

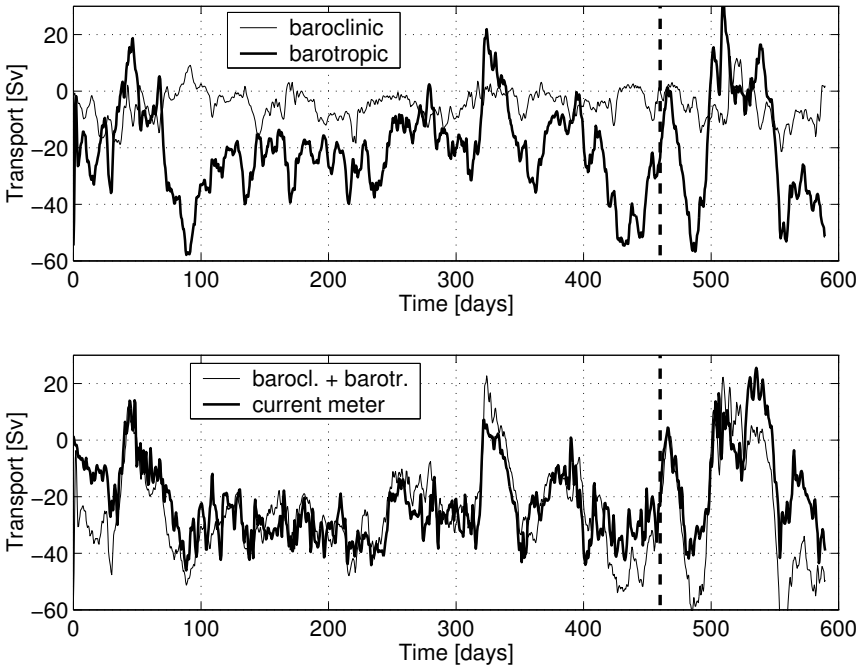

Figure 2.5: *Meridional transports in the DWBC regime below 1200 dbar from the ACCP-3 array, integrated between the sites B and D (see Fig. 2.3). Upper panel: Internal and external transports, here referred to as barotropic and baroclinic, respectively. Lower panel: Absolute geostrophic (i.e. sum of internal external contributions (thin line) and directly measured (bold line) transport. This Figure has been published by JKZ2004. The dashed vertical line near day 470 denotes the point of time when the top flotation at site B was lost. Afterwards, mooring B exhibited a very low positive net buoyancy, such that it became subducted deeper than 2000m during strong current events. Accordingly, the internal transports probably display large error margins and should be used with caution.*

a reliable tool for transport monitoring at time scales larger than the period of inertia.

2.5 Summary

In this chapter a detailed description of design of the MOVE experiment has been given. It was shown that a number of requirements (geographic, geometric, dynamic) have to be accounted for, which are assumed to be met with the current design and geographic location. Subsequently the ACCP-3 array has been introduced. Finally, the geostrophic balance was shown to hold to a high degree of accuracy under the measurement configuration applied, which represents the basic requirement for the MOVE experiment to successfully monitor deep integrated transport fluctuations.

It should be added that in the beginning of 2004 a new monitoring system started its operation in the Atlantic: Within the UK RAPID project the MOC will be continuously observed at 26°N. It is found from simulations based on numerical models that by continuous density measurements over the entire extent of the water column at the western and eastern end points of the western and eastern trough of the Atlantic, the mean strength of MOC and its fluctuations can be monitored accurately, when Ekman transports are accounted for the Florida Current transports are measured directly (Hirschi et al., 2003), which is done by voltage measurements (e.g., Larsen and Sanfort, 1985). Whether these findings apply for the real ocean as well, has yet to be demonstrated.

3 Acquisition, Calibration and Processing of Data and Sensor Performance

3.1 Introduction

This chapter deals with the important aspects of calibration and processing the hydrographic and bottom pressure data. After general remarks on density and bottom pressure, the moored instruments are presented briefly. To reduce errors in the internal NADW transports to ± 1.5 Sv, which is the error limit of this method (Kanzow, 2000), accuracies in temperature and salinity measurements of $\pm$ 0.002 °C and 0.003 have to be reached, respectively. The calibration technique to meet these standards is described. Additionally, the calibration data acquired during 5 mooring service cruises allows for an assessment of the sensors' long-term performance. This is followed by processing aspects of the moored dynamic and bottom pressure data. The bottom pressure records are contaminated by long-term instrumental drift. The consequences of the empirical drift removal for signal characteristics of the external transport is simulated using output from a numerical model.

3.2 Short Remarks on Density and Bottom Pressure

Prior to describing the measurements used in the MOVE experiment some introductory sentences are spent on the two main variables of interest, i.e., density and bottom pressure. Thereby the emphasis lies on bottom pressure, which cannot be considered such a standard variable as density in physical oceanography, such that the reader may only have marginal background knowledge about it.

Density measurements have been key tool for many decades to study the most basic oceanographic aspects, such as general circulation patterns, heat transport, water mass formation and distribution as well as mixing. In the deep waters of the low-latitude ocean away from water formation regions, from the direct influence of Ekman pumping and from surface fluxes of heat and freshwater, changes in the density structure are dominated by horizontal advection and therefore are mostly limited to lower frequency variability, involving mechanisms such as Rossby waves (periods longer than several months) or changes in the thermohaline circulation (decadal time scales).

Although bottom pressure measurements have been used in oceanography for several decades (e.g., Filloux, 1980), until today they have only sporadically been applied to determine the variability of the flow field, in contrast to density or direct current measurements. Whereas dynamic height yields the steric expansion of sea water as a consequence of its density depending on temperature and salinity, bottom pressure fluctuations correspond to mass changes in the overlying ocean-atmosphere system. The most dominant signature in bottom pressure records is generally that of daily and semi-daily tides. The ocean's response to atmospheric mass (or pressure) forcing can be approximated to that of an "inverted barometer" (IB), which means that a decrease in sea level atmospheric pressure by 1 mbar results in a rise of the sea level by 1 cm. From analysis of altimeter data, this has been shown to hold well in extra-tropical

regions (Fu and Pihos, 1994; Gaspar and Ponte, 1997) with regression coefficients of about -0.9 cm per mbar. The IB compensation is generally established within not more than few days. Due to the accomplishment of this pressure compensation right at the sea surface, only negligible geostrophic flow is associated with atmospheric pressure forcing. Largest parts of departures from the IB response in extra-tropical regions are explainable by wind forcing (Ponte and Gaspar, 1994), but small contributions may also result from the dynamic response of the ocean to atmospheric pressure in the form of gravity and Rossby waves (Wunsch and Stammer, 1997). Deviations from IB response (-0.7 to -0.8 cm per mbar) are observed in the tropics as a result of the frequency band of free waves being wider than in the extra-tropics (Fu, 2001). However, the tropical atmospheric pressure forcing is generally small with r.m.s. signals of 0(2 mbar) when compared to 0(15mbar) in the Southern Ocean.

Therefore, bottom pressure signals at periods longer than one week will mainly reflect local wind forcing through Ekman convergence as well as barotropic Rossby waves. Also, advective changes of the density structure of the water column (going along with changes in the circulation) and hydrological signals (evaporation, precipitation, continental freshwater discharge) may be observed. On decadal or longer time scales vertical displacement of the sea floor (e.g. due to post-glacial rebound or plate tectonics and volcanism) might have a non-negligible influence in certain (mostly coastal) regions.

3.3 Instrumentation and Data Acquisition

DATE	CRUISE	TASK
Feb. 2000	RV KNORR 161	joint deployment of MOVE and GAGE
Jan. 2001	FS SONNE 153	recovery and 2nd deployment of MOVE
Feb. 2002	L'ATALANTE	recovery and 3rd deployment of MOVE
Jun. 2003	FS SONNE 172	recovery and 4th deployment MOVE
Feb. 2004	FS METEOR 60-4	recovery and 5th redeployment MOVE

Table 3.1: *Schedule of cruise carried out within the framework of MOVE. During all of these cruises in-situ calibration checks of the moored instruments were carried out prior to mooring deployments.*

The MOVE moorings were first deployed in February 2000 and are replaced at approximately annual intervals (Table 3.3). Data from four different types of moored sensors were acquired, namely MicroCAT, MTP, Aanderaa current meter and PIES. The MicroCATs manufactured by Sea-Bird Electronics carry an aged thermistor for temperature observations. Sea water conductivity is acquired by conductance measurements with an electrode cell. According to the manufacturers the main advantage of the Sea-Bird cells is that the electric field is fully internal, which guarantees a stable and undisturbed cell geometry. Some of the instruments are also equipped with pressure sensors by Druck Inc. which are based on piezo-resistive silicon technology. The data return rate from the recovered MicroCATs has proven to be better than 95%.

The pressure sensor of the MTP is built by Keller AG and makes use of the piezo-resistive technology as well. With 0.1% its typical accuracy resembles that of Druck. The data return rate of the MTP has been better than 80%. The PIES, which are manufactured by R. Watts (University of Rhode Island) use a high precision Paroscientific pressure sensor featuring a dual beam quartz resonator technology. Paroscientific indicates the accuracy and resolution of its sensors with 0.01% and 0.0001% of full scale, respectively. The data return rate of the PIES have reached about 90%. In one case a Bourdon tube bottom pressure sensor with electrooptical

feedback (Filloux, 1980) was used. Those devices have a comparable resolution to Paroscientific but do not measure absolute pressures. They are equally reliable but lack a built-in correction of the temperature dependence of the pressure measurement. The latter has been found empirically using regression analysis (see section 3.6) and has been applied after the recovery of the Bourdon tube. The PIES' travel time measurements (from the inverted echosounder) reach a resolution of 9 microseconds.

Initially the majority of the Aanderaa current meters consisted of the well-known RCM8 type. Those instruments still use the traditional concept of rotor and vane, which encounters problems in measuring low current speeds accurately. Step by step the RCM8 types are replaced by acoustic RCM9/11 instruments. The data return rate here is better than 90 %. In the American GAGE experiment conventional EG&G VACM (vector averaging current meter) were used, originally developed in the 1970s. The instrumentation used in the ACCP-3 experiment is described by JKZ2004.

During all of the cruises mentioned in Tab. 3.3 CTD profiles used for the in-situ calibration of the MicroCATs and MTDs have been acquired. Additional CTD data covering the MOVE 16°N section have been supplied for this study by the group of M. Rhein (University of Bremen) from two cruises in December 2000 and June 2002 aboard FS SONNE and FS METEOR. On the same cruises the 16°N section has also been covered by lowered acoustic Doppler profiler (lADCP) measurements, which are used in chapter 6 for the referencing of the geostrophic transport fluctuations.

3.4 Calibration of Temperature, Conductivity and Pressure

Prior to the first deployment in February 2000 the planned mooring design (i.e. the number of MicroCATs and MTP required and their vertical positioning within the moorings) had been simulated and optimized based on historical CTD data (Kanzow, 2000). In summary, accuracies of internal transports from dynamic height of about 1.5 Sv in the depth range of 1200 - 5000 m can be reached under the following conditions: About 15 MicroCATs are required, which need to be calibrated thoroughly (to ensure accuracies of better than 0.002°C and 0.003 mS/cm ≡ 0.003 psu) and whose instantaneous depths have to be known within ± 5 meters. To meet this baseline the moored MicroCAT temperatures (T) and conductivities (C) as well as the MTP pressures (P) are carefully calibrated in-situ against a Seabird CTD probe, before and after each deployment period (in total five times so far, see Tab. 3.3). That way, a linear drift correction of the following type can be applied

$$\begin{bmatrix} C \\ T \\ P \end{bmatrix}_{cal}(t) = \begin{bmatrix} C \\ T \\ P \end{bmatrix}_{raw}(t) + \frac{t}{\Delta t}\left(\begin{bmatrix} \Delta C \\ \Delta T \\ \Delta P \end{bmatrix}_{pre} - \begin{bmatrix} \Delta C \\ \Delta T \\ \Delta P \end{bmatrix}_{post}\right) - \begin{bmatrix} \Delta C \\ \Delta T \\ \Delta P \end{bmatrix}_{pre} \tag{3.1}$$

with the indices *cal* and *raw* referring to calibrated and raw time series. The Δ indicates MicroCAT (or MTP) minus CTD differences from the in-situ calibration obtained prior (pre) and after (post) the deployment, whose time and duration are given by t and Δt.

First discuss some essential technical aspects of a precise calibration are discussed. Subsequently the long-term performance of the sensors is addressed. Reference CTD temperature, conductivity and pressure have all been calibrated according to the WOCE standard, i.e. ±0.002 °C, ±0.002 mS/cm and 0.02% in pressure (Saunders et al., 1991). The ultimate goal of this MicroCAT calibration is to reduce the uncertainties in T and C to below ± 0.002 °C and below ± 0.003 mS/cm, respectively (relative to the CTD). This can only be achieved when the MicroCAT sensors themselves exhibit a drift during a deployment of not much more than 0.01 °C or 0.01

mS/cm. Otherwise the assumption of a predominantly linear drift during the deployment may not be a good approximation.

The in situ calibration has to be carried out with care. Normally up to 14 MicroCATs are attached to the CTD rosette frame which sample at their highest rate (i.e. 10 s). Best results were obtained when comparing MicroCATs against the CTD in the deep ocean below 2000 m. The surface mixed layer does not provide a stable enough environment for the accuracy requirements stated above and the strong vertical temperature and conductivity gradients in the thermocline would add strong depth dependent offsets to the comparison. Figure 3.1 shows the vertical conductivity gradient from a CTD profile. At a depth of 200 m the gradient is

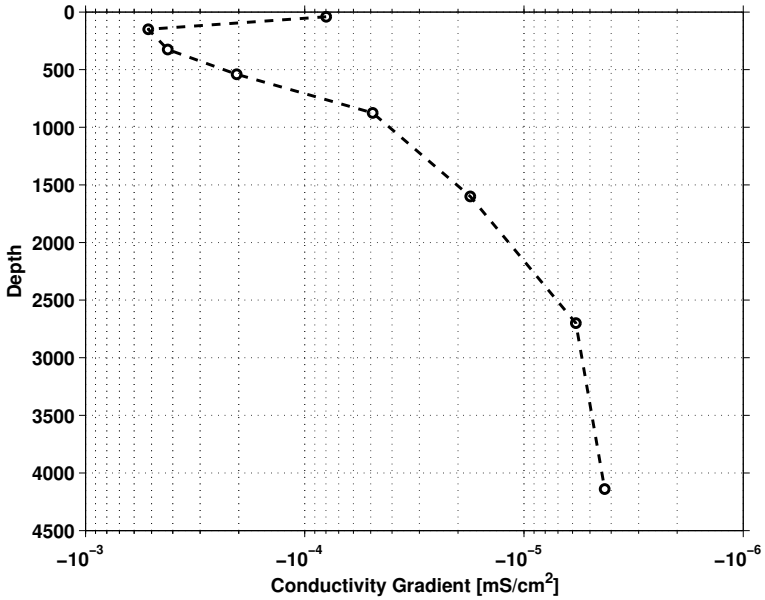

Figure 3.1: *Vertical conductivity gradient [mS/cm^2] derived from a CTD profile at 15.4° N / 51.5° W. The the pressure dependence of conductivity has been substracted prior to the computation. Note the logarithmic scale of the conductivity gradient.*

$-5 \times 10^{-4}\, mS/cm^2$. Provided there would be a depth difference of 1 m between vertical position of the CTD and a MicroCAT attached to its frame (which for practical reasons is often the case), this would result in an offset of $5 \times 10^{-2}\, mS/cm$ (or about 0.05 psu in terms of salinity). Below 2000 m depth this effect is reduced by 2 orders of magnitude and thus becomes insignificant. Temperature records are affected in a similar way.

Due to the equilibration times and sampling rate of the MicroCAT sensors, accurate calibrations can only be obtained during bottle stops, i.e., when the CTD does not exert a strong vertical movement and thus the environment is not subject to large changes. The limiting sensor in terms of equilibration time is the conductivity cell. Figure 3.2 shows the typical evolution of a Sea-Bird CTD's (gray) and several MicroCATs' (black) conductivity records during a bottle stop. Upon arriving at the depth of that particular bottle stop (minute 0) the CTD with a sampling rate of 25 Hz almost immediately adapts to the surroundings. Its subsequent slow drift until the end of the bottle stop (minute 9) appears to be real, maybe due to residual vertical movement of the CTD. The large majority of the MicroCATs however (with the notable exception of one instrument), show a quite noisy and fluctuating behavior up to minute 4. The fluctuations of the MicroCATs look surprisingly coherent so that one must assume that this behavior is related to the instruments' internal electronics. While during the first 4 minutes the CTD displays a conductivity change of < 0.004 mS/cm, the MicroCATs drift > 0.04 mS/cm. Accordingly, a comparison between the CTD and MicroCAT should only be made more than 4 minutes after the begin of a bottle stop. The calibration bottle stops (typically each cast has 6-8 between

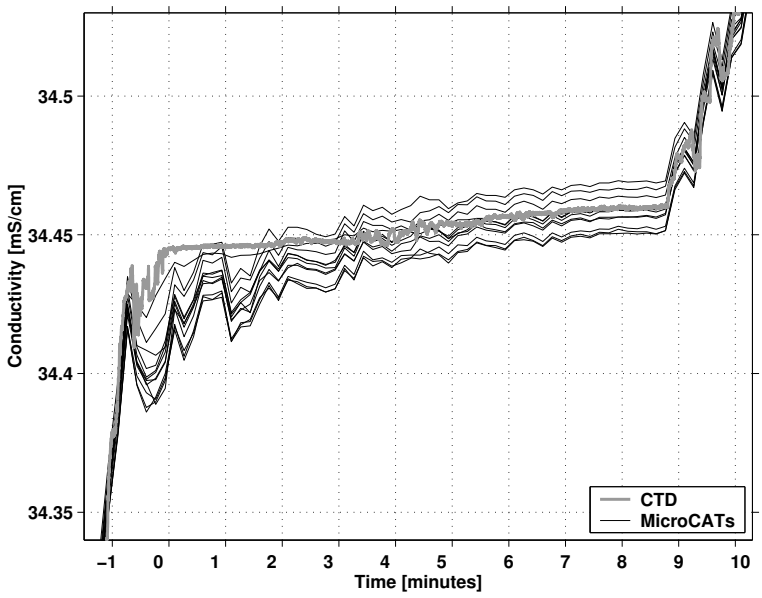

Figure 3.2: *Time series of conductivity records during a bottle stop from the CTD probe (gray) and several MicroCATs (black).*

stops between 1000 and 5000 m) each last around 8 minutes for this reason. It should be added that the strong fluctuations at the begin of the bottle stops show up only in instruments that have been bought before January 2000. The later versions tend to adapt much faster, as can be seen from the positive exception in Fig. 3.2. Nonetheless, this instrument still exhibits a significantly larger drift than the CTD record during the first 4 minutes.

It is further worth noting that conductivity data of MicroCATs which do not have their own pressure sensors need to be depth corrected. The conductivity cell geometry changes with applied pressure and likewise does the conductivity measurement. The simple correction formula for this effect provided by Sea-Bird Inc. (SeaBird-Electronics, 2002) is $\frac{C_{ind}}{C_{true}} = 1 - 9.57 \times 10^{-8} P$, where C_{ind} and C_{true} are the indicated and true conductivity and P denotes pressure in decibar.

Obeying those 3 important items (deep ocean, long bottle stops, depth correction) one obtains depth independent offsets between the individual MicroCATs and the CTD probe, both in temperature and conductivity. In Fig. 3.3 those individual offsets are shown for the 5 in-situ calibrations that have been carried out between the deployments. The MicroCAT temperatures have been performing remarkably stable throughout those 4 years. In addition, no temperature sensor has shown a mean deviation from the CTD reference of more than 0.01 °C. Obvious is also that almost all MicroCATs show a slightly higher temperature than the CTD instrument, with a mean offset between a 0.002 and 0.004 °C (see top right panel of Fig. 3.3). There is no indication that the temperature calibration has changed significantly during those 4 years, as the cruises' standard deviation of ΔT remains constant in time. As said earlier, temperatures can only be corrected to the required $\pm$ 0.002°C, when the sensors' stability during a deployment period is not much larger than 0.01 °C. They clearly fulfill this requirement such that accuracies (relative to the CTD) should amount $\pm$ 0.001°C.

The conductivity deviation ΔC of the individual MicroCATs is typically less than 0.01 mS/cm, however there are few exceptions. Some of the instruments, which have proven to be unreliable, have been replaced by new ones and thus not all of the individual MicroCATs deployed in 2000 were used until February 2004. Still, the conductivity measurements are extremely stable in time and a linear drift throughout each deployment period seems a valid approximation in most

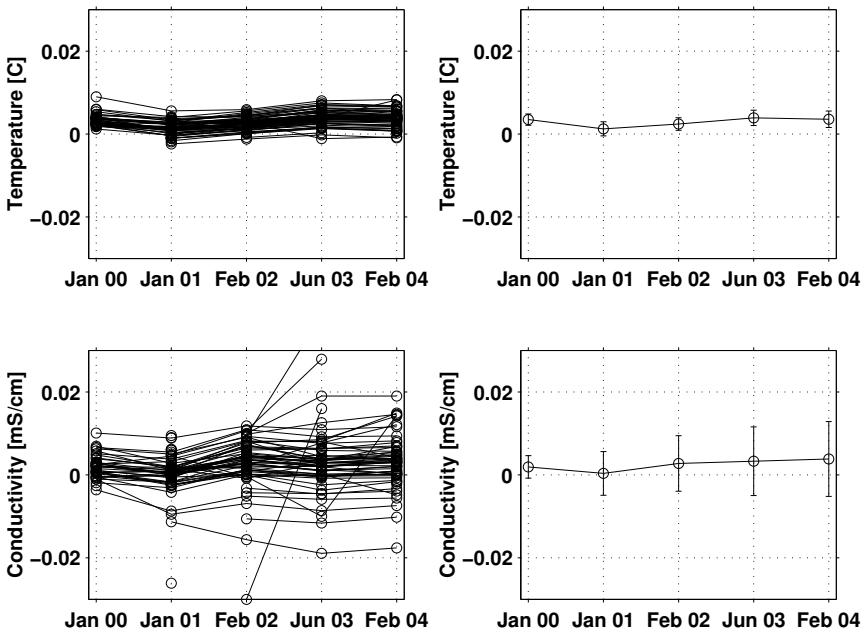

Figure 3.3: *In-situ calibration: differences MicroCAT minus CTD for temperature (top left) and conductivity (lower left panel) for all individual MicroCAT instruments as obtained during the 5 service cruises. Also shown is the cruise mean deviation MicroCAT minus CTD and the standard deviation for temperature (top right) and conductivity (lower right)*

cases. Accordingly, like the temperature sensors also the individual conductivity cells display the temporal stability required to reach accuracies of 0.002 mS/cm after applying the correction. The cruise-mean ΔC increases slowly in time (from 0.002 to 0.004 mS/cm). Similarly the standard deviation, which is a measure for stability, grows from 0.003 to 0.009 mS/cm during those 4 years. The r.m.s. changes in ΔC amount to less than 0.003 mS/cm. It is concluded that the uncertainty in conductivity (relative to the CTD) can be reduced to $\pm$ 0.002 mS/cm.

Concluding, the MicroCATs exhibit an outstanding long-term stability in temperature and as well as conductivity with better performance than indicated by the manufacturer. Their small deviations can be removed such that the remaining error caused by the linear drift correction should typically be about 0.001 °C and 0.002 mS/cm. These errors are meant relative to the CTD reference which itself has uncertainties. But even if an offset from the CTD is added identically to each of the MicroCATs, this is not a problem: in calculating geostrophic currents - which involves density differences - these small CTD-related offsets cancel out almost entirely.

Likewise, the MTP pressures have to be calibrated against the CTD reference to ensure an exact (i.e. time dependent) depth assignment for the MicroCATs during the deployments. As can be seen from Fig. 3.4 the pressure difference $\Delta P = P_{MTP} - P_{CTD}$ displays a depth dependence which has a similar shape for most of the MTP: From the surface downwards ΔP is decreasing and from roughly 1000m onwards growing again until in very large depths it seems to make a turn towards lower values again. Contrary to the MicroCATs (which show no depth dependence against the CTD) here it is important to correct every individual MTP with ΔP obtained at the depth where the MTP is actually located in the mooring. As pre- and post-deployment calibrations have been carried out, again a linear drift correction has been applied according to Eq. 3.1. The long-term stability of the MTP pressures can be studied in Fig. 3.5. Here, the individual offsets ΔP during the 4 years are displayed. For the purpose of demonstration ΔP has been evaluated at 3500 dbar to avoid ambiguities caused by its depth dependence. With the year-to-year differences in ΔP of individual instruments being generally < 5 dbar the linear drift correction should be able to provide MTP pressure time series with residual errors of about

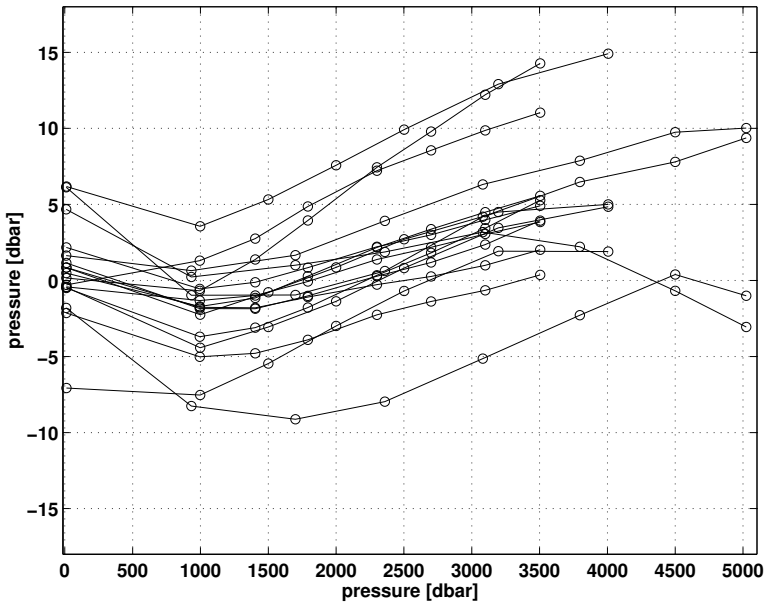

Figure 3.4: In-situ calibration: pressure deviation of individual MTD from the Sea-Bird CTD as obtained during calibration casts aboard FS Meteor in Feb 2004.

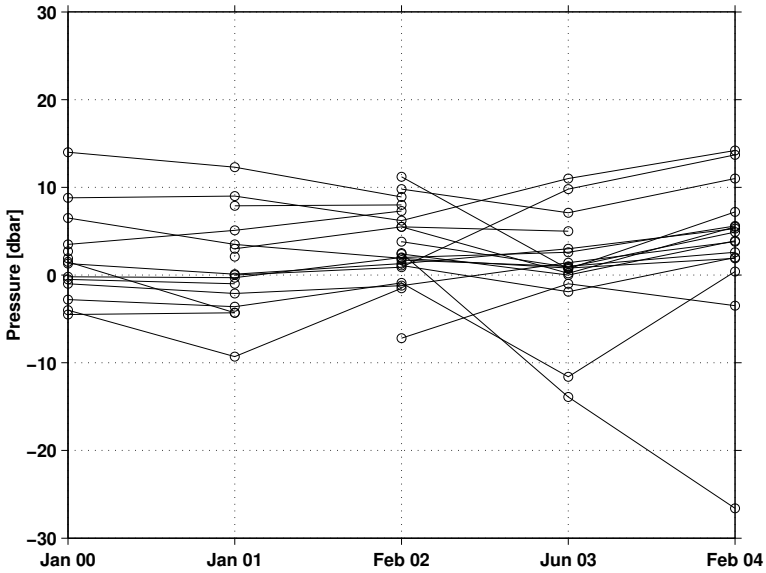

Figure 3.5: *Pressure deviation ΔP of individual MTD from the Sea-Bird CTD as obtained during the 5 service cruises on the KNORR. ΔP has been been evaluated at 3500 dbar.*

1 dbar relative to the CTD standard. The CTD-induced pressure offsets again cancel out with respect to geostrophic velocities.

Concluding, a thorough in-situ calibration of the MicroCAT and MTP sensors is able to correct multi-annual moored temperature, conductivity and pressure measurements with unprecedented accuracy.

3.5 Processing of Moored Hydrographic Measurements

To obtain internal velocities according to equation 1.3, time series of $S(P,t)$ and $T(P,t)$ at the mooring sites M3, M2 and M1 have to be generated, from which $\delta(S,T,P,t)$ is computed.

To ensure high accuracies a thorough depth assignment of the MTPs and MicroCATs within the mooring is necessary throughout the deployment period. When deploying a mooring, which in the MOVE case can be up to 5000 m long, the water depth from vessel-mounted echosounder measurements is originally known within 10-20m accuracy. The exact length of the mooring wires is subject to further uncertainties of few meters and its stretch due to tension from the buoyancy of up to 20 m must be taken into account. Errors of this magnitude are not acceptable: When converting C to S, an inaccuracy in sensor depth of 20m would result in errors in S of 0.01.

Therefore, a careful depth determination is applied: The lowest value of each of the typically 5 MTP pressure time series belonging to one mooring are extracted. It is assumed that they represent the mooring in its upright position. Those pressures are converted to depth via the hydrostatic equation and then compared with the nominal depths of the MTP from the mooring construction plan. The latter is generated feeding a mooring simulation program with the mooring configuration (Berteaux, 1976). The program version that has been use (IMP) takes into account the vertical wire stretch due to buoyancy with high precision (Helmbrecht, 2001) but still comprises the errors from water (i.e. anchor) depth and mooring wire length. Typically, as the error in water depth clearly dominates, one observes a rather depth independent offset between the nominal and the observed MTP depths. By adjusting water depth in the mooring program a good match between the observed and the nominal depths is achieved (uniform vertical offset) which is typically better than 3 dbar for the individual MTP. This gives us confidence that a) the wire and component lengths are very accurate, b) the MTP have been positioned with high precision to the designated depths, c) the pressure calibration yields reliable results, d) the mooring program works well. The actual vertical positioning of the sensors is such that each of the vertically evenly distributed MTP is co-located with a MicroCAT. From those (typically 5) MicroCATs the depth is known better than 3 dbar (relative to the CTD calibration). The depths of the other typically 10 MicroCATs (without direct pressure information) can be obtained from the revised mooring plan. The value of 3 dbar coming from the mismatch the nominal and observed pressures is a realistic estimate for the depth assignment error, comprising residual effects of the 4 error sources mentioned above.

After the static depth assignment, a correction of vertical mooring motion caused by ocean currents is carried out on a 2-hourly basis to resolve tidal periods. This can be very important when tidal flows amplify a strong current event (see Fig. 3.6). In practice the MTP pressures are linearly interpolated onto the MicroCATs, so that for each instrument a pressure time series is obtained. However, Helmbrecht (2001) has shown that during strong current events like displayed in Fig. 3.6, when the western boundary mooring M3 gets subducted by several hundred meters, simple linear vertical interpolation between the pressure sensors might yield errors of several 10 meters in the MicroCAT depths. During those events the IMP mooring simulation program constrained by the observed current velocities and pressures is used to determine the

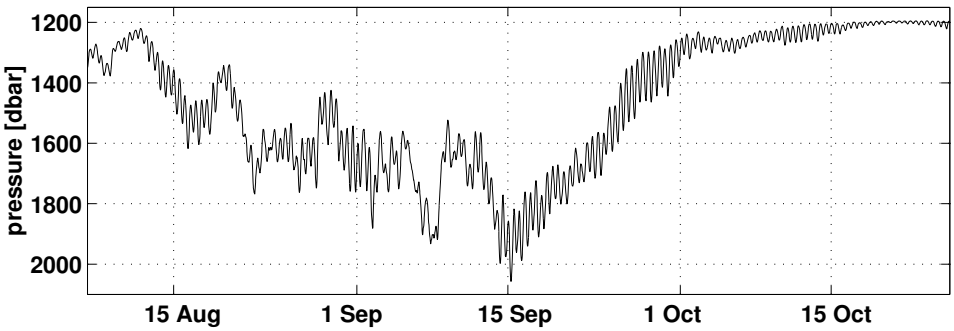

Figure 3.6: *Pressure timeseries of MTP sensor during an extremely strong current event in year 2000 at mooring M3.*

mooring curvature (Helmbrecht, 2001).

Finally S can be computed from the T,C,P time series. Subsequently, T and S are then 48 hour low pass filtered and interpolated onto a regular pressure and time grid of 20 dbar and 12 hours, respectively. From this product quantities like density or δ can easily be computed. The local $\theta - S$ relationship within the NADW is generally stable enough in time for consistency checks (see JKZ2004 and chapter 4.2) . Thus, comparing the moored T and S series to shipboard CTD data acquired in the vicinity of the moorings is a reliable and easy way to perform a final overall quality check of the calibration and processing techniques. The example in Fig. 3.7 shows the

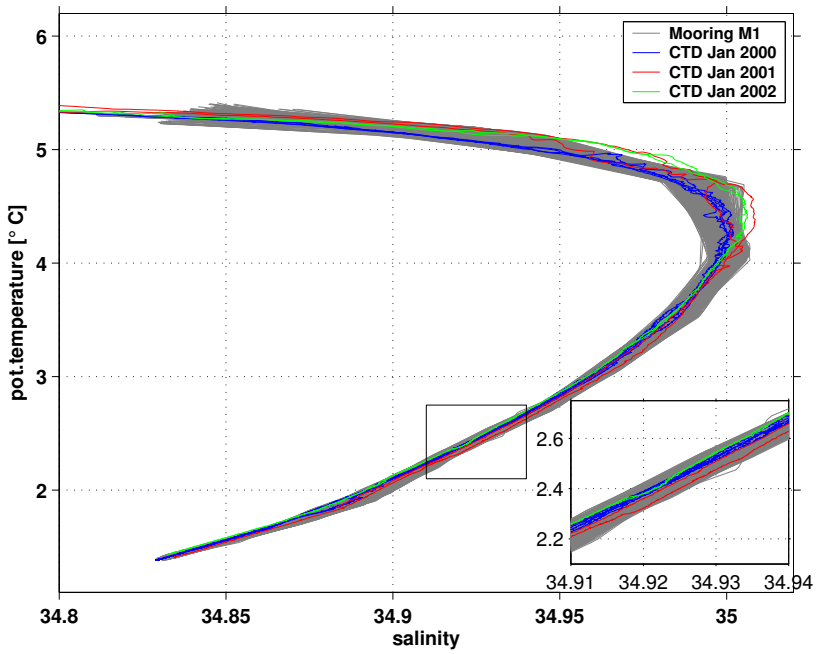

Figure 3.7: *θ - S diagramme from NADW/AABW range: Daily profiles from mooring M1 from the year 2001 deployment period (grey), superimposed are shipboard profiles acquired near M1 in Jan 2000, Jan 2001 and Jan 2002. The close agreement between lowered and moored measurements is confirmed by the inset in the lower right corner.*

good agreement between the mooring and CTD data. Any larger errors in the mooring data would become clearly visible in this kind of comparison. Time series of anomalies of T below 1000m are displayed in Fig. 3.8 for the period Feb 2000 - Feb 2004, showing the whole data availability. The data gaps caused by the mooring service at approximately annual intervals are shortest at the site M1: To economize on ship time this mooring is always recovered last

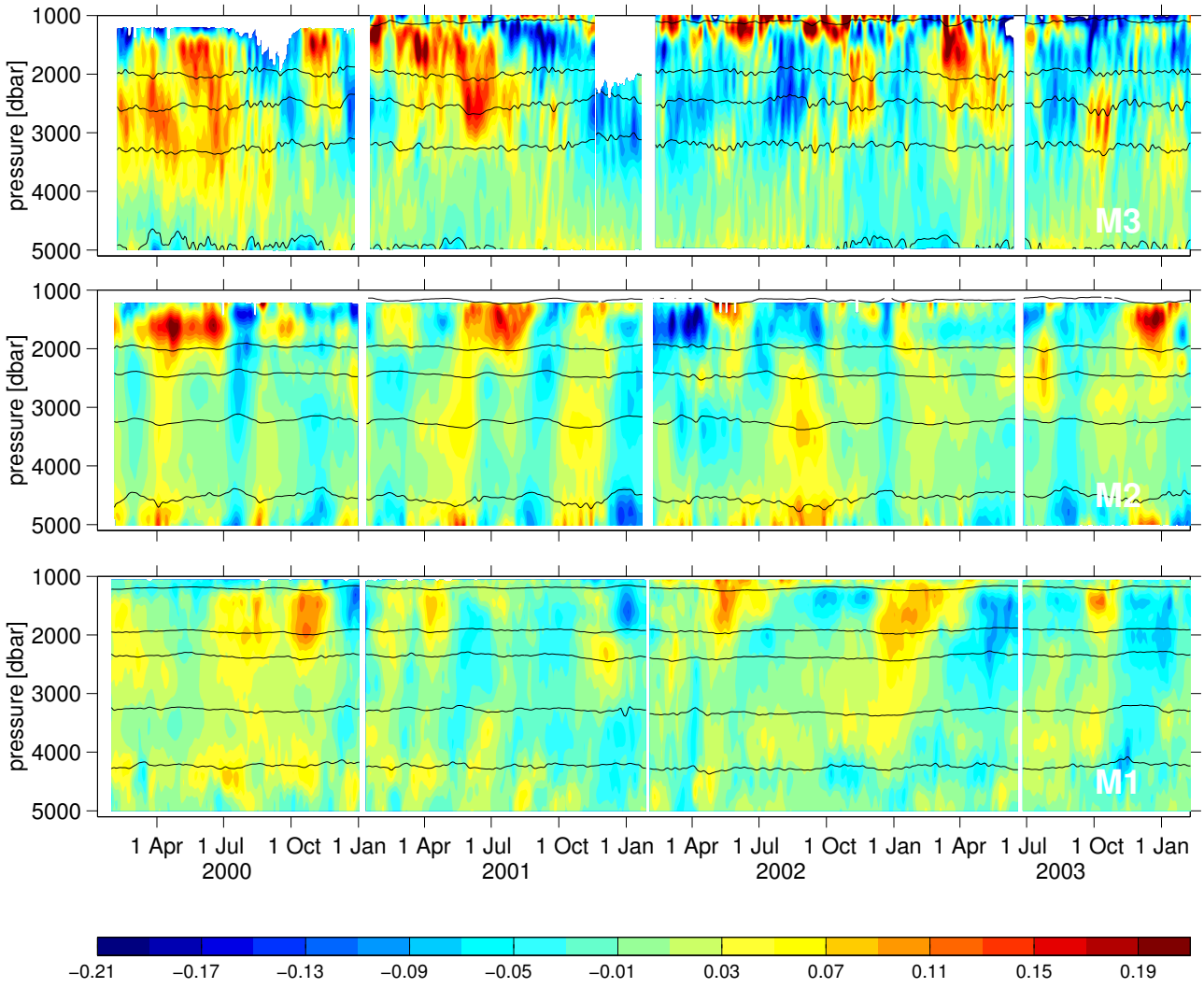

Figure 3.8: *Temperature anomalies from moorings M3 (west), M2 (center) and M1 (east) from Jan 2000 till Feb 2004. Gaps in Jan 2001 and Feb 2002 are due to mooring service. Missing data in the upper NADW range from mid 2001 to Feb 2002 are caused by a mooring breakage. Superimposed are the density levels* $\sigma_{1.5} = 34.42$, *34.70, 34.755 and* $\sigma_4 = 45.83$ *and 45.90. See Fig. 4.2 for details.*

redeployed first. Therefore this site offers the best opportunity for further data consistency checks. The time series of geopotential anomaly (or dynamic height) according to equation 1.2 from mooring M1 displayed in the in Fig. 3.9. The course of the curve across the data

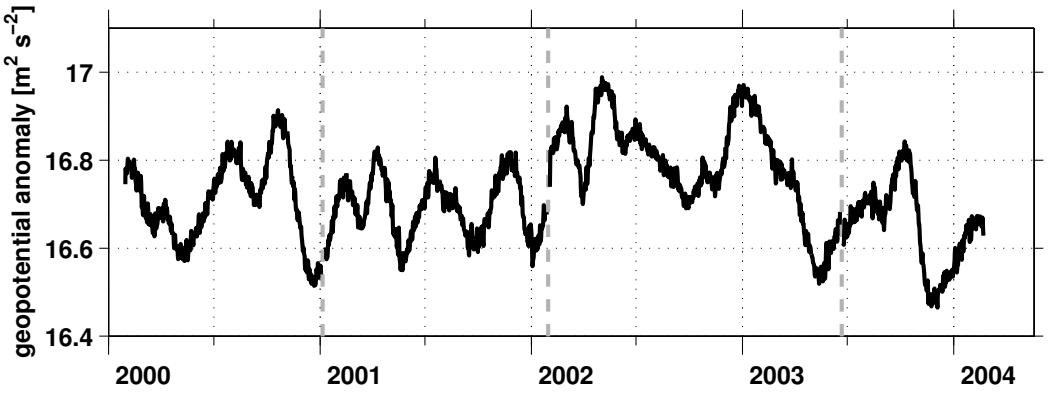

Figure 3.9: *Geopotential anomaly at 1200 dbar (rel. 4950 dbar) from mooring M1 between Feb. 2000 and Feb. 2004. The short data gaps resulting from mooring recovery and redeployment are marked by gray dashed lines.*

gaps (marked by the dashed lines) displays no suspicious jumps: The time series continues as expected after each gap.

3.6 Processing of Bottom Pressure Measurements

The bottom pressure records, exhibiting a sampling rate of 10 minutes, are despiked and subsequently 48 h low-pass filtered (see Fig. 3.10, top) to suppress daily and semi-daily tides. The removal of long-periodic tidal constituents is carried out as the last step of the processing. Therefore it is mentioned later in this section. Clearly, each of the displayed time series exhibits a long term instrumental drift whose rate is largest at the beginning and then decreases with time. Some of the records show an almost linear long-term trend. Interestingly, the sign of the drift is not uniform among the different sensors. The procedure considered to work best to determine the trend characteristics of the digiquartz sensors (used in the PIES) is to apply an exponential-linear least square fit (Watts and Kontoyiannis, 1990)

$$P_{drift}^{PIES}(t) = A[1 - e^{Bt}] + Ct + D \tag{3.2}$$

where t is time since recording begin and A, B, C and D denote the free parameters. For the electro-optical Bourdon tube, the long term drift has been explained entirely in terms of material creep, and thus can be represented as follows (Filloux, 1980)

$$P_{drift}^{Bourd}(t) = \hat{A} + \hat{B}[t + \hat{C}]^{\hat{D}} \tag{3.3}$$

where $\hat{A}, \hat{B}, \hat{C}$ and $\hat{D}$ represent the free parameters.

The typical annual pressure drift rates of the PIES are O(0.1) dbar, which is remarkably small and has been partly reached by pre-pressurizing the sensors prior to deployment for periods of months. The Bourdon's rate (at site M3 in 2001) is about one order of magnitude larger (note condensed scale Bourdon tube drift in Fig. 3.10, top). After subtracting the drift curves, the time series of M3, M2 and M1 become almost indistinguishable from each other (Fig. 3.10, bottom). With the distance between M3 and M1 of 1000 km, horizontal correlation scales of bottom pressures in the tropical North Atlantic are clearly very large, which is a well-known ocean feature (Hughes and Smithson, 1996). This close agreement here already demonstrates,

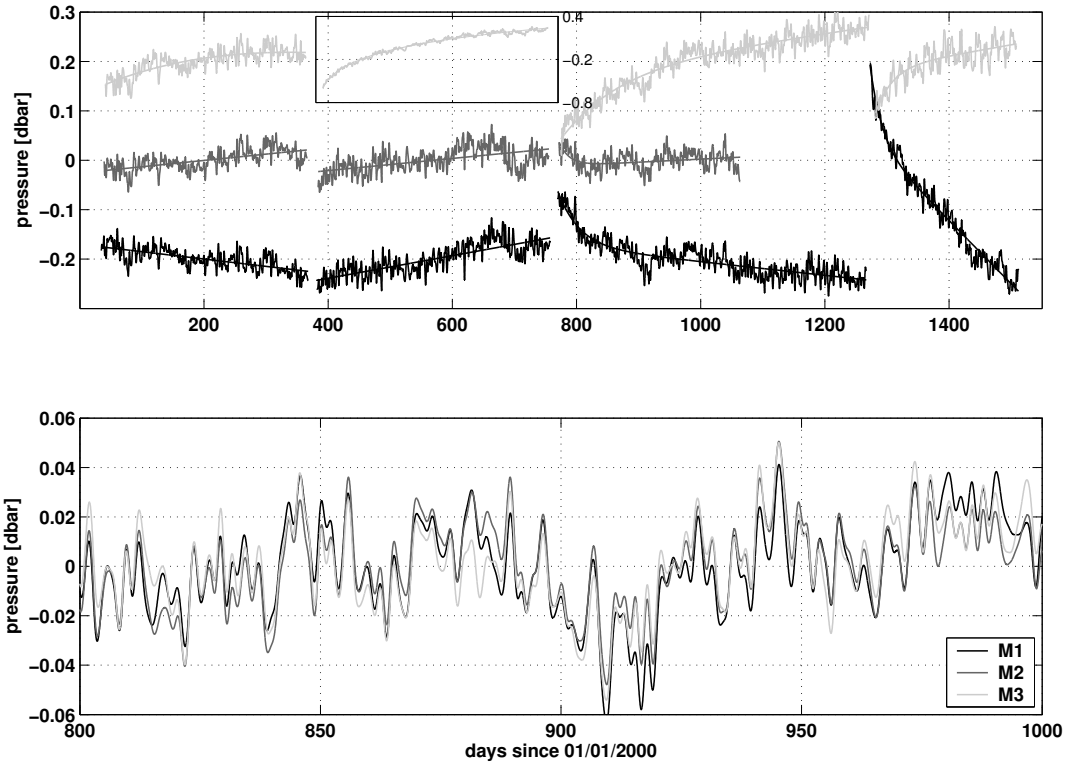

Figure 3.10: *Top: Bottom pressure fluctuations (mean substracted and 48 hour low-pass filtered) from sites M1, M2 and M3. Note the condensed pressure scale for the Bourdon tube in the inset (second time series at site M3). For each time series a least square fit is displayed (see text for details). For better visualization arbitrary offsets have been added. Bottom: Same time series with trends subtracted in the time interval from day 800-1000. Note the extremely high correlation between M1, M2 and M3.*

that sub-centimeter (water column equivalent) bottom pressure fluctuations can accurately be resolved. In the following a more detailed discussion of the expected errors due to instrumental drift is presented.

The drift estimation as described above is a straightforward and widely used procedure, yet it has some consequences that need to be considered in the interpretation of the bottom pressure signal: In Fig. 3.11 (upper panel) two detrended bottom pressure time series obtained simultaneously at M3 by a PIES and a Bourdon tube are compared, which had been moored only few kilometers apart from each other. They exhibit each an r.m.s. variability of 0.021 dbar. In the lower panel

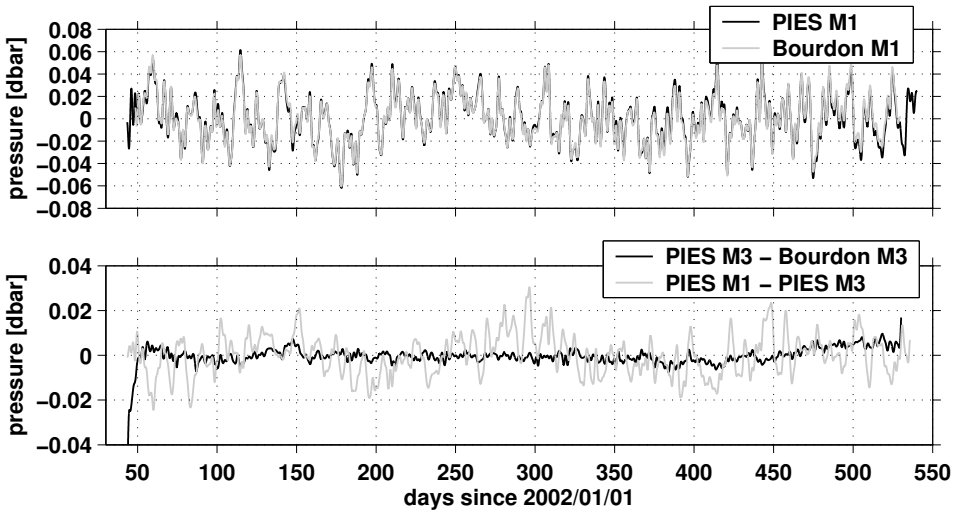

Figure 3.11: *Top: Bottom pressure fluctuations (with trend subtracted) from PIES (black) and Bourdon tube (gray) during the 3rd deployment at site M3. Bottom: Difference of the above time series (black). As a comparison the M1-M3 bottom pressure difference (from PIES) is displayed (gray), which represents variability associated with velocity fluctuations.*

their difference is displayed which yields a strongly reduced r.m.s. amplitude of 0.003 dbar (or 3 mm water column equivalent), when neglecting the first few days. On the basis of this graph the two main disadvantages of the otherwise obviously well working least square detrending procedure can be highlighted: The empirical dedrifting cannot distinguish between instrumental drift and the true ocean pressure signal, so that parts of the ocean signal must leak into the fit on two time scales. Due to the exponential nature of the drift, the least square fit will be susceptible to short-period ocean signals (smaller than the decay-scale $1/B$ in equation 3.2) at the beginning of the time series. This may explain the large and fast decaying difference between the PIES and the Bourdon tube during the first few days. On the other hand, the empirical fit is susceptible to ocean signals of periods in the order of or longer than the time series itself (which about 1 year in this case). Those signals generally have their largest effect on the ends of a time series, because the subtraction of the fit results in flattening of long-term trends. This can be shown from simulations (see also the discussion by JKZ2004). It might correspond to the small but growing differences one observes between the PIES and the Bourdon tube towards the end of the records. The positive aspect is that when neglecting the first few days and last 2 months (where the drift estimate is likely to be most affected by the ocean signal) the r.m.s difference between PIES and the Bourdon tube reduces further to about 0.002 dbar. With both sensors having been deployed a few kilometers apart from each other, at most 50 % of that difference could be possibly be attributed to true ocean signals. This estimate originates from converting typical near-bottom velocities measured by Aanderaa current meters into geostrophic bottom pressure gradients via equation 1.4). A remaining error of 0.001-0.002 dbar may appear negligible at first, but scaled for a 4000 m thick layer at 16°N it corresponds to an uncertainty in cross-array transport fluctuations of 1-2 Sv. For comparison it should be noted that the r.m.s. amplitude of

the signal of interest, i.e. of the difference between bottom pressure fluctuations at M3 and M1 (gray line in lower panel of Fig. 3.11), from which the external transports are derived, is about 10 mm and is thus much larger than the instrumental errors.

A problem however is that due to the presence of a high frequency ocean signal, as visible in all the time series, and largest uncertainties in the drift estimates occurring at the beginning and at the end of each time series, it is impossible to concatenate reliably the annual data segments. The end-point matching technique of Whitworth and Peterson (1985) - according to which data segments from successive deployments can leveled by matching the low-frequency components of the time series - seems somewhat arbitrary in this respect. Due to errors in the leveling an artificial low-frequency variability is likely to be introduced (since an integration results in a spectral shift towards red). Here the successive data segments are simply strung together- each of which is left relative to its time mean - to obtain a "quasi-continuous" multi-annual pressure time series (Meredith et al., 1996). It is clear that this technique is bound to reduce any existing inter-annual variability.

For a deeper understanding the reader is referred to chapter 3.7, where the effect of detrending on long-term bottom pressure variability is discussed in more detail based on model simulations. The most important results are that from annual data segments the annual cycle can only partly be recovered and that the use of multi-year uninterrupted time series would lead to strong improvements. When overlapping segments are available some skill exists for the assessment of variability on periods longer than the duration of the single segments. Additionally on annual and longer time scales bottom pressure measurements could be possibly constrained by satellite altimetry (Schmidt, 2004). Assuming a typical error of a single sea surface height measurement of 2 cm, the annual mean is known within about ± 2 mm, when assuming a weekly sampling rate. To estimate bottom pressure changes from altimetry, the steric contribution of sea level change has to be subtracted. This in turn requires precise knowledge of the full water column vertical density distribution. Those measurements are carried out at the MOVE sites M3 and M1 (since February 2002). In the near future bottom pressure fluctuations derived from satellite measurements of time-varying gravity within the framework of the Gravity Recovery and Climate Experiment, GRACE, (Tapley and Reigber, 2001) over the oceans might serve as an additional constraint for long-term trends in the in-situ observations. However, as will be shown in chapter 8, preliminary results indicate that bottom pressure fluctuations of sufficient accuracy can presently not derived from the ongoing GRACE twin-satellite mission.

Concluding, since the detrended time series from the different stations do not show any strong residual drift relative to each other one may assume that the exponential-linear fit quite reliably eliminates the instruments' drift. However inter-annual variability in bottom pressures and external transports will be underestimated by the applied method in the currently available 1-year deployment segments. This problem can be overcome in future applications by modification in the sensor deployment scheme. Also, on longer than inter-annual time scale external transport fluctuations are thought to be less dominant than the internal ones, as findings from numerical models suggest (Dong and Sutton, 2001). Therefore the apparent problems of this measurement component cannot be regarded a failure of the monitoring system is a whole. Internal transports can be observed without any limitations in the low-frequency range.

Finally, before external transport fluctuations are calculated from the bottom pressures according to equation 1.4, the fortnightly (Mf) and monthly (Mm) tides are eliminated empirically. To a good approximation these should cancel out with respect to transports (as bottom pressure differences are involved). But as has been shown from observations and simulations, small zonal differences in the amplitude and phase exist for Mf, so that tidal residuals might leak into the external transport time series (Egbert and Ray, 2003b). A tidal harmonic fit was applied to the bottom pressure records using the T_Tide toolbox (Pawlowicz et al., 2002), which results in

amplitudes of about 0.0174 and 0.0080 dbar for Mf and Mm, respectively.

3.7 Limitations of Bottom Pressure Signal due to Sensor Characteristics and Processing

How much of the long-term true ocean bottom pressure signal can be recovered from detrended and subsequently concatenated bottom pressure data segments? Being not aware of any explicit study covering this subject, some simple simulations have been performed. The basis are two 8-year-long time series of bottom pressure (1995-2002) extracted from the 1x1°ECCO (acronym for Estimating the Circulation and Climate of the Ocean) model (e.g. Stammer et al., 2003). This model version is constrained by observations such as satellite altimetry using the iterative adjoint technique (see also Appendix A.2). There is little knowledge on inter-annual evolution of bottom pressure (or ocean plus overlying atmosphere mass) from in situ observations due to the sparseness of the presently existing data set and the problems in detrending and concatenating data segments, as described and studies based on altimetry are mostly limited to the seasonal cycle (Chen et al., 1998). The ECCO model however should have some skill in assessing longer periodic fluctuations. The two time series are displayed in Fig. 3.12. They have been selected

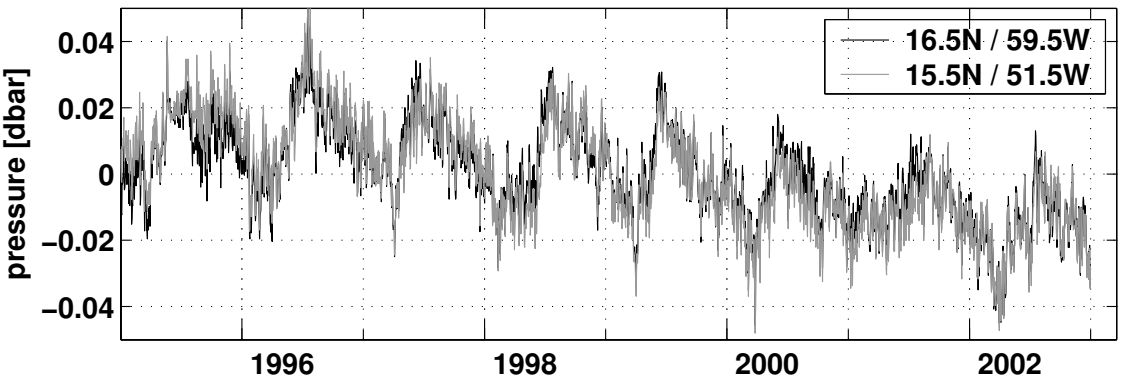

Figure 3.12: *Bottom pressure time series from constrained ECCO model (time mean substracted) from two locations in the tropical North-Atlantic (extracted near MOVE sites M1 and M3).*

such that the one location is close to the mooring site M1 whereas the other is close to M3 in order to simulate as realistically as possible the detrending that has been applied to the observations. Both time series show a long-term trend towards lower values and an annual cycle with an amplitude of 0.01 dbar. It is beyond the scope of this study to assess the causes of these signals and especially whether the long-term trends are realistic or not (the interested reader is referred to Condi and Wunsch (2004)).

Whether real or not, the existence of seasonal and inter-annual signals in the time series offers a good opportunity to simulate the effect of detrending on the low-frequency fluctuations: For this purpose, the 8-year model time series are cut into segments (computations with segment lengths of 1 and 2 years have been carried out). Then to each of the segments an artificial exponential-linear drift (according to equation 3.2) is added to simulate instrumental "raw data" from each deployment period. The drift coefficients A, B, C are determined by a random number generator within the observed limits and are different for each data segment (offset D is a constant). Then for each segment the drift is estimated by applying a least square fit to the data (according to equation 3.2), which yields a best guess $\tilde{A}, \tilde{B}, \tilde{C}$. Those will obviously differ from the true A, B, C, since oceanic signal leak into the fit. The best guess drift is then subtracted from the "raw data", which is exactly the procedure one would apply to observations. The data segment length was varied as well as the way how to subsequently re-concatenate the segments (see Table

segment length	segment concatenation	colour
1 year	segment mean substracted	blue
2 year	segment mean substracted	red
2 year	1 year overlap	green
1 year	end-point matching	magenta
2 year	end-point matching	cian

Table 3.2: *Effect on detrending and subsequent concatenation of data segments: The simulated cases differ in segment length and concatenation technique. Also given is the color in which they are represented in Fig. 3.13.*

A3.2 for an overview). The results of these simulations in terms of bottom pressure difference (between M1 and M3) can be found in Fig. 3.13. All time series displayed are 60 days low-pass

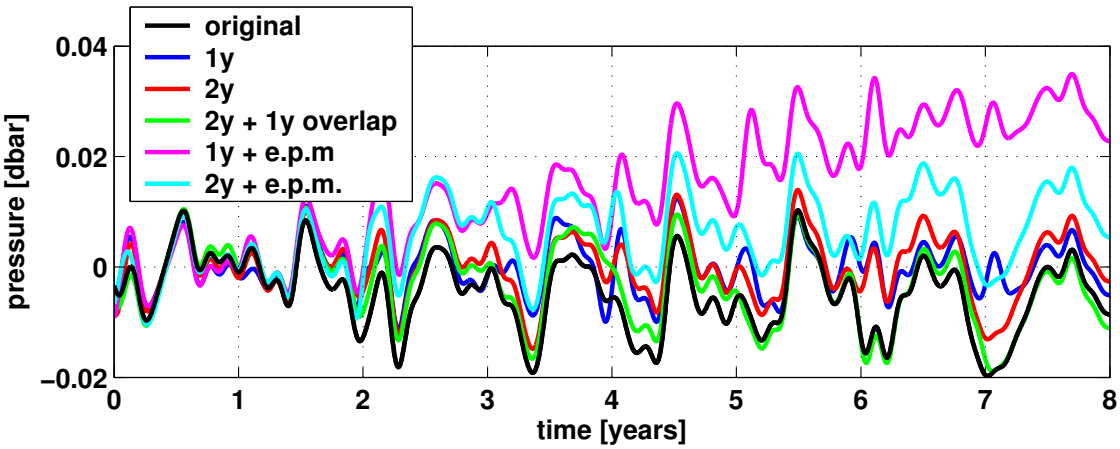

Figure 3.13: *The black line represents the difference of the bottom pressure time series (of ECCO 1x1° model) displayed in Fig. 3.12 (2 month low-pass filtered). The colored lines are the bottom pressure differences resulting from of the various detrending simulations (based on different segment lengths and concatenation techniques, see also table 3.2). Each time series is leveled such that the first year's mean is set to zero. The abbreviation e.p.m. in the legend stands for the end point matching technique.*

filtered (after the simulations were carried out) in order to focus on the long-term variability. The short-term variability is not affected by the detrending.

In the first case, which comes closest to how the observations have been treated so far, a segment length of one year was chosen and the detrended segments were concatenated after simply subtracting the mean from each segment. Compared to the original time series (black line in Fig. 3.13) variability on periods shorter than one year can be recovered well. However the amplitude of the annual cycle is already weakend and the long-term trend cannot be recovered at all. The representation of the annual cycle improves drastically when choosing a 2 year segment length (red line). But of course by subtracting the mean from each segment the longer periodic signals are suppressed by this technique as well.

In the next case under consideration the segment length was kept two years with segments overlapping each other for one year. This simulates a measurement strategy where one keeps two bottom pressure sensors at each site and annually recovers and redeploys the instruments alternately. This would combine annual data retrieval with the availability of 2-year time series. By best adjusting the overlapping time series there is no need any more to subtract the mean from each time series. If the empirical drift removal worked perfectly in the sense that only

the instrumental drift (and no ocean signal would be subtracted), one would be able to recover the true ocean long-term signals with this technique. The simulations show (green line) that the original signal's long-term characteristics is by far best represented using this approach. However at times smaller differences can still be observed.

Finally a very simplified version of the end-point matching technique is put to test. This time data segments do not overlap. The leveling of two segments is carried out such that the average of the first two months of the second segment corresponds to the average of the last two months of the first segment. Thus it is relied upon the continuity of the longer term fluctuations. Theoretically one should recover at least parts of the true ocean long-term trend, if the instrumental drift removal worked perfectly. In the simulation this technique turn out to be very unreliable: The simulations have been carried out with segment lengths of 1 or 2 years, with the latter performing somewhat better. Both simulations (magenta, cyan) display a long-term trend of opposite sign compared to the original time series. The poor capability of the end-point matching technique in recovering long-term characteristic is explainable from the fact that errors in drift removal are generally largest at segments' end-points (see above). The concatenation then results in a temporal integration of those errors, introducing arbitrary long-term trends. It should be noted that the end-point matching described by Whitworth and Peterson (1985) is not done using this objective criteria but is carried out subjectively by eye. That might yield somewhat better results but still is far from being a reliable tool for long-term trend assessment.

Generally it should be noted that these simulations represent only one realization for each case and are per se not statistically representative. But having repeated these simulations several times the results presented here are typical.

Concluding, the simulations have shown that case 1 (annual segments with mean substracted) yields good results for periods shorter than one year. The annual cycle is partly suppressed and there is a complete lack of inter-annual variability. Doubling the segment length leads to an almost perfect recovery of the annual cycle but only when allowing for a 1 year overlap of the segments the long-term trend is well represented. These results can be extended to longer deployments of 4-5 years with 50% overlap. End-point matching cannot be recommended.

3.8 Summary

After a short presentation of the instrumentation used in the MOVE experiment, the in situ calibration and long-term performance of the moored temperature, conductivity and pressure sensors has been discussed. Accuracies in temperature, conductivity and sensor depth of $\pm$ 0.002°C, $\pm$ 0.002 mS/cm and $\pm$ 3 m can be reached using state of the art sensors and a thorough calibration technique in combination with a mooring simulation program. Thus errors in internal NADW transports should amount to less than 1.5 Sv. The uncertainties in this component could be reduced further reduced if the number of MicroCATs and MTD sensors per mooring would be increased. A large degree of consistency is observed between dynamic height records of the different deployment periods. The bottom pressure fluctuations display errors of less than 0.002 mbar. However, as simulations show, the elimination of long-term instrumental drift in the annual data segments leads to a near extinction of possible inter-annual variability of external transports. One solution to overcome this present deficiency is to use longer than annual deployment durations of the bottom pressure sensors, ideally overlapping in time. Also satellite altimetry data might help to constrain long-term bottom pressure trends.

4 Hydrographic and Velocity Fields

4.1 Introduction

This chapter aims to describe the spatial and temporal characteristics of the hydrographic and velocity field with respect to the MOVE transport monitoring approach. First a brief introduction in water mass characteristics and stratification at the 16°N section is given. Subsequently, the temporal variability of the density field and its dependence on salinity and temperature are discussed, followed by an assessment of the stability of the $\theta - S$ relationship, which both have direct implications for the transport monitoring. Then the attention is focused on the deep meridional internal velocity distribution, which is thought to reflect the southward branch of the Atlantic MOC. Also, principal patterns of the time varying internal velocities are presented, followed by a description of external velocities. Finally, current meter timeseries from the DWBC are presented.

4.2 The Hydrographic Field

First basic features of the characteristics of the water masses in the tropical North Atlantic are highlighted, which is required for the later analyzes. The $\theta - S$ diagram in Fig. 4.1 can roughly be

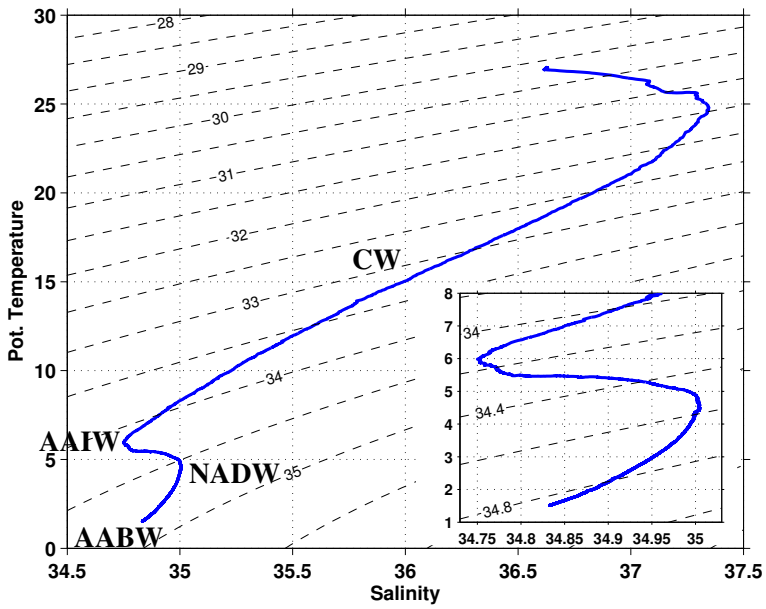

Figure 4.1: *Typical $\theta - S$ diagram from a CTD cast acquired on FS SONNE cruise 172 in June 2003 at 15.4° N / 51.5° W. The deep water masses below 8° C are displayed enlarged in the box on the right. Superimposed are density ($\sigma_{1.5}$) levels*

subdivided into 4 different segments (from high to low temperatures): Underneath the surface waters, the warm thermocline Central Water (CW) displays an almost linear positive relationship between salinity and temperature. It is followed by the Antarctic Intermediate Water (AAIW),

featuring a salinity minimum and temperatures of about 6 °C. The transition towards the North Atlantic Deep Water (NADW) is characterized by a strong increase in salinity and slightly decreasing temperatures. Towards the Antarctic Bottom Water (AABW), the deepest water mass, a decrease in both temperature and salinity is observed.

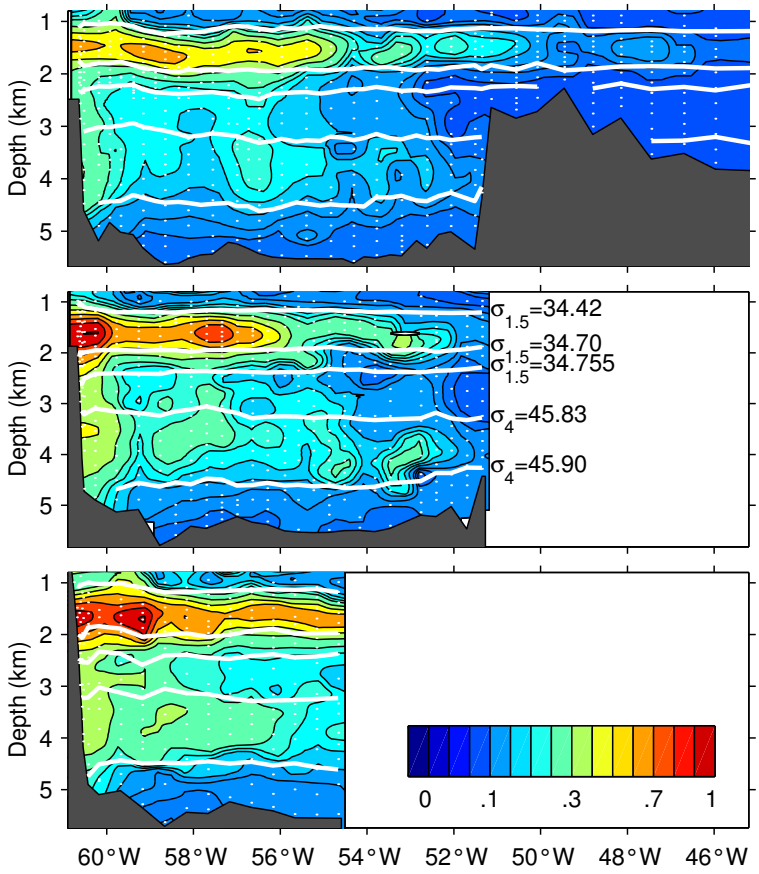

Figure 4.2: *CFC-11 concentrations [pmol/kg] along the MOVE 16 °N section, taken during cruises aboard FS SONNE in Dec. 2000 (top) and June 2003 (bottom) as well as FS METEOR in June 2002 (center). Superimposed are density levels $\sigma_{1.5}$ = 34.42, 34.70, 34.755 and σ_4 = 45.83 and 45.90 used to classify the boundaries of the different composites of the deep water masses after Rhein et al. (1995). See text for details. Courtesy of M. Rhein. This Figure has been published by Rhein et al. (2004).*

Now a closer look at the deep water masses is taken, since meridional transport variability in these layers is the main target of this study. In the following, the water mass classification in terms of density classes from Rhein et al. (1995) is applied. CFC-11 concentration acquired at the 16 °N section by Rhein et al. (2004) during three different cruises are displayed in Fig. 4.2.

The boundary between low saline AAIW and the underlying NADW has been defined by the $\sigma_{1.5}$ = 34.42 level. It is found at a depth of about 1200m. The highest CFC concentrations are found in the uppermost NADW composite, namely in the shallow upper North Atlantic Deep Water (suNADW) layer ($\sigma_{1.5}$ 34.42 - 34.70), indicating most recent contact with the atmosphere. Values are slightly decreasing from the western boundary towards the Mid-Atlantic Ridge (MAR) in the east. There is a decrease in CFC towards the Labrador Sea Water (LSW, $\sigma_{1.5}$ 34.70 - 34.755), reaching a minimum concentration in the lower North Atlantic Deep Water (lNADW, $\sigma_{1.5}$ = 34.755 - σ_4 = 45.83). An increase is visible in the overflow North Atlantic Deep Water (oNADW, σ_4 45.83 - 45.90), the deepest water mass of the NADW, with maximum values again near the western boundary. Similar to the uNADW, patches of high CFC concentrations can be found up to the MAR. Finally in the AABW, the lowest concentrations are observed. The

reader is referred to Rhein et al. (1995) for a more thorough discussion on the deep water mass properties in the tropical Atlantic. The boundary between the NADW and AABW (defined by the $\sigma_4 = 45.90$ level) displays a significant deviation from the horizontal plane: Directly at the western boundary it can reach up to 4900m, then rising towards the east to about 4500m. East of 54 ° west a further rise to 4300m is visible. This has to be kept in mind when calculating transports in water mass classes. The results presented here are found to be in good agreement with the $\sigma-$ levels of the moored density measurements in Fig. 3.8.

The fact that the CFC signals extend all the way to the MAR and their patchy nature indicate that the southward transport of NADW is not necessarily concentrated near the western boundary. Interior recirculation might exist, whose pathway may be subject to temporal variations. A second possible mechanism is that of eddy mixing of DWBC properties into the interior. Evidence for the latter will be presented in section 5.4. The general CFC structure compares well in the three sections. Nevertheless many differences can be observed, especially away from the western boundary. The obvious spatial and temporal variability justifies monitoring strategy applied here, which integrates horizontally transports across the whole western basin of the North Atlantic. Another interesting aspect of Fig. 4.2 are the extremely low values in CFC found in the vicinity of the MAR (east of 52 °W) in all water mass layers. Those are evident (at least below the suNADW) in both sections and correspond to results observed by Mauritzen et al. (2002) in the tropical North Atlantic. They interpret those anomalous tracer concentrations in terms of enhanced vertical mixing over the rough topography of the MAR, supported by micro-structure measurements over the MAR in the South Atlantic (Polzin et al., 1997), showing the diffusivities up to 1-10 $\times 10^{-4} m^2/s$. Thus, the MAR could play an important role in the global ocean upwelling budget, which is required to maintain the strength of the thermohaline circulation (e.g. Marotzke and Scott, 1999; Wunsch and Ferrari, 2004).

Now the temporal variability of the hydrographic field is focused on, starting with a description of the evolution of temperature, salinity and density. Subsequently, the relative importance of temperature and salinity on density fluctuations is discussed, which is shown to have direct implications for the transport measurement technique. Fig. 3.8 displays temperature anomalies acquired at the mooring sites M1 (east), M2 (center) and M3 (west) in the deep layers of NADW and AABW. Maximum amplitudes peak at about 0.2 °C. The temperature anomalies tend to exhibit a large vertical extent, sometimes coherent fluctuations can be found throughout the whole NADW/AABW layer. The largest variability is found in the suNADW, in the west extending down into lNADW. At the center mooring the AABW features a second layer of large variability. In the east fluctuations below the suNADW are generally lowest. At the center site and in the east the variability is dominated by monthly scales, in the west a broad spectrum from weekly to annual fluctuations is found. Also, the eastward rise in the NADW / AABW boundary becomes evident. Its interface varies between 4700 and 5000 dbar in the west, between 4400 and 4700 dbar in the center and between 4400 and 4200 dbar in the east. This compares well with the CFC distribution in Fig.4.2. The spatial and temporal patterns observed at the different sites are closely related to the flow field. This will become apparent later in chapter 4.3.

The records of temperature as well as density surfaces look consistent: The transitions across the data gaps (from one deployment period to the next) do not exhibit any abrupt changes in the observed properties. A more condensed representation of the temporal variability of the hydrographic fields is obtained from Fig. 4.3, where the standard deviation of salinity, temperature and density is displayed. Generally, the variability of temperature and salinity compare well in shape. Salinity fluctuations are generally lower than 0.005 below the suNADW (i.e. 2000 dbar) and increase drastically toward the AAIW. In the east a secondary deep maximum is found at the NADW/AABW interface. Strong increase in salinity fluctuations towards the AABW can be seen at the center site and somewhat weaker in the west, indicating the transition between

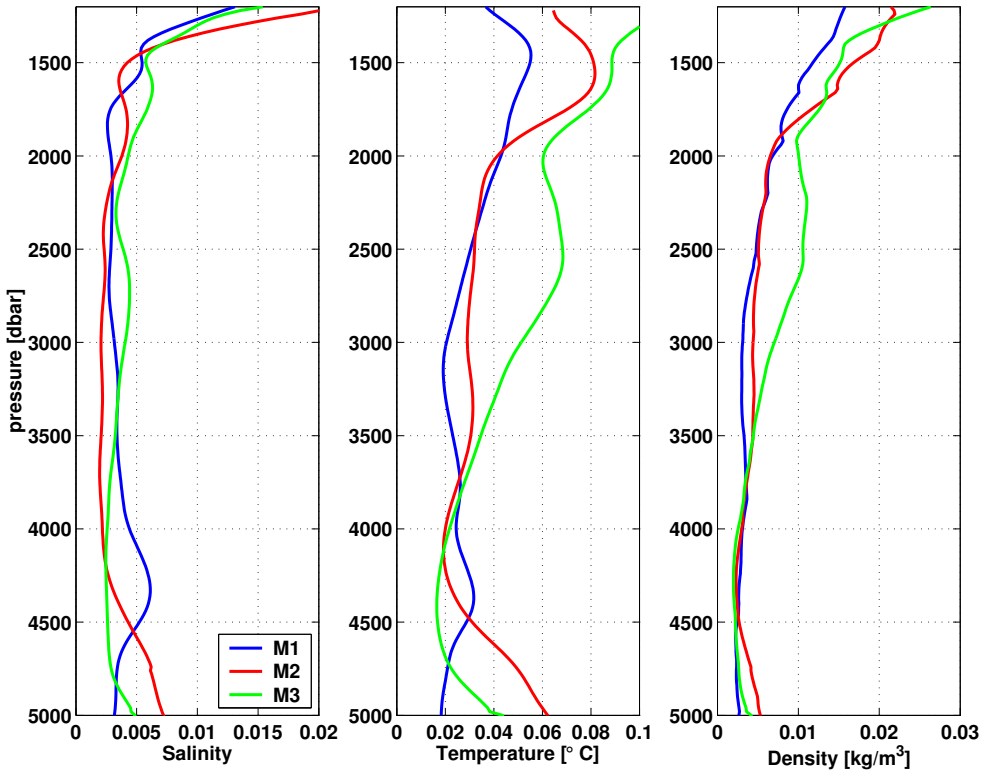

Figure 4.3: *Standard deviation of salinity (left), temperature (center) and density (right) at the mooring sites M1, M2 and M3. Calculation are based on the Feb 2000 - Feb 2004 time series. Linear interpolation has been carried out in the vertical.*

the two water masses. This increase goes along with bottom-intensified velocity fluctuations, which are strongest at the center location (not shown) and which might topographically trapped waves. All of these pattern find their expression in the temperatures as well. It should be noted that over most of the depth range displayed, temperature dominates salinity in terms of density fluctuations. This can be seen from Fig.3.8 where most density layers tends to rise when temperature decreases. The overall largest density fluctuations within the NADW/AABW take place within the suNADW, in the west extending into the lNADW. Therefore, the strongest changes in vertical velocity shear are expected to be concentrated in this layer.

After February 2002 the hydrographic measurements have covered the whole water column. The salinity time series obtained till Feb 2004 are displayed in Fig.4.4. Most prominent features at both mooring sites are the subsurface salinity maximum in about 150m (see also Fig. 4.1) and the salinity minimum in the AAIW layer. The interface between the AAIW and the NADW, defined as the $\sigma_{1.5} = 34.42$ density level, is of particular interest. It exerts an "anomalous" upward displacement with increasing salinity. At this level salinity dominates temperatures in terms of density fluctuations. This aspect will be treated in more detail as it has direct consequences for the transport observation strategy.

The temperature dependence of acoustic travel time has often been exploited to observe the vertical displacement of the thermocline or dynamic height ocean bottom mounted inverted echo sounders (Rossby, 1969; Watts and Rossby, 1977; Meinen and Watts, 1998). In the MOVE project time series of acoustic travel time measurements from PIES at M1, M2 and M3 have been obtained. Earlier investigations had already shown that at these sites travel time is not a reliable variable to describe near surface dynamic height changes relative to the sea floor (Schmidt, 2004). Whereas travel time is highly correlated with vertically averaged temperatures (with correlation coefficients of better than 0.9, not shown) only a correlation of about 0.4 - 0.5 is found between vertically integrated density and travel time (Fig. 4.5, left panels). Thus,

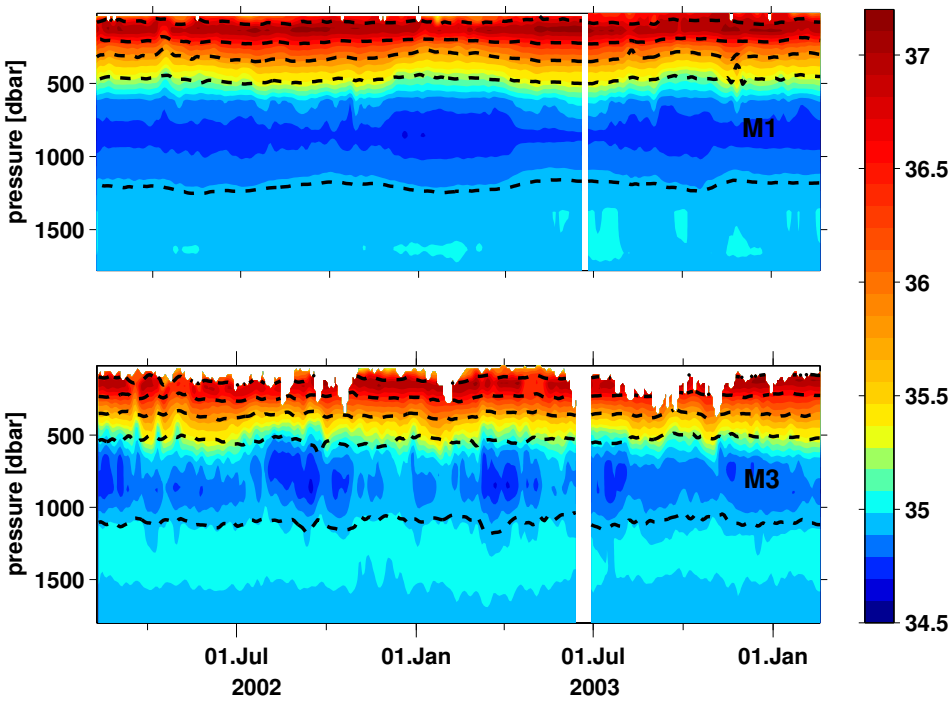

Figure 4.4: *Salinity above 1800 dbar from mooring sites M1 (east,top)and M3 (west,bottom) from Feb 2002 to Feb 2004. Superimposed are density levels (σ = 24.5, 26.3, 26.8, 27.1 and $\sigma_{1.5}$ = 34.42). Near surface data gaps at M3 are caused by mooring subduction during episodes of strong currents.*

salinity must play an important role in density changes as well. Over most of the water column temperature and salinity changes are highly correlated (green line in Fig. 4.5, center panels), which must lead to a partial compensation in terms of density. There is a notable exception at the AAIW/NADW interface and above, where temperature and salinity show no correlation at M3 and negative correlation at M1. Over most of the water column (in the AABW, NADW and CW) the $\theta - S$ relationship is organized such that and increase in temperature goes along with an increase in salinity (Fig. 4.1). However, a notable exception is observed near the NADW/AAIW interface, where increasing salinity corresponds to decreasing temperature. This explains the negative correlation between temperature and salinity at this depth.

The importance of temperature and salinity for density fluctuations is displayed in Fig. 4.5 (right panel). The characteristics at the sites M1 and M3 are similar: In the deep ocean (below 1200 dbar) temperature dominates the salinity influence on density. From 1200 dbar upwards to about 800 dbar, which is the level of the AAIW salinity minimum, salinity fluctuations dominate density at M1 and exhibits a comparable influence as temperature at M3. This corresponds to the "anomalous" displacement characteristics of density level $\sigma_{1.5} = 34.42$ in Fig. 3.8. Finally, in the CW temperature returns to be the driving agent for density changes. Concluding, it is the salinity dominance in the AAIW that reduces the skill of acoustic travel time to provide exact estimates of dynamic height fluctuations.

The relative importance of salinity on density in the AAIW as well in the abyssal ocean stresses the necessity to observe this quantity with high precision. Former experiments like ACCP-3 needed to estimate salinities from temperatures using empirical $\theta - S$ relationships (see chapter 2.3). In simulations using historic CTD data this has been shown to work well in the deep ocean, where the relationship is stable in time (e.g. JKZ2004 and Whitworth (1983)). With the MOVE data set, this approach can be tested, computing salinities from a mean $\theta - S$ relationship and comparing these to the actually measured salinities (Fig. 4.6). In the first case (black line)

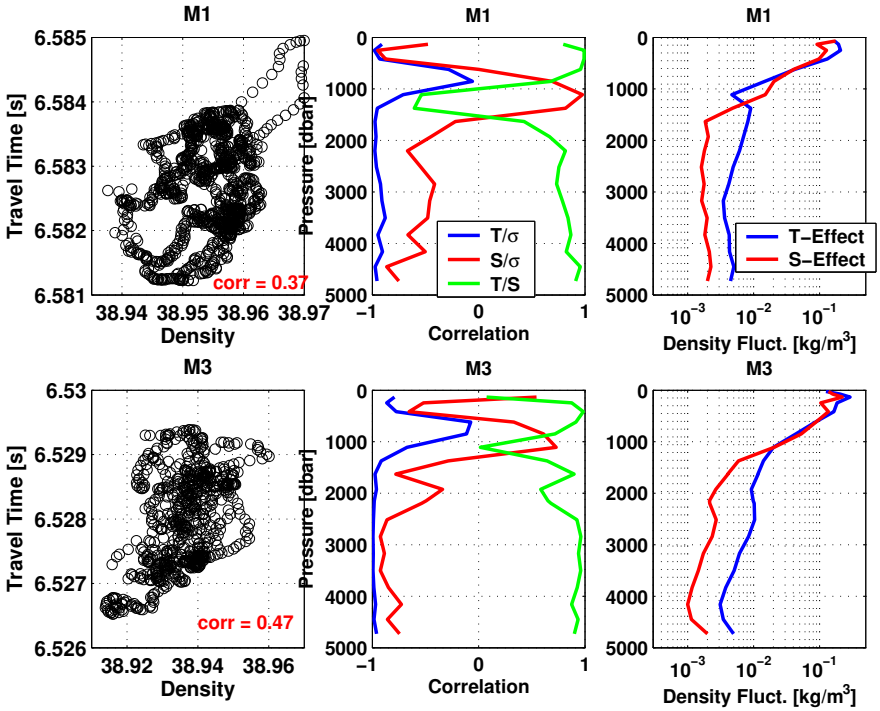

Figure 4.5: *Left panels: Acoustic travel time (from PIES) versus vertically averaged density (between 100 and 4900 dbar). Correlation coefficient is indicated. Center panels: Vertical structure of correlation between density σ, temperature T and salinity S. Right panels: Standard deviation of density fluctuations caused by temperature (blue) and salinity (red) fluctuations. In the first case the observed time variable temperatures but mean salinities and in the second case time variable salinities but mean temperatures have been used. Note the logarithmic scale. Analyzes from mooring M1 and and M3 are displayed in the upper and lower panels, respectively. All of the computations are based on data from the 3rd deployment period.*

data from all mooring sites (M1, M2 and M3) is used. This represents a scenario, where the $\theta - S$ relationship would be obtained from a regional data set. In the second test (gray line) measurements only from M1 have been used, simulating the 'ideal' case, where a truly local data set exists. In both cases the r.m.s. difference between directly measured and empirically estimated salinities (as a function of temperature) are generally small (close to 0.002) in the deep ocean below 2000 dbar. However, towards the Antarctic Intermediate Water (whose lower boundary is found at approx. 1200 dbar), the $\theta - S$ relationship fails to allow precise estimates of salinity. Near 800 dbar salinity errors reach 0.03 using the local and 0.07 using the regional data set. The transition of NADW to AAIW is characterized by comparably strong changes in salinity over a small temperature interval (see Fig. 3.7). Therefore a slight vertical displacement of the wass mass interface results in a strong change in $\theta - S$ characteristics, explaining the large salinity estimates at this level. Also, small uncertainties in the temperature measurements will lead to comparably large uncertainties in the salinity estimate. But also within the AAIW core (at about 800 dbar) the $\theta - S$ relationship is too unstable in time (and space) to be used as a salinity proxi. These examples show that temperature measurements are not sufficient in regions or water masses with variable $\theta - S$ relationships, or in regions where different water masses meet. Also, salinities derived from θ can only be used with confidence, where the $\theta - S$ relation is well known including its uncertainties and variability in space and on various time scales. Most importantly, when applied in multi-year climate monitoring experiments, long-term changes in the $\theta - S$ relationship may occur and thus salinities have to be measured to detect these and to avoid errors in the internal transports.

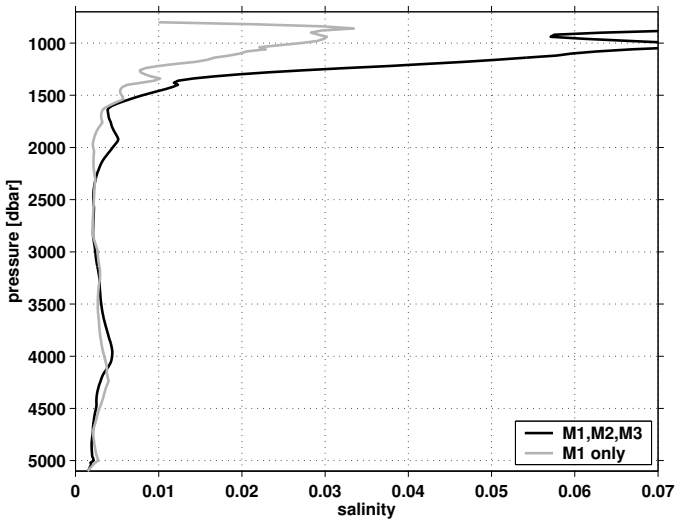

Figure 4.6: *R.M.S. difference in salinity obtained from a mean θ-S relationship and measured directly. The computation is based on temperature and salinity data obtained at all 3 mooring sites M1, M2, M3 (black line) between Feb 2000 and Jan 2004. The mean θ-S relationship was obtained from the same data set. The same computation was repeated using data from site M1 only (gray line).*

4.3 The Velocity Field

This section presents an overview over the mean and time-varying internal velocities derived from dynamic height (equation 1.3). Also the external velocity fluctuations computed from differences of bottom pressure measurements at the sites M1, M2 and M3 are discussed (equation 1.4). First a description of the mean internal velocity shear profile is given. Its shape will be shown to be closely related to the vertical water mass distribution in Fig. 4.2. The analysis of the shape is needed for referencing the relative geostrophic currents (i.e. for calculating absolute mass transports) in chapter 6.

Mean Velocity Field The Feb. 2000 to Feb. 2004 mean internal velocity profiles (rel. to 5000 dbar) of the whole, east and west section display remarkably similar shear characteristics: In each profile two southward cores are visible: the more prominent one in the suNADW/LSW layer and the lower one in the oNADW. Their depths correspond to the maxima in CFC concentration from Fig. 4.2. Waters in these 2 density classes have been generated by convection at high latitudes. In the west section (red profile) the structure of 2 cores can be directly linked to the DWBC: The existence of two deep cores of intensified southward flow near the western boundary has been established for a long time (see Fine and Molinari (1988) for a summary). However, it is rather surprising to observe a similar (or even more pronounced) 2-core current structure in the east section (green line) as well. The east section only starts 400 km away from the western boundary (see 2.1) and should therefore be out of reach of the DWBC, which exhibits a cross-current scale of typically not more than 100 km in the tropical North Atlantic (e.g. Fine and Molinari, 1988; Fischer and Schott, 1997). The author is not aware of any other study showing this velocity structure within the NADW away from the boundary. Whether those two southward velocity cores represent a coherent pattern across the entire western trough of the Atlantic cannot be concluded from the internal velocities acquired from moored dynamic height moorings: Velocity measurements with a much better horizontal resolution would required.

Another explanation could be the possible existence of second boundary current in the east of the section (at the MAR), with similar vertical shear as the DWBC. As a consequence of poten-

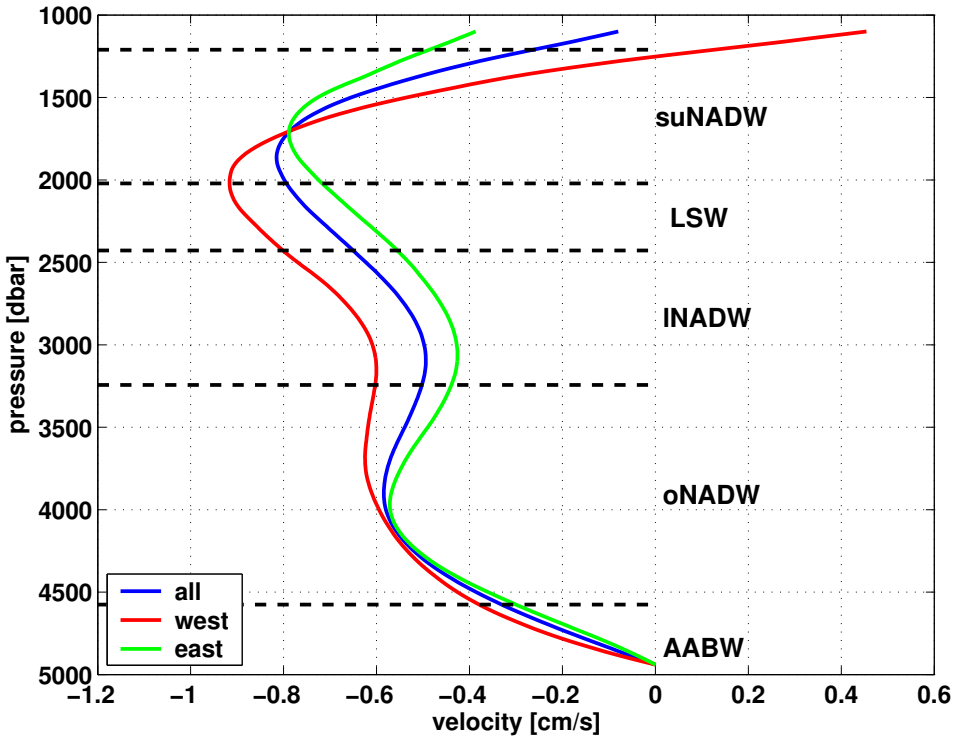

Figure 4.7: *Mean internal velocity profile [cm/s], relative to 5000 dbar, integrated over the whole (M1-M3, blue), west (M2-M3, red) and east (M1-M2, green) section. Each profile represents an Feb 2000 - Feb 2004 average. Superimposed are the approximate interfaces of the different water masses (see Fig. 4.2).*

tial vorticity conservation, meridional flows in the deep ocean interior may exist in the presence diverging vertical velocities (vortex stretching) induced by enhanced non-uniform mixing over the MAR (Webb and Suginohara, 2001a; Mauritzen et al., 2002). Evidence for enhanced northward flow of AABW (and oNADW) in the vicinity of the MAR is found from lowered ADCP measurements conducted by (Rhein et al., 2004) and also from the MOVE/GAGE current meter measurements, as shown in Fig. 6.5. However, two northward maxima are not present in either of these observations. Therefore this pattern, which is a result of a 600 km wide zonal integration, might be composed zonally separated current features. A closer investigation of the hydrographic sections acquired along 16 °N might give more detailed information about the horizontal distribution of the vertical velocity shear.

It should be added that the results presented here can be considered very robust: The two cores of southward flow in the west as well as east section are found in the mean shear profiles from every single of the 4 deployment period. Additionally, they can also be observed in internal velocity profiles computed from lowered CTD measurements (Fig. 4.8). For completeness it must be kept in mind that the mean velocities displayed in Fig. 4.7 (and 4.8) lack the directly measured DWBC contribution from the boundary triangle west of M3 (see Fig. 2.1). An inclusion would result in an even more pronounced upper (suNADW/lNADW) velocity core in the west.

The strongest velocity shear is observed at the NADW/AAIW and the NADW/AABW interfaces. This confirms the well-known concept of southward moving NADW being bounded by two water masses originating from the Southern Ocean. Those interfaces of opposing flow have often be used to define a level of no motion for the referencing of geostrophic currents. In the chapter 6 the potential of several referencing approaches will be examined, where the vertical velocity shear plays an important role.

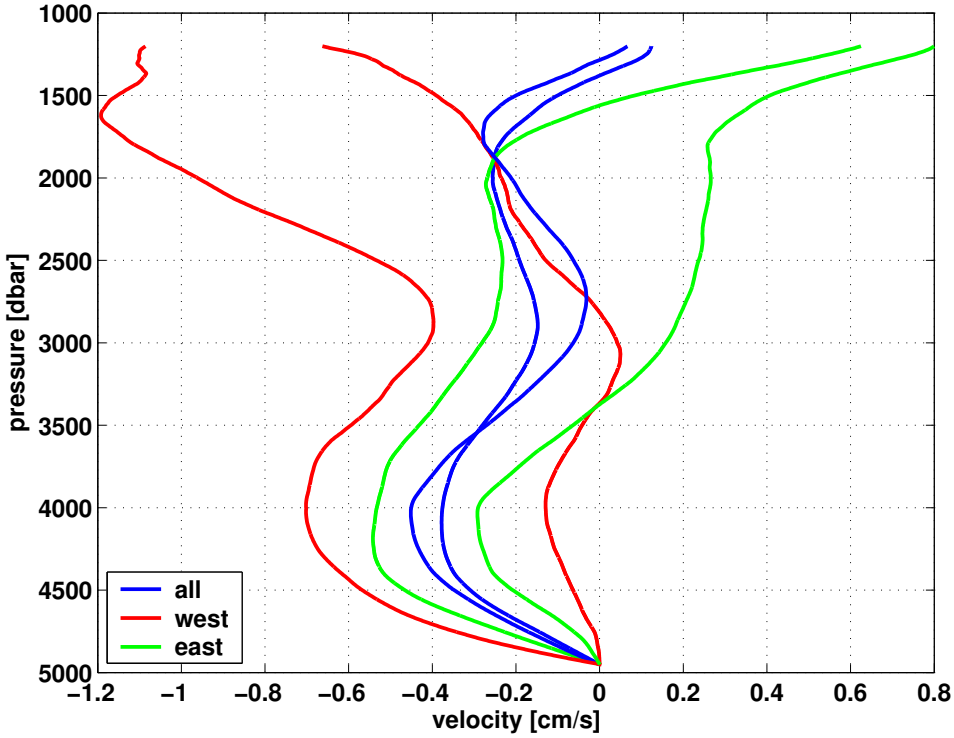

Figure 4.8: *Internal velocities below 1200 dbar [cm/s] relative to 5000 dbar from 2 hydrographic surveys acquired aboard l'ATALANTE and FS METEOR. Velocities integrated across the whole (M1-M3), west (M2-M3) and east (M1-M2) section are displayed as blue, red and green lines, respectively.*

Internal Velocity Fluctuations Now the time variable internal velocities are described (see Fig. 4.9). Velocities below 1200 dbar (rel. 5000 dbar) range between -3 and 1.4 cm/s with the largest amplitudes being present in the west section (middle panel). A partial compensation of fluctuations in the west and east with respect to the whole section (top panel) is observed. This interesting aspect will be investigated in more detail in chapter 5. Also the presence of the two cores of pronounced southward flow can be observed, even though it is covered by strong fluctuations, especially in the west. Like the temperatures in Fig. 3.8 also the internal velocities tend to fluctuate at periods of few months. Velocities integrated across the whole section (top panel) also show changes on longer time scales: Between Oct 2001 and April 2003 a significantly reduced southward flow is observed. This aspect, too, will be taken up in the chapters 5.2 and 5.3.

Full water column internal velocities integrated across the whole section can be computed from Feb 2002 and Feb 2004 measurement period (Fig. 4.10). Largest southward velocities are reached at about 2000 dbar (suNADW/LSW) and near the surface. Maximum northward velocities can be observed in the center of the AAIW (at approx. 800 dbar). This is true for the time averaged velocity profile as well. Compared to the strong shear at the transition from AAIW and NADW (about 1 cm/s over 1200 dbar), the velocity distribution within the NADW looks rather uniform. Nevertheless its 2 southward cores remain clearly visible. The negative velocity shear from the AAIW towards the surface has several reasons: The moored array exhibits a small meridional extension (with the western and eastern moorings being located at 16.3 °and 15.4 °N, respectively). In this sampling configuration the westward North Equatorial Current (NEC) projects a negative velocity. Also, a compensation of the trade wind driven northeastward surface Ekman flow results in negative near surface velocities below the Ekman layer. A possible further candidate for upper ocean southward geostrophic flow is supply from the tropical upwelling from the subtropical downwelling region, the so-called shallow tropical-subtropical cell (Schott et al.,

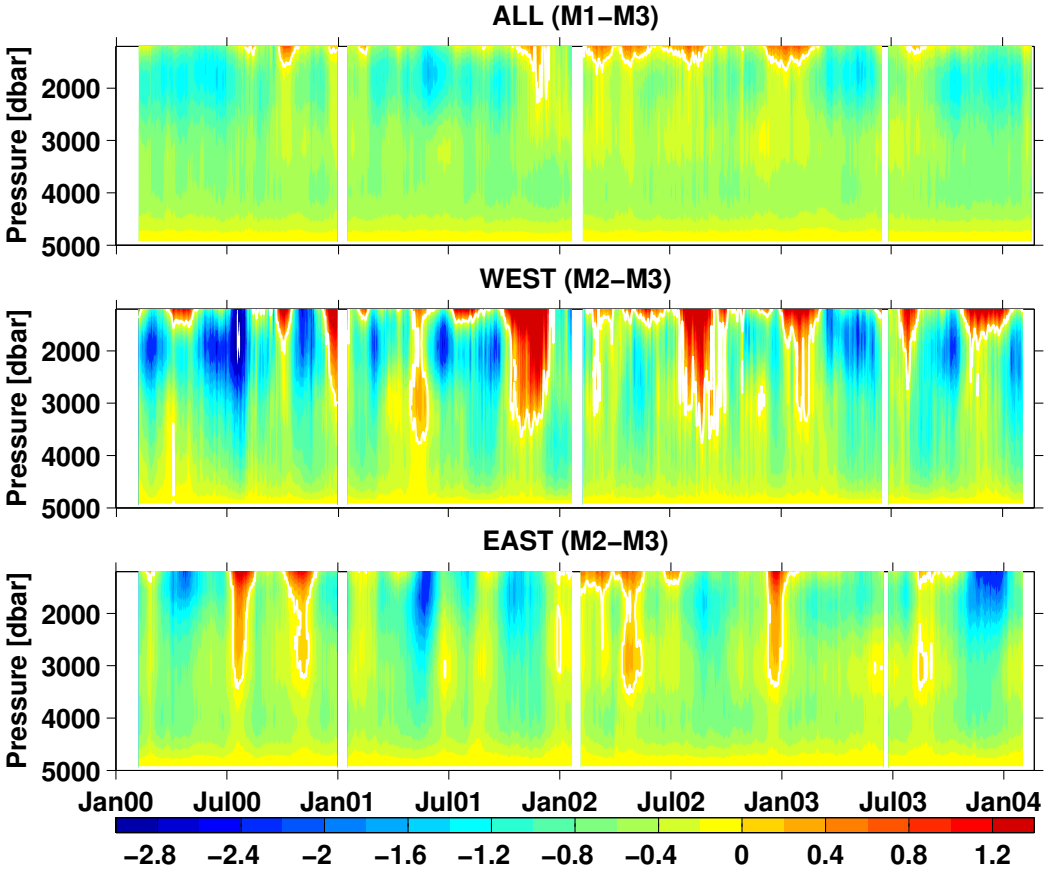

Figure 4.9: *Internal velocities below 1200 dbar [cm/s] relative to 5000 dbar from Feb 2000 to Feb 2004. Velocities integrated across the whole (M1-M3), west (M2-M3) and east (M1-M2) section are displayed in the top, middle and bottom panel, respectively. Time series are 48 hour low-pass filtered. The white contour lines indicate zero velocity.*

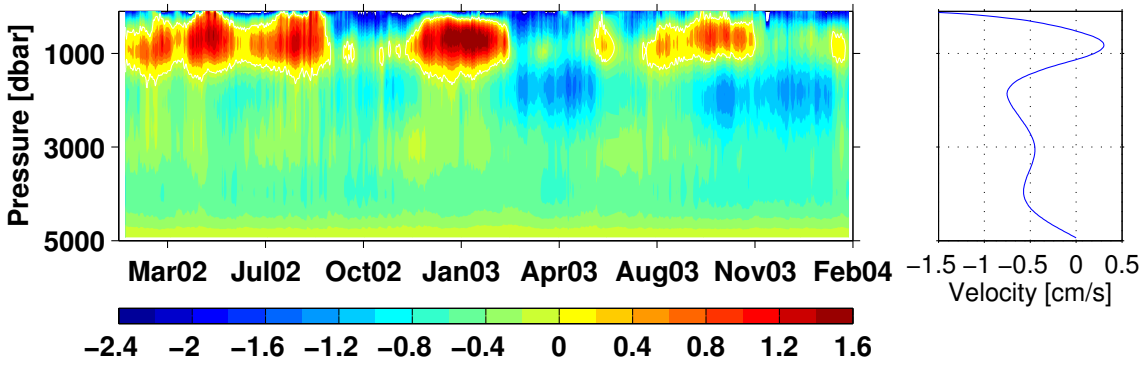

Figure 4.10: *Left: Full water column internal velocity [cm/s] integrated across the whole section (M1-M3) relative to 5000 dbar from Feb 2002 to Feb 2004. Time series are 48 hour low-pass filtered. White contour lines indicate zero velocity. Right: Time averaged internal velocity.*

2004a).

To determine to dominant vertical patterns of variability, an EOF analysis of the internal velocities has been carried out. Let $\mathbf{D}(P,t)$ be the internal velocity data matrix of size L $\times$ N, depending on discrete values of P and t. The EOF analysis yields the following decomposition

$$\mathbf{D}(P,t) = \sum_{i=1}^{N} [a_i(t)\mathbf{m}_i(P)] \tag{4.1}$$

into modes $\mathbf{m}_i$ depending only on P and their corresponding amplitude functions depending only on t. The modes represent the eigenvectors of the covariance matrix of D. It can be shown that any number of leading modes represents the maximum fraction of the total variance, i.e., no other separation can be found for which an equal number of leading modes explains more variance (e.g. Emery and Thomson, 1998). For an efficient computation, singular value decomposition (SVD) as described by Emery and Thomson (1998) has been used: The operation $\mathrm{SVD}(\mathbf{D}) = \mathbf{USV}^{\mathrm{T}}$ yields the EOF modes as columns of the matrix $\mathbf{U}$.

Since such an analysis represents a purely statistical approach, the physical interpretation has to be carried out with care. In contrast to the mean internal velocity distribution (Fig. 4.7) the vertical structure of the fluctuations does not reflect a direct relationship to the water mass distribution. For the deep internal velocities (Fig. 4.11, top panel), the first mode explains 90% of the variance . It displays uniform shear throughout the water column. The second and third mode cover 6% and 3% of the variance. The third mode displays a maximum at 2000 dbar, the center of upper velocity core of the NADW. Thus it might be related to flow changes suNADW/LSW layer like meandering of the DWBC. The leading EOF modes for the east and west sections are very similar in shape and explain a similar amount of variance (not shown).

The first mode, second and third mode of the full water depth internal velocities (Fig. 4.11, bottom panel) display 73%, 17% and 7% of the variance. In order to assign to them physical mechanisms, they are compared to quasi-geostrophic (QG) velocity modes, independently computed from CTD casts acquired along the 16 °N section. QG modes represent the vertical structure of quasi-geostrophic motions with zero mean for a flat bottom ocean as a function of stratification and latitude (comprised by the Brunt-Väisälä frequency N and the Coriolis parameter f, respectively). Mathematically, they are represented by the eigenvectors ψ of the regular singular second-order Sturm-Liouville system of the form (Pedlosky, 1979)

$$\frac{\mathrm{d}}{\mathrm{d}z}\left[\frac{f^2}{N^2(z)}\frac{\mathrm{d}\psi_k}{\mathrm{d}z}\right] + \lambda^2\psi_k(z) = 0 \tag{4.2}$$

with rigid-lid boundary conditions at the surface (z=0) and the bottom (z=-H): $\frac{\mathrm{d}\psi_k}{\mathrm{d}z} = 0$ at z=0, -H. The index k denotes the mode index.

Reasonable agreement between EOF and QG (displayed in Fig, 4.12) modes can be observed, with the exception of first EOF mode displaying a local extremum at 500dbar. From fact that the condition of a flat bottom is clearly not fulfilled at the MOVE site (in the presence of steep topographic features like the MAR in the east and the continental rise in the west), it cannot be expected that the QG mode give an exact representation of the true modal velocity structure. However, the correspondence of QG and EOF modes suggests, that the latter do indeed represent not only have statistical but also a physical description of the dominant patterns of variability.

The 3 leading modes account for more than 95% of the variance. Thus, the principal patterns of internal velocity variability exhibit a relatively simple vertical structure. Therefore, a possible application of these modes could be a vertical extrapolation of the velocities towards the surface during times where there are no measurement available (either due to design shortcuts during the first two deployment periods or during mooring subduction events).

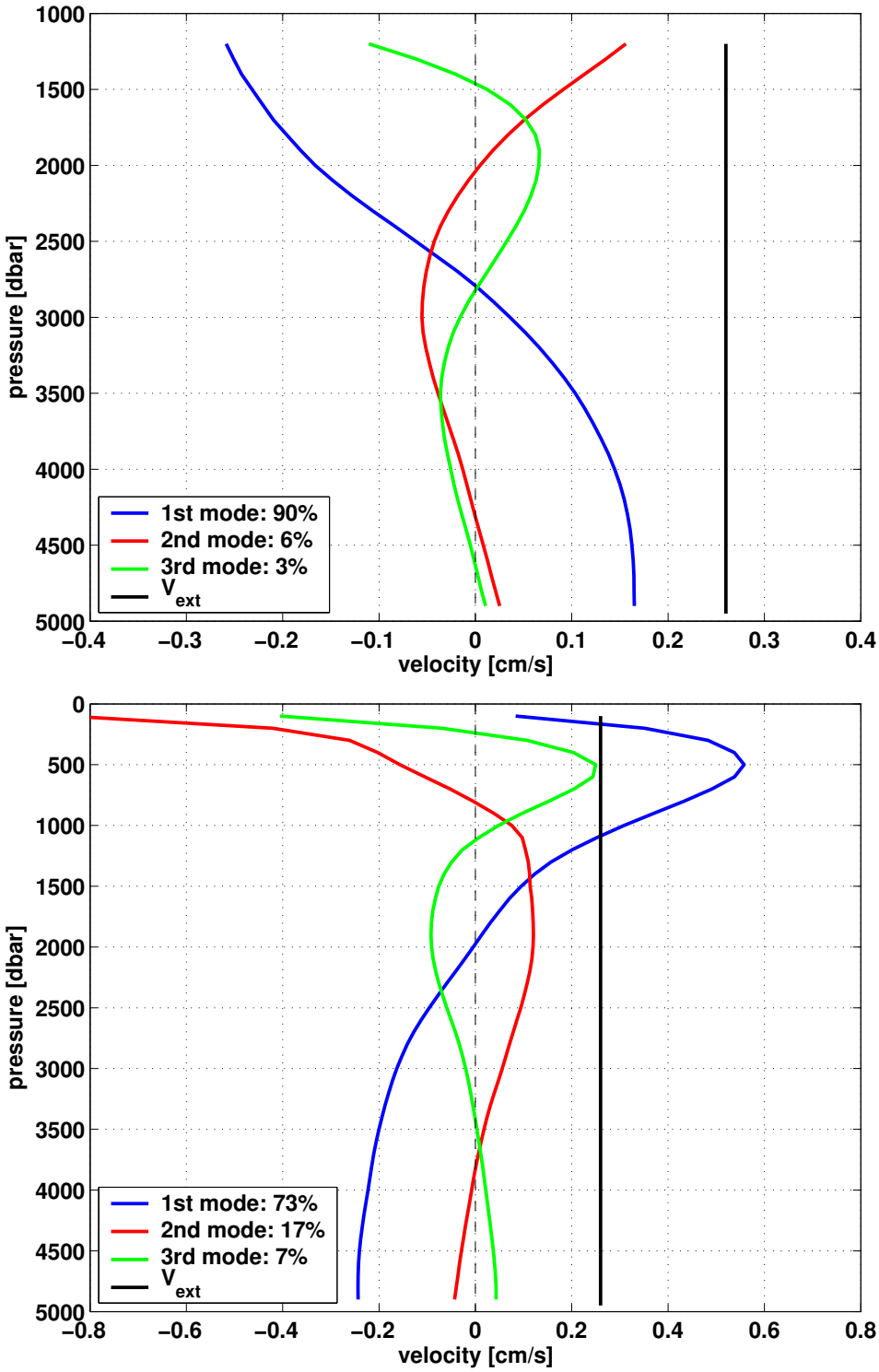

Figure 4.11: *EOF Modes of internal velocity (rel. 5000 dbar) integrated across the whole section (M3-M1). The leading 3 EOF modes of velocity below 1200 dbar and for the full water column are displayed in the top and bottom panel, respectively. The former are based on Feb. 2000 - Feb. 2004, the latter on Feb. 2002 - Feb. 2004 data. The vertical mean of each mode has been removed. Prior to the computation the time averaged velocity profile has been subtracted. The modes have the unit cm/s, since they have multiplied by the standard deviation of their corresponding amplitude functions. The solid black line denotes the r.m.s. amplitude of the external velocity fluctuations (M3-M1).*

The observed energy distribution among the different EOF modes (with a dominating first mode) generally corresponds to findings of Wunsch (1997), who computed vertical velocity modes from set of deep-reaching current meter moorings, mainly concentrated in the North-Atlantic and North Pacific. Since the energy distribution is shown to differ substantially in space and furthermore depends on the duration of the mooring operation and varies with time (Müller and Siedler, 1992), an objective comparison is difficult to carry out with the MOVE internal velocity modes. Also, current meters represent point measurement whereas the internal velocities are a result of zonal integration. It will be shown in chapter 5.3 that the horizontal averaging scale may suppress motions of certain horizontal wavelengths.

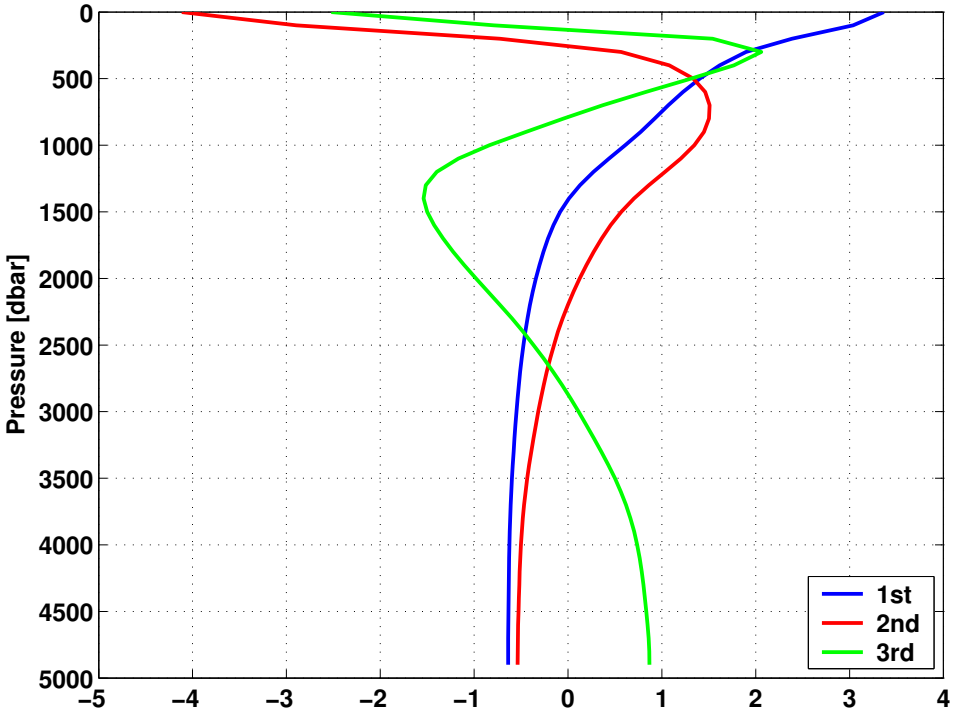

Figure 4.12: *First three quasi-geostrophic velocity modes computed from a along section averaged CTD profile (using 28 CTD profiles aquired along the 16°N section during the FS SONNE cruise 152 in December 2000).*

In order to investigate which patterns of meridional velocity are associated with MOC variability, output from the CONTROL run of the FLAME 1/3 °model (see Appendix A.1 for details) has been analyzed. In Fig. 4.13 the 3 leading EOF modes of the vertical derivative of the meridional overturning stream function are displayed. One might think of these as modes of zonally averaged meridional velocity (multiplied by the zonal basin width). The first mode, explaining 48% of the total variance is rather surface intensified. Since it displays very little vertical shear below a depth of 400 m, it might be associated with external velocity fluctuations and therefore partly be "invisible" for internal velocities. It might possibly reflect the time variable surface Ekman flow and its rather barotropic compensation at depth (e.g. Jayne and Marotzke, 2001). The shapes of the 2nd and 3rd modes, explaining 24% and 15% of the variance, resemble those of the 1st and 2nd modes of the observed internal velocities in Fig. 4.11. However it has to be kept in mind that the model results are based on computations from 2-year low-pass filtered output, whereas the measurements have been 2-day low-pass filtered. The important point to make here is that meridional velocity patterns associated with MOC fluctuations on inter-annual time scales are not dominated by one simple mode displaying velocities of opposite signs near the surface and at depth, with a zero-crossing near the NADW/AABW interface, as one might suggest from the velocity distribution associated with the steady state of the MOC. However there is indication

that this is true at decadal and longer time scales (Dong and Sutton, 2001).

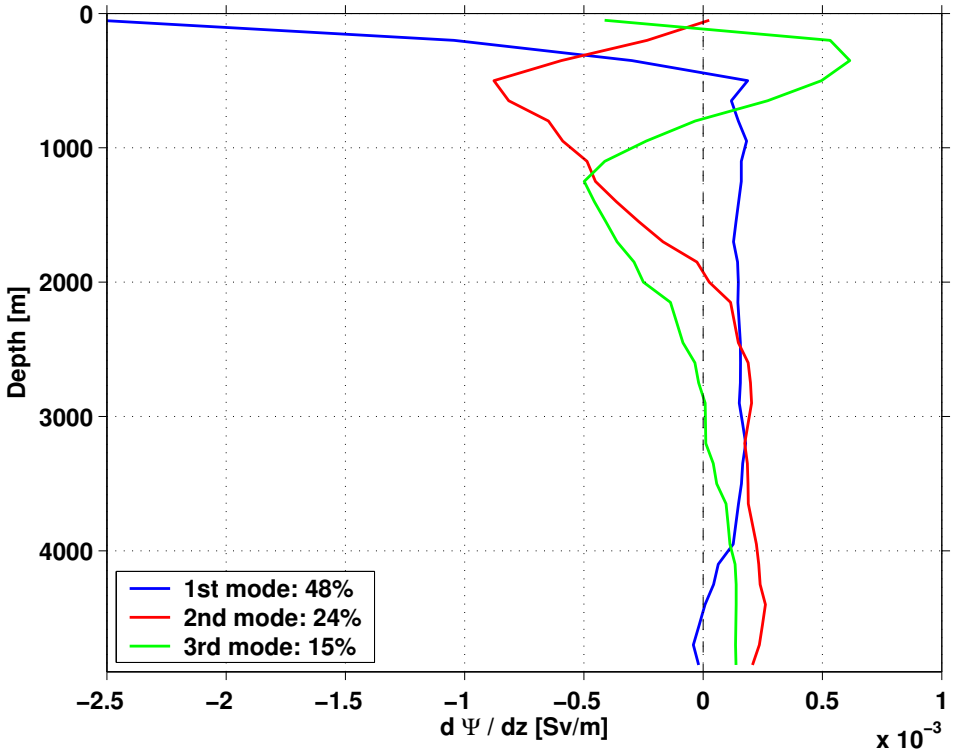

Figure 4.13: *The three leading EOF modes of the vertical derivative of the meridional overturing stream function* $\frac{\mathrm{d}\Psi}{\mathrm{d}x}$ *[Sv/m] at 16°N from the CONTROL experiment of the FLAME 1/3° model (see also Appendix A.1). Computations are based on 2 year low-pass filtered output from the 58 year long model run. The EOF modes exhibit the unit Sv/m, since they have multiplied with the standard deviation of their corresponding amplitude function.*

External Velocity Fluctations The external velocities are dominated by high frequency variability of periods < 1 month. In the west section the largest signals are observed with peak to peak amplitudes sometimes reaching 2 cm/s. As a comparison, the internal velocities display amplitudes of not more than 0.5 cm/s. The r.m.s. amplitude of external velocity fluctuations amount to 2.6, 5.2 and 3.8 cm/s for the whole, west and east section. Fig. 4.11 confirms that at least in the deep ocean external velocities dominate the internal ones. However as will be seen in chapter 5.3 in more detail, internal and external velocities display rather different spectral characteristics, such that towards longer periods the internal component gains increasingly more weight. At periods of few months east and west external velocities seem exhibits a 180 ° out of phase behavior. This leads to a compensation with respect to the total external velocities in the frequency band. This aspect will be taken up again in chapter 6, where a thorough comparison of external and internal contributions will be carried out, based on analyzes of their spectral characteristics. It will be shown that the inherent averaging scale of the MOVE measurement configuration yields favorable consequences for the signal-to-noise ratio of longer periodic variability, which is the target of the MOVE experiment, is increased.

Western Boundary Triangle Velocities For completeness, the direct current characteristics observed over the continental rise (in the western boundary triangle), based on current meter measurements, are highlighted exemplarily in Fig. 4.15. Currents in upper DWBC core are dominated by strong topography following southeastward flow throughout large parts of the

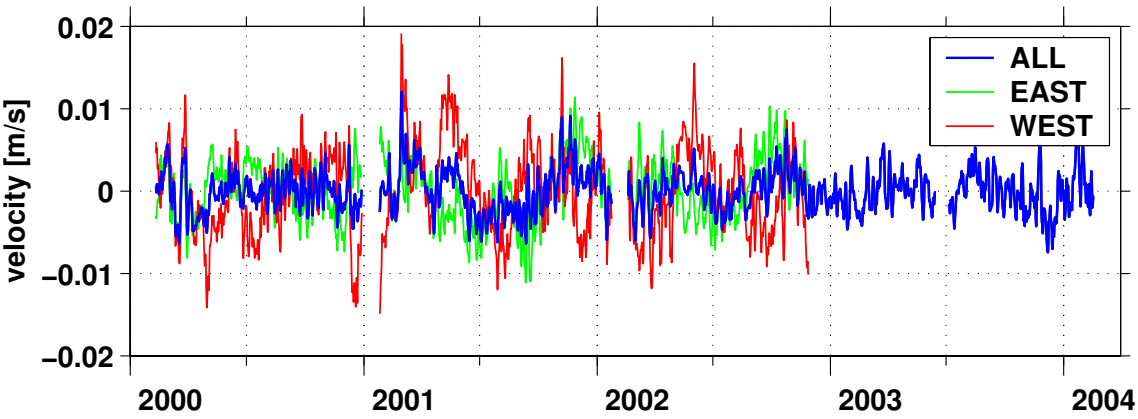

Figure 4.14: *External velocity fluctuations [m/s] derived from bottom pressures. Velocity fluctuations integrated across the total, west and east section are indicated by blue, red and green curves. After November 2002 failures of the bottom pressure recorders at site M2 did not allow for a computation of velocities in the east and west section.*

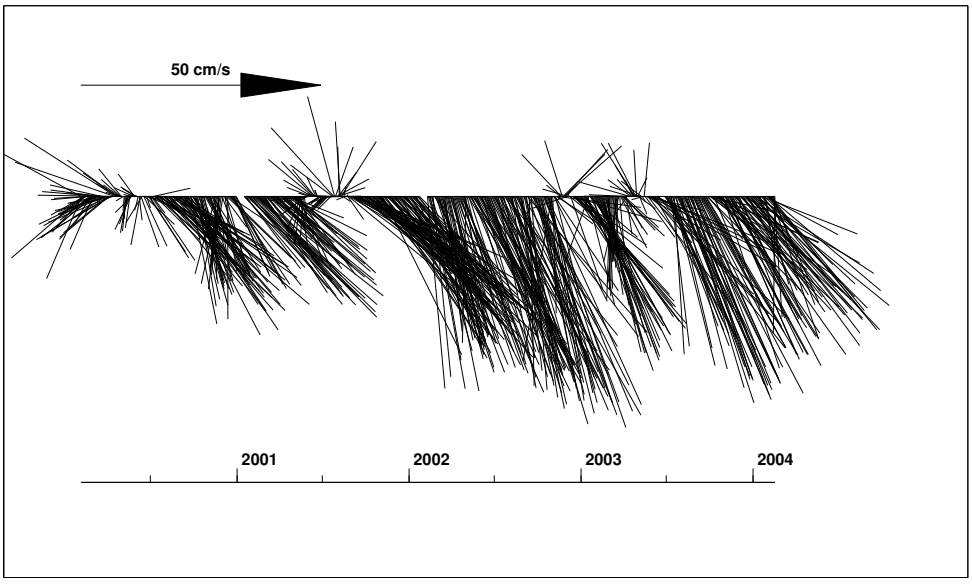

Figure 4.15: *Currents in the core of the DWBC: Vector plot of 2 week low pass filtered velocity data from current meters near 2200m depth in mooring M3.*

record, exceeding velocities of 50 cm/s at times. These characteristics observed here may be considered typical, since they compare well with results from other locations in the tropical Atlantic. (Fischer and Schott, 1997) report that current velocities in the DWBC of more than 70 cm/s were observed just north of the equator.

4.4 Summary

After an introduction of the (deep) water mass characteristics at 16°N the temporal variability of the hydrographic field was analyzed with a focus on implications for transport monitoring. As expected, density fluctuations within the NADW are dominated by changes in temperature, whereas near the AAIW/NADW interface salinity becomes equally important. Accordingly, acoustic travel time does not provide an accurate measure of the depth-integrated density field. In agreement with earlier studies the $\theta - S$ relationship was found to be extremely stable in the NADW and AABW, with uncertainties in salinity of $\pm$ 0.002 psu. In contrast, in the transition zone towards the (and within the) AAIW much larger variability is observed, such that errors in salinity estimated from an empirical mean $\theta - S$ relationship exceed 0.03 psu.

The mean internal velocity distribution was found to be closely related to the vertical distribution of the water masses. Surprisingly this does not only account for the western section, where the southward velocity cores may be attributed to the DWBC. In the eastern section a very similar vertical velocity distribution is observed within the NADW/AABW layer. The principal patterns of variability of the internal velocities (as represented by EOF modes) resemble quasi-geostrophic modes, thus there is evidence that they exhibit a physical rather than only a statistical meaning. Also, the energy distribution among the modes (with a dominating first mode) is broadly consistent with current meter observations in the North Atlantic, although both approaches are not directly comparable. The first 3 modes account for more than 95 % of the variance. Whereas internal fluctuations are dominated by periods of several months the external velocity fluctuations exhibited large variability on weekly time scales. Model results suggest that the dominant vertical modes of meridional velocities associated with MOC fluctuations on inter-annual time scale reflect a rather barotropic compensation of the surface Ekman flow as well as baroclinic response, whose shape resembles that of quasi-geostrophic modes. Finally a current meter record from the DWBC was presented, with velocities exceeding 50 cm/s at times.

5 Volume Transports

5.1 Introduction

In this chapter the transport time series are analyzed in detail. First basic features of variability will be described with a focus on the consistency between data from different deployment periods and measurement techniques. Then the spectral characteristics are presented which allows for the identification of different dynamic regimes. Subsequently independent observations as well as output from numerical models are used to assign physical mechanisms to the observed variability. These analyzes allow for a verification of the MOVE monitoring design.

5.2 Consistency Assessment and Basic Description of Transport Time Series

At the time of writing, the MOVE experiment has been operated for four consecutive deployment periods with an average duration of 1 year each. The gaps of one or two weeks between the different deployments result from the time necessary to service the moorings. As has been stressed already, the jump of a time series from one deployment to the next across the gap is an important indicator for the consistency and accuracy of the time series. A high degree of consistency has already been demonstrated exemplarily for the dynamic height record at site M1 (in Fig. 3.9). Fig. 5.1 (top) shows the internal meridional transports below 1200 dbar relative to the bottom. These were computed according to equation 1.5. Each of the time series displays 3 gaps, caused by recovery and redeployment of the moorings. At those break points, the transitions of the time series from one deployment period to the next display no signs of inconsistencies in all of the cases. This can best verified, where data gaps are shortest. The gaps in eastern transport (M2-M1) records are in all cases shorter than the western or whole section (M3-M2 or M3-M1) records by several days. These smooth transitions in a otherwise highly variable time series lead to confidence that the accuracy for internal transport fluctuations of less than 1.5 Sv on sub-inertial time scales has been reached (Kanzow, 2000), confirming the good instrument performance, calibration and processing results illustrated in chapter 3. Thus, the variability in the internal transports presented here can be considered robust. This is a remarkable result, as is shows that long-term continuous monitoring of large scale horizontally integrated flows using end-point moorings is feasible with high precision. The author is not aware of other studies demonstrating similar consistency of multi-year large-scale integrated transport time series.

Therefore, the end-point monitoring design can be considered a efficient and cost-effective alternative to traditional measurement methods: Reaching similar accuracy with a classical coherent current meter array is only possible, when the baroclinic Rossby radius (of approximately 70 km at the MOVE site) is fully resolved, which would require a horizontal spacing about 50 km and thus 20 moorings along the MOVE section. Additionally, traditional current meters like the well-known Aanderaa RCM-8 face problems in detecting weak flows (i.e. velocities < 2cm/s) in the ocean interior accurately. On the other hand the use of acoustic Doppler current meters may be problematic due to the small amount of suspended matter in the deep ocean at 16°N

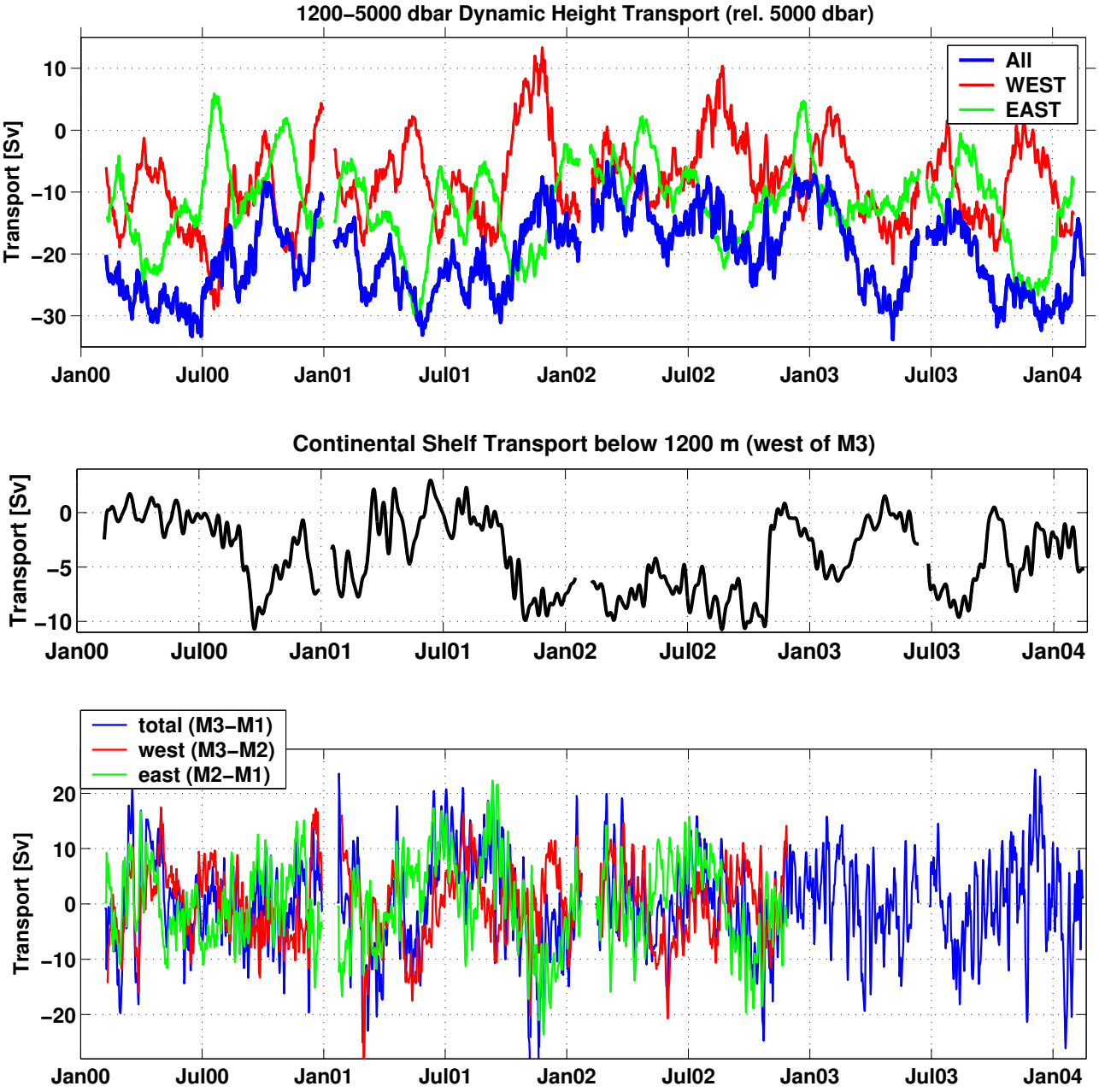

Figure 5.1: *Top: Internal transport below 1200 dbar rel. 5000 dbar. Center:Transport below 1200 dbar over continental shelf (west of M3), acquired by current meter measurements. Bottom: External (bottom pressure derived) transport fluctuations below 1200 dbar. Time series in the top and bottom panels have been 2-day low-pass filtered, whereas a 10-day cut-off for the current meter time series in the center panel has been chosen.*

(see also chapter 6).

It should be noted that during times when the uppermost density sensor was below 1200 dbar at M3 (either due to loss of the top part of in November 2001 or during strong current events as can be seen in Fig. 3.8) the internal transports could not be calculated directly for the whole desired vertical range from the bottom to the upper limit of the NADW. During those phases the velocity shear was extrapolated upward from the uppermost density sensor on 1200 dbar. It is reassuring that even an upward extrapolation of more than 800 dbar during the last two months of the second deployment does not create an abrupt transition (see transition from 2nd to 3rd deployment in western time series).

The internal transports shown highlight a major benefit of the overall monitoring strategy. The transports in the western and eastern part of the array display an out-of-phase behavior of the variability on time scales of a few months with a typical magnitude peak to peak of the order a 10-20 Sv. Thus a part of the variability within the basin cancels out when the transport is integrated over the whole section. This phase relationship is typical of either waves of certain wavelengths or a spin-up of interior northward recirculation (see also discussion in chapters 5.3 and 5.4) . Keeping in mind that the primary goal of MOVE is to determine fluctuations of the strength of the MOC, this class of motions may be considered noise which needs to be suppressed.

This is confirmed by Table 5.1: The standard deviation of total internal transport yields 6.0 Sv and thus is about 10% lower than the western and eastern contribution which exhibit 6.3 and 6.4 Sv, respectively. Also, while the western and eastern contributions are visually dominated by fluctuations of about 3 months, the total internal transport displays variability on longer time scales. This confirms the method's characteristics of integrating out eddies, waves, recirculations etc. over western trough of the North Atlantic in certain frequency bands, resulting in an increased signal-to-noise ratio of the low frequency large-scale variability. A more quantitative analysis of these visual impressions will be carried out in chapter 5.3 using transport spectra.

transport	mean	stand. dev.	accuracy
internal (M1-M3)	-20.1	6.0	1.5
internal (M2-M3)	-11.6	6.3	1.5
internal (M1-M2)	- 8.5	6.4	1.5
external (M1-M3)	0.0	8.4	2.0
external (M2-M3)	0.0	7.0	2.0
external (M1-M2)	0.0	7.6	2.0
boundary (west of M3)	-4.0	3.4	0.3
int. (M1-M3) + bound.	-24.1	4.6	1.6
int. + ext. (M1-M3) + bound.	-24.1	9.7	2.5

Table 5.1: *Mean, standard deviation and accuracy of observed transports below 1200 dbar in Sv. Internal transports are given relative to 5000 dbar. The mean external transports are zero by definition. Error estimates refer to instantaneous observations on subinertial time scales. Time averaged transports will be more accurate, with the exception of external transport, that do not comprise low-frequency fluctuations. The error estimates of the last two entries are based on the assumption that the uncertainties of the different contributions are statistically independent from each other.*

The transport through the boundary triangle over the continental slope (west of M3) was obtained by interpolation of directly measured currents at M4, M3 (and when available also M5) and a horizontal shear extrapolation towards the western boundary. For this a precise topography on the continental slope was used as acquired from the multi-beam Hydrosweep echosounder

system aboard of FS SONNE. Other extrapolation schemes, like no flow at the boundary or no velocity shear between the western-most mooring and the boundary yield almost identical results, with deviations of about 0.3 Sv (not shown). Furthermore, later calculations showed that the transport change by including M5 (only available during third and forth deployment) is almost negligible. Based on these tests, the error estimate of the boundary triangle transport is 0.3 Sv. The flow is clearly dominated by the DWBC (see Fig. 5.1, middle panel). Periods of strong flow are observed from October 2000 to March 2001 and from October 2001 to November 2002. The 4 year mean (Feb 2000 - Feb 2004) southward transport below 1200 m over the slope amounts to 4.0 Sv, its standard deviation yields 3.4 Sv. Estimates of the mean strength of the DWBC in the tropical North-Atlantic range between 18.5 and 29 Sv (Schott et al., 1993; Johns et al., 1993; Rhein et al., 1995; Fischer and Schott, 1997). Thus, at this location exhibiting a particularly steep western boundary topography (see chapter 2.2), obviously only a small fraction of the DWBC is concentrated west of M3 over the continental slope. During times of weak flow through the boundary triangle, an increased southward internal transport can be observed further off-shore (compare figure 5.1, top). This may be interpreted to be the signature of the DWBC meandering in the off-shore direction. The standard deviation of total internal plus boundary triangle transport amounts to only 4.6 Sv and thus is significantly lower than variability of the internal transport alone (table 5.1). Thus, a further improvement of the signal-to-noise ratio is reached. One example of the high degree of correspondence between the two datasets, which are based on different measurement techniques, shall be highlighted: At the transition from the first to the second deployment period (January 2001) the internal transport in the west section exhibits a jump of about -7 Sv, which by itself might misinterpreted as a manifestation of uncertainties in the measurements or the processing. However, simultaneously a jump of opposite sign and similar magnitude (+5 Sv) in the boundary transport is observed, leading to a near compensation of the changes in the internal transports. It should be added that it is not straightforward to assume that a DWBC meandering offshore does have to result in an exact transport compensation of internal and boundary triangle transports. It might depend on the conditions under which the meandering occurs, such as the strength of the DWBC or the fraction of it recirculating in the interior. The degree of compensation between both timeseries (which might be represented by a linear regression coefficient) is certainly dependent on the reference level of the internal transport and on the degree to which fluctuations are barotropic. However, since no visual indication for a correlation between external and boundary triangle triangle transports can be seen in Fig. 5.1, the meandering will be dominated baroclinic signals.

The external near-bottom velocity fluctuations are obtained from bottom pressures according to Eq. 1.4. They are scaled to transports by multiplication with the mooring separation and water layer depth (here 3723 m between 1200 and 5000 dbar) as indicated by Eq.1.6. Based on the error estimates in the bottom pressures of about 0.002 dbar (corresponding to 2 mm water column equivalent) the resulting uncertainties for the external transports scale to 2 Sv. The transports have a zero mean by definition (as they are computed from pressure fluctuations), their standard deviations amount to 8.0, 7.6 and 7.0 Sv for the whole, east and west section, respectively. After November 2002 only transport for the whole section could be derived due to problems with the PIES at M2. The time series are dominated by fluctuations on short time scales ($<$ 20 days) as well as periods in the order of a few months (Fig. 5.1,bottom). A closer look reveals that the high frequency fluctuations of the western and eastern contribution are highly coherent (see chapters 5.3 and 5.4). On monthly time scales east and west transports reveal a 180° out-of-phase behavior. This could either represent the signature of eddies or waves of certain wavelengths or it could as well reflect the spin-up and spin-down of an interior recirculation (Lee et al., 1996; Lux et al., 2001). External transports do not appear to be correlated with internal or boundary triangle transports since the r.m.s. variability of the sum of these contributions amounts to 9.7 Sv.

Judging the consistency of the transitions from one data segment to the next is more difficult

for the external transport due to the presence of high-frequency fluctuations. However a closer looks reveals the general continuity of the longer period signals across the data gaps. The drift removal of the bottom pressure time series in chapter 3.6 thus appears to have worked satisfactorily, although the simulations in chapter 3.7 show that a hypothetical inter-annual variability is suppressed by the requirement to subtract the mean of each data segment.

The inter-annual r.m.s. variability of internal (M3-M1) plus boundary triangle transports amounts to 2.4 Sv, which is larger than the measurement error associated with this technique. Typical values of O(2 Sv) of inter-annual MOC fluctuations are exhibited by numerical models forced by realistic momentum and buoyancy fluxes (Beismann et al., 2002). However the 4-year long transport time series from MOVE is still much too short to establish any statistical significant relationship between the observed lower frequency variability and possible remote forcing fields of MOC fluctuations, as will be shown in chapter 7.

5.3 The MOVE Spectrum

In the following, results from spectral analyzes of the transport data are discussed. This allows for an identification of different dynamical regimes and provides an objective measure for the strength of the different transport contributions as a function of frequency. Also, possible relationships between the various transport time series is focused on by means of cross spectra. Based on these results, independent observations and numerical model output will then be used to explain the observed characteristics of variability in the chapter.

The transport time series used in the computation (see Fig. 5.1) span the interval from Feb. 2000 to Feb. 2004, with an exception being the external transport through the east and west section, which due to instrument failures already end in Nov 2002. Spectra (and coherences) of external and internal transports are displayed in Fig. 5.2. They have been estimated using the multiple prolate window technique after Thomson (1982), which was specifically designed to allow for the extension of spectral estimates to long periods (personnel communication A. Chave). The code was provided by A. Chave (WHOI). The partitioning into external and internal transports may appear arbitrary and arise from the convenience of analyzing the different instrumental components separately (see also discussion in chapter 2.2). However, as will be shown below, this strategy has some physical justification, since it essentially corresponds to a separation into barotropic and baroclinic contributions.

Caption of Fig. 5.2: Spectral analysis of MOVE 1200-5000 dbar external and internal (rel. 5000 dbar) transports: Panels A and B display variance conserving spectra of external and internal transports, respectively. Panels C (E) and D (F) show squared coherence (phase relationship) between transports through the east and west section, again separately for internal and external contributions. The zero coherence level at 95 % significance is denoted by the dashed line. Panel G and H display coherence and phase relationship between internal and external transport. In panels showing more than one curve (A,B,G,H), transports through the whole (M3-M1), west (M3-M2) and east (M2-M1) section are illustrated by black, red and green color, respectively. The magenta line in panel B represents the sum of boundary triangle (west of M3) and whole section (M3-M1) internal transports. Positive phase means that the second time series (mentioned in the title) leads. One those phase values have been displayed whose corresponding squared coherences exceed the zero coherence level.

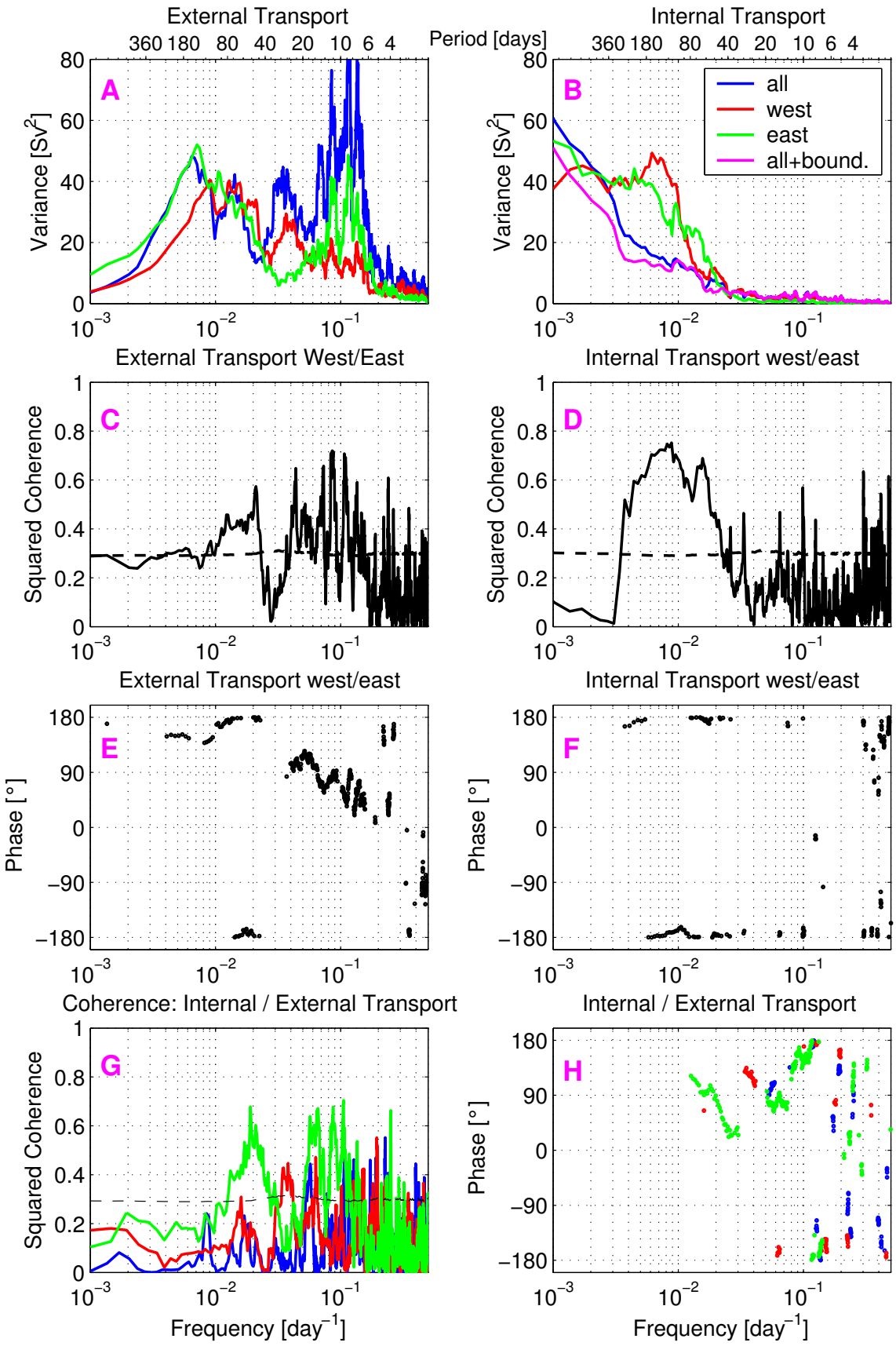

Figure 5.2: *The caption of this Figure can be found on page 62*

External Transports The variability of the external transports (Fig. 5.2 A,C,E) can be subdivided into different regimes. In periods $\tau < 6$ days only little variability is seen and no significant coherence exists between east and west transports. In the band from 6 days $< \tau <$ 18 days much energy is concentrated, with 4 distinct peaks being visible at 7.3, 8.6, 11.8 and 14.2 days. In this range fluctuations of east and west transports appear to be almost additive with respect to the total, with their contribution approximately scaling with the ratio mooring spacing squared $((\frac{590\text{km}}{370\text{km}})^2 = 2.5)$. Thus, it appears that the horizontal correlation scale of this type of flow yields more than 1000 km. This matches with the fact, that this band displays significant coherence between the east and west transports (panel C). Maximum coherence is found at those 4 distinct periods. The phase relationship ranges between 45 and 90 degrees with east leading west transports.

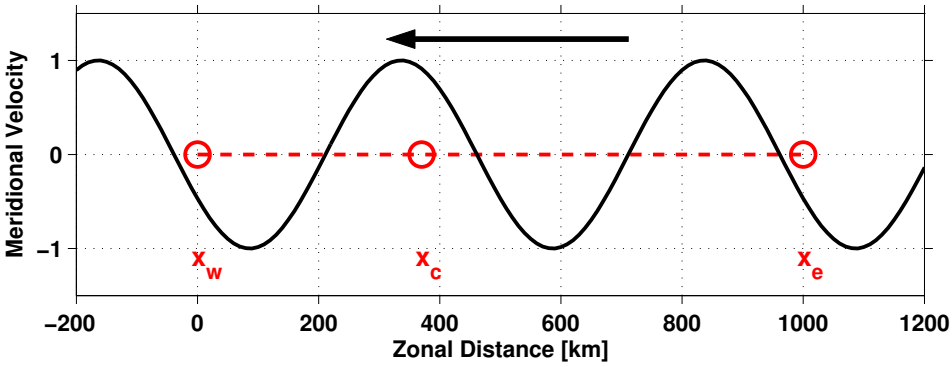

Figure 5.3: *Simple model used to simulate aspects of zonally integrated transports of the MOVE experiment: Meridional transports associated with a westward propagating linear wave (of dimensionless amplitude) are integrated between x_w and x_c as well as between x_c and x_e, separately, mimicking the east and west section of MOVE (see Fig. 2.1)*

This pattern may be explained by a simple westward propagating linear waves of the type

$$v(x,t) = \sin(\frac{2\pi}{\lambda}x - \frac{2\pi}{\tau}t) \tag{5.1}$$

with v, x, t, λ standing for meridional velocity, zonal distance, time and zonal wave length, respectively (see Fig. 5.3). If one assumes λ to be large compared to the mooring separation, say $\lambda = -3000$ km, for a westward propagating wave. Let x run from $x_w = 0$ to $x_e = 1000$ km, and be $x_c = 370$ km, mimicking the MOVE moorings. Zonal integration yields transports through the western $[x_w x_c]$ and eastern $[x_c x_e]$ part of the section: $t_w = \int_{x_w}^{x_c} v(x,t)dx$ and $t_e = \int_{x_c}^{x_e} v(x,t)dx$. Easy computation shows that t_e leads t_e by about 65 ° (Fig. 5.4, lower panel). The ratio of the variances of t_e and t_w yields 2.8 (Fig. 5.4, lower panel). All of this matches very nicely with the observations. Varying λ between 2000 and 4000 km results in phase shifts between t_e and t_w of 90 ° to 45 °. Thus these are the diagnosed wavelengths matching with the observed phase shifts, These will be contrasted to results from model analyzes in chapter 5.4, which suggest that barotropic Rossby waves represent a plausible cause of the observed variability in this frequency band.

Theoretically, this model exhibits bands of shorter wavelengths resulting in similar phase relationships, for example near 280 km. However, these bands appear highly unstable, with phase changing rapidly as a function of wavelength. Also, the variance distribution east and west transports does not correspond to the observed ratio. The limitations of this simple model are obvious: Any motion deviating from a westward propagating undamped linear wave is not represented. Also, the model assumes open boundaries in the east and west whereas the MOVE section is bounded by the MAR and the Antilles Arch.

The next band under consideration reaches from 20 to 40 days: Here eastern transports display

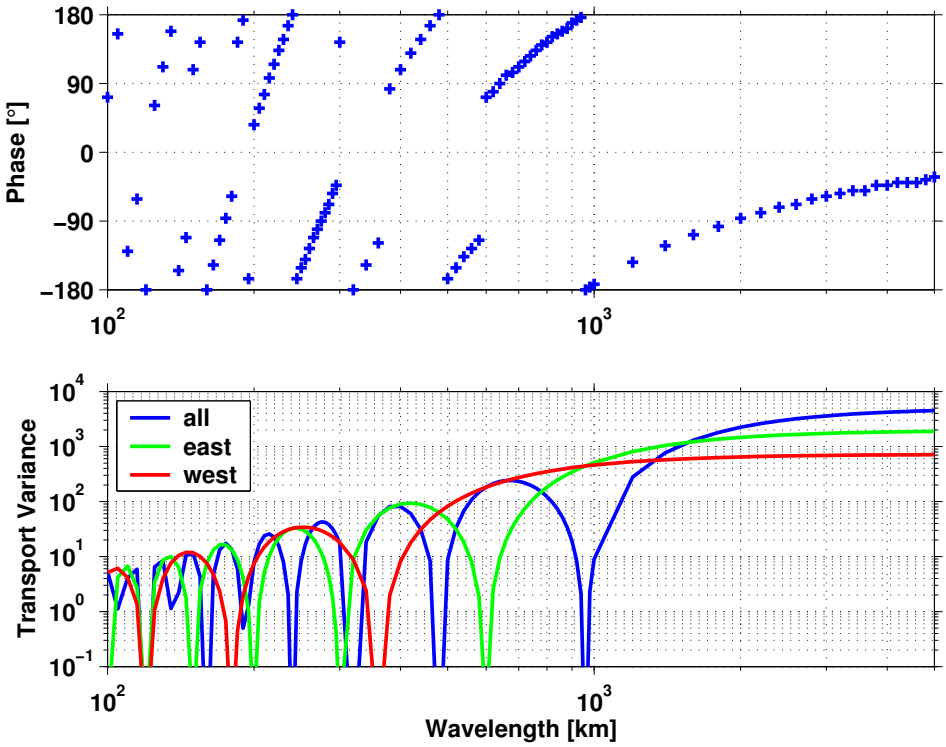

Figure 5.4: *Top: Phase relationship between meridional transports associated with a westward propagating linear wave (equation 5.1) are integrated between x_w and x_c (west section) as well as between x_c and x_e (east section) as a function of zonal wavelength. A negative phase means that east lead west section transports. Bottom: Resulting dimensionless meridional transport variance, integrated across the east, west and total section.*

an energy minimum, whereas western transports show a minor peak around 25 days. This might arise from topographic waves at the western boundary or fluctuations propagating towards the the section from the south, as altimeter observations from TOPEX/POSEIDON suggest (pers. communication H. Schmidt). At periods longer than 40 days (spectral gap) to about 90 days, east and west transports exhibit energy levels of about equal size. Their coherence amplitude exceeds the zero coherence level at 95% significance (panel C), with the signals showing a 180 ° out of phase relationship (panel E). This could explain, why the energy in the total transport does not exceed that of the contributions from east and west, since parts of east and west signal cancel out with respect to the total.

Finally at periods longer than 90 days the spectra reach peaks at about 100 - 130 day and then decay sharply (panel A). The total transport is dominated by the eastern contribution which are about twice as large as the western. In this band the phase switches from 180 ° to 140 °, which has to be viewed with caution as the coherence is hardly significant. As has been discussed in chapter 3.7, the empirical elimination of instrumental drift from bottom pressure records must go along with a reduction of low-frequency amplitudes in external transports: Therefore spectral estimates for $\tau > 180$ days underestimate the degree of true variability. The total external transport displays a peak at the semi-annual period, however there is no indication for an annual signal.

Internal Transports The spectra of internal transports are organized more simple (panel B): Below periods of 50 days an extremely small fraction of the energy is concentrated and east and west transports are not correlated. At time scales larger than that, energy steadily increases and significantly coherent fluctuations of east and west transports with a phase shift of 180 ° are

observed (panel D and F). Accordingly, large parts of them get canceled out with respect to the total transport (panel B), thus explaining its relative low energy level. This situation can again be modeled using the above sine wave approach: If λ of O(480km) is chosen (comparable to the separation of the moorings) is chosen, a 180 ° phase shift between t_w and t_e can be observed, with east and west transports displaying the similar variance levels. This corresponds well to the observed spectrum. However the model also displays the same phase relationship at other wavelengths (near 240 and 930 km) with the same ratio of east and west transport variances, which make the result ambiguous.

For periods $>$ 100 days the energy level in the east and west transports remains relatively stable. An abrupt decrease in coherence (below the significance level) between the two time series is seen at a period of 300 days. This can be regarded as an indication for a change in the dynamics on longer periods. The energy of the total transport (blue line) keeps steadily increasing to towards lower frequencies. No indication for outstanding annual (and semi-annual) cycles can be observed, which one might have expected due to the seasonally varying wind field. However results from (Jayne and Marotzke, 2001) indicate the response to wind stress in this frequency band results in a rather barotropic compensation, which should rather be reflected by the external transports. Also, it should be added that according to numerical simulations of the CONTROL run of the FLAME 1/3 ° model (see Appendix A for details) the seasonal transport cycle of the MOC is much less pronounced at 16 °N than towards the equator or the subtropics (not shown), which was one of the reasons why this area was chosen as monitoring site of the MOC (see chapter 2.2).

It had been shown already in the preceding section (Table 5.1) that the r.m.s. variability of the total internal transport is slightly smaller than that of its east and west contributions. The spectral analysis clearly demonstrates that an integration of the transport across the entire western trough of the Atlantic (M3-M1) significantly suppresses variability in the 50-250 day band by averaging out dynamics of wavelengths smaller than the mooring separation, when compared to the contributions from the eastern and western sections (which represent integrated transport as well). A further reduction in variance in accordance with results from Table 5.1 can observed for periods $>$ 50 days when adding to the whole internal transport the boundary triangle contribution (magenta line in panel B). These findings refute presumptions, that transport signals, acquired by the MOVE endpoint mooring strategy, would be highly contaminated with noise introduced by eddies, Rossby waves or meandering. The large zonal integration scale leads to a significant noise reduction in the 50-250 day band. The fact the the spectral energy continues to increase towards inter-annual time scales is encouraging, however it is unclear whether these fluctuations are attributable to the MOC.

General Discussion Comparing internal (panel B) to external (panel A) transports it becomes evident, that at periods $<$ 80 days external fluctuations clearly dominate the internal ones. At periods $>$ 1 year internal variability displays a higher energy level. This result however has to be regarded with some caution, due to the artificial reduction of inter-annual external transport signals, caused by the detrending of the bottom pressure time series. On the other hand it is encouraging to observe that the spectra of internal transports continue to increase towards longer periods, when integrated across the whole section. This may mean that inter-annual variability can be de-masked already after only 4 years of continuous measurements as a consequence of the suppression of higher frequency fluctuations due to the long zonal integration scale. A future challenge is to relate these inter-annual changes to changes in the MOC and its forcing fields.

Coming back to the discussion of treating internal and external transport separately, one may ask, whether there is significant coherence between the two contributions (see panel G and H for coherence and phase). The band of periods $<$ 50 days can disregarded in this respect

due to the low energy content of internal dynamics there. At lower frequencies, no significant coherence is observed with the exception of a peak at around 50 days between the two transport contribution in the east section with external leading internal fluctuations by 50 ° (i.e., 7 days). No physical mechanism could be assigned to this dynamics. Together with the fact that east internal transport fluctuations are rather small and furthermore no such feature can be observed in the western part of the section, it remains doubtful, whether this peak represents a physical relationship between internal and external transport variability.

In general, a decomposition of the vertical velocity structure into barotropic and baroclinic modes reveals, that baroclinic modes have an impact on bottom pressure, since for example the velocity associated with the first baroclinic mode is non-zero at the bottom (Fig. 4.12). However, studies reveal that the temporal evolution of bottom pressures is dominated by barotropic motions (e.g. Luther and Chave, 1993). Therefore, external (i.e. bottom pressure) fluctuations are often used a synonym for barotropic flow (e.g. Johns et al., 2004). In the MOVE case this is a valid assumption in the high-frequency limit (i.e. Periods < 50 days). At lower frequencies, where internal and external transport display a similar level of energy, the situation becomes less definite. However, since also in the lower frequency limit no explicit relationship between internal and external transport variability could be established, one may consider it justified to treat them separately (not just for reasons of convenience). Both contributions clearly differ not only in temporal, but also in spatial scales and will therefore be explainable by different dynamics, such that at lower frequencies assumption of external transport fluctuations corresponding the barotropic motions might still be a good approximation. However this may not be regarded as a general result holding everywhere in the ocean, since there is recent evidence from a truly mass conserving (i.e. non-Boussinesq) model simulation that in the equatorial Pacific baroclinic instability waves to have a strong imprint on bottom pressure with maximum amplitudes at 4 ° north and south of the equator reaching amplitudes of 2 mbar (Song and Zlotniki, 2004). In this respect it is worth noticing that bottom pressure signals (or non-vanishing near bottom velocities) indicate an exchange of momentum between the ocean and the solid earth, influencing the earth's rotation and orientation (e.g. Ponte and Rosen, 1994; Eubanks, 1993; Dickey, 1993).

For the interpretation of horizontally integrated flows the width of the integration scale has to be considered explicitly, which for example complicates comparisons with current meters point measurements. Fig. 5.4 (bottom panel) reveals that the integrated transport variance resulting from westward propagating linear waves (as a function of λ) depends on the section width X. The wave signal is suppressed on condition that X is an integer multiple of λ, i.e. $X = n\lambda$, whereas local extrema are found for $X = (n + \frac{1}{2})\lambda$. Superimposed is the general tendency that the longer the zonal correlation scale (wavelength) of the signal, the larger becomes the transport variance. Large amplitude short wavelength signals ($\lambda \ll X$), which might dominate current meters point measurements, will cancel out partly in the zonal integral, which is therefore more likely to be dominated by longer wavelength signals. Thus, the energy distribution of among EOF modes of point and integral measurements are not directly comparable (see also the discussion in chapter 4.3).

5.4 Dynamical Aspects of Transport Variability

In the preceding chapter distinct patterns of horizontally integrated transport variability have been revealed by spectral analysis. Now additional observational data as well as model output is analyzed to unravel the dynamics responsible for these, focusing on the implications for the end point monitoring design applied. One additional data source to study are meridional current fluctuations measured by the MOVE/GAGE current meter array (its design is displayed in Fig. 2.1). Fig. 5.5 shows spectra of meridional velocities as measured by current meters along the

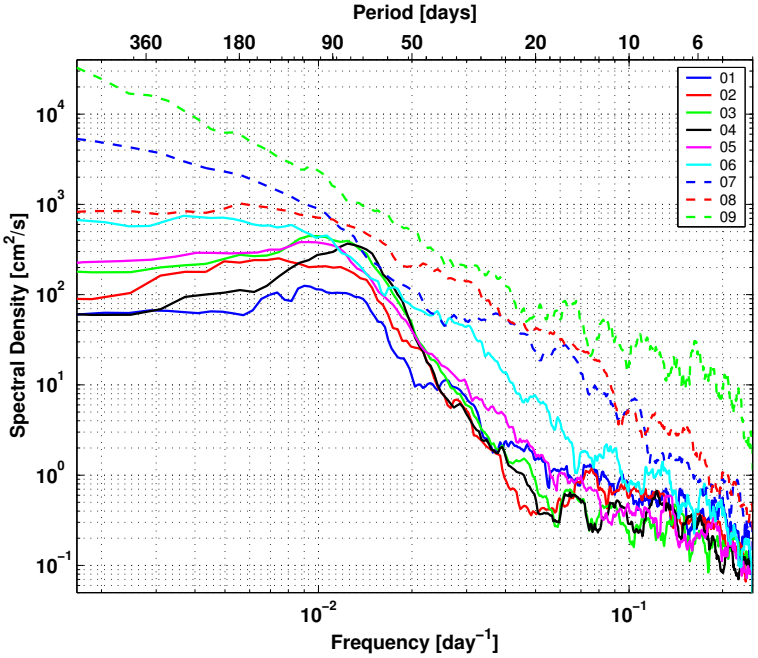

Figure 5.5: *Variance conserving spectra of meridional velocity in 1600 m measured by the current meters of the 9 MOVE/GAGE moorings (see Fig. 2.1). The numbering goes from east to west, such that the MOVE mooring M1, M2 and M3 correspond to the sites 1, 6 and 9, respectively.*

16°N section. At most mooring sites a peak around 80-120 days is observable, corresponding to that seen in the internal east and west internal transports (Fig. 5.2B). Furthermore, it is interesting to observe how the energy level keeps steadily increasing from east to west (i.e. From mooring 1 to 9) at all frequencies. Simultaneously, the general character of the spectra changes: Whereas in the east the 3-month maximum clearly towers above the energy levels of the longer and shorter period ranges, towards the west this peak becomes increasingly broader and shifted towards longer periods. Currents in the extreme west, i.e. in the DWBC (site 9), display no such intermediate maximum any longer. Again, these observations are highly consistent with has been found in the spectra of the internal east and west transports (Fig. 5.2B): At around 80 days a higher level of variability is found in the east whereas at 140 day fluctuations in the west dominate.

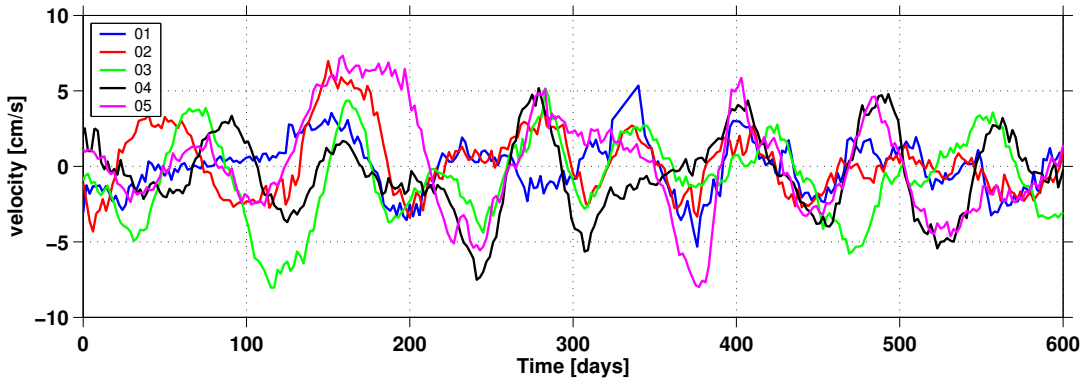

Figure 5.6: *Time series of the meridional current velocities at 1600m, that had been used to compute the spectra in Fig. 5.5. Only data from the sites 1-5 are shown. The time series have been shifted in time relative to site 1 in order to achieve maximum agreement between the peaks. Best agreement is found by shifting time series 2,3, 4 and 5 backward in time by approximately 1, 2, 3 and 4 months, respectively.*

The physical cause for the 3-month fluctuations are westward propagating waves, as Fig. 5.6 clearly demonstrates. By shifting the time bases of the velocity records backward in time by about one month more at a time from east to west, good agreement between the meridional current extrema is found. This allows to read-off the typical propagation speed of these waves, which amounts to $c = 5$ cm/s, taking 4 months for the signal cover the distance of 500 km between the moorings 1 and 5. However, a closer look reveals that different peaks move towards the west with slightly differing velocities. Choosing a typical signal period, say $\tau = 100$ days, the corresponding wavelength $\lambda = c\tau$ amounts to 430 km. This is in reasonable agreement with the linear wave model estimate of 480km based on the 180° phase shift between east and west internal transports observed in this period band (see Fig. 5.2D). Since we are obviously dealing here with predominantly baroclinic dynamics (no significant coherence is observed at 100 day between west and east external transports), there is only one obvious type of waves to explain the pattern observed: baroclinic Rossby waves. Their dispersion relationship reads for purely zonal propagation

$$c_i = -\frac{\beta}{k^2 + \frac{1}{R_i^2}} \tag{5.2}$$

with c_i, β, k, R_i denoting phase velocity, meridional gradient of the Coriolis parameter $\frac{\partial f}{\partial y} = 2.2 \cdot 10^{-11}\mathrm{s}^{-1}\mathrm{m}^{-1}$, zonal wavenumber and baroclinic Rossby radius, respectively (e.g. Cushman-Roisin, 1994). Inserting the observed wavelength $\lambda = 2\pi/k = 430$km and $R_i = 70$ km a phase speed of $c_i = 4.8$ cm/s is obtained. This is in reasonable agreement to the propagation speed of 5 cm/s computed from the current meters. Additionally, solving equation 5.2 for the wave period $\frac{2\pi}{c_i k}$ yields 100 days (black solid line in Fig. 5.7). It should be added that according to the theory (equation 5.2) the minimum period of baroclinic Rossby waves (for $R_i = 70$ km) is about 100 days and goes along with wavelengths of 420 km. Longer as well as shorter wavelengths result in longer periods. Since the observed waves partly show periods of less than 100 days (which is the minimum period expected from theory) it is not clear whether exclusively free Rossby waves have been observed (pers. comm.§. Brandt). Also, the influence of background velocity, velocity shear and topography may affect the simple relationship 5.2.

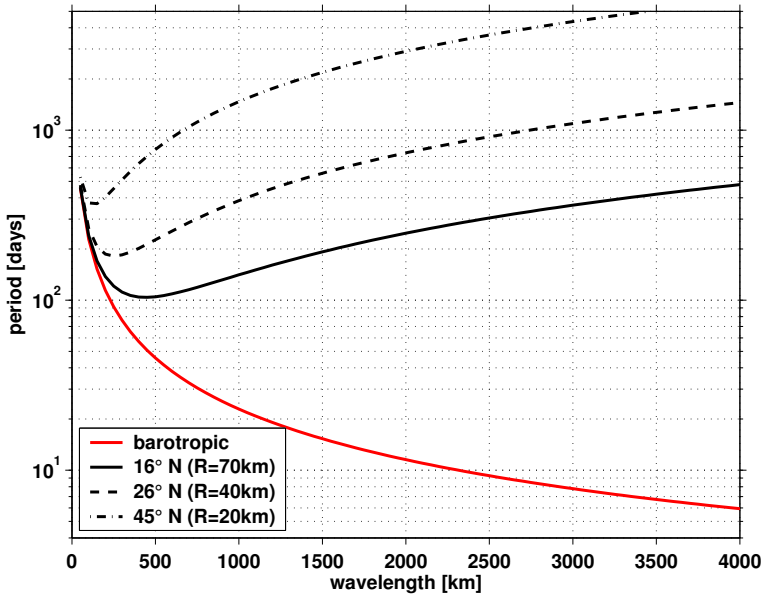

Figure 5.7: *Dispersion relation of baroclinic Rossby waves (black lines) for $R_i = 70, 40$ and 20 km, according to equation 5.2, which are found in the Atlantic near 16, 26 and 45° N, respectively : Wave period as a function of zonal wavelength $\frac{2\pi}{k}$. The relation for barotropic Rossby waves, using the barotropic equatorial Rossby radius of 3300 km, is shown as red line.*

A more complete picture of the variability at 16°N can be obtained from the FLAME 1/12° high resolution model (Fig. 5.8). Away from the DWBC (represented by strong negative transports west of 60.0°W in the left panel) westward propagating Rossby waves represent the most dominant pattern of variability at 16°N below 1200m, visualized as coherent stripes in the Hovmoeller diagram. The models' baroclinic Rossby wave phase speed, which can be read off as the slope of the stripes, amounts to 4.8 cm/s and therefore corresponds well to the observed 5 cm/s. The resulting zonally integrated "east" and "west" meridional transport fluctuations (right panel), visually display a near 180° out of phase behavior, just like the one observed in the internal transports (top panel of Fig. 5.1 and the corresponding panel D of Fig. 5.2).

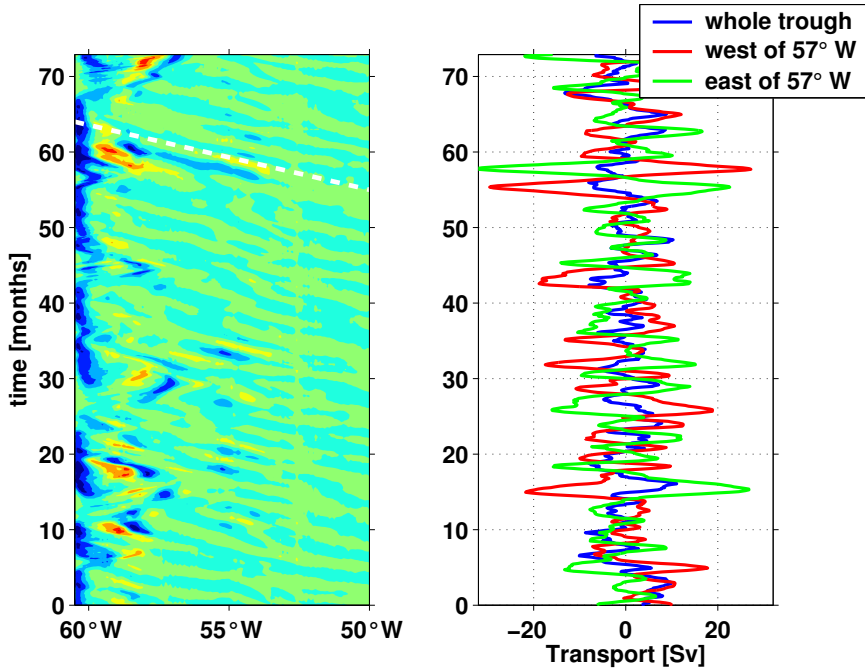

Figure 5.8: *Left panel: Hovmoeller diagram of transport density (transport per unit zonal distance [Sv/m]) across 16°N below 1200 m. Right panel: Resulting meridional transport fluctuations [Sv] below 1200 m, integrated across the entire western trough (61.0°-51.5°W, blue) as well as the eastern (61.0°-57.0°W, green) and western (57.0°-51.5°W, red) part of the section, mimicking the MOVE monitoring design. The computations are based on output from the 1/12° FLAME model.*

Furthermore, the FLAME 1/12° model displays other similarities with the observations. There is significantly larger variability (of transport density) in the western part (61.0°-57.0°W) than in the eastern part (57.0°-51.5°W), corresponding the current meter velocity spectra in Fig. 5.5, which at times substantially upsets the Rossby wave pattern there (left panel in Fig. 5.8). This matches with the fact that Rossby wave propagation in the west section cannot be tracked by current meters as easily as in the east section (not shown). Especially noticeable are the large eddy structures of coherent positive and negative transports centered at 59°W at the months 10, 18 and 60. Fig. 5.9 (upper row) highlights normal conditions with a dominating DWBC and a relatively calm interior. However the 3 consecutive snapshots in the lower row clearly display such an eddy structure off the western boundary. Exactly speaking, it consists of twin eddies, rotating in opposite directions and exchanging inertia and at the same time interacting with the DWBC. The stronger of the two eddies, displaying a comparable velocity amplitude as the DWBC, reaches a diameter of 200 km. These simulations reveal that at times rather complicated and strong circulation patterns may exist east of the DWBC with may partly be responsible for carrying the CFC signal signal extending far into the basin interior as observed in Fig. 4.2.

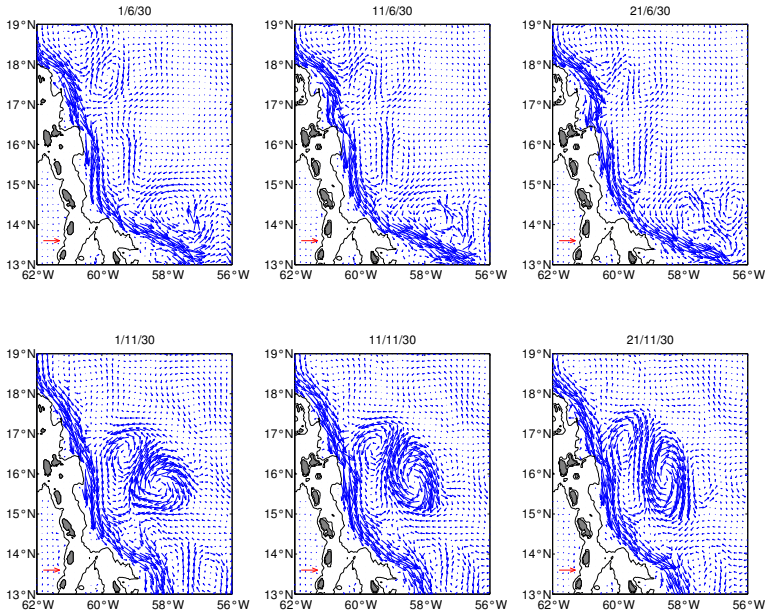

Figure 5.9: *Horizontal velocity distribution at 1800 m in the tropical North-Atlantic near the Lesser Antilles from the FLAME 1/12° model. In the top row three consecutive snapshots (with a time offset of 10 days at a time) of "normal" conditions with a strong DWBC are depicted, whereas the lower row displays "anomalous" conditions. The red arrow represents a velocity of 25 cm/s. The gray line denotes the 1800 m contour.*

Concluding, Rossby waves and eddies are dominant sources of variability in the ocean interior at 16°N and therefore would decrease the signal to noise of the MOC monitoring, if measurements were restricted to the DWBC only. This again stresses the necessity to extend the zonal integration scale of the meridional transports sufficient far into the ocean interior, to average out these signals. The MOVE integration scale of 1000 km meets this requirement since it is much larger than the typical length scales of eddies and baroclinic Rossby waves. The significant increase of the signal to noise ratio by integrating across the whole western trough[1] the Atlantic had already been demonstrated by in geostrophic transport observations (Table 5.1 as well as Figures 5.1 and 5.2) . The effect variance reduction in the model simulations amounts to a factor of 4. Whereas the modeled east and west transports (shown in Fig. 5.8) each exhibit a standard deviation > 8.5 Sv, that of the whole section amounts to only 4.3 Sv. In the observations in certain spectral bands a variance reduction of a factor of 2 has been reached (Fig. 5.2 B) but the overall reduction is only 1.2. Several reasons may account this discrepancy: No reduction is seen in the observations at periods > 1 year. Whereas the real ocean is forced at all frequency the model experiment used here experienced climatological forcing only. Therefore inter-annual fluctuations are underestimated by the model. Additionally, in the model high transport amplitudes associated with large compensations seem to be related to the appearance of the large eddies (see Figs. 5.8 and 5.9). Whether these eddies can be found at 16°N in the real ocean is currently unclear. Finally, measurement errors may lead to a minor contribution to the smaller variance reduction in the observations than in the model.

Another interesting aspect of the dynamics near 16°N is revealed by the model. Most of the time a strong DWBC can be seen (left panel of 5.8). However during certain time intervals (between the month 12-15 as well as 23-29, 42-46 and 67-71) no DWBC seems at exist at this

[1] Please note that areas east and west of about 51°W (MAR) are referred to as eastern and western trough, respectively. This should not be confused with the east and west sections, which denote the MOVE M2-M1 and M3-M2 sections within the western trough of the Atlantic, respectively.

latitude. This may correspond to the current meter measurements in the DWBC (Fig. 5.1,

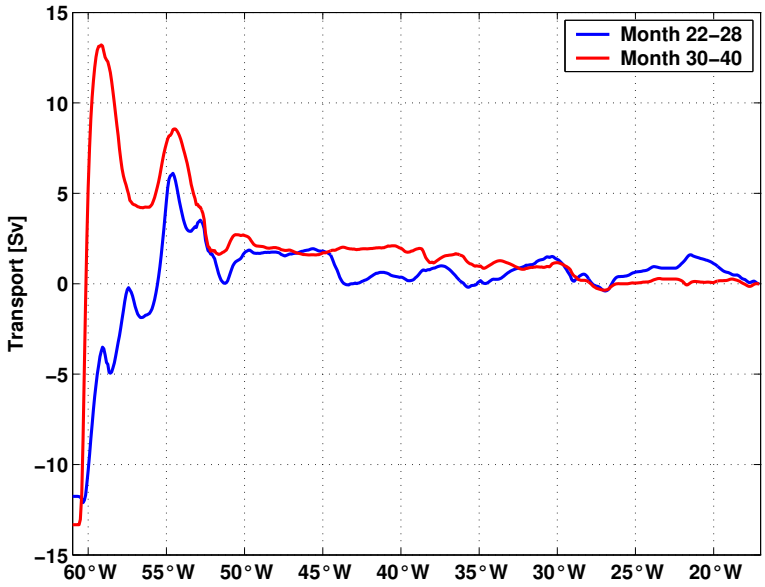

Figure 5.10: *Cumulative meridional transports across 16°N below 1200m (integrated from east to west). The blue and red curve represent the time average of the months 22-28 and 30-40 representing periods of weak and normal strength of the DWBC, respectively (see also Fig. 5.8). The net meridional transport can thus be read off at the left side (western boundary) of the graphics.*

middle panel), where periods of extremely weak flow lasting several months have been observed (e.g. Feb.-Sep. 2000 and Apr.-Sep. 2001). During those events increased offshore southward flow had been observed in the internal transports. In the model one may test, where this interior compensation occurs and what the absence of the DWBC means for the zonal transport integral across the entire Atlantic basin (Fig. 5.10). During "normal" conditions (red line), a strong and narrow DWBC west of 59.5°W is observed, carrying 26 Sv to the south. This is partly compensated by an offshore northward recirculation of 9 Sv between 59.0 and 56.5°W. The total transport below 1200m across 16°N amounts to 13.4 Sv. During times, when Fig. 5.8 does not display a clear DWBC structure, the total southward transport still amounts to 11.8 Sv (blue line in Fig. 5.10). Even though west of 59.5°W only 8 Sv move southward, which represents a decrease of 16 Sv compared to normal conditions. On the other hand, an offshore northward recirculation cannot be found. Moreover the area of southward flow extends all the way from the western boundary up to 55.0°W and thus covers a substantial part of the western trough. The MOVE zonal integration scale of 1000 km is sufficient to completely capture the interior compensation during such extreme events. However, a weak point of the MOVE design becomes apparent as well: net transports below 1200 m in the eastern trough of the Atlantic (i.e. east of 50°W), which are not covered by the measurements, are found to be non-zero in both case, but amount to about 2 Sv of northward flow. The consequences of this deficiency will be examined in chapter 7.

Now the dynamics of the strong high-frequency external (barotropic) transport fluctuations (seen in Figs. 5.1 and 5.2 A, C, E) is further examined. From the phase relationship of the variability in the east and west section in the 6 - 14 day period range it was concluded that westward propagating large scale O(3000 km) waves might be responsible. Such waves would exhibit a phase speed 0(300 km/day) and would therefore be hardly detectable from the current meter array in the presence of tidal and internal wave dynamics. Therefore the subsequent analysis is restricted to numerical model results. Here, tides are absent and internal waves are suppressed, and most importantly, the analysis can be extended to the zonal basin width of the

Atlantic, which is required for the study of almost basin-scale wavelengths. The constrained version of the ECCO 1°x 1°model (e.g. Stammer et al., 2003), using the adjoint technique for data assimilation, was chosen for this purpose, because daily meteorological forcing fields had been used (see Appendix A.2 for details). The FLAME model is based on monthly fields instead and therefore does not realistically represent fluctuations in the frequency range of interest. Additionally, the fact ECCO is constrained by sea-surface height (SSH) from satellite altimetry and other observational data sets should add further realism to the model output. Since large-scale barotropic patterns are to be examined, the relatively low horizontal resolution of ECCO is not considered a major deficiency. In a first step external transports from ECCO model are compared against the observations (Fig. 5.11). The high-frequency fluctuations in the model

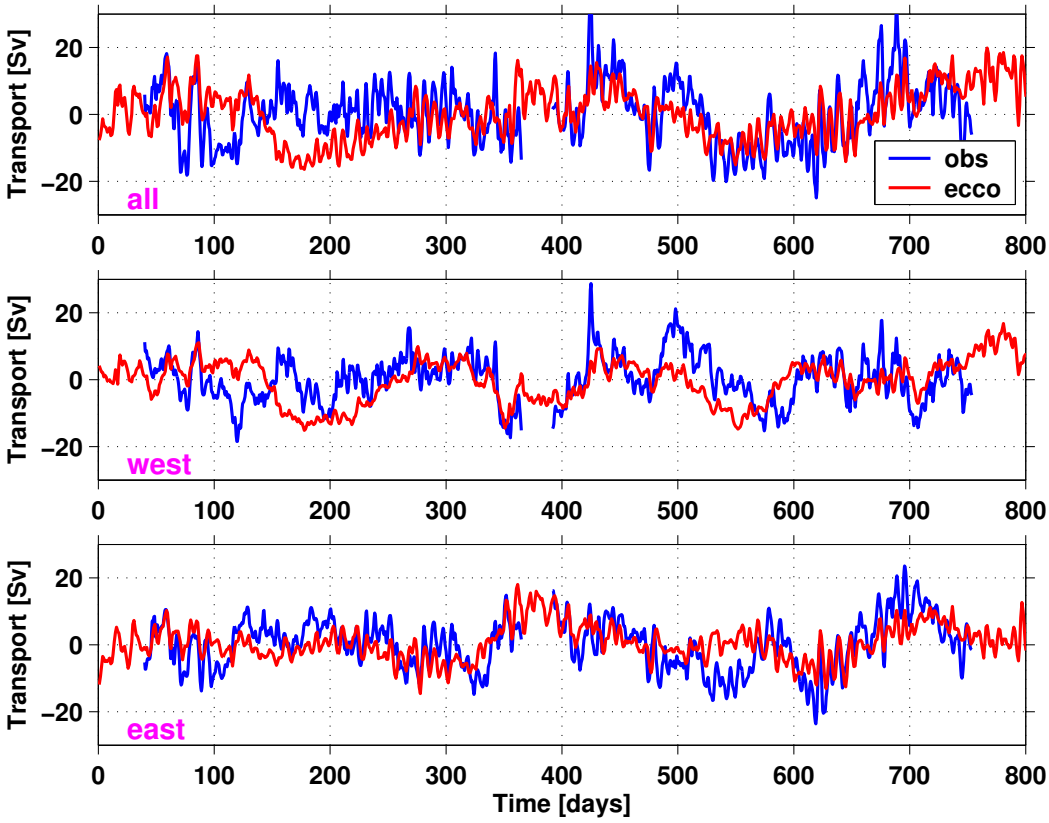

Figure 5.11: *External transport fluctuations below 1200 dbar from observations (blue line, identical to time series in Fig. 5.1, bottom panel) and from the constrained ECCO 1° x 1° model (red line, see also Appendix A.2). Transports through the whole, west and east section are depicted in the top, middle and bottom panel, respectively.*

and the observation display significant correlation of 0.54, 0.40 and 0.59 for total, west and east transports, when a 30 day high-pass filter is applied to each time series. Further confidence, that the model is reasonably suited for this analysis is gained by the fact, that it displays larger amplitudes of high-frequency fluctuations in the east as in the west section, which matches with the observations. At longer than monthly fluctuations, which are not focused on in this study, many similarities between both products can be observed.

In the model (Fig. 5.12) external meridional transport fluctuations east and west of 50°W (red and blue line in upper panel, respectively) display almost the same level of variability in the 6-12 day band, which goes along with a statistically significant coherence (black line in middle panel). The integral across the whole Atlantic basin (blue line) results in a clear variance reduction, which is explainable by the near 180° out-of-phase relationship of the east and west contributions. Interestingly there is a high coherence > 0.8 between the west contribution (which is measured by the MOVE M3-M1 array) and the total transport, displaying a near 90°

out of phase shift. That would mean that in this frequency band, an external transport of a certain amplitude in one direction measured by the MOVE array in the western trough, goes along with a net cross basin integrated transport of opposite direction of significantly weaker amplitude. Concluding the zonally averaged meridional transport variability in this frequency range is presumably much weaker than suggested by the MOVE external transports. On the other hand it should be mentioned that ECCO underestimates the variability in the western trough, with variance levels being smaller by a factor of 2-3 compared to the observations (compare red line of Fig. 5.12 to blue line in Fig. 5.2A).

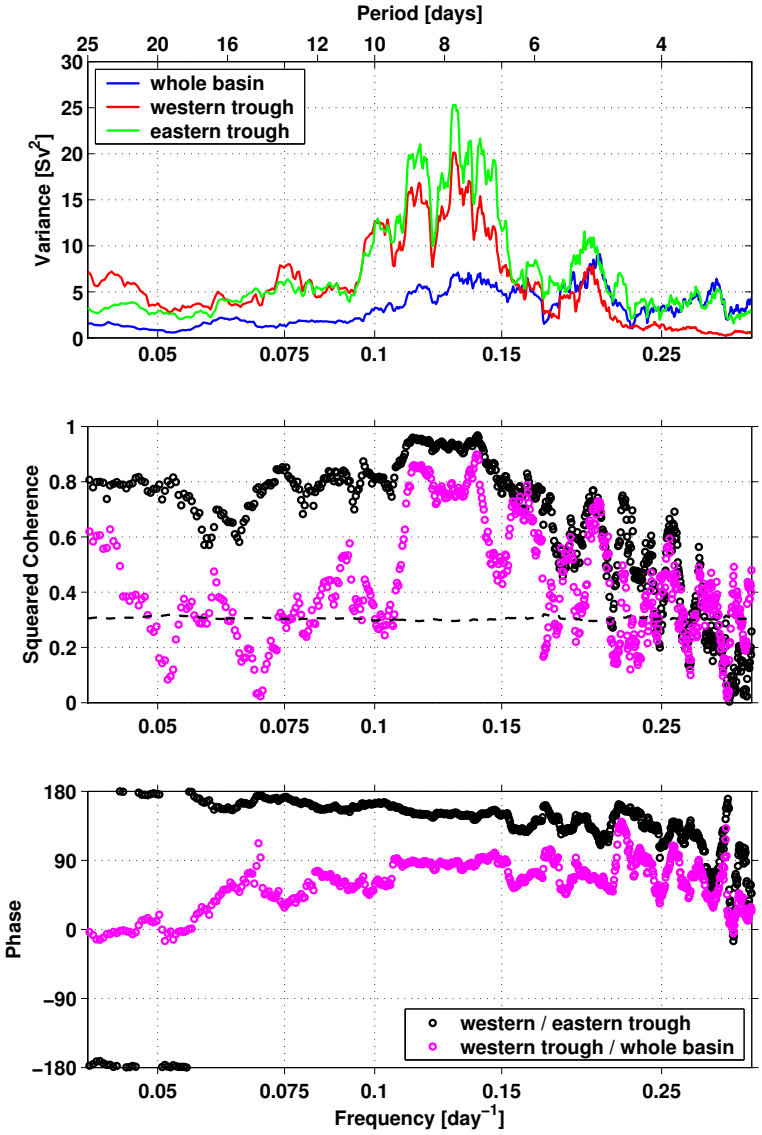

Figure 5.12: *Meridional external transports at 16° N in the ECCO (adjoint) model. Top panel: Variance conserving spectrum of transports integrated across the whole basin of the Atlantic (blue) as well as separately across the western (red) and eastern (green) trough. Middle and bottom panel show coherence and phase between the western and eastern trough (black) as well as between western trough and total transport (magenta) fluctuations, respectively. Positive phase means that the last-mentioned variable leads.*

The wavelength associated with these waves can be read off Fig. 5.13. In the 6-9 day band maximum variance in bottom pressure differences (corresponding to external transport fluctuations) is found between the western boundary and a location about 1500-2500 km further east, which is right in the center between the Lesser Antilles and African coast. Since maximum transport

variability is expected to be detected for an integration scale corresponding to waves' half wavelength, this in turn would result in a wavelength being on the order of the basin width (i.e. 4000 km).

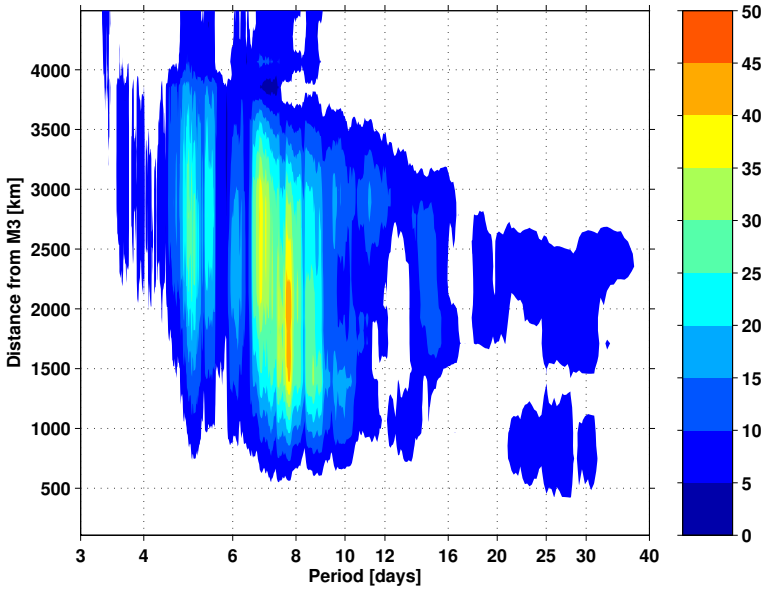

Figure 5.13: *The contour plot is composed of variance conserving spectra of external transports [Sv^2] at 16° N between 60.5° W (western boundary, mimicking mooring M3) and locations east of it, given as distance to M3. The distance of 4500 km roughly represents the African coast.*

Barotropic Rossby waves represent the only waves that could explain this phenomenon. Their dispersion relation is computed in Fig. 5.7 (red line). We find that a wave with an 8-day period (which dominates in the model) is expected to exhibit a wavelength of 3000km. That would roughly confirm the findings in Fig. 5.13 and matches with the estimate of 2000-4000km, based on the observed 45°-90° phase shift between external transport through the west (M3-M2) and east (M2-M1) section (Fig. 5.2E). According to the dispersion relationship, periods of 11 day (which represents a prominent peak in the observations) corresponds to a wavelength of 2000 km, which is about half the basin scale. A further interesting aspect is that according to Fig. 5.7 short barotropic Rossby waves with wave lengths of 300 km may exist at periods around 80 days, which might explain the relatively high energy level seen in the external transport (Fig. 5.2A).

In the discussion of the transport spectra in Fig. 5.2 it has been pointed out that no indication of an annual cycle and possible a very week indication for a semi-annual cycle (at least in the external transports) has been observed. One likely source of such signal at 16°N would be a deep ocean compensation of near-surface Ekman flow driven by the annual and semi-annual cycle of the trade winds. Theory and results from ocean models suggest that this compensation on shorter than inter-annual time scales should mostly involve barotropic flow (e.g. Willebrand et al., 1980; Jayne and Marotzke, 2001), which would contribute to external transport fluctuations. The Ekman transport integrated across the western trough of the Atlantic at 16°N (thin blue line in Fig. 5.14) shows a high degree of variability on weekly time scales. However the amplitudes of its annual and semi-annual cycles computed from harmonic analysis amount to only 0.3 and 0.4 Sv, respectively. The r.m.s. amplitude of inter-annual variability (based on the 4 year of data) is 0.2 Sv. Due to the deployment and processing scheme applied, annual and inter-annual variability in the external transport may largely be suppressed (chapter 3.7). In the presence of rather variable external transport time series, which exhibit an r.m.s. amplitude of about 8 Sv (Table 5.1), it is not surprising that the comparably week semi-annual cycle resulting from the compensation of Ekman flow does not stand out clearly from the spectra. Even

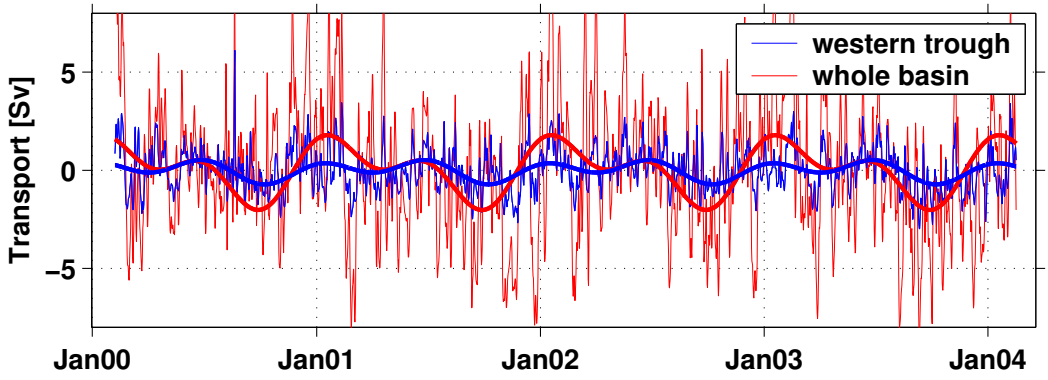

Figure 5.14: *Meridional Ekman transport fluctuations [Sv] across 16°N computed from Quickscat scatterometer wind stress data (see Appendix B). The thin blue and red lines denote 2-day low-pass filtered transports zonally averaged across the western trough (i.e., 60°- 51°W) and the whole Atlantic basin (i.e., 60°- 22°W). Superimposed as thick lines are the annual and semi-annual cycles for both cases, as obtained harmonic analysis.*

if the deep compensation of inter-annual fluctuations of the Ekman transport would be baroclinic, the value 0.2 Sv in the western basin would be much too small to explain the inter-annual deep meridional transport variability of 2.4 Sv as observed by MOVE. As can be expected from the generally large scale wind patterns, when integrating meridional Ekman transports zonally across entire Atlantic at 16°N, the amplitudes of inter-annual, annual and semi-annual variability increase to values of 0.9, 1.2 and 1.0 Sv, respectively, and thus approximately scale with the integration interval.

5.5 Comparison of Transport Fluctuations during MOVE and ACCP-3

It is also illuminative to compare the transport variability observed at the MOVE site with that at the ACCP-3 site at 26.5°N. Transport time series acquired at the ACCP-3 site within the 80 km wide B-D section (see Fig. 2.3) near the western boundary comprising the DWBC had already been presented in Fig. 2.5. To allow for a more objective comparison with MOVE results, a comparable horizontal integration scale should be used in both cases. Therefore transports integrated across the 390 km west section (M3-M2) from MOVE are compared with those from the 440 km wide B-E section from ACCP-3.

External B-E transport fluctuations clearly dominate the internal ones (Fig. 5.15, top), with the former and the latter displaying r.m.s. amplitudes of 17.6 and 6.6 Sv, respectively. Whereas internal transports display about the same level of variability at the MOVE site (6.3 Sv), the external contribution is significantly weaker (7.0 Sv). This matches with findings of Baehr et al. (2004), who find that when designing an MOC monitoring system based on the end point technique, the proper detection of the external transport component become increasingly important towards higher latitudes. Another interesting aspect is revealed in Fig. 5.15 (bottom). Geostrophic transport fluctuations in the B-D section are 180° out-of-phase relative to those in the D-E section. This compares well with results from MOVE (see Fig. 5.1), where westward propagating baroclinic Rossby waves were found to be responsible. However at the ACCP-3 site barotropic motions clearly dominate. With a baroclinic Rossby radius of O(40 km) at 26°N the minimum period at which free Rossby waves should be observed is about 200 days (see Fig. 5.7).

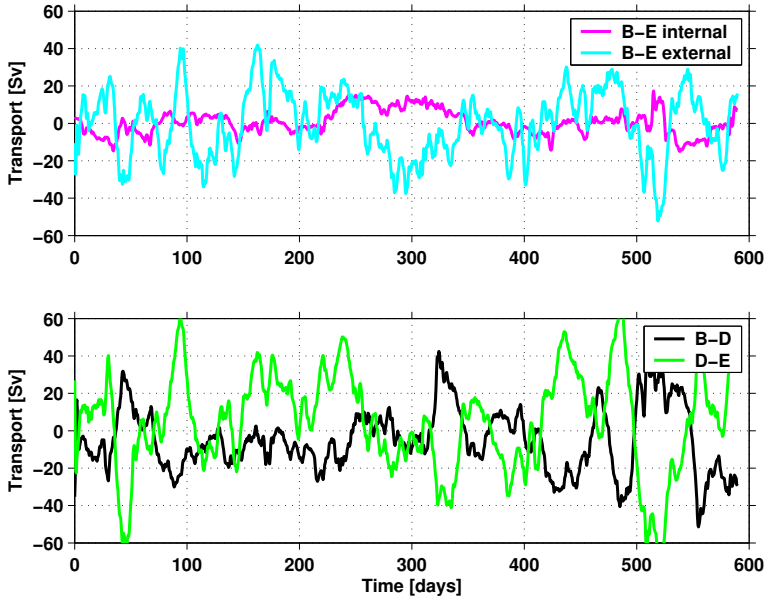

Figure 5.15: *Top: Internal and external meridional transport fluctuations below 1200 m integrated across the B-E section of the ACCP-3 array. Bottom: Geostrophic (external + internal) transport fluctuations below 1200 m integrated across the B-D (black) and D-E (green) sections.*

The largest fraction of energy in the B-E external transport fluctuations is contained in the 30-100 day band, with values exceeding those from the MOVE M3-M2 section by more than a factor of 5 (Fig. 5.16). The out-of-phase behavior between B-D and D-E transports suggests that barotropic Rossby waves (or eddies) might be the dominant mechanism of variability. B-E internal transport fluctuations peak at a period about 90 days. Whereas at shorter periods internal transports from ACCP-3 display a slightly larger energy level than those from MOVE the situation is reversed at longer periods (Fig. 5.16).

5.6 Summary

In this chapter the variability of the MOVE transport time series has been discussed. A high degree of consistency between records of internal transports from consecutive deployment periods as well as between internal and boundary triangle transports has been demonstrated. This can be taken as an indication that the accuracy limit of 1.5 Sv (Kanzow, 2000) has been reached for the internal transports. The external transports reveal consistent high-frequency fluctuations of the east, west and total transports. Also, the continuity of lower frequency signals across the data gaps has been shown. The r.m.s. transport fluctuations amount to 6.0 Sv for whole section internal transports, which reduce to 4.6 Sv when including the boundary triangle contribution. Whole section external transports display fluctuations of 8.4 Sv.

The spectra of external and internal transports display completely different characteristics, with large parts of the energy of the former being confined to periods < 40 days. Instead internal transports are dominated by lower frequency fluctuations ($\tau > 2$ months). As phase relations between signals in the east and west section suggest, internal and external signals also differ in spatial scales. Simple estimates, based on the assumption of linear westward propagating waves, attribute dominating wavelengths of O(480 km) and O(3000 km) to the former and the latter contribution, respectively. This yields the positive aspect, that large parts of east and west internal fluctuations of periods O(3 months) obviously average out when integrating transport across the whole section. Including the transport through the western boundary triangle leads to

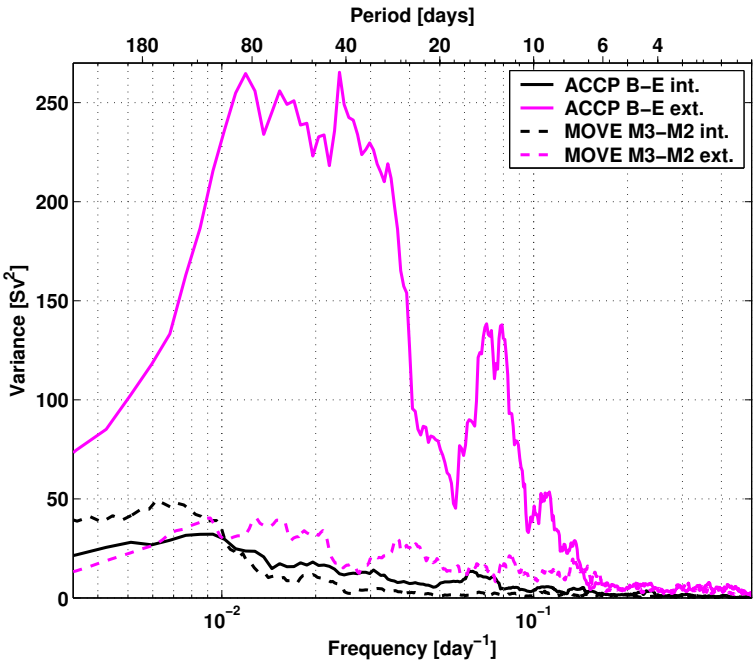

Figure 5.16: *Variance conserving spectra of internal (black) and external (magenta) transport fluctuations below 1200m from the ACCP-3 B-E (solid line) and the MOVE M3-M2 (dashed line) sections.*

further improvements of the signal to noise ratio. As a result of the long wavelengths associated with the short-term external fluctuations, integration across the whole section yields no signal reduction when compared to the east and west contribution. External and internal signals show hardly any significant coherence, thus it is concluded that the former are dominated by barotropic dynamics, which would justify the subjective decomposition in these two components.

Short-term external fluctuations from the ECCO model are significantly correlated with the observed signals. The model allows to track those signals across the whole zonal extent of the Atlantic basin, revealing wavelengths of O(3000-4000 km) and thus reasonably agreeing with the estimate based on the spectral characteristics of the observations. The frequency - wavelength characteristics is found to be in accordance to barotropic Rossby waves.

At the same time, estimates of dominating wavelengths of O(430km) in internal fluctuations are found to be consistent with baroclinic Rossby waves, as could be demonstrated using MOVE/GAGE current meters as well as the FLAME 1/12°model. Theory yields a minimum period of 100 days for free baroclinic Rossby waves (for $R_i = 70$km), associated with a wavelength of 420 km, which is close to the observed values.

Additionally, the FLAME model highlights two other aspects of dynamics relevant for the design of transport monitoring experiment. Offshore the DWBC strong meso-scale eddies (consistent with increased energy levels in the current meter spectra towards the west) are observed, which require the zonal integration scale to extend several hundreds of kilometers into the interior to average out their transport contribution. Also, intervals of several months of extreme reduction of the DWBC strength of 16 Sv can be identified, again in accordance with observations. At the same time, as a result of a compensation concentrated in the western trough, the net transport zonally integrated across the whole Atlantic basin remains relatively stable (within 2 Sv). Thus, the MOVE array should be capable to capture this interior compensation.

The variance levels of external transport fluctuations at 26.5°N (ACCP-3) are by a factor of 5 larger than those at 16°N in the 30-100 day band. Together with the findings from Baehr et al. (2004) this suggests that the bottom pressure component of a MOC monitoring system becomes

increasingly crucial towards higher latitudes. Finally it is worth mentioning again that when interpreting zonally integrated transports, the length of the integration scale has to be taken into account.

The inter-annual variability in deep meridional transports observed by MOVE amount to 2.4 Sv. It cannot be explained by a compensation of meridional Ekman transport integrated across the MOVE section which only display changes of O(0.2 Sv). It should also been reminded that the true low frequency fluctuations of meridional transports are likely to be larger than 2.4 Sv, since the contribution from the external transports has been suppressed as a consequence of data processing. For the discussion of the representativeness of these signals for MOC variability at 16°N, the reader is referred to chapter 7.

6 Absolute Transports

6.1 Introduction

Ganachaud and Wunsch (2000) attest mass flux to be the "most basic element of the circulation". The strength of the Atlantic MOC is of particular interest, since it is associated with the oceanic meridional transport of heat (e.g. Böning et al., 1996). As a direct consequence, it is directed northward in the not only in the North but also in the South Atlantic. The present-day strength of the Atlantic MOC is subject to scientific discussion. A recent estimate, based on a global inversion of hydrographic data, yields a production rate of NADW of 15 Sv in the North Atlantic (Ganachaud and Wunsch, 2000). Such results could serve as benchmarks for today's climate models which still differ substantially not only in climate sensitivity of the MOC but also in its present-day magnitude. Furthermore model studies indicate that the sensitivity the MOC to changes in the forcing could be depend on its basic state (Prange et al., 2004). On the other hand, a one time estimate of the MOC strength is not sufficient, because it is only valid for that specific point of time (or time interval). Model projections indicate that today's greenhouse forcing might reduce the Atlantic overturing by more than 1 Sv per decade (IPCC, 2001).

The MOVE experiment was primarily designed to monitor changes of the Atlantic overturing strength. Nevertheless, there several ways to reference its geostrophic transport fluctuations and thus add a new direct transport estimate to the already existing ones (some of which are listed by Bryden and Imawaki (2001)). The classical approach is to assume a level of no motion, typically at an interface of two water masses which are assumed to move in opposite directions (e.g. Pond and Pickard, 1978). Other referencing techniques require additional velocity measurements. Technically MOVE provides geostrophic velocity fluctuations at each pressure level and each point of time. To derive absolute velocities v_{abs} a time-independent offset Δv has to be obtained from additional velocity measurements:

$$v_{abs}(P,t) = v_{int}(P,t) + v_{ext}(P_{ref},t) + \Delta v \tag{6.1}$$

Therefore, as a minimum requirement, these have to resolve the horizontal scales of the cross section flow at at least one pressure level and one point of time (e.g. Whitworth, 1983; Kanzow, 2000) or have to be able to integrate across the flow field. Candidates are lADCP (Lowered Acoustic Doppler Profiler) sections, drifting floats (deployed across the section in a certain depth) and the MOVE/GAGE current meter data. In the following the potential of all of these referencing options will verified. Long term averaged satellite altimeter data in combination with a precise geoid description may also serve as an option soon, provided that experiment like the upcoming GOCE (Gravity Field and Steady-State Ocean Circulation Explorer) satellite mission will be successful.

6.2 Level of no Motion

The level of no motion Generally speaking, a fixed level of no motion does not exist in the ocean, neither on a certain isopycnal nor on an isopleth. Everywhere motions occur on a broad range of temporal scales. Nonetheless, this referencing method bears on certain justifications.

The idea is that at the interface of two water masses moving in opposite directions the vertical velocity profile exhibits a zero-crossing, at least when integrated over sufficiently large spacial and temporal scales. Such a behavior can be observed in ocean models for the zonal basin integral of the meridional flow in the Atlantic (see Fig. 6.1): Over most of the latitudinal extent, local maxima in about 1000m and 4000m can be found. These maxima are necessarily associated with a zero-crossing of the underlying vertical velocity profile. Thus in a zonally integrated sense one could speak of a two levels of no motion that might be used as a constraint.

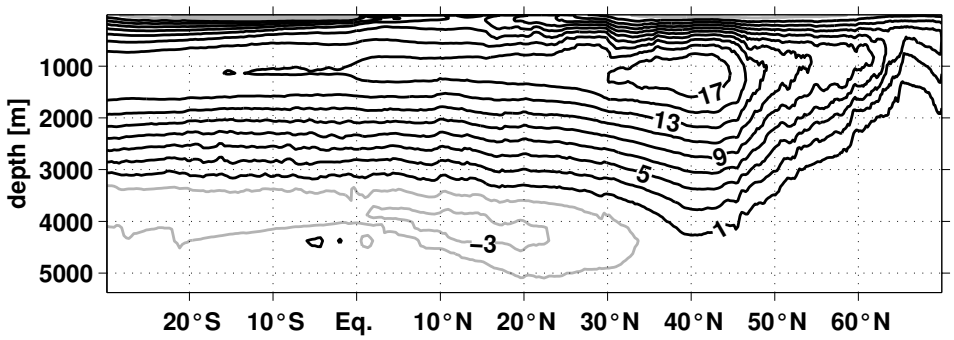

Figure 6.1: *1958-1999 mean meridional overturning streamfunction [Sv] from the FLAME 1/3° model. Positive and negative values are displayed in black and gray lines, respectively.*

In the subtropical and tropical Atlantic these levels closely coincide with the water mass interfaces. The upper and lower one represent the boundaries between AAIW / NADW and NADW / AABW (see also Fig. 4.2), respectively, with the southward moving NADW being enclosed by northward flow within the AAIW and AABW.

In practice an application of this concept to the moored hydrographic measurements from MOVE turns out to be problematic for several reasons. First of all the exact depth of the zero-crossing is not known. It is certainly dependent on the temporal averaging scale. Model analyzes of the AAIW / NADW interface show that an averaging interval of at least one year should be used to eliminate seasonal variability at the zero-crossing depth (not shown). Additionally, in the MOVE case transports are not integrated across the whole zonal extent of the Atlantic basin. Per se it is not clear how far one has to integrate from the western boundary into the basin interior until the depth of velocity zero-crossing and the water mass interface closely agree with each other. In Fig. 6.2 (left panel) the 5-year mean of the deep meridional velocity component

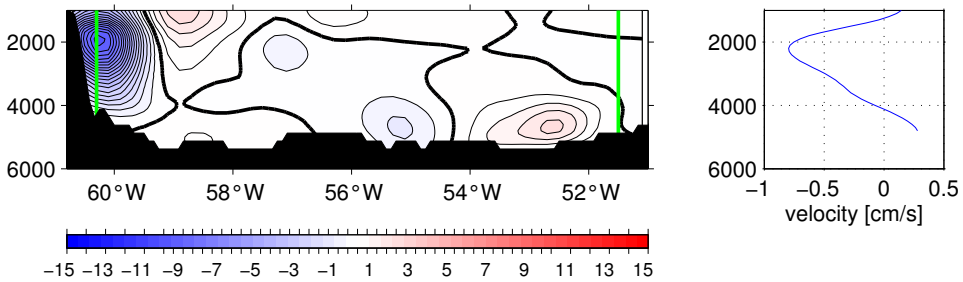

Figure 6.2: *Left: Section of 5 year average of the meridional velocity component [cm/s] at 16° N below 1000 m from the FLAME 1/12° model. The zero-croosing is indicated by the thick contour line. Note the non-linear colorbar. Right: Velocity profile horizontally averaged between the two green lines of the left panel. The lines mimic the moorings M3 and M1.*

is displayed. The most apparent feature is the core of strong southward flow associated with DWBC. Offshore of the DWBC a branch of northward recirculation is observed. In the basin interior zones of extremely weak flow without a preferred direction are visible. Abyssal northward flow of AABW is found close to the Mid-Atlantic Ridge. Most importantly, no continuous level

of zero (or constant) flow can be observed along the section. Also, close to the western boundary the NADW/AAIW interface would be a bad choice to constrain the flow. However the zonally integral (between two end point mooring according to the MOVE design) yields a zero-crossing in about 1200 m. This simulation demonstrates that for the MOVE sampling design a level of no motion at the NADW/AAIW interface may be be applicable. However this argument only holds for sufficiently long temporal averaging intervals.

As said above, the AAIW/NADW as well as the NADW/AABW interface could be used for as a reference. The former is defined by the isopycnal layer $\sigma_{1.5} = 34.42$, the latter by $\sigma_4 = 45.90$ (Rhein et al., 1995). See also Fig. 4.2. With the horizontal mooring spacing in the MOVE case being several hundreds of kilometers, the exact course of the isopycnals between the moorings cannot be resolved. However, both moored measurements and repeated hydrographic surveys have revealed that the AAIW/NADW interface displays only weak deviations from the horizontal. Thus the cross-section average depth of this layer can be computed with high precision. The NADW/AABW interface exhibits comparably strong deviations from the horizontal. It is found at about 4900 dbar at M3. Approximately 1000 km further east at M1 it is observed at about 4300 dbar (Fig. 3.8). Its irregular course between the mooring positions (Fig. 4.2) makes it difficult to derive a section mean depth of this level. A further restriction for the use of the $\sigma_4 = 45.90$ level is that such a mean depth is unlikely to be associated with a section mean zero-crossing in velocity.

Concluding, the AAIW/NADW interface seems more suitable to serve as a layer of no motion when currents are integrated across the whole section from M3 to M1. The cross-section mean depth of the $\sigma_{1.5} = 34.42$ level derived from hydrographic surveys yields 1180 dbar. A level of no motion of the horizontally integrated flow between M1 and M3 is applied to the Feb 2000 - Feb 2004 average internal velocities. The M3-M1 transport in the NADW layer amounts to 12.0 $\pm$3 Sv. The error of this technique can be obtained from the sensitvity of the transport estimate to the depth of the reference level. Near that $\sigma_{1.5} = 34.42$ level a dependence of 0.06 Sv/dbar is found. Accordingly, assuming an uncertainty in the depth of the velocity zero-crossing $\pm$ 50 dbar, a transport error of $\pm$3 Sv is derived.

The directly measured contribution of the DWBC over the continental slope (west of M3) adds another 4.0 Sv of southward flow. Thus, an estimate from this referencing method for the for the deep integrated southward flow of NADW across 16°N yields 16.0 Sv. This value compares well with the findings of Klein et al. (1995), whos estimate of southward NADW transport across 14.5°N amounts to 16.2 Sv. The errors of the internal and directly measured transports are less than 2 Sv. Assuming the errors from the measurements and the referencing technique to be independent from each other, the total error amounts to 3.5 Sv.

6.3 Lowered Velocity Measurements

As mentioned above, the minimum requirement for reference velocity measurements is, that they resolve the horizontal scales of the flow at at least one depth level and one point of time. lADCP measurement yield vertical velocity profile of the whole water column. Using those profile acquired along a section instead of measurements at one depth level only yields the advantage that referencing adjustment can be applied over the total depth range covered by the moored measurements.

Technically the referencing procedure is straightforward: the internal velocity is added to the relative external velocity in the time interval $t1 < t < t2$ when the lADCP section was recorded. Then the temporal and vertical average (over the desired pressure range $P_{bot} > P > P_{top}$) is computed. The latter is then subtracted from the vertical and horizontal mean of the lADCP

velocities v_{ladcp} between the mooring positions $x1$ and $x2$:

$$\Delta v = \frac{1}{\Delta P} \int_{P_{bot}}^{P_{top}} \left[\int_{x1}^{x2} \frac{1}{\Delta x} v_{ladcp}(P,x) dx - \int_{t1}^{t2} \frac{1}{\Delta t} \left[v'_{ext}(t) + v_{int}(P,t) \right] dt \right] d\mathrm{P} \qquad (6.2)$$

with $\Delta P = P_{top} - P_{bot}$ and $\Delta t = t2 - t1$ and $\Delta x = x2 - x1$. Absolute geostrophic velocities are then obtained by adding the velocity offset Δv to the geostrophic velocities according to equation 6.1.

Likewise, lADCP profiles have successfully served as a reference for moored geostrophic velocities in the ACCP-3 experiment by JKZ2004: Two lADCP sections acquired several months apart from each other were used. Each section was composed of 5 profiles to resolve the synoptic variability the 80 km wide section between the mooring sites B and D in the DWBC at 26.5°N. The referenced geostrophic transport below 1200 dbar was compared with simultaneously acquired direct current meter measurements (from sites B,C and D). A remarkable agreement between the two independent approaches was obtained, with the mean southward geostrophic and current meter transport amounting to 25.0 and 25.5 Sv, respectively.

In the MOVE experiment two major problems are encountered: The moored array spans a section width of approximately 1000 km, making it a hard task to obtain synoptic measurements in the presence of the high frequency barotropic velocity field. Moreover, the deep ocean at 16°N seems to be a particularly unfavorable area for Doppler shift measurements due its to its extremely low content of suspended matter. The resultant low signal-to-noise ratio finally may lead to a bias in the leading baroclinic velocity modes (pers. comm. M. Visbeck), resulting in strongly overestimated vertical velocity shear: The final lADCP vertical velocity profile is a composed of many vertically overlapping segments of velocity shear. When the signal-to-noise ratio is extremely small, the vertical integration of noise leads to a spectral shift towards long wavelengths, which contaminate the leading modes a vertical velocity shear. This effect has been shown to be partly suppressed by constraining the solution with additional information (e.g. bottom track and vmADCP data), following the approach of Visbeck (2002).

As could be expected from the above discussion, the cross section mean velocity profile derived from the lADCP sections at 16°N resulted in strongly overestimated vertical shear (compared to the internal velocities). The 1000km horizontally averaged meridional velocity component from 2 sections of lADCP measurements at 16°N is displayed in Fig. 6.3: The section mean from FS SONNE (blue line) yields an almost linear velocity shear of 8 cm/s between 1000 and 4800 dbar. No similarity with the typical 2-core structure observed in the internal transports (Fig. 4.7) is displayed. Superimposed are small vertical scale features with amplitudes exceeding 3 cm/s at times. Those may either represent measurement noise or may be related to residual non-geostrophic short time scale motions, such as internal waves. The latter do not necessarily average out in the horizontal mean. The section average profile from FS METEOR does not display such a strong overall vertical shear. However, like the FS SONNE data, it exhibits an unrealistically large shear at pressures > 4000 dbar. Also typical structure of 2 maxima of southward flow cannot be seen. Due to the mismatch in velocity shear between the lADCP and geostrophic velocities the referencing becomes strongly depth dependent and thus highly ambiguous. Tests applying the alternative processing technique based on data inversion of Visbeck (2002) have been carried out, however the apparent mismatch in vertical shear between the geostrophic and directly measured velocities could not be resolved satisfactorily.

As said above, a second major problem arises from the high frequency external velocity fluctuations with typical periods of < 2 weeks. Therefore it would be preferable to cover the lADCP section within about 3 days (i.e. one quarter of a cycle) to recover a reliable temporal and spacial average of the synoptic flow field. On the other hand the horizontal scales of the flow have to be resolved. With the internal Rossby radius of deformation yielding about 70 km in at

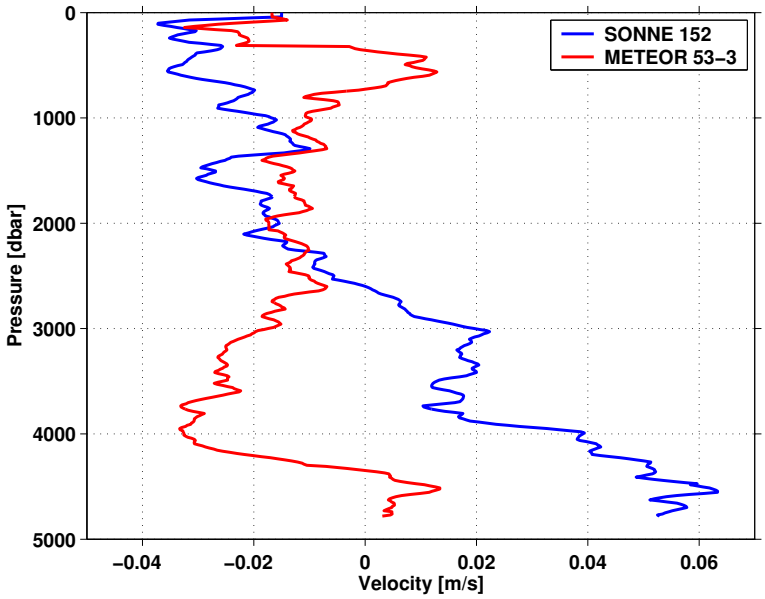

Figure 6.3: *Horizontally averaged meridional velocity component [m/s] from lADCP sections acquired aboard FS SONNE (December 2000, blue line) and FS METEOR (June 2002, red line). The average was computed from lADCP profiles along the MOVE section between 60.5° and 51.5° W (corresponding to the M3-M1 section). The number of profiles used to compute the average velocity amounts to 21 and 19 for the FS SONNE and FS METEOR data, respectively. This yields an average horizontal spacing of about 50 km.*

this latitude, a lateral spacing in the order of 50 km is therefore recommended. Covering the 1000km width of the MOVE section with such a resolution takes about one week.

The referencing of the geostrophic velocity fluctuations from the 1st and 3rd deployment period has been carried out according to equation 6.2 using the lADCP data from FS SONNE and FS METEOR, respectively. A pressure interval of 1200 dbar $< P <$4000 dbar was chosen for either case. As a consequence of the unrealistic large shear observed in the near bottom lADCP velocities, values for $P >$ 4000 dbar have been excluded from the procedure. Adding Δv to the geostrophic velocity fluctuations, average absolute southward transports in the NADW range (i.e. 1200-4600 dbar) for the 1st and 3rd deployment period of 6.6 and 61.1 Sv are obtained. The difference of more than 50 Sv between both estimates confirms the above discussion about large uncertainties in using lADCP measurements as a reference for the MOVE geostrophic velocities.

Therefore this referencing option is discarded for the time being. As MOVE is a multi-year experiment, a reference data set consisting of several lADCP and vmADCP (vessel-mounted) sections, is built up bit by bit. A sufficiently large number of such sections might help to constrain the geostrophic measurements. The present data obviously does not allow for a precise referencing of the geostrophic velocities. The vmADCP sections, which have not been used for referencing yet, bear the disadvantage that they only cover the upper 800 m of the water column with sufficient accuracy. Thus they could only be applied to the MOVE transport fluctuations after the second deployment period. Also, most of the vmADCP sections have been acquired during the mooring service cruises, where the array has not been in full operation.

6.4 Float Trajectories

A third approach used RAFOS floats deployed along the MOVE section at a distinct density level. A detailed analysis of the MOVE float data has been published by Lankhorst (2003).

Compared to the lADCP data is was thought that float trajectories would yield 2 main advantages: In the former case the time interval over which the referencing can be applied is limited to the time required to acquire the lADCP section. In the MOVE case, this takes typically one week. In the deep ocean it was thought that the floats would stay long enough close to the MOVE section such that their immanent spacial averaging (Davis and Zenk, 2001) would allow for a robust estimate of mean velocity across the section. Moreover, float trajectories from several location along the section can be obtained simultaneously. This allows for a computation of a true time and horizontal mean velocity. In contrast, with lADCPs every measurement site is covered at a different point of time.

12 floats were launched in January 2000 aboard RV KNORR. Originally they had been intended to float in approximately 1400m depth, but by accident had been configured for a 780 m level. At that time this depth level was not covered by the MOVE mooring, whose uppermost sensors were positioned in about 1200m. In January 2001 another 12 floats were launched aboard FS SONNE (see Table 6.1). This time the target depth of 1400m was reached. 10 of the 12 floats returned data after accomplishing their mission.

Instr ID	Mission [days]	Launch Date	Time	Latitude	Longitude
521	305	31.12.00	17:58	16°N 18.980	60°W 20.860
522	305	31.12.00	20:26	16°N 16.174	59°W 56.017
523	305	01.01.01	00:47	16°N 10.715	59°W 07.820
524	305	01.01.01	05:00	16°N 05.362	58°W 20.285
525	305	01.01.01	09:17	16°N 00.014	57°W 32.398
526	305	02.01.01	02:00	15°N 54.640	56°W 44.590
506	275	02.02.01	06:48	15°N 49.231	55°W 56.556
494	275	02.01.01	11:29	15°N 43.853	55°W 08.632
512	275	02.01.01	16:14	15°N 38.467	54°W 20.806
509	275	02.01.01	23:47	15°N 33.072	53°W 32.869
508	275	03.01.01	03:52	15°N 27.702	52°W 45.041
517	275	03.01.01	07:57	15°N 22.300	51°W 57.077

Table 6.1: *RAFOS floats deployed aboard FS SONNE in January 2001. The mission depth was 1400 m and the mission duration about 9-10 months. 2 of the 12 floats (#522 and #525) did not return data.*

For the purpose of deriving a reference velocities the daily float velocities (obtained from daily position changes) were projected onto the section taking into account the actual time dependent float positions. The projection was carried out using an objective analysis scheme. To test the sensitivity (i.e. uncertainty) of this referencing procedure, the mean cross section velocity was derived for various time intervals. Subsequently the moored geostrophic transport fluctuations were referenced in those different intervals (see Table 6.2). The projection was carried out, applying 2 different sets of parameters to the objective analysis. In the first case a Gaussian half-width influence radius of 1° in meridional and zonal direction was used, which corresponds to about 110 km. In the second case the meridional influence radius was extended to 2°. The cut-off radius was set to 3° in either case.

Generally it turned out that the resultant absolute geostrophic transports were strongly dependent upon both the parameters of the objective analysis as well as on the averaging interval (Table 6.2). For example, a change in the interval length of 10 days could result in a change of resulting NADW transport estimate by 10 Sv.

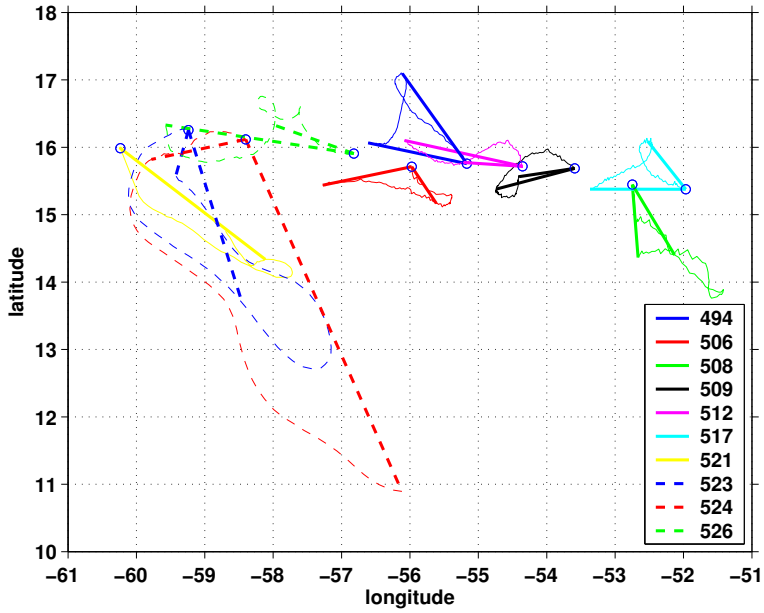

Figure 6.4: *Trajectories from 10 RAFOS floats deployed in January 2001 aboard FS Sonne. The floats target depth was 1400 m. The curves lines represent the actual trajectories. The 2 straight lines for each float denote the average net drift after 50 and 100 days. Time origin is 2001/01/01 0:00 h.*

Interval days	Trans. west 1	Trans. west 2	Trans. east 1	Trans. east 2
20 30	-25.8	-15.8	-6.9	-5.2
20 40	-16.9	-4.3	-5.8	-6.1
20 50	-22.6	-13.4	-15.6	-16.9
20 60	-33.4	-27.3	-23.0	-22.2
20 80	-28.7	-24.2	-18.0	-20.5

Table 6.2: *Average geostrophic transport [Sv] of the 2nd deployment period. The referencing was carried out by velocity measurements from RAFOS floats. Different averaging intervals between 10 and 60 days were used. The results have been computed for 2 sets of parameters for the objective analysis. The referencing has been carried out separately for the west (M3-M2) and east (M2-M1) section. More details are found in the text. The reference time is 2001/01/01 0:00 h.*

Additional problems became apparent in the western part of the section: The floats (#521,#523,#523) deployed in the vicinity of the DWBC drifted to the south along the western boundary rather fast, so that information from the DWBC near 16°N could only be obtained for less than a month. Moreover, two of the floats launched in the western part (#522 and #525) did not return any data, which reduced the horizontal resolution in that part drastically. Especially float#522, which was launched in the DWBC resulted in a major loss of information. Thus, velocity information from the most critical part of the section was hardly available.

In the west section the absolute transport estimates range between 4 and 33 Sv of southward flow, depending on the interval and the parameters of the objective analysis. In the east, where all of the float returned their data, the results look more stable (Table 6.2): The two different sets of parameters result in differences of typically less than 1-2 Sv. However, the results are still strongly dependent on the averaging interval and result in estimates of total southward flow in the NADW range between 5 and 23 Sv. Fig. 6.4 reveals the reason for this: The meridional displacement between adjacent floats looks rather arbitrary. Whereas float #526 displays a net northward movement, the adjacent #506 drifts towards the south and the next one #494 again to the south. Concluding, even after 100 days the zonal scales of the flow field have not been sampled with an adequate resolution. The floats have been launched with zonal separation of about 100 km which is apparently not sufficient to resolve the baroclinic Rossby radius of 70 km in this region. It would require either averaging intervals much longer than the typical time scale of Rossby waves (i.e. 100 days) or a drastic decrease of the zonal separation by a factor of 2, to provide accurate float reference measurements in the interior of the basin. In the DWBC the use of floats cannot be recommended due to the large advection velocities.

In summary, no stable reference velocities could be derived from RAFOS float trajectories. However, this option has indeed the potential to work more reliably, at least away from the DWBC, if the number of floats was more than doubled. This however, would result in large costs, considering the price of a single float of about 4500 Euro. Therefore this referencing option has been discarded after the second deployment period due to funding limitations.

6.5 Moored Current Meter Measurements

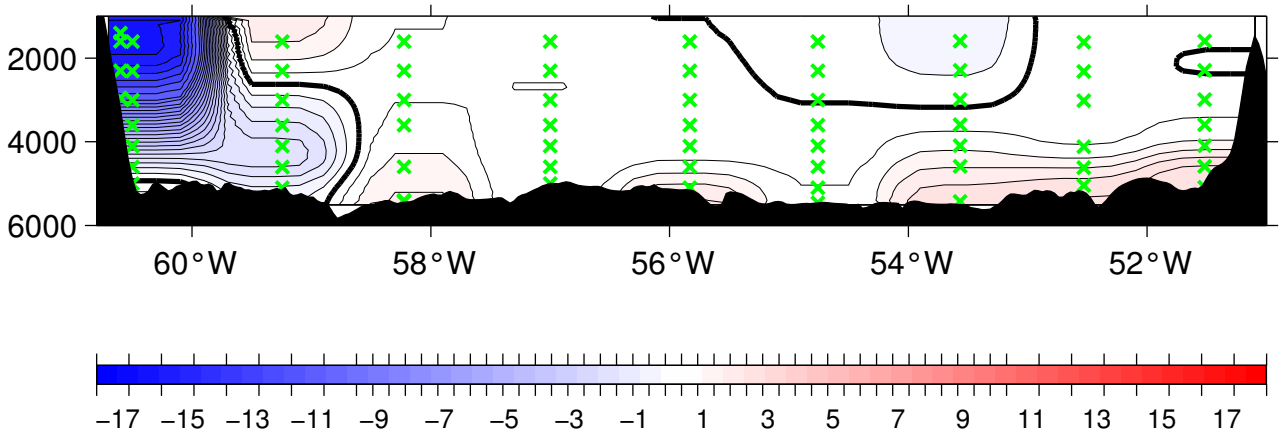

Figure 6.5: *Mean meridional velocity distribution [cm/s] computed from the 10 MOVE/GAGE current meter moorings (Feb 00 - Apr 02). Green crosses indicate the nominal depths of current meters. During the 2nd and 3rd deployment period of MOVE, current meters had also been deployed above 1600 at M1, M2 and M3 and beginning from February 2002 the depths of the current meters were slightly changed in those 3 moorings. Mind the non-linear velocity scale.*

The final referencing technique that is described, uses current meter data from the MOVE/GAGE

array. The joint array operated from February 2000 until the final recovery of the 6 GAGE moorings in April 2002. This option features the advantage that the adjustment between geostrophic fluctuations and direct reference measurements can be accomplished over a long averaging interval of 27 months. With 9 moorings covering the section between M3 and M1 a similar horizontal resolution as in the previously described RAFOS float case is available.

The 27 month average meridional velocity distribution along the 16°N section is displayed in Fig. 6.5. Similar to the FLAME 1/12° model (Fig. 6.2) the DWBC represents the dominant feature with average velocities of up to 18 cm/s. Also a net northward recirculation in the upper range of the NADW adjacent to the DWBC is observed. The interior of the basin displays weak net flow. Enhanced northward near-bottom flow can be found in the AABW range, particularly close to the MAR. All in all, the current meter data display a consistent picture of the cross section flow. However in some parts of the section the horizontal scales of the velocity field appear to be bounded by horizontal mooring separation. Accordingly there is indication that the zonal sampling rate (i.e. number of moorings) is too low to fully resolve the average velocity distribution. This is especially true for the DWBC and the adjacent recirculation, but can also be observed in the eastern part of the section. This important fact will be returned to later in this section. It should be remembered that the GAGE experiment targets the possible interior abyssal northward recirculation involving water masses below 3000m (i.e. AABW and oNADW). Thus, the current meter array was not designed to fully resolve the DWBC.

The horizontal and temporal average velocity profiles for the east, west and total section were computed by simple time and horizontal integration (see 6.6). All 3 profiles show a similar

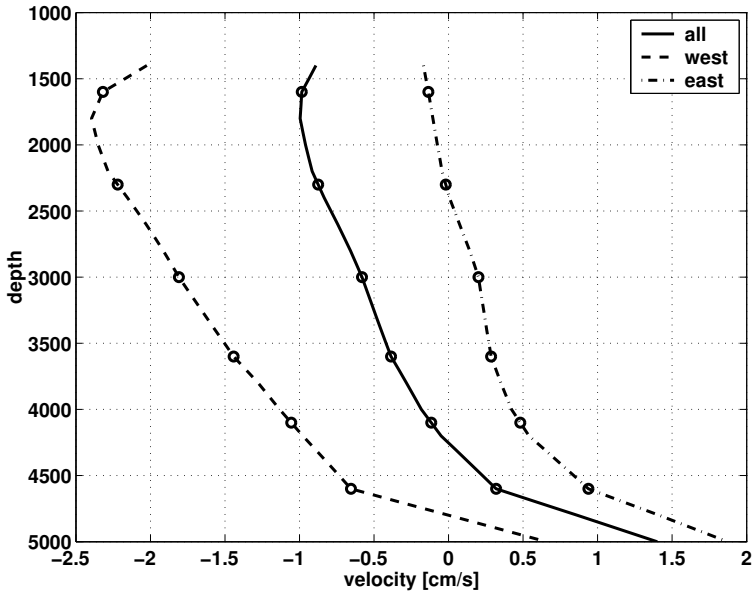

Figure 6.6: *Mean meridional velocity calculated from the 9 MOVE/GAGE current meter moorings (Feb 00 - Apr 02), for the whole (M1-M3, solid line), west (M2-M3, dashed) and east (M1-M2, dashed-dotted) section. Circles indicate nominal depths of current meters. During the 2nd and 3rd deployment period of MOVE current meters had been deployed above 1600 at M1, M2 and M3 as well and beginning from Feb 02 the depths of the current meters were changed in those 3 moorings.*

shape with largest vertical shear below 4500m and weaker shear above that. The (2000-4500m) shear is larger in the west (1.6 cm/s) than in the east (0.8 cm/s). In the west the maximum southward velocity is located at 1800 m while in the east no such local maximum is visible. The zero-crossing occurs in the west at about 4800m and in the east at 2400m, which could be an indication of the deep recirculation there. The shape of the velocity profiles qualitatively

compare well to the velocity shear obtained by dynamic height (Figure 4.7), however with some restrictions. Especially west of M2 (57°W) the shear from the current meters is much stronger and the two deep southward cores are not visible. This is expected to result primarily from not resolving adequately the horizontal scale of the DWBC (the mooring separation there is about 130 km), such that horizontal average becomes biased especially in the LSW range. In the east, the correspondence between the 2 data sets is much better. There is even slight evidence for the existence of two deep cores in the current meter data. Below 4500 m the current meters display negative velocity shear of about 1 cm/s within 500 m. This is about twice as strong as seen in the internal velocities.

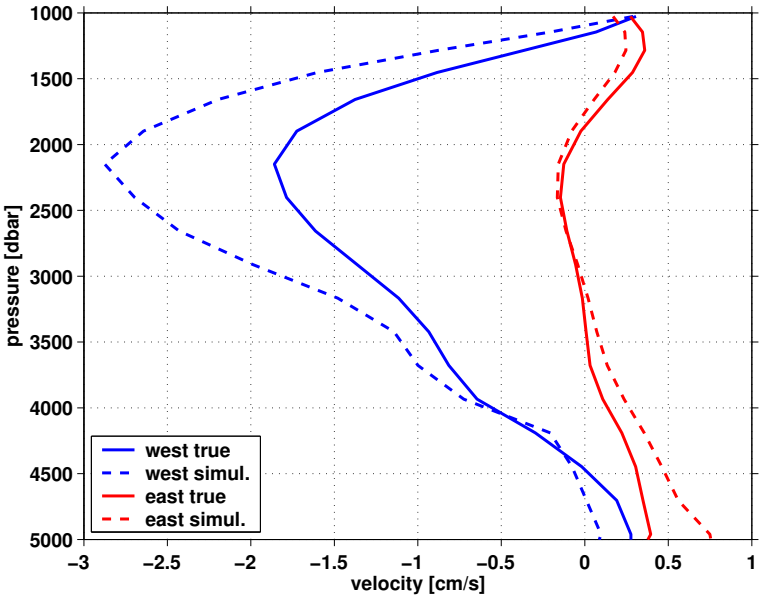

Figure 6.7: *Simulation of the errors resulting from the MOVE/GAGE current meter sampling of meridional velocities in the FLAME 1/12° model: The solid lines indicate the true zonally avagered model velocities in the west (blue) and the east section (red). The dashed lines display the respective averaged velocities when linearly interpolating between the current meter mooring positions (shown in Fig. 6.5). Each of the curves represents a 5-year average.*

There exists supporting evidence for the fact, that moored current meter measurements have indeed difficulties in resolving the horizontal scales of the flow (Fig. 6.7): The effect of zonally interpolating the meridional velocity between the MOVE/GAGE mooring positions has been simulated using output of the high resolution FLAME 1/12°model at 16°N. In the west section the resultant velocity shear is strongly overestimated compared to the true shear. Whereas in the deep ocean (at pressures > 4000dbar) comparable time averaged velocities are obtained, the DWBC maximum displays a significantly larger amplitude than the "true" model velocity by about 1cm/s (or 60%). In the east section linear interpolation amounts to much smaller absolute errors. However, they become increasingly pronounced towards the bottom, differences of up to 0.4 cm/s are observed. Errors are smallest in the 2000 -3000 dbar layer. The interpolated data yield slightly overestimated vertical velocity shear, especially near the sea floor. All of this is consistent with what is seen in the comparison of internal and current meter based observations.

The above discrepancies between vertical shear from current meter and dynamic height (seen in both observations and simulations) demand that referencing of the geostrophic velocities has to be carried out with care. Current meter velocities are likely to be least biased in a depth range where the current magnitude and the difference in shear between both data sets is smallest (see also simulations in Fig. 6.7). Additionally, the average current meter velocity from the first and the second year was computed separately to identify depths where both realizations showed minimal deviations from each other (not shown). It was found from the observations, that in the

west section differences between the two years were strongest near the bottom (below 4800m) and in the upper range of the NADW (not shown). In the east changes were most pronounced below 3500m. That may have partly been caused by a slight change in the position of the eastern most mooring (M1), which in the second year had been launched about 10 miles north of the original position. Strong northward flow within the AABW and oNADW range throughout the first year had been detected. Since the beginning of the second year the velocity magnitude was strongly reduced. In contrast, the abyssal internal velocity shear did not display such changes between the two deployment periods. This again points towards current meter moorings not adequately resolving the scales of the near bottom flow. Evidence for this had already been presented in Fig. 6.5. Especially close to the MAR the currents could be steered by complex topography.

Taken all of the above considerations together, it was then concluded that most robust estimates from the average current meter velocities are obtained in the west section from a depth layer between 4000m-4800m and in the east between 1600-3000m. Thus, mean internal and current meter transports from the 27 month period were averaged over the above depth intervals. The resulting offsets (for the east and west section) were then added to the internal velocities. In table 6.3 estimates of the absolute geostrophic and directly measured transports are confronted with each other. Geostrophy yields a net southward NADW transport of 14.9 Sv. There is a

bound. c.m.	west geo./ c.m.	east geo. / c.m.	all geo. / c.m.	
-2.6	-4.6 / -8.9	-0.5 / -0.6	-7.7 / -12.1	suNADW/LSW
-0.8	-2.9 / -5.8	+0.7 / +0.8	-3.0 / -6.0	lNADW
-0.4	-4.5 / -6.2	+0.7 / +3.0	-4.2 / -3.6	oNADW
-3.8	-12.0/-20.9	+0.9 / +3.0	-14.9/-21.7	NADW

Table 6.3: *Transport estimates [Sv] for different the water masses of the NADW from current meters (c.m.) and referenced geostrophic currents (geo.). Water mass interfaces have been approximated by the σ levels shown in Fig. 4.2. Transports from the western boundary triangle (bound.), the western (M3-M2) and eastern (M2-M1) section are accounted for separately, as well as for their sum (all)*

weak northward recirculation (0.9 Sv) in the eastern part while west of M2 (including the 3.8 Sv over the continental slope) a total of 15.8 Sv moves southward. The uncertainties of this approach can be assessed by vertically shifting the depth intervals used for referencing. Shifting the original interval applied in the west section (4000-4800m) downwards and upwards by 100m , changes the absolute NADW transport estimate by +1.2 and -0.9 Sv, respectively. Thus, a sensitivity of about 0.01 Sv per meter interval change is obtained. Transports in the east section display a sensitivity of one order of magnitude less. Here, a 100m shift of the interval (1600-3000m) results in deviations of +0.10 and -0.05 Sv, respectively.

As could be expected from the above discussion and simulation, the absolute transport estimate in the east section can be regarded as rather robust. Here, in upper range of the NADW no indication of unresolved scales has been found in Fig. 6.5. Nevertheless, the error in referencing will be larger than the 0.1 Sv indicated above, as the 1600-3000m current meter derived mean transports might be biased. A conservative estimate of the uncertainty in referencing the NADW transport through the east section yields 1.0 Sv, which is twice the value that would result from the simulations in Fig. 6.7. In the west, the susceptibility to the reference level is much larger than in the east. This finds its expression in the mismatch in vertical shear between the internal and current meter velocities and is presumably caused by not adequately resolving the scale in the vicinity of the DWBC by the current meter array (see Fig. 6.5). Here a conservative estimate of the referencing yields 2.4 Sv which is three times the value that would result from

the simulations (Fig. 6.7).

The net southward flow of NADW obtained from the current meters adds up to 21.7 Sv (Table 6.3), which differs substantially from the estimate of 14.9 Sv from referenced geostrophy and other recent results (e.g. Ganachaud and Wunsch, 2000). Differences in the east section yield 2Sv, with from current meters displaying an enhanced northward recirculation. In the west (including the continental slope) current meters show an enhanced southward flow of 24.7 Sv (or about 60% more than from geostrophy). Once again, these results could be expected from the simulations (including the magnitude and the sign of the differences) and are for the most part attributable to current meters not adequately resolving the horizontal scales of the flow. While the direct current measurements do not provide consistent absolute transports, they have proven to be very useful in providing a reference for the geostrophic transport fluctuations.

In this approach the external velocity fluctuations are not used, as their time averaged contribution was (arbitrarily) set to zero. It is trivial to demonstrate that choosing a different offset would not altered the above transport estimates. However external fluctuations should be added to the referenced internal velocities (with a zero time mean) to account for the complete spectrum of variability.

6.6 Summary

Four techniques to reference the geostrophic velocity fluctuations have been presented. A southward transport of 14.9 $\pm$3.0 Sv within the NADW layer can be regarded as the best estimate, which has been derived from referencing the internal velocities with the MOVE/GAGE current meter data. The choice of the different reference layers in the east and west section had been based on comparisons between directly measured and internal velocity shear profiles as well as on model simulations. Especially in the west, the transport estimated is very sensitive to the reference layer. It is important to remember that the mean transport estimate is only valid for the February 2000 to April 2002 period (final recovery of GAGE). At later times no current meter based referencing can be applied.

Choosing the AAIW-NADW interface as level of no motion between M3 and M1 gave an estimate of 16.0 $\pm$3.5 Sv of southward transport of NADW (including the directly measured contribution in the western boundary triangle), when averaged over 4 years. As mentioned above, a level of no motion does not exist in the ocean. However when averaged over long time and spacial scales it might be justified to associate water mass boundaries (whose depth does not change significantly in time), with level of minimal net flow. Some confidence in this technique arises from the fact the the NADW transport estimate only deviates by 1.1 Sv from the "best" estimate from the current meters. However, it should be kept in mind that both estimates are based on data from different time intervals and thus are not comparable directly.

Referencing of the deep ocean geostrophic velocities using lADCP data taken along the MOVE section turned out to be unreliable. Unrealistically large differences were obtained in absolute transports between the first and the second deployment period. The extremely low content of suspended matter in the deep layers at 16°N resulted in a reduced data quality of the single velocity profiles. This in turn corrupts the leading baroclinic mode of the single profile as well as the zonally averaged velocity. Additionally, resolving the temporal and spacial scales of the flow was found to be problematic: On the one hand a 1000 km wide section has to be covered with an horizontal sampling rate of 50 km. On the other hand fast barotropic fluctuations with periods of 7-14 days would require a lADCP survey duration of no more than 3 days to avoid aliasing. This referencing option has been discarded for the time being. Nevertheless, during the ACCP-3 experiment referencing using lADCP sections had been conducted successfully. It

can be explained by the fact, that the section with only amount to 80 km and thus could be covered with a horizontal resolution of 20 km.

Another technique that was tested, used an ensemble of RAFOS floats, that had been deployed along the 16°N section. The low horizontal resolution (of about 100km) together with the fact that the floats departed quickly from the array (especially in the DWBC) were responsible for unstable transport estimates. The latter were found to be highly sensitive to the averaging interval as well as the interpolation procedure. Doubling the resolution (i. e. number of floats) and a deeper target depth well below the upper DWBC core could have provided more reliable constraints for the geostrophic fluctuations.

Since the MOVE/GAGE current meter array is not available any longer and the use of lADCP as well as RAFOS float data has shown to result in large uncertainties, the only option that remains for future applications is the level of no motion. In case that MOVE will be modified such that the zonal integration scale is extended far into the eastern trough (as suggested by the author in chapter 7), errors associated with this approach might reduce.

Theoretically there are two more alternatives to derive absolute transport estimates. If measurements cover the whole zonal section and the whole water column and if the surface Ekman transport is included, the referencing can be carried out based on the assumption of zero net flow through the section (conservation of mass), which is the strategy pursued by the RAPID monitoring array at 26°N (Hirschi et al., 2003). On the other hand in near future the combination of precise satellite geoid measurements (e.g., GOCE) with altimetry data, averaged over a sufficiently long period of time, might serve as a constraint.

7 Simulation of MOC Fluctuations and Requirements for a Monitoring Strategy

7.1 Introduction

In this chapter the deep meridional transport signal will be further investigated using numerical model output. The first question under consideration is in how far observations limited to the western trough of the Atlantic are representative for the transatlantic transport integral at 16°N. Subsequently the overturing transport across different latitude bands in the Atlantic will be compared to assess its time and meridional correlation scales. The aim of this study is to find out how long one would have to measure in order to detect coherent overturing signals over the whole meridional extent of the Atlantic, which are then attributable to the thermohaline circulation.

7.2 Simulation of the MOVE monitoring design

Deep transports from the FLAME 1/3° model (see Appendix A) integrated across the western trough (i.e., west of 50°W) and the total basin width of the Atlantic at 16°N are contrasted to each other in Fig. 7.1. For monthly values a relatively low correlation of 0.45 is found. Using a 3-year low-pass filtered time series, which suppresses the seasonal cycle, leads to a strong increase in correlation to 0.73. This means that on longer than seasonal periods deep meridional transport fluctuations in the western trough can be regarded as representative for the whole basin integral to a certain degree, however some differences still persist at multiannual periods.

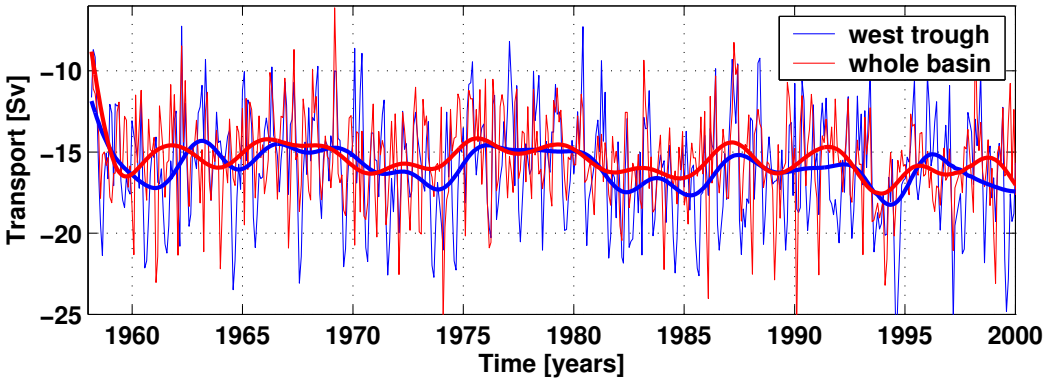

Figure 7.1: *Meridional transports across 16° N below 1200 m in the FLAME 1/3° model: Blue and red lines denote transports integrated along the western trough (west of 50° W) and the whole basin, respectively. Thin lines are composed of monthly averages, whereas bold lines represent 3-year low-passed filtered data. Output from the control run has been used, refer to Appendix A for details.*

Spectral analysis reveals that large differences are apparent at the annual cycle, where the western trough signal displays a much larger energy level than the total basin integral (Fig. 7.2,

left panel). Also, squared coherence found at this period cannot be regarded significant(right panel). At periods longer than 2 years coherences clearly exceed the significance level. Several

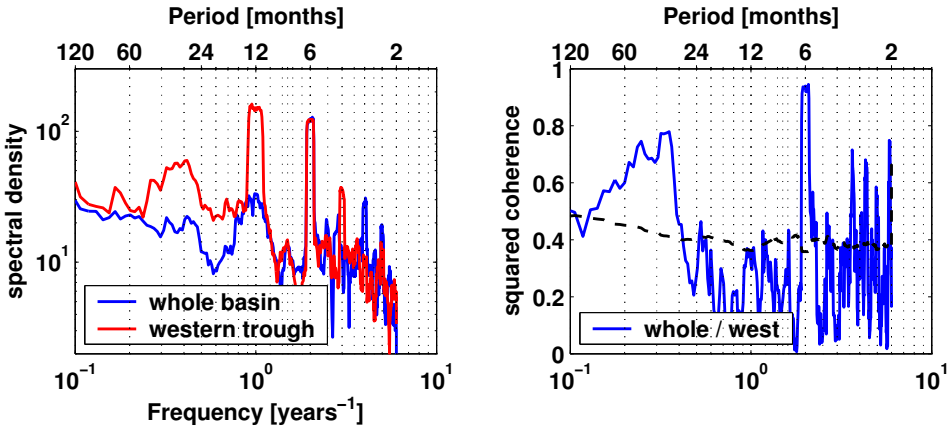

Figure 7.2: *Left: Spectra of meridional transports across 16°N below 1200m in the FLAME 1/3° model [Sv^2/frequency]: Blue and red lines denote transports integrated across the western trough and the whole basin, respectively. Right: Squared coherence between both time series. The zero coherence level at 95% significance is given by the black dashed line.*

reasons can be thought of, why the deep meridional transport in the western trough of the Atlantic might deviate from total transatlantic integral on seasonal to inter-annual time scale. One candidate is the westward propagation of baroclinic Rossby waves, which were already found to explain large fractions of differences observed between the west and east section within the western trough of the Atlantic (see Fig. 5.1). These may also cause differences between transports in the western and eastern trough. Regarding low frequency fluctuations, baroclinic Rossby waves have been shown to be forced by the seasonal cycle (or even longer term changes) of the wind stress curl (e.g. Kessler and McCreary, 1993). Since the focus here is on MOC variability, such Rossby wave signals would be considered noise, which naturally would decrease the signal to noise ratio.

On the other hand, as already mentioned in the introductory chapter of this study, MOC perturbations due to buoyancy or wind stress forcing in deep-water formation regions at high latitudes of the Atlantic are communicated southward along the western boundary via coastal Kelvin waves, as model results suggest (Kawase, 1987). Upon reaching the equator within few months, they generate equatorial Kelvin waves, which propagate along the equator towards the eastern boundary, where in turn coastal Kelvin waves move poleward, radiating Rossby waves into the ocean interior.

The mechanism of fast adaptation of transports within the North Atlantic involving the initial western boundary Kelvin waves represents a signal of interest in MOC studies, and it should be detectable by a measurement confined to the West Atlantic trough, such as MOVE. The rather slow Rossby wave mechanism involves much smaller transport signals at a time due to the limiting effect of the "equatorial buffer " (Johnson and Marshall, 2002). It might become important for signals communicated across the equator at decadal and longer time scales (Johns et al., 2004). It also affects transports in the eastern trough (since signals are radiated from the eastern boundary).

Another mechanism leading to differences in deep transport fluctuations in the western trough compared to the total basin integral would be deep compensation of surface Ekman transports induced by trade winds at 16°N: Temporal fluctuations in the trades are not necessarily coherent along the latitude band from coast to coast, such that the deep compensation is not either. Finally, long-period MOC changes advected southward by the DWBC would be detectable by

measurements confined to the western trough.

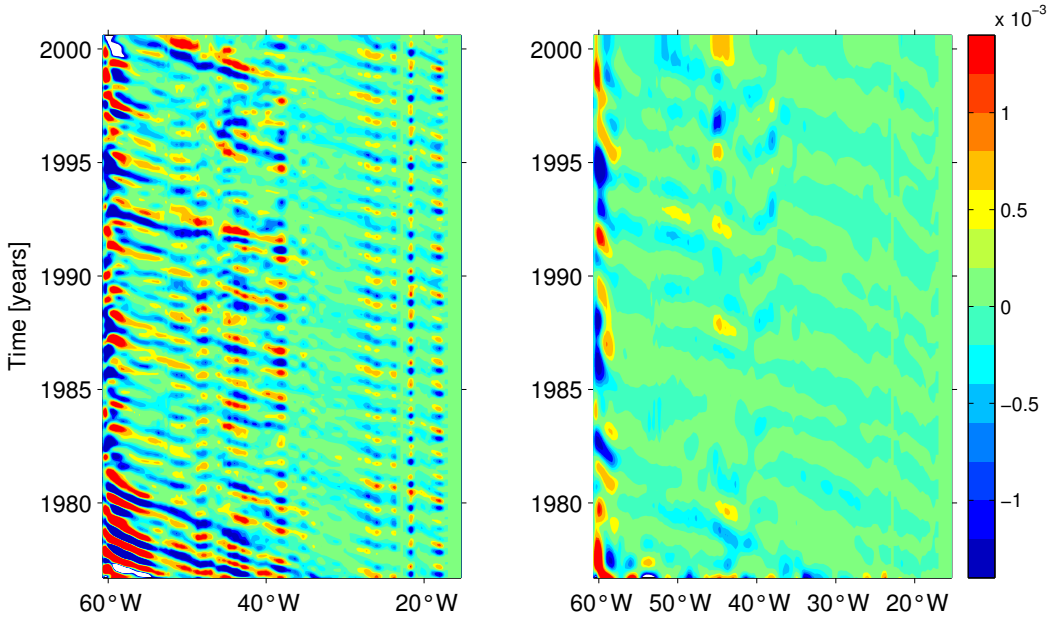

Figure 7.3: *Hovmoeller diagrams of anomalies (i.e., the mean value at each latititude has been subtracted) of meridional transport density [Sv/m] below 1200m from from the FLAME 1/3° model (see Appendix A for details). The left panel denotes 4-month low-pass filtered and the right panel 2-year low-pass filtered data.*

The Hovmoeller diagram in Fig. 7.3 (left panel) demonstrates that the seasonal variability in the FLAME 1/3 °model is dominated by annual Rossby waves exhibiting wavelengths of about 1200 km which are most intense in the western trough. This explains the differences seen in the annual cycle: The zonal integration scale of about 1000 km in the western trough is not sufficient to average out the net meridional transport of the annual Rossby waves. Using an integration scale of 4000 km of the whole basin instead, efficiently cancels out the Rossby wave contribution to the annual cycle and this explains the much lower energy level seen in the spectrum. Using 2-year low-pass filtered data (Fig. 7.3, left panel) reveals the existence of even lower frequency Rossby waves, which might explain the transport differences observed at periods longer than one month. Also pronounced multi-annual changes in the DWBC are observed.

Whether these model results apply for the real ocean as well is not clear. Whereas the models shows a clear annual cycle (of about 2 Sv) in the western trough transports, no such indication could be seen in the observations (Fig. 5.2). However it is difficult to directly compare both data sets due to the less steep western continental rise in the model and other differences in topography, which leads to different separations of boundary triangle and internal transports. The annual cycle in the model internal transports (1200-4400 m, rel. 4400 m) in the western trough (60°- 51.0°W) at 16°N amounts to only 0.4 Sv (with large parts of the DWBC passing west of 60°W). No indication for annual Rossby waves is seen in the observed internal transports. This may be simply due to the fact that their amplitude is too small to uncover them in a time series of only 4 years length. If reasonable agreement between model and observations had been found, one might have considered to use the model to eliminate the effect of annual (and longer term) Rossby waves in the observations, since they do not represent a signal of interest in this study. On the other hand, since no annual cycle is visible in the measurements, such a correction does not make much sense at this (early) stage.

Nonetheless there is a simple lesson to learn from the model: Increasing the zonal integration scale of the end point array might average out net transport contributions of possible longer periodic Rossby waves. In the following a modification of the current MOVE experiment design

is tested in the model, that does not require additional moorings (see schematics in Fig 7.4). It is proposed to keep the moorings M3 and M4 as before (compare to Fig. 2.1, eliminate M2 and move M1 far into the eastern basin (near 27°W), right at the base the of topographic rise of the Cap Verde Islands. Strictly speaking, it is not clear to which degree end point measurement at M3 and $M1_{new}$ would provided accurate estimates of zonally integrated transport fluctuations, if a prominent topographic feature like to Mid-Atlantic Ridge (MAR) rises to shallower depth levels than the water depth at the end-points: Zonal pressure gradients in the western and eastern trough could balance meridional flows such, that the zonally averaged meridional transport fluctuations (between M3 and $M1_{new}$ might not correspond to the M3-$M1_{new}$ pressure gradient. Only above the crest of the MAR it is valid to assume the end-point design to work. Model simulation however suggests, that the MAR does not significantly upset the relationship

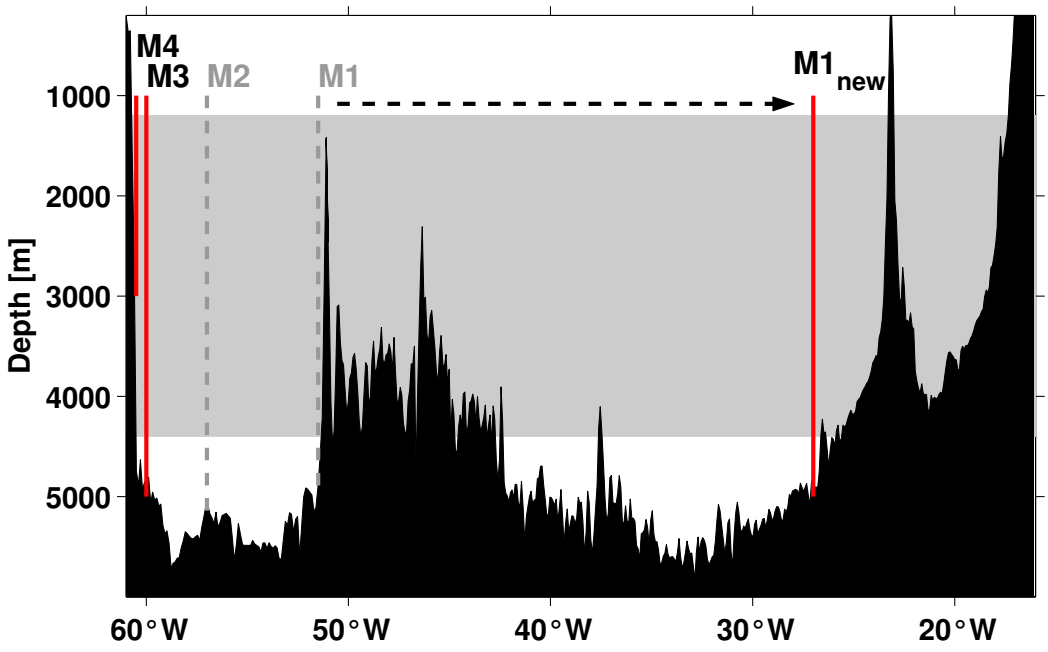

Figure 7.4: *A possible modification of the MOVE array: Instead of covering only the western trough (west of 51.5° W) with the moorings M4,M3,M2 and M1, mooring M1 could be moved far into the eastern trough at the base of the Cap Verde Islands to expand the zonal integration scale (*$M1_{new}$*). The maintenance of M2 would not be required any longer. However its instrumentation could be used to maintain the current M1 position as well, in order to study the relationship between transports in the western and eastern trough.*

between fluctuations of zonally integrated meridional transports and the zonal pressure difference (Fig. 7.5): The correlation between true model transports and those seen by the modified end-point array amounts to 0.90 for monthly averaged values. This means that a more effective monitoring is feasible by a simple modification of the present MOVE design. According to the model results, moving mooring M1 eastward up to the base topographic rise of the Cap Verde Islands is sufficient to obtain accurate estimates of MOC fluctuations, even on time scales much shorter than one year.

As mentioned before, the Atlantic MOC has received much interest for it represents the most important mechanism for meridional oceanic heat transport. In model studies a quasi-linear relationship between fluctuations of the MOC and heat transport has been obtained (e.g. Böning and Semtner, 2001), at least at lower latitudes. Subsequently investigations based on the FLAME 1/3° model focus on the question, to what degree the present and the modified array may be used to estimate its variability. Correlation between western trough transport fluctuations (as obtained by the present MOVE design) and the meridional advective heat transports, defined

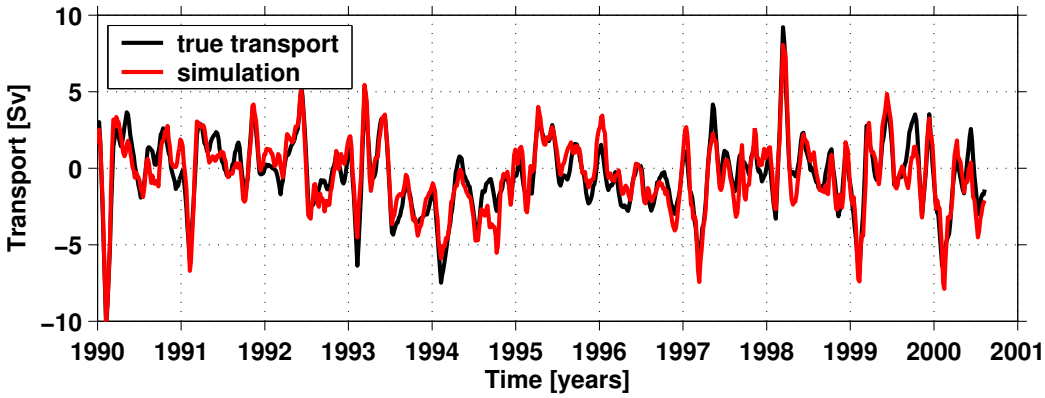

Figure 7.5: *Transport fluctuations between 1200 m and 4400 m (NADW) across 16° N in the FLAME 1/3° model: The black line displays true model transports integrate across the whole zonal extent of the Atlantic basin. The red lines shows a simulation for transports east of 27° W as they would be detected by the modified end-point array in Fig. 7.4. It is assumed that transports in the western boundary triangle (west of M3) are measured directly, so that this contribution is taken from the the models' true transports. Further it is assumed that bottom pressure fluctuations are added to hydrostatic pressure fluctuations (which are obtained by density measurements in the water column), such that pressure fluctuations at 1200 m depth (above the crest of the MAR) can be computed. Horizontal M3-*$\mathrm{M1_{new}}$ *differences of these then can be scaled to external meridional transport fluctuations (where again in this simulation the true model values are used). The red line represents the sum of fluctuations of the external and the internal geostrophic contributions (derived from model densities at M3 and* $\mathrm{M1_{new}}$*), as well as the boundary triangle transport.*

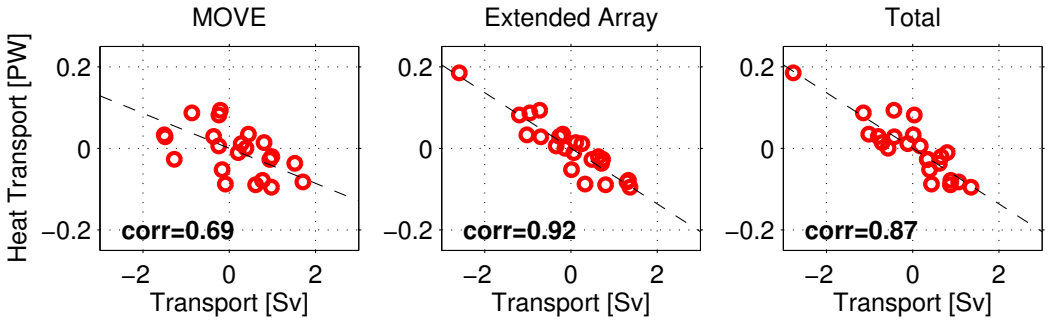

Figure 7.6: *Fluctuations of annual mean advective heat transport and deep mass transport across 16° N. The result of the simulation of the present (western trough only) and the suggested eastward extended MOVE design are displayed in the left and middle panel, respectively, whereas in the right panel the transports integrated across the the whole Atlantic basin are used. The dashed line in each panel represent a linear least-square fit between mass and heat transports.*

as $H(t) = \int\int v(t,x,z)\,T(t,x,z)\,\mathrm{d}x\,\mathrm{d}z$, amounts to 0.69 for annual mean values, which is statistically significant (Fig. 7.6, left panel). This means that the present monitoring configuration exhibits moderate skill to estimate inter-annual heat transport changes. However, using deep transports obtained from the modified array (Fig. 7.4) clearly increases the skill, with a correlation reaching 0.92. A NADW transport change of 1 Sv goes along with a change in heat transport of about 0.07 PW, roughly corresponding to findings of Böning and Semtner (2001). It is not surprising to find a high correlation, if one considers the close correspondence between the simulated and the true basin wide integrated model transports presented in Fig. 7.5. For the latter basically the same level of correlation with heat transport is found.

7.3 Scales of the Overturning Transport Signal

After having treated the representativeness of meridional transport fluctuations integrated across the western trough for basin-integrated MOC fluctuations, now the next step is taken: Presuming the MOC variability across a certain latitude circle could be measured perfectly, what could be learned from these observations? What dominates the evolution of the MOC at a certain latitude and how representative is the signal for other latitudes? The ocean's response to wind stress has been shown to be dependent on the frequency-wavenumber characteristics of the forcing patterns (Willebrand et al., 1980): For a mid-latitude ocean large spatial scale wind stress forcing results in a predominantly barotropic response over a broad range of weeks to inter-annual time scales. Beismann et al. (2002) show in a coarse-resolution model (4/3°) that in the off-equatorial Atlantic a high level of correlation between inter-annual changes in (zonally integrated) zonal wind stress and meridional transports can be found, even in the deep ocean. This suggests as rather barotropic compensation of the meridional surface Ekman flow. Their findings are generally confirmed using output from the CONTROL run of the FLAME 1/3° model displayed in Fig. 7.7, where a moderate correlation of 0.69 between inter-annual changes wind stress and deep meridional transports is obtained. This is in line with findings of Dong and Sutton (2001), whose analysis based on a climate model however suggests that towards decadal time scales MOC variability becomes increasingly baroclinic. This again is broadly consistent with the oceanic response to wind forcing in the low-frequency limit (Willebrand et al., 1980).

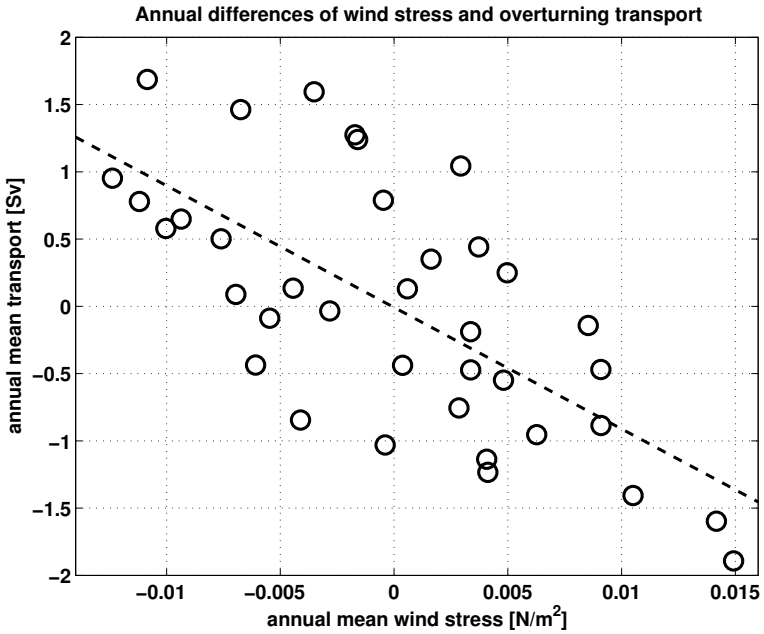

Figure 7.7: *Connection between wind stress and MOC fluctuations at 16° N: Year-to-year differences of annual mean zonal wind stress [N/m^2] and meridional overturning stream function [Sv] at 1200 m in the CONTROL run from the FLAME 1/3° model. The correlation coefficient is 0.69.*

However the type of analysis presented in Fig. 7.7 especially emphasizes the year-to-year changes and masks lower frequency bands. The local relationship between zonal wind stress and deep meridional transports at 16°N becomes increasingly less evident towards longer periods (Fig. 7.8): At periods > 2 years, squared coherences between both variables do not exceed the significance level of 0.4.

From Fig. 7.9 (top panel) an explanation for the relatively low local coherence may be obtained. Coherent patterns of MOC fluctuations can frequently be found, exhibiting meridional scales of

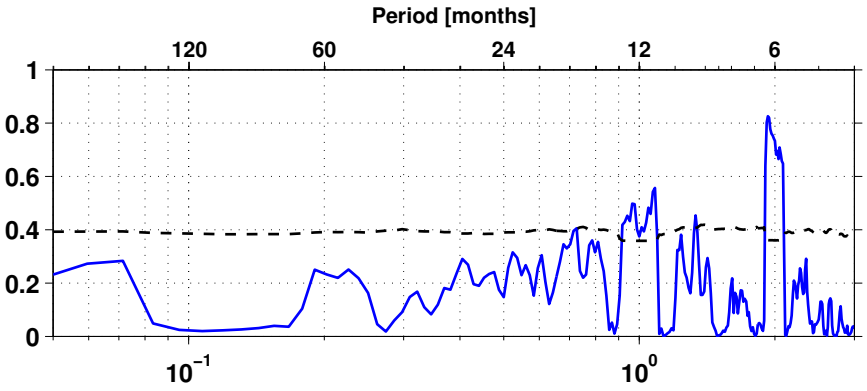

Figure 7.8: *Squared coherence between zonal wind stress and meridional transports below 1200 m, zonally averaged across the whole Atlantic basin (60° W- 22° W), computed from the CONTROL run of the FLAME 1/3° model. The dashed line denotes the zero coherence level at 95% confidence.*

4000 km and more. The general direction of signal propagation is towards the South, however in the South Atlantic, this becomes less evident. At times, MOC perturbations appear to propagate along the entire domain from 50°N to 33°S, for example during year 8 or 15. Thus remotely forced transport perturbations have the potential to upset a local relationship between deep transports and surface wind forcing. At other times signal propagation is less obvious (e.g., after year 37), with the anomalies exhibiting an in-phase relationship over the whole meridional extent. A detailed analysis of the forcing fields (and the ocean dynamics) would be required to explain the different events, which is beyond the scope of this study. These inter-annual transport anomalies appear to be wind driven to a large extent, which again corresponds to findings of Dong and Sutton (2001): In the lower panel of Fig. 7.9 MOC anomalies from the HEAT experiment are displayed, which emphasizes buoyancy driven effects, since the forcing comprises NCEP/NCAR heat flux anomalies between 1958 and 2000 on the one hand and climatological wind stress on the other hand. The resulting amplitudes of the transport anomalies are reduced by more than a factor 2 relative to the CONTROL case. This goes along with a shift towards longer periodic variability, which is masked to a large extent in the CONTROL experiment (see also Fidler (2003)). These heat flux induced MOC fluctuations are thought to be related to low frequency fluctuations of the winter NAO (e.g. Fidler, 2003). In some instances the equator seems to act as a barrier, restricting anomalies to one hemisphere, which corresponds to findings of Johnson and Marshall (2002). It should be noted that on decadal time scale buoyancy forcing at high latitudes becomes more and more important for MOC variability (Eden and Willebrand, 2001). On the other hand low-frequency wind stress curl fluctuations may decelerate or accelerate the horizontal subtropical and subpolar gyres, causing anomalous advection of density anomalies (Pasquero and Tziperman, 2004), which may have a similar impact on long-periodic MOC fluctuations (Dong and Sutton, 2001).

To specifically analyze the representativeness of MOC at one latitude circle and to determine time-scales involved in the signal propagation, squared coherences between MOC fluctuations at different latitudes have been computed (Fig. 7.10). In the CONTROL run (left column) MOC fluctuations at 50°N and 16°N display a moderate but significant coherence up to periods of 4 - 5 years. The phase steadily decreases from 180° to 90° from periods of 2 towards 4 years. Thus the 50°N signal leads by one year in this band. At longer time scales coherences become insignificant. Only at periods $>$ 17 years significant values are found again. Interestingly, again a signal delay of one year (corresponding to a phase shift of roughly 20°) between both latitudes is found. This uniform time scale over a broad range of periods suggests that the same oceanic mechanism is responsible for the signal propagation. No significant coherence can be observed between 16°N and 20°S on periods $>$ 1 year. Hence, MOC fluctuations at different

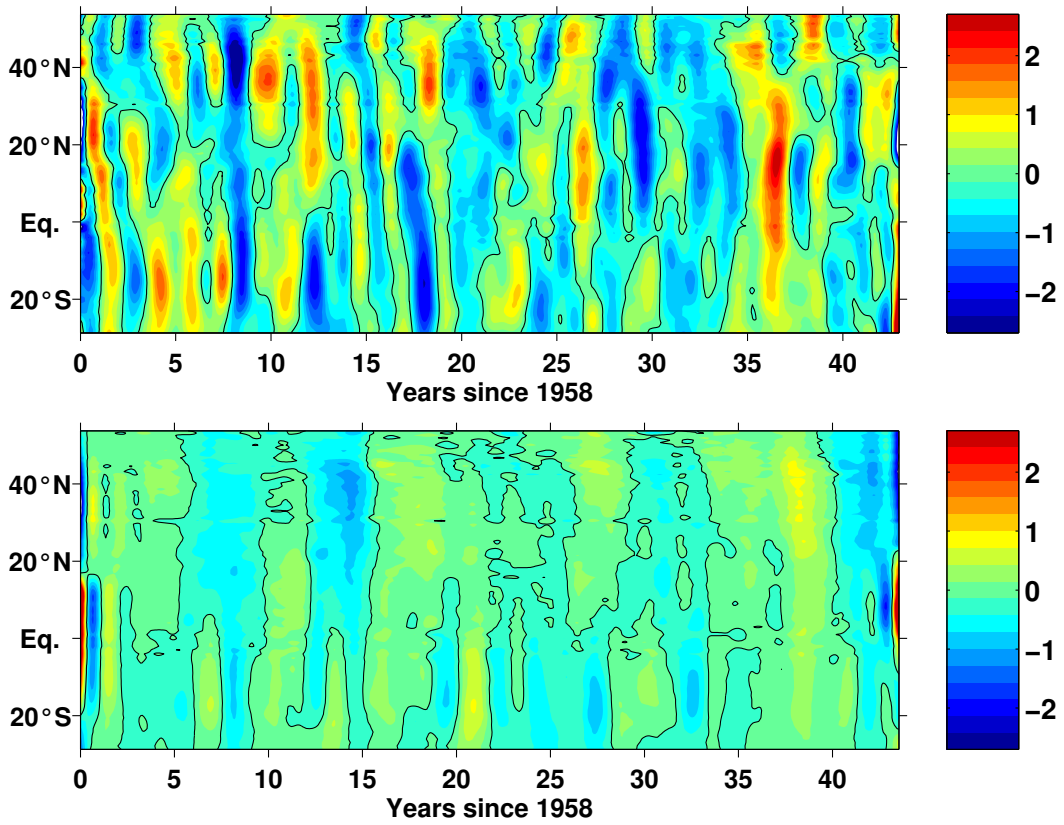

Figure 7.9: *Hovmoeller diagram of anomalies of 18-month low-pass filtered Atlantic zonally averaged meridional transport [Sv] below 1200m from FLAME 1/3° model. The upper and lower panel comprises output from the CONTROL and the HEAT run, respectively (see Appendix A.1 for details). This Figure is composed of the same data as Fig. 5.7 in Fidler (2003), which however is confined to latitudes north of 10° N and processed slightly different.*

latitudes within the northern hemisphere are moderately representative for each other in certain spectral bands. Inter-hemispheric variability, at least in the frequency range considered here, is not. As one might already have concluded from the visual impression in Fig. 7.9 (bottom), in the HEAT experiment (right column in Fig. 7.10) highly significant coherences (amounting to about 0.6) between MOC fluctuations at 50° and 16° can be found at periods > 5 years, corresponding to the heat flux related shift towards longer time scales. The delay time of the signal is 3 months at a period of 2 years and increases steadily to a delay of 12 months towards lower frequency fluctuations. Thus, a slightly faster propagation seems to be associated with the heat flux forcing, corresponding to the fast southward communication of high-latitude MOC perturbations via Kelvin waves (e.g., Kawase, 1987; Döscher et al., 1994; Dong and Sutton, 2002). Again, no significant coherence is found for signal propagation across the equator, confirming the visual impression in Fig. 7.9 (bottom) and being in line with the equatorial "buffer" described by Johnson and Marshall (2002).

In the steady state the MOC essentially involves inter-hemispheric (and inter-oceanic) exchange of deep and near-surface waters. At which time scale may one expect to find a mode of coherent inter-hemispheric MOC fluctuations? In order to extend this analysis towards longer time scales, data from the coupled climate model ECBILT-CLIO (Opsteegh et al., 1998) has been analyzed (consult Appendix A.3 for details), which allows for long integration intervals due to its coarse resolution (the ocean component is evaluated on a 3°x 3°grid). In this experiment MOC perturbations at decadal and longer time scales appear to propagate relatively undisturbed southward across the equator. However at times local high latitude anomalies north of 40°N are found,

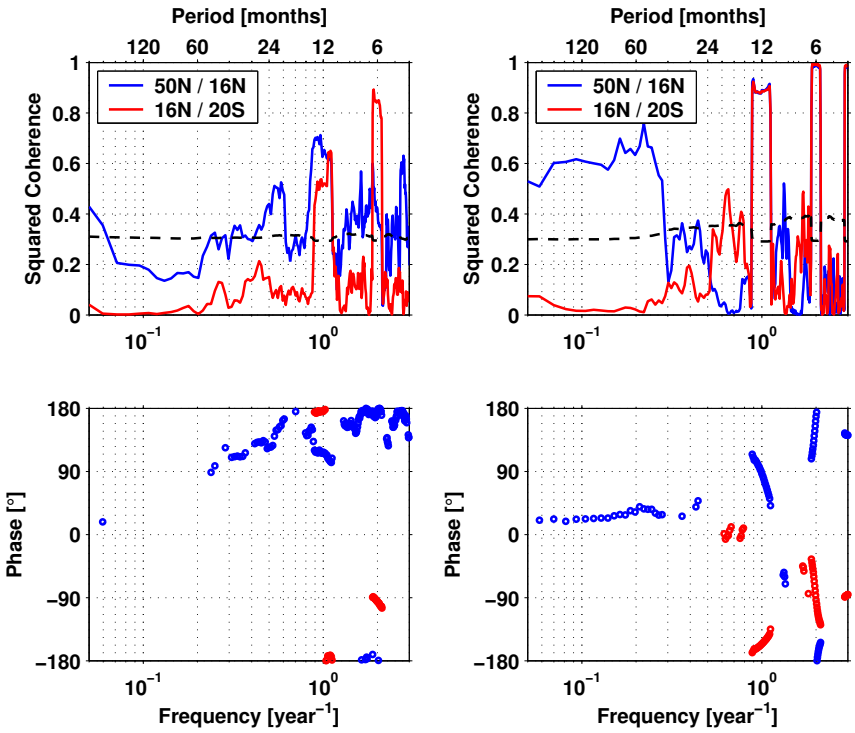

Figure 7.10: *Squared coherence (top) and phase (bottom) of zonally averaged meridional transports (below 1200 m) between 50° N and 16° N (blue) as well as between 16° N and 20° S (red) in the FLAME 1/3° model. Results from the CONTROL and from the HEAT experiment are displayed in the left and right column, respectively. The dashed line denotes the zero coherence level at 95% significance. Positive phase means that the signal at the latitude mentioned first leads. Only those phase values are computed for which the squared coherence exceeds the significance level.*

which are not communicated towards lower latitudes.

Increasing coherences between MOC fluctuations at 50°N and 16°N are observed for periods starting from about 14 years, with values exceeding 0.9 at centennial time scales (Fig. 7.12). The delay is about 3 - 4 years for periods < 100 years (which is smaller than typical time scales commonly associated with advection), above that no significant phase shift can be observed. The results for the inter-hemispheric signal propagation (i.e., between 16°N and 20°S) are quite similar, however showing generally even larger coherences at inter-decadal time scales than the North Atlantic case, confirming the visual impression from the Hovmoeller diagram in Fig. 7.9. Also, delay times are somewhat shorter. Thus, in this model inter-decadal MOC fluctuations at one latitude in the Atlantic may be regarded representative for its entire basin, if signal propagation is taken into account. At centennial time scales fluctuations appear to be in phase over the whole meridional extent of the Atlantic. In a recent analysis of another coarse-resolution climate model Latif et al. (2004) have found high correlation between multi-decadal fluctuations of subpolar SST and MOC fluctuations in the subtropical North Atlantic. In the light of the findings presented above, these multi-decadal MOC changes are likely to be coherent over the entire Atlantic basin. If this relationship could be shown to hold in the real ocean, the large scale low frequency evolution of the MOC could be reconstructed and monitored by satellite observations of large scale SST patterns. Due to the dominance of multi-decadal variability in the model, the MOC may even exhibit a certain degree of predictability.

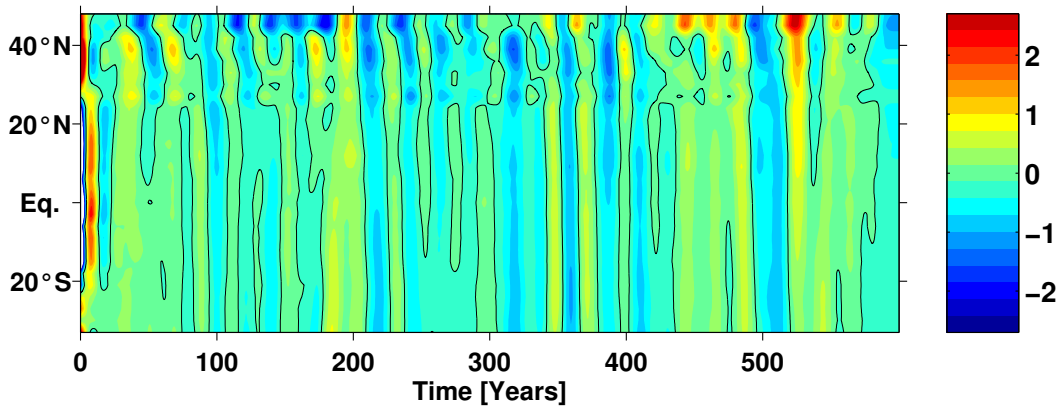

Figure 7.11: *Same quantity as in Fig. 7.9, but computed from the ECBilt-Clio coupled model (see Appendix A.3).*

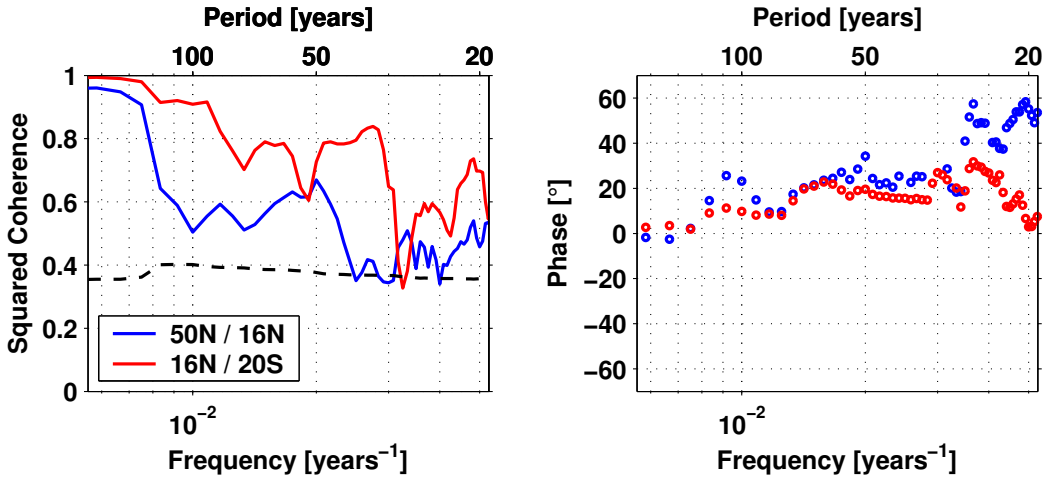

Figure 7.12: *Same quantities as in Fig. 7.10 but computed from the ECBilt-Clio coupled model (see Appendix A.3).*

7.4 Implications for Observing MOC Variability

A number of implications arise from these finding for observing systems of the MOC. Even if essential components of the MOC, such as the strength of the DWBC, deep-water formation at high latitudes and time scales of southward tracer advection have been observed rather intensely, from observations hardly any information exists about the magnitude as well as time and spatial scales of MOC variability. Therefore it would be important to verify the basic pattern of MOC variability, including meridional signal propagation, shown by ocean and climate models. Since different time and spacial scales are involved as well as different forcing mechanisms and regions (see also chapter 1.2), a coherent monitoring approach would be required to efficiently observe MOC fluctuations, integrating benefits of various different measurement techniques.

A backbone of such an approach could be experiments using an end point measurement approach to efficiently monitor MOC fluctuations across latitude circles such as MOVE at 16°N or the RAPID array covering the 26°N line since March 2004 (Hirschi et al., 2003). At least two latitude circles in the North Atlantic should be covered simultaneously for at least a decade in order to study the representativeness of the MOC signal at different latitudes and to be able to distinguish between local and remote forcing of MOC perturbations. Additionally, wind data from satellite measurements or reanalysis should be used to remove the oceanic compensation to local wind forced surface Ekman flow, which has been shown to play an important role on up to inter-annual time scales.

Since a zonally integrating end point technique is obviously not particularly sensitive to certain mechanisms involved in remotely forced MOC variability, it would be highly desirable to add additional monitoring elements specifically designed to observe the different aspects of MOC variability. That would provide better estimates of the relative impacts of the different mechanisms and of the time scales involved .

Coherent signals of fast communication of MOC perturbations by Kelvin or other coastal-trapped waves are best observed by simultaneously deployed permanent monitoring arrays at several sites along the western continental slope. Each of these should consist of a line of bottom pressure recorders, extending down the slope. Two such lines are already in operation since the beginning of this year (personnel communication C. Hughes).

Decadal variability involves southward advection of density anomalies by the DWBC. Thus, additional measurements sensitive to density changes would be required within different locations of the DWBC. These could be a combination of moored temperature and salinity sensors as well as PIES on the one hand, which provide a good temporal resolution, as well as repeated CTD and tracer sections, allowing for a high spatial resolution. It should be noted that tracer advection in the DWBC is a complex process to due to recirculations and interaction with the Gulf Stream (Bower and Hunt, 2000). Hence estimating tracer advection in the DWBC is not straight-forward.

Additionally measurements in key regions of the MOC should be carried out. These should involve hydrographic repeat sections for estimates of deep-water formation rates in the Labrador Sea as well as time series observations of the strength of the dense Denmark Strait and Iceland-Scotland overflows. At inter-decadal time scale changes in the NADW to AAIW conversion in the Southern Ocean would be of interest.

Also, it is tempting to apply proxies to reconstruct and monitor certain aspects of MOC variability, such as the temperature index proposed by Latif et al. (2004). However their applicability in the real ocean must be preceded by an assessment of their correlation with the MOC, which might take decades. It is still a subject of ongoing scientific discussion whether the strength of the MOC is related to meridional density gradients or not (Greatbatch and Lu, 2003). On the

other hand, once having been established from observations, such a relationship would provide an efficient way to monitor the evolution of the MOC.

Recent findings show evidence for substantial freshening of high latitude oNADW and LSW (Dickson et al., 2002; Curry et al., 2003) during the last 4 decades and substantial changes in the LSW formation rate appear to have occurred in the 1990s (Kieke et al., submitted in 2004), but even so there is no observational indication of changes in the strength of the DWBC at the exit of the Labrador Sea (Schott et al., 2004a). Thus, for example LSW layer thickness might not be a reliable index for MOC strength.

It has been shown that the traditional separation of the oceanic flow field into a wind driven horizontal and a buoyancy driven meridional circulation cannot be justified, since both interact with each other (e.g. Delworth et al., 1993; Dong and Sutton, 2001; Pasquero and Tziperman, 2004). Therefore the observation of changes in the strength of the horizontal gyres in the Atlantic, for which there is recent indication from Häkkinen and Rhines (2004), is a natural component of a coherent approach to monitor MOC variability. This would involve space-borne large scale measurements of SSH and wind stress curl as well as moored measurements of the temporal evolution of western boundary currents.

Many of the observational components are already in operation but represent mostly uncoordinated efforts which are subject to limited funding periods. A joint effort to sustain simultaneous measurements of the different aspect of MOC variability for at least a decade would be required. Additionally, the evolution of the MOC in future global warming projections (IPCC, 2001) displayed in Fig 1.1 suggest that and end point monitoring array, such as MOVE, would have to remain maintained for several decades, to allow for observing statistically significant trends. The ensemble average decrease in MOC strength in these projections is about 0.6 Sv per decade, which is less than half of the r.m.s. amplitude of inter-annual MOC variability (as shown by most ocean models). Model results suggest that the MOC displays rather strong inter-decadal variability (Latif et al., 2004), which might mask a possible gradual weakening of the MOC related anthropogenic influences for more than a century.

7.5 Summary

In the first part of this chapter the monitoring design of MOVE has been verified and in the second part the representativeness of MOC fluctuations observed at one latitude circle for the North Atlantic and the entire Atlantic has been analyzed.

Summarizing briefly, the model simulations have shown that meridional transport fluctuations zonally integrated across the western trough of the Atlantic by the MOVE array are moderately representative for MOC fluctuations across 16°N at inter-annual and longer time scales. At seasonal and shorter periods MOVE does not seem to provide reliable estimates of the evolution of the MOC. Baroclinic Rossby waves appear to be the main mechanism of introducing noise. However simply extending the horizontal averaging scale towards the East, which would not require additional instrumentation, would largely increase signal-to-noise ratio and thus would allow for robust estimates of MOC fluctuations at time scales longer than one month. In the simulation the correlation between MOVE transports and the MOC amounts to of 0.7 for 3 year low-pass filtered data and the correlation between inter-annual changes of the MOC and the wind-stress is 0.7 as well. Therefore it is not surprising in the observations presented in chapter 5 no relationship between inter-annual changes of Ekman transports in the western section and the MOVE transports have been found after only 4 years of measurements (4 data points). A longer time series and and extension towards the East are needed. It is also too early for a physically relevant comparison between MOVE transport fluctuations with a MOC

index derived from large-scale meridional density gradients (e.g. Thorpe et al., 2001; Latif et al., 2004), since such indices only have been shown to hold only decadal and longer time scales. The same is true for indicators like the thickness of LSW, which displays strong decadal rather than inter-annual fluctuations (Kieke et al., submitted in 2004).

But even if one would be able to perfectly monitor deep transport fluctuations across 16°N, the significance of such measurements might strongly depend on the time scales involved. At seasonal to inter-annual periods, the MOC appears to be largely wind driven, which masks the meridionally coherent lower frequency variability driven by buoyancy forcing within the North Atlantic. Thus coherences between MOC anomalies at tropical and subpolar latitudes may hardly exhibit any statistical significance on up to decadal time scales. No coherence is found between North and South Atlantic signals in the same frequency band. However it appears that from inter-decadal towards centennial periods MOC fluctuations become increasingly coherent, meaning that at these time scale measurements at one latitude would be sufficient to observe basin scale evolution of the MOC.

An end point monitoring technique applied at one latitude circle is not particularly useful to distinguish between different (local and remote) mechanisms responsible for MOC variability. The use of two such systems at different latitudes in the North Atlantic would be required to detect meridionally coherent signals. To be able to distinguish between (and to quantify the relative importance of) different mechanisms of MOC variability additional observing elements, specifically designed to isolate these, should be applied, such as western boundary arrays, hydrographic campaigns and satellite measurements of wind stress, SSH and SST. But even if such a system would contribute much to the understanding of MOC variability, the possibility cannot be ruled out that due to the tendency of the MOC to display rather strong inter-decadal fluctuations the detection of an anthropogenic contribution might be masked for longer than a century. That does not mean that the natural MOC variability is not of interest, since there are fluctuations in heat transport associated with it.

8 Space-borne Bottom Pressure Measurements

8.1 Introduction

In chapter 3 difficulties in recovering bottom pressure signals of periods in the order of or longer than the deployment duration of the instruments had been described. Longer deployments and overlapping signal as well as the use combination of dynamic height and satellite altimetry had been proposed to overcome this shortcut. In the following the potential of satellite gravity measurements obtained within the presently ongoing Gravity Recovery and Climate experiment (GRACE) to obtain information about the lower frequency time evolution of bottom pressure is assessed.

The GRACE mission (Tapley and Reigber, 2001), which is a joint U.S. / German project, carries out spaceborne measurements of the Earth's time variable gravity field. The basic idea of the experiment design is fairly simple (see schematics in Fig. 8.1): Two satellites, launched in March 2002, follow each other with a nominal distance of 220 km on an almost polar orbital track. They are interconnected using a K-band microwave link to precisely measure their separation and its temporal rate of change with an estimated accuracy of 1 μm/s: Due to their spacial distance, regional gravity anomalies result in slightly differing amplitudes of gravity force exerted on the two satellites. These differences cause an acceleration of the first satellite relative to the second. Thus, this measurement configuration is very susceptible to gravity anomalies. To accomplish a precise attitude and account for non-gravitational forces, both platforms are equipped with a star camera and an accelerometer. Their position and velocity is measured using GPS navigation. Preceding experiments, such as CHAMP (Challenging Minisatellite Payload), had only been based on tracking orbits of single satellites, which is less precise. In fact, GRACE has provided a mean geoid solution of the Earth with unprecedented accuracy (Reigber et al., 2004). The expected life time of the twin satellites is about 5 years. Due to atmospheric drag, the initial altitude of 500 km will decrease during the mission by 50 - 200 km, depending on the actual solar activity.

The research objectives of GRACE are manifold: Improvements in estimates of the mean geoid are thought to lead to advances in studies of ocean heat flux, sea level change, upper ocean heat content and absolute geostrophic ocean currents. Analyzes of the time variable gravity field will allow to study changes in deep ocean currents, soil moisture, mass balance of ice shields and glaciers or continental water storage.

8.2 Deriving Fluctuations of Bottom Pressure from Gravity Measurements

Presently, monthly mean gravity field solutions are provided independently from two procession center, namely the GeoForschungsZentrum Potsdam (GFZ) and the University of Texas Center for Space Research (UTCSR), in the form of spherical harmonic coefficients C_{lm} and S_{lm} up to degree l and order m 120. An expansion of a monthly solution to a certain l, m is roughly associated with horizontal (half wavelength) scale of 20000km / l. A classical geophysical appli-

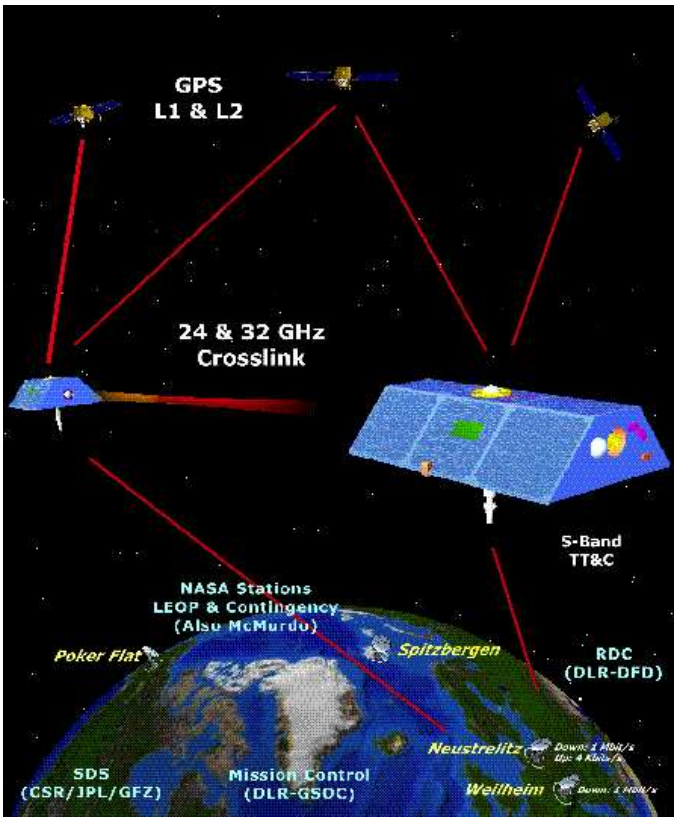

Figure 8.1: *GRACE experiment configuration: Two satellites follow each other on a near polar orbit. The key piece is the accurate distance measurement between the two satellites. Source: www.gfz-potsdam.de*

cation of such data represents the computation of Earth's geoid. An overview over the GRACE monthly solutions used in this study can be obtained from Table C.1. Unless explicitly noted, the monthly solutions processed at GFZ have been used in this study. It should be noted that at this early stage of the experiment the data is be to considered preliminary.

Changes in the Earth's gravity field (between two monthly solutions) correspond to changes in its mass distribution. Wahr et al. (2002) developed a method to infer bottom pressure fluctuations from the monthly gravity solutions: Presuming that these mass redistributions take place entirely within a very thin near-surface layer (compared to the Earth's radius) as in the ocean and atmosphere or by continental water storage), then this mass change can be converted into a density change $\Delta\rho$ of that layer (Wahr et al., 1998), which in the ocean corresponds to a bottom pressure change $\Delta P_{bot} = g\Delta\rho$. Inserting into this expression his Eq. 14 for $\Delta\rho$, the evolution of bottom pressure can be evaluated

$$\Delta P_{bot}(\theta,\phi) = \frac{ag\rho_E}{3}\sum_{l=0}^{\infty}\sum_{m=0}^{l}\frac{2l+1}{1+k_l}\tilde{P}_{lm}(\sin\theta)[\Delta C_{lm}\cos(m\phi)+\Delta S_{lm}\sin(m\phi)] \qquad (8.1)$$

with θ and ϕ denoting the geographical latitude and longitude, respectively, a the Earth's semi-major axis (6378 km), g the mean gravitational acceleration and ρ_E the mean density (5517 kg/m^3). $\tilde{P}_{lm}$ are the normalized Legendre polynomials for degree and order l and m, and k_l are the Love numbers representing the Earth's response to surface loads. The k_l used in this study have been computed by Farrell (1972). ΔC_{lm} and ΔS_{lm} represent temporal changes of C_{lm} and S_{lm}. Over continents ΔP_{bot} can be interpreted in terms of water column equivalent, with a pressure of 1 mbar corresponding to a column height of 1 cm. The assumption that mass contribution to fluctuations of ΔP_{bot} from the solid earth are negligible is a reasonable approximation on shorter than decadal time scales. Theoretically the difference of ΔP between

two locations could be used to evaluate external velocity changes using Eq. 1.4

$$\Delta v'_{ext}(t) = \frac{1}{\rho f L}\left[{\Delta P'_{bot}}^{A}(t) - {\Delta P'_{bot}}^{B}(t)\right] \tag{8.2}$$

However in practice there are three aspects that need to be considered. The first issue is that the GRACE gravity measurements suffer from aliasing problems, which apart from measurement noise are also caused by not adequately sampling the diurnal and semi-diurnal ocean, earth and atmosphere tides as well as other high frequency oceanic and atmospheric signals (Knudsen, 2003; Han et al., 2004). Very much like in satellite altimetry (e.g. Stammer et al., 2000) a de-aliasing procedure has to be carried out: Different models are applied to predict and eventually eliminate these signals. If the elimination worked perfectly (which is not the case as will be seen later), the differences between the monthly GRACE fields would be dominated by mass redistributions associated with continental hydrological signals including ice mass variations (Schmidt et al., 2004), whereas variations in bottom pressure should be negligible. However, since in this application the focus is on ocean bottom pressure, after the de-aliasing procedure the monthly averaged non-tidal ocean and atmosphere mass fluctuations as predicted by the models have been re-added to the monthly GRACE solutions. Model details can be obtained from Appendix C, here only the processing steps are described briefly.

Secondly, as noted above the spherical harmonic coefficients are associated with certain horizontal scales. In this application, where GRACE bottom pressure will be compared to in-situ measurements from MOVE, a high horizontal resolution is obviously desirable to reduce possible leakage of remote mass signals into the GRACE data used for locally restricted comparisons.

Finally, the coefficient C_{20} describing the Earth's flattening exhibits unrealistically large time variability for unknown reasons (personnel communication F. Flechtner, GFZ-Potsdam). Therefore this coefficient has been excluded from the expansion in Eq. 8.1, which is currently a common practice in investigations using GRACE monthly fields. Since C_{20} only affects the longest wavelengths, this cannot be regarded a major restriction for this study.

In Fig. 8.2 the bottom pressure difference between two monthly GRACE solutions is displayed. Carrying out an expansion up to $l, m = 40$ results in a pattern dominated by rather intense narrow meridional stripes of regularly alternating sign, whose amplitudes reach peak at 60 mbar and whose width corresponds approximately to the associated length scale of 500 km. Obviously, this pattern does not present true geophysical signal, since it would balance extremely strong meridional currents, which are not present in the real ocean. In fact, as a consequence of vorticity conservation, in the deep ocean away from topography the flow field tends to be rather zonal. Also one would expect a signal increase from lower to higher latitudes as a consequence of the geostrophic balance as well as wind stress patterns. Instead the signal distribution observed here resembles GRACE aliasing characteristics simulated by Han et al. (2004).

The signal distribution becomes more realistic when the expansion is restricted to $l, m = 20$ (1000 km), as displayed in the center panel Figure 8.2. At certain regions over continents (Amazon Basin, Congo Basin, North Russia, India) anomalies begin to stand out from the still apparent meridional pattern. The former signals correspond have shown to be related to changes in continental water storage (Döll and Lehner, 2003; Schmidt et al., 2004; Wahr et al., 2004). Thus, over continents one may attest the GRACE monthly solutions at this resolution a limited usefulness. However, over the oceans where much smaller geophysical signals are to be expected, as model simulations suggest (Condi and Wunsch, 2004), the meridional aliasing pattern still dominates, which impedes the computation of reliable bottom pressure fluctuations.

The actual GRACE degree errors, which are defined as $\delta E_l = \sqrt{\sum_{m=0}^{l}(\delta C_{lm}^2 + \delta S_{lm}^2)}$, (with δ denoting errors in the coefficients) and which arise from uncertainties in measurements and

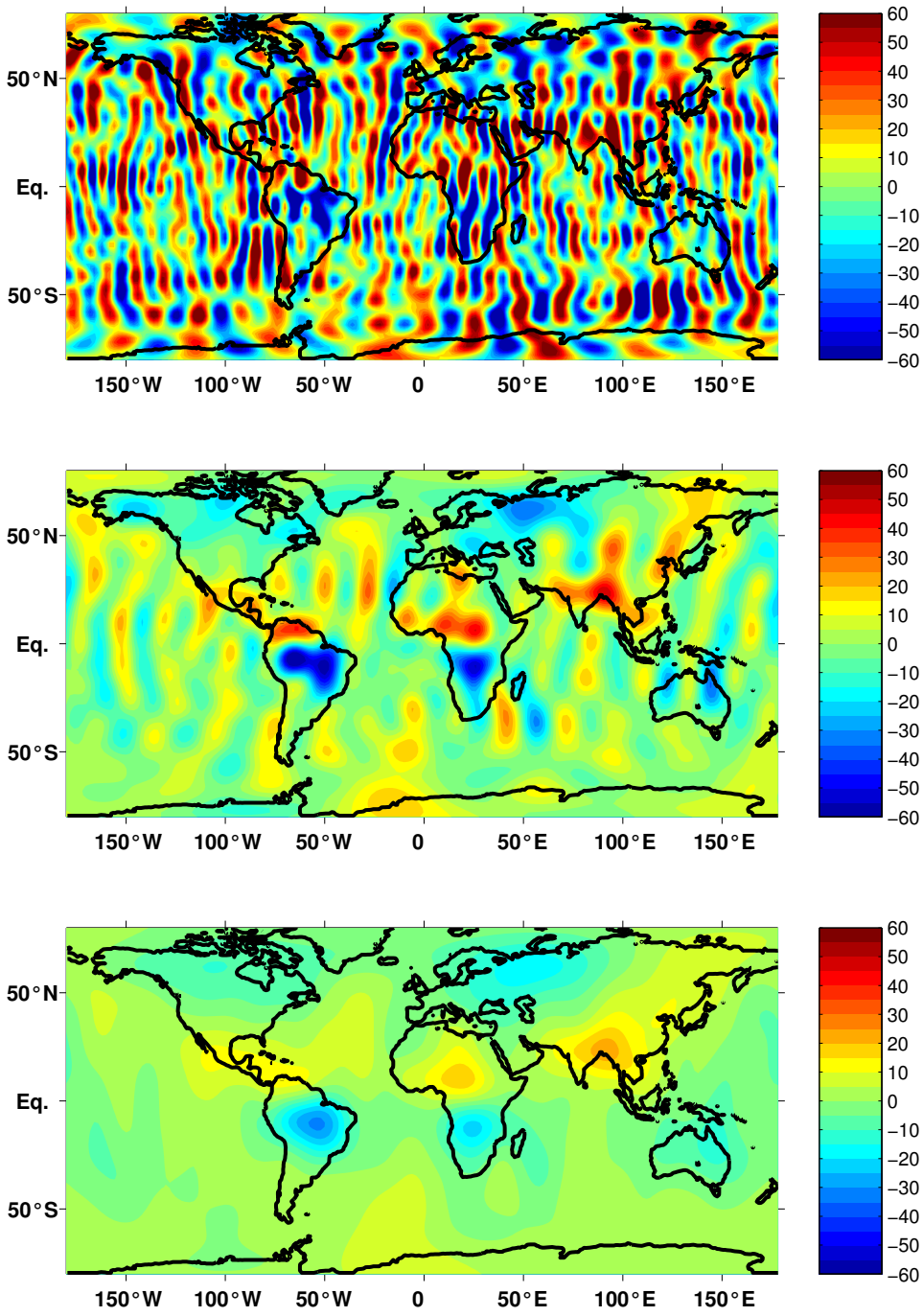

Figure 8.2: *Difference between the November 2003 and April 2003 monthly averaged GRACE bottom pressures solutions [mbar] using different expansions. Over continents this quantity may be interpreted as water column equivalent [cm]. The right and middle panel represent expansions up to* $l, m = 40$ *and 20, corresponding to horizontal (half wavelength) scales of 500 and 1000 km, respectively. In the bottom panel the coefficients* C_{lm} *and* S_{lm} *have been spatially averaged using a Gaussian weighting function of 1000 km half width. See text for details.*

processing as well as erroneous de-aliasing, have been shown to increase with increasing degree (for $l > 15$). They are presently 40 times larger than the baseline GRACE error according to Wahr et al. (2004), whose comparisons with a combined ocean and hydrology model suggest that for $l > 15$ GRACE seems to be dominated by errors rather than geophysical signals.

In the center panel of Fig. 8.2 the zonal width of the meridional stripes is set by the horizontal resolution again. This makes clear that a "hard" cut-off of the expansion at a certain degree might produce similar patterns even for lower values of l. In order to reduce the dominance of the shortest wavelengths included in the expansion an alternative "soft" method is tested, which involves a spacial averaging of the C_{lm} and S_{lm} using a Gaussian shaped weighting kernel (Jekeli, 1981; Wahr et al., 1998). In the bottom panel of Fig. 8.2 a Gaussian half-width averaging scale of 1000 km has been applied before expanding the fields to $l, m = 50$. Obviously coefficients for $l > 20$ will only have a small contribution in this realization. The method applied leads to a clear enhancements compared to the hard cut-off. Over the entire map the meridional stripes are almost eliminated, with the continental hydrological signals now clear dominating the overall anomalies. Thus, using this type of data smoothing leads to a reasonable representation of geophysical signals. It is therefore applied in the subsequent analyzes of GRACE derived bottom pressure (unless noticed otherwise).

It represents a compromise between spatial resolution and reproduction of signals. A further reduction of the horizontal resolution might lead to significant leakage of the prominent continental mass variations over South America into the area of the MOVE experiment. Also, the mooring separation between M3 and M1 of about 1000 km corresponds to the Gaussian half-width scale. A longer scale would impede the comparison of GRACE versus MOVE M3-M1 bottom pressure differences.

8.3 Comparison of GRACE Derived Fluctuations of Bottom Pressure and External Velocity with In-situ Measurements

For comparison with GRACE, tides have to be eliminated from the MOVE in-situ bottom pressures. If not mentioned otherwise, daily and higher frequency tides have been removed using a 48-h low pass filter. Longer-periodic tides (fortnightly and monthly) were subtracted explicitly using harmonic analysis (Lohmann, 1999). Verifications of GRACE solutions using in-situ measurements should be carried out in regions, where the horizontal correlation scale of bottom pressure is larger than the applied spatial filter scale (1000 km). This is shown to be the case at the location of the MOVE experiment: The observed bottom pressure time fluctuations at M1 and M3 show a correlation of roughly 0.9 for 2-day as well as for 1-month low-pass filtered data.

The comparison between MOVE and GRACE immediately shows, that GRACE strongly overestimates the variability at the "ground-truth" sites (i.e. the MOVE mooring sites displayed Fig. 8.3 top). While GRACE amplitudes peak at 5 mbar, the in situ observations hardly reach 1 mbar. Also, the GRACE OBP signal is not correlated with the in situ measurements. On the other hand high correlation among the GRACE time series at M1 and M3, as well as among the in situ observations is found. Fluctuations of the M1-M3 bottom pressure difference (Fig. 8.3, bottom), which correspond to external velocity fluctuations (see scale at the right hand side) according to Eq. 8.2, are again overestimated by GRACE, even though not by the same magnitude as the single bottom pressure records. Especially in 2003, there appears to be slightly increased similarity to the evolution of in situ external velocities, at least in amplitude. This is correlated with different GRACE onboard software upgrades which led to improved instrument data sets since early 2003 (personnel communication F. Flechtner, GFZ). That could be inter-

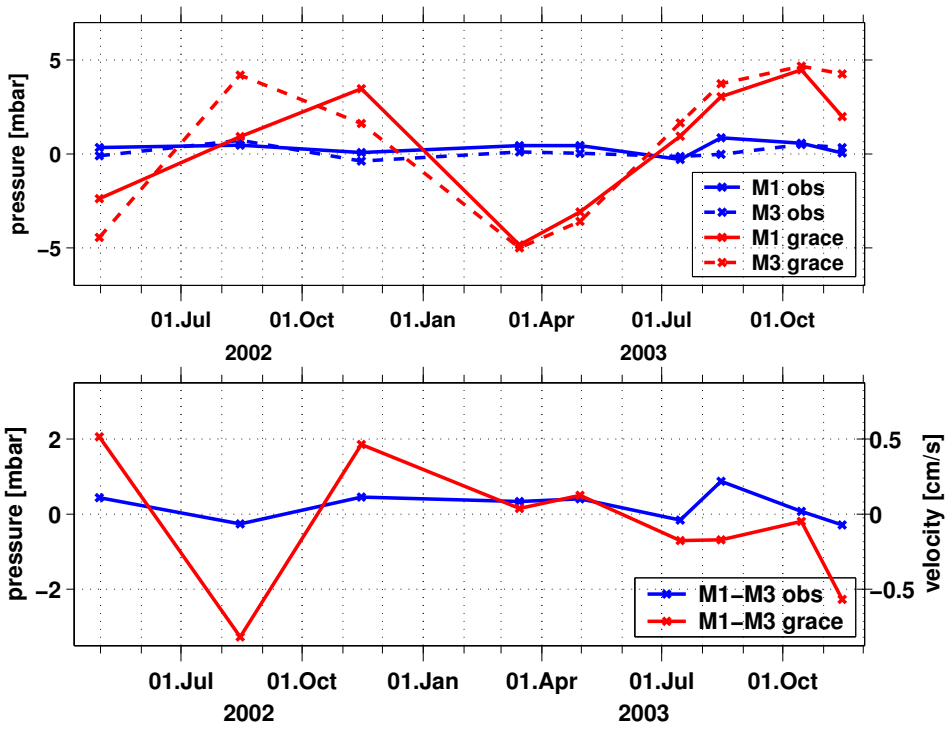

Figure 8.3: *Comparison between montly averaged GRACE derived and in-situ measured bottom pressures at M1 and M3 (top) and M1-M3 differences (bottom), corresponding to external velocity fluctuations according to Eq. 8.2 (the velocity scale is given at the right hand side).*

preted in terms of GRACE having marginal skill in observing the temporal evolution of spatial bottom pressure gradients. Nevertheless, differences between GRACE and MOVE gradients are still large.

The skill of GRACE to recover bottom pressure gradients might be spatial scale dependent: An inclusion of C_{20} would have caused even larger temporal changes between the monthly solutions, but it would not have affected the spatial gradient on scales of few thousands of kilometers within a monthly solution. This in turn could explain why the temporal evolution of the GRACE bottom pressure M1-M3 gradient compares slightly better to observations than the single time series at M1 and M3. On the other hand a Gaussian filter scale of 1000 km half-width of will automatically limit the magnitude of the M1-M3 OBP gradient.

First results indicate that GRACE realistically maps the strong annual continental hydrological cycle (Wahr et al., 2004; Schmidt et al., 2004), which displays to an amplitude of up to O(10 mbar). The key question which must be answered is: What could likely cause the r.m.s differences of 3.4 mbar between in situ and GRACE derived bottom pressure?

Errors in the in situ measurements account for only about 0.2 mbar (see chapter 3.6). Numerical simulations indicate that the expected amplitude of the annual bottom pressure cycle over the oceans typically displays amplitudes of 1mbar (e.g. Condi and Wunsch, 2004). This makes them much harder to detect. Additionally, the de-aliasing of GRACE data over the oceans is far more complicated than over land. The amplitudes of the fast moving tidal and non-tidal fluctuations (which have to be eliminated accurately) are much larger than those of the monthly bottom pressure fluctuations that ought to be recovered by GRACE. Thus, the accuracy of de-aliasing the GRACE observations crucially depends on the models' skill to recover the true ocean variability. In the following, this will be verified by validating the non-tidal and tide models using MOVE in situ observations. It can be concluded already, that the errors in bottom pressure fluctuations derived from the preliminary GRACE solutions are much too large to constrain with

this data the long term changes in external velocity measured within the MOVE experiment.

8.4 Validation of Ocean Models used for De-aliasing of GRACE Gravity Fields

The large errors observed in GRACE derived bottom pressure fluctuations may (apart from measurement noise and processing errors) also be caused by uncertainties of the models used in the de-aliasing process (see Appendix C and Han et al. (2004)). In the following output from ocean non-tidal and tide models will be compared to in situ measurements to study potential insufficiencies.

For non-tidal de-aliasing the barotropic "PPHA" ocean model driven by 6-hourly atmospheric ECMWF forcing fields is applied (consult Appendix C for model details). Unless explicitly noted, 2-day low-pass filtered model time series have been used. From the visual impression, there is a reasonable agreement between the model and the in-situ observations in terms of amplitude and phase at the sites M1 and M3. The correlation of modeled and observed data yields about 0.7 at both sites. Both data sets are dominated by high-frequency variability (Fig. 8.4 , top and middle panel). The r.m.s amplitudes of the MOVE observations and the PPHA model amount to 1.65 and 1.22 mbar, respectively. On the other hand the temporal evolution of external velocity is highly underestimated by PPHA. Its r.m.s. amplitude of 0.07 cm/s yields only one third of the observed value of 0.23 cm/s, even though a correlation is 0.4 between model and observations can be found.

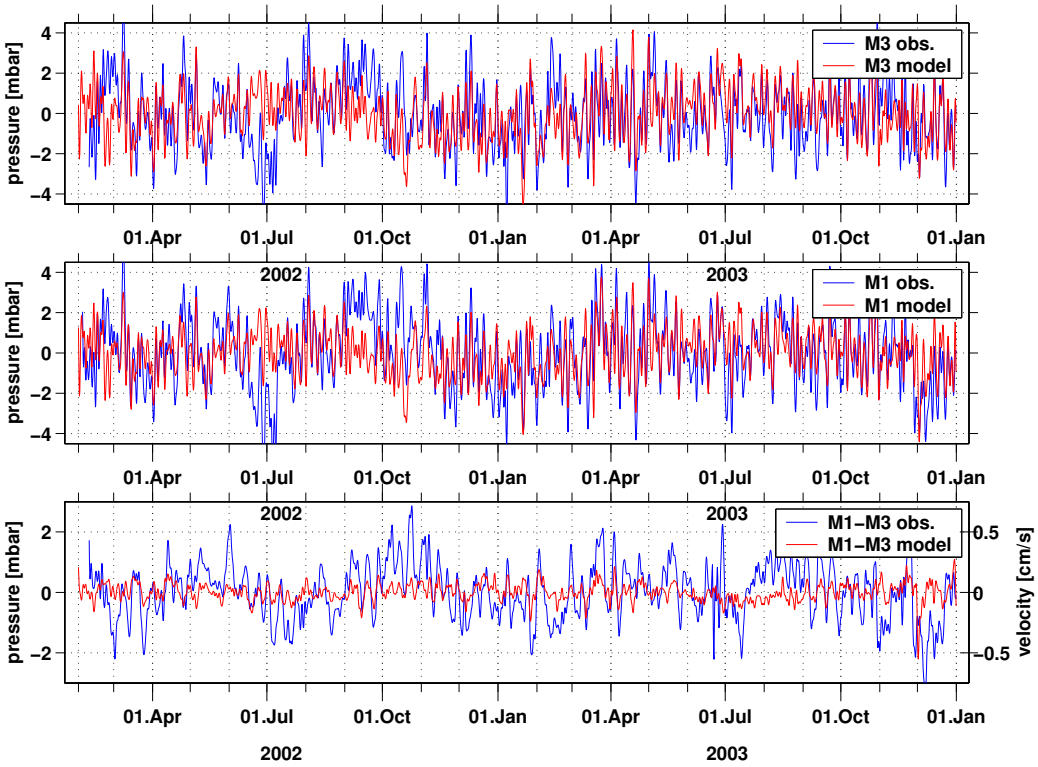

Figure 8.4: *Bottom pressure from in situ observations (blue) and the PPHA model (red) at the sites M3 (top) and M1 (center). M3-M1 bottom pressure differences are displayed in the lower panel. Note the corresponding external velocity scale on the right. All time series are 2 day low-pass filtered and monthly and fortnightly tides in the observations were eliminated empirically using a harmonic fit (Lohmann, 1999).*

Spectral analysis of modeled and observed bottom pressures (Fig. 8.5) reveals that the PPHA model reaches the observed energy levels in period bands between 2 and 6 and between 10 and 15 days. At longer periods the modeled variability is significantly underestimated. Furthermore, the modeled bottom pressure gradient strongly underestimates the observed one at all frequencies. This obvious mis-modeling at lower frequencies will surely affect the quality of the de-aliasing and therefore contaminate the monthly GRACE solutions.

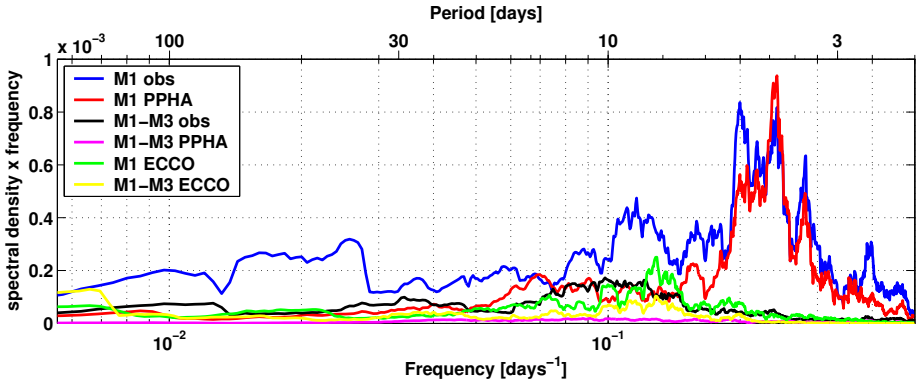

Figure 8.5: *Variance conserving spectrum of the time series in Fig 8.4. For a comparison, also spectra from the ECCO model are displayed. The forcing of ECCO does not include atmospheric sea level pressure, explaining its low energy at periods < 6 days.*

The obvious model limitations on longer periods are a critical point and may partly attributed to the lack of baroclinic dynamics. However, a comparison of the observed bottom pressure with the adjoint version of the 1° x 1° constrained ECCO model (see Appendix A) does not show a much better agreement at longer periods either (Fig. 8.5). This may be due to the fact that the model is not eddy resolving. Instead, the bottom pressure gradient reaches realistic values between 6 and 10 days (see also Fig. 5.11). Thus, a replacement of the barotropic by a eddy resolving full ocean general circulation model might lead to enhancements in the GRACE non-tidal de-aliasing (at periods larger than one month). The mismatch between ECCO and observations at the lowest periods (< 6 days), can be explained by the fact that ECCO does not include forcing from atmospheric sea-level pressure (SLP), which dominates bottom pressures in this frequency band (Tierney et al., 2000). However SLP has only a marginal effect on the external transport fluctuations, as can be seen in Fig. 8.5.

So far only time-scales of a few days to about one year have been analyzed. Since the PPHA model output, which is available with 6 hourly resolution (Appendix C), is interpolated in space and time during precise orbit determination (pers. communication F. Flechtner, GFZ), the PPHA's performance on very short time scales is of special interest. In Fig. 8.6 a data segment of 30 days near site M1 is compared with in situ observations. Unlike before, for this comparison the tidal components in the half-daily to monthly band have been removed empirically from the in-situ observations, using a harmonic fit (Lohmann, 1999).

The modeled bottom pressures are dominated by fluctuations corresponding to the sampling rate of 6 hours. SLP forcing is found to exhibit in phase signals, however with lower amplitudes. These fluctuations could partly be explained by atmospheric tides which are not present in the observed bottom pressure time series, since they have been removed empirically. To allow for an objective comparison between model and observations, the high-frequency (i.e. 36-hour high pass filtered) atmospheric contribution has been added to the observations. But even so Fig. 8.6 suggests that the PPHA model overestimates the variability on 6-hourly time scales. The r.m.s. amplitude of the 6-hourly bottom pressure differences yields 1.9 mbar for the observed (including the short-term SLP signal) and 3.2 mbar for the modeled time series. The overestimation of variability on these shortest time scales is likely to contribute to aliasing effects

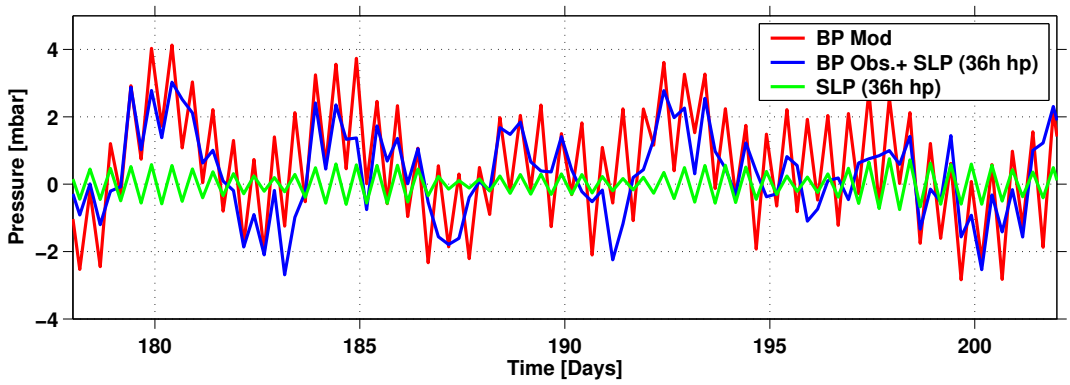

Figure 8.6: *Comparison of high-frequency bottom pressure fluctuations at site M1 between the PPHA model (red) and in situ observations (blue). Semi-diurnal, diurnal, fortnightly and monthly tides have been removed empirically. Subsequently, the observations have been subsampled at a rate of 6 hours, corresponding to that of the model. The 36-hour high-pass filtered ECMWF atmospheric SLP contribution has been added to the observations. See text for details.*

in the GRACE gravity fields: The 6-hourly fluctuation could be regarded as a signal with an exactly half-daily period. As has been pointed out recently by Knudsen (2003), certain half-daily tidal components (*S2, K2*) are associated with alias frequencies much longer than one month in the present GRACE sampling configuration. Similar arguments could be applied to the regular half-daily fluctuations seen in the PPHA model.

At these short time scales a full OGCM model would not lead to any improvements, as baroclinic signals are confined to much longer time scales. On the other hand a higher temporal resolution or a better representation of the atmospheric tides (Ponte and Ray, 2002) in the meteorological forcing fields could possibly reduce the noise level. Such a product is currently not available. Han et al. (2004) have shown that mis-modeling of the atmosphere may lead to significant aliasing effects (i.e. it exceeds the effect of measurement noise). The resulting perturbations in the monthly solutions find their representation in a pattern dominated by narrow meridional stripes, similar to that in Fig. 8.2.

A further candidate for overestimating bottom pressure fluctuations by GRACE are errors in the tidal de-aliasing (Knudsen, 2003; Han et al., 2004). Therefore time series of 9 months of hourly bottom pressure data deduced from the FES2002 and CSR4.0 ocean tide models, used in the de-aliasing process at GFZ and UTCSR, respectively, (see also Appendix C) were compared to the in-situ observations at the MOVE mooring sites. A harmonic fit including 48 tidal components in the band between half-daily and monthly periods was applied to the tide models' output as well as to the in situ bottom pressure records using an algorithm developed by Lohmann (1999). In Fig. 8.7 the amplitude (top) and phase (bottom) of the largest tidal components are displayed. Generally, there is a good overall agreement between the modeled and observed amplitudes and phases except for the half-daily *M2* and *S2* tides. *M2* reaches about 28 mbar at site M1 and 10 mbar at site M3 in the observations. At site M1 the difference of the CSR4.0 and FES2002 *M2* amplitude is 10 mbar with CSR4.0 overestimating and FES2002 underestimating the observed values by approximately 5 mbar. At site M3 the situation is reversed: CSR4.0 underestimates and FES2002 overestimates the observed *M2* value by 2 mbar. Because the harmonic fit itself introduces errors less than 1 mbar, the substantial difference of 10 mbar in the estimate of the *M2* tide can be regarded significant. In contrast, the model phases of all of major tidal components compare well at the ground-truth site.

To quantify the impact on tide model errors on the monthly GRACE fields, recent findings of Knudsen (2003) is referred to. He points out that different tidal components are associated with different alias periods T_a according to the GRACE sampling configuration, which can be

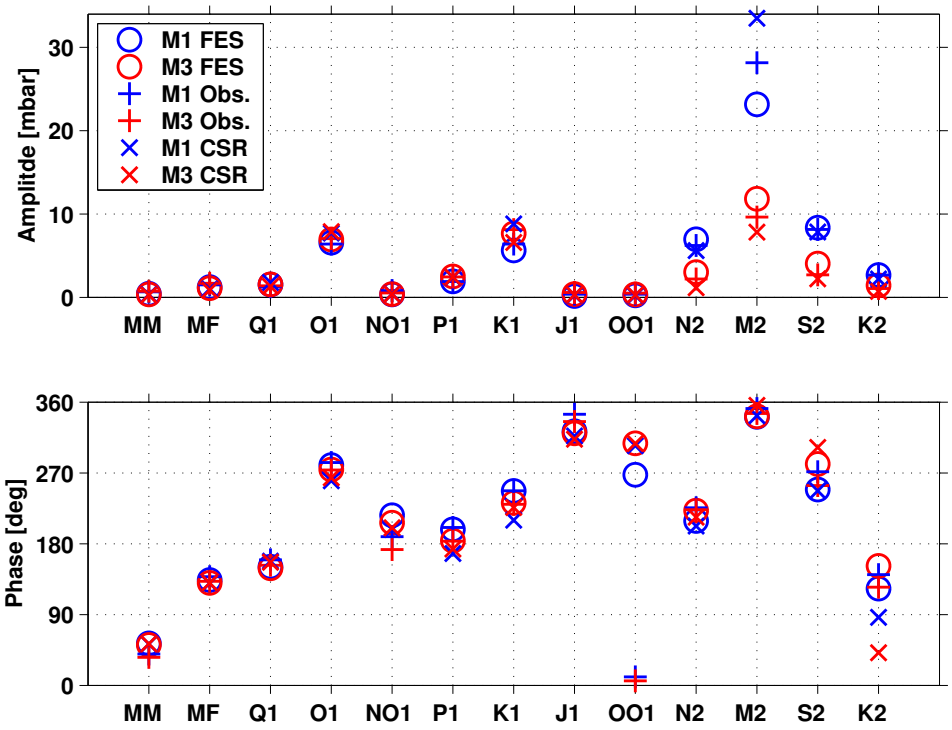

Figure 8.7: *Comparison of tidal components from in situ observations and from the FES2002 and CSR4.0 ocean tide models. Amplitudes and phases are displayed in the upper and lower panel, respectively. Both were obtained applying a tidal fit to the respective time series (Lohmann, 1999). The phase is indicated relative to the beginning of the time series.*

computed using the relation of Parke et al. (1987)

$$\frac{1}{T_a} = \left| \mathrm{mod}\left(\frac{1}{T_s} + \frac{1}{T_N}, \frac{2}{T_N}\right) - \frac{1}{T_N} \right| \tag{8.3}$$

with T_N and T_s denoting Nyquist period and signal period, respectively. Based on a choice of a sampling rate $T_{N/2}$ corresponding to half a sidereal day, the dominant *M2* tide is associated with an alias period of 13.6 days, leading to a reduction of the tidal errors of 90% in the monthly averages. A 90% reduction of a 5 mbar error (i.e. half the difference between the estimates of FES2002 and CSR4.0) in mis-modeling of *M2* at mooring site 1 yields a residual monthly error of 0.5 mbar. It should be noted that the relation 8.3 may be very sensitive to the choice of the sampling rate and the signal period. Spatial aliasing patterns in the monthly GRACE solutions associated with *M2* are composed of meridional bands of negative and positive values (Han et al., 2004). Those can be drastically reduced by applying a Gaussian filter with appropriate horizontal radius (as seen in Fig. 8.2). However, *S2* and *K2* exhibit alias periods of 162 and 1460 days, respectively. Mis-modeling of those tidal components decreases the errors by only 8% and 0%, respectively (Knudsen, 2003). Aliasing of *S2* however appears to be associated with a long-wavelength pattern, which cannot be smoothed with a comparable filter (Han et al., 2004). Mis-modeling of *S2* and *K2* at the ground-truth site does not exceed 1 mbar and 0.3 mbar, respectively (see Fig. 8.7), which might nevertheless affect the GRACE bottom pressure significantly, since the expected annual bottom pressure cycle displays amplitudes of the same order of magnitude (e.g. Condi and Wunsch, 2004). Errors of all daily tidal components average out almost completely in the monthly fields (Knudsen, 2003), because their alias frequencies are about one day. Based on the above results, further investigations should focus on the tidal de-aliasing. However apart from *S2*, which has the potential to introduce long periodic long wavelength aliasing pattern, perturbations from other tidal components with shorter alias frequencies can be reduced applying dedicated filters.

8.5 Regional Variability of GRACE Derived Bottom Pressure

Spacial patterns of time variable bottom pressure fluctuations are typically characterized by a clear zonal extension (e.g. Condi and Wunsch, 2004). However these patterns cannot be observed in the GRACE bottom pressure solutions.

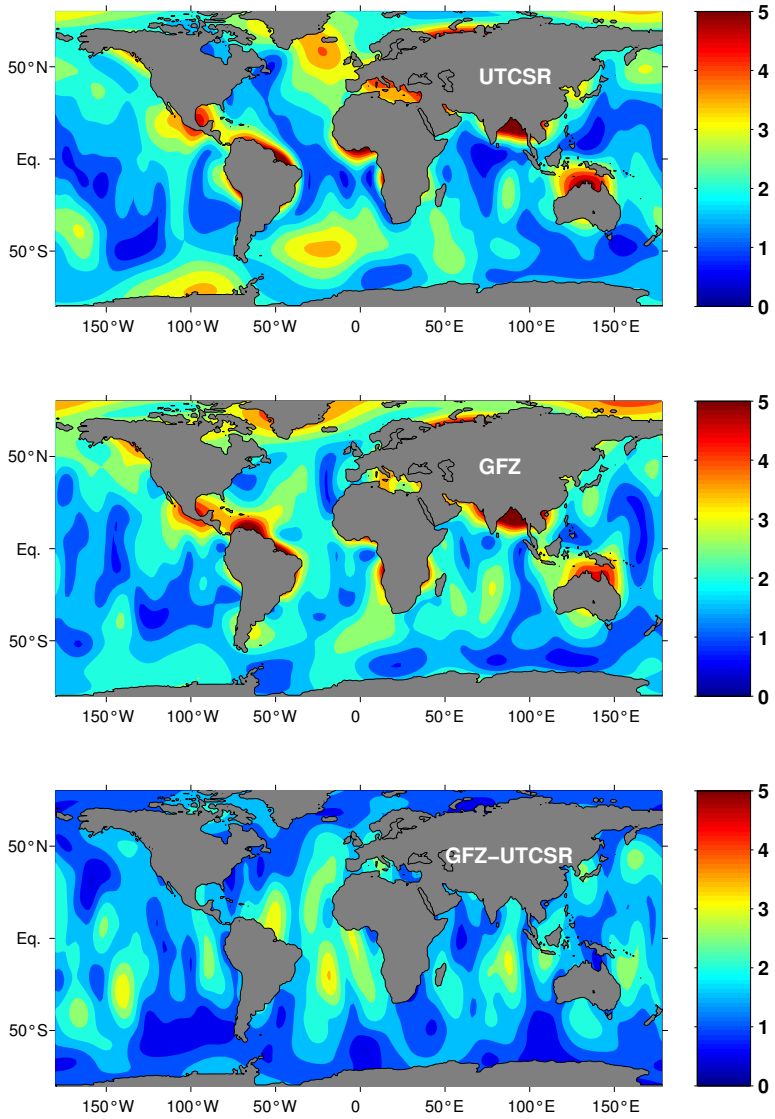

Figure 8.8: *Standard deviation of bottom pressure [mbar] from UTCSR (top) and GFZ (middle), based on 9 monthly solutions (see Appendix C). The standard deviation of the UTCSR-GFZ difference is displayed in the lower panel.*

Fig. 8.8 displays the standard deviation of bottom pressure computed from the 9 monthly solutions (see Table C.1) processed independently at UTCSR (upper panel) and GFZ (middle panel). Both products are based on the same GRACE satellite measurements and use similar processing and de-aliasing procedures. However, they differ in choice of the ocean tide model used for de-aliasing (see Appendix C). Data from both processing centers exhibit the same level of overall variability but differ much in detail. The most prominent feature in both cases is the leakage of the tropical continental hydrological cycle into the ocean at its boundaries between 20°N and 20°S. Zonally coherent patterns cannot be found in either product. Instead, GRACE bottom pressure seems rather to be dominated by meridionally coherent patterns, Additionally, on these time scales ocean models show a typical variability of about 1 mbar (e.g. Condi and Wunsch, 2004), which is only about half of what is seen in the GRACE derived fields.

In bottom pressure differences between UTCSR and GFZ solutions (Fig. 8.8, bottom panel) the leakage of the continental hydrological signal vanishes almost completely. This means that amplitudes as well as phases agree well between both products. Instead, the pattern of differences emphasizes the meridionally oriented characteristics. Based on the above discussion, one may interpret this as an aliasing pattern, introduced by tidal and non-tidal mis-modeling as well as measurement noise. Best agreement between the GFZ and UTCSR solutions is seen at high latitudes (e.g north of 60°N and south of 60°S), whereas largest deviations are observed at low latitudes. This corresponds to findings of V. Zlotniki (personnel communication). At the same time amplitudes of true bottom pressure fluctuations typically decrease towards lower latitudes (as a consequence of the nature of the geostrophic balance as well as the wind stress characteristics). Therefore it can be expected that the signal-to-noise ratio of GRACE derived bottom pressure is best at high latitudes.

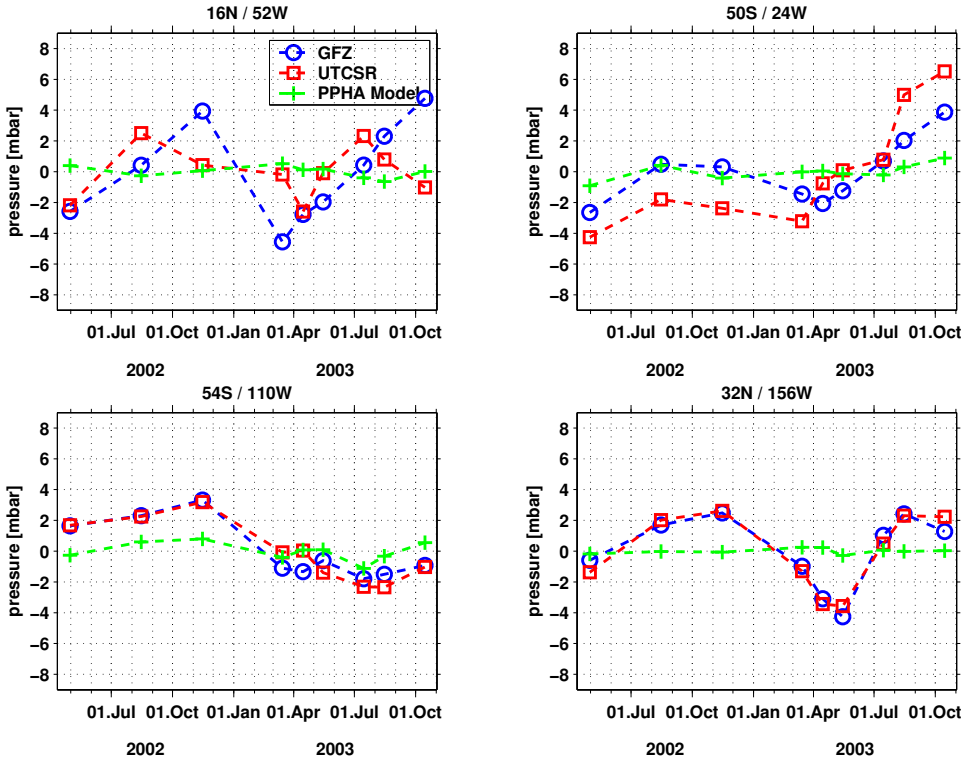

Figure 8.9: *Time series of bottom pressure fluctuations [mbar] at different locations in the world ocean derived from UTCSR and GFZ monthly solutions. For comparison, the modeled monthly mean contribution (from the PPHA model) is displayed for each location as well.*

Fig. 8.9 displays bottom pressure time series derived from GFZ (blue) and UTCSR (red) monthly solutions at four different globally distributed locations. The green lines yield the fraction of the signal simulated by the PPHA model. Near the ground truth site (top left) both gravity products differ in phase and amplitude, with the GFZ solution showing slightly larger variability. This is in agreement with the rather large differences seen at this location in the global comparison (Fig. 8.8, bottom). At a location in the South-Atlantic (top right), the UTCSR solution shows larger amplitudes. The phase compares well to that of GFZ, explaining why the GFZ-UTCSR differences (Fig. 8.8, bottom) do not display a local maximum at this location. At the two locations in the Pacific sector (bottom left and right) minimal differences between both products are observed, even though especially at the North-Pacific example, variability in the single time series is rather strong. Here phases and amplitudes match almost perfectly.

It is interesting to note, that all of the time series displayed in Fig. 8.9 are not dominated by noise on a monthly scale but display long-term fluctuations, which sometimes resemble an

annual cycle. The monthly contribution from the PPHA model is very small in all cases (less than 1 mbar). This means that the de-aliasing procedure does not work satisfactorily or that non-recoverable measurement noise dominates the monthly solutions.

One might wonder whether at this early stage of the mission GRACE derived bottom pressure fluctuations exhibit realistic patterns at all. Since at the time of writing the constrained (adjoint version of the) ECCO model did not cover the year 2003 yet, no direct comparison between the model and GRACE could be carried out. Therefore, its annual cycle over the North Atlantic from the three year period 2000 to 2002 has been extracted, applying a harmonic fit to the model. This region was chosen inspired by recent model studies of (Condi and Wunsch, 2004). They found large areas of coherent phases for the annual cycle in the North Atlantic and North Pacific. When averaging bottom pressure over the whole North Atlantic, we find a reasonable agreement

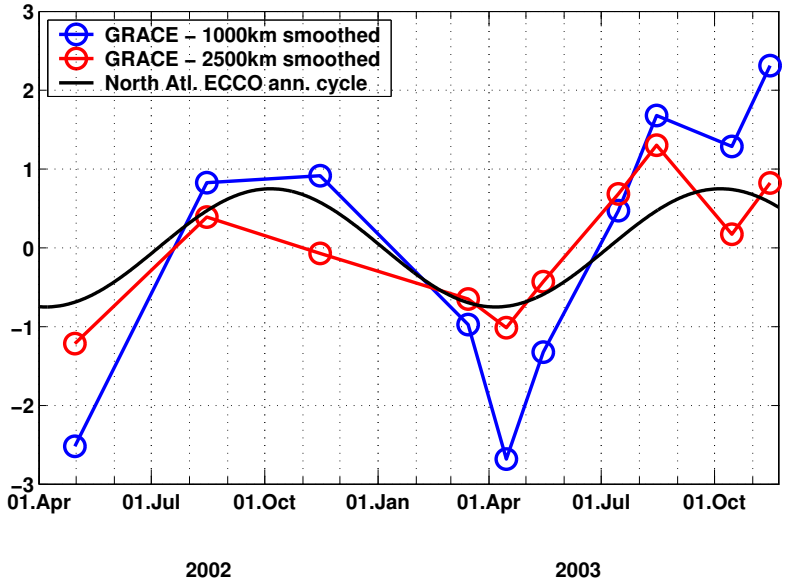

Figure 8.10: *Temporal evolution of GRACE bottom pressure averaged over the North Atlantic (10° to 65° N) based on monthly GFZ solutions using the standard 1000km (blue) as well as 2500 km Gaussian half-weight averaging scale for the spherical harmonic coefficients. The black line indicates the annual bottom pressure cycle averaged over the North Atlantic from the 1° x 1° ECCO model. To reduce possible leakage of the continental of the continental hydrological cycle into the ocean, only data from oceanic regions exhibiting more than 2000 m water depth were included.*

between the model annual cycle and the actual temporal evolution of the GRACE signal in terms of phase (Fig. 8.10). However, smoothing GRACE data with the standard Gaussian filter of 1000 km half width results in a significant overestimation of the amplitude. When applying a 2500 km filter instead, a much better correspondence in amplitude is obtained as well. Similar results have been found for the North Pacific (Wenzel et al., 2004). Thus, there is evidence for the usefulness of GRACE time varying bottom pressure signal, since the measurements seem to exhibit sensitivity to basin scale fluctuations. Interestingly similar correspondence in the South Atlantic cannot be established (not shown). This does not mean, that GRACE is doing wrong in that part of the ocean. It might as well be attributable to the ECCO model instead, with the phase of the annual cycle varying substantially within the South Atlantic (Fig. 9 of Condi and Wunsch, 2004), which might as well not be realistic.

8.6 Summary

The ability of GRACE to recover the extremely small time varying bottom pressure signals can be regarded as the largest challenge of the GRACE mission: Over the oceans the monthly geoid variability is much one order of magnitude smaller than over certain continental regions and large amplitude high-frequency tidal and non-tidal signals have to be corrected for. There are indications for substantial aliasing effects in the geoid solutions. In oder to suppress these, a Gaussian filter of 1000 km half-width has been applied to the spherical harmonic coefficients prior to the expansion. As could be shown from comparisons at the ground truth site, at this stage GRACE still largely overestimates the bottom pressure and external velocity variability. If not caused by basic instrumental problems, it is likely that the processing and de-aliasing has not been performed with sufficient accuracy so far.

From the validation carried out with in-situ measurements at the MOVE ground-truth site in the tropical West Atlantic, apparent deficiencies of the GRACE gravity fields and the models used for de-aliasing have been revealed. To remove problems at the high and low frequency limit, it would be desirable to replace the PPHA model used for non-tidal de-aliasing by a full (baroclinic plus barotropic) ocean general circulation model driven by atmospheric forcing field with a resolution better than 6 hours. At the same time ocean tide models (FES2002, CSR4.0) need improvements. From the comparisons at the ground-truth site alone no judgment can be made which of the two tide models comes closer to reality on a global scale. However both models show uncertainties of comparable magnitude at the ground-truth site.

The time variable bottom pressure derived from GFZ and UTCSR gravity field solutions display the same level of variability, but neither product is able to recover zonally coherent patterns, which are robust features of ocean models. Also, time series of GRACE derived bottom pressure do show long periodic characteristics rather than being dominated by monthly fluctuations (which is not evident from the in situ observations). An explanation for this fact is still lacking.

Finally, an encouraging result arises from comparing the annual bottom pressure cycle from the ECCO model with GRACE data: Both time series agree in amplitude and phase when the signal is averaged over the entire North Atlantic and a filter scale of 2500 km has been applied. Thus, GRACE might possess some skill in recovering the temporal variability on scales of some thousands of kilometers. A thorough study on the ability of GRACE to recover ocean dynamics should be carried out. Here spatial scales might be of importance as well. GRACE bottom pressure signals will likely be most useful at higher latitudes where the signal-to-noise ratio is largest.

Validation using in situ measurements will remain a key tool to assess the quality of GRACE fields. Although these observations will always lack a satisfactory spatial coverage, they are highly accurate and applicable over a broad range of periods, from hours to years. This, together with the fact that bottom pressure signals often tend to have large correlation scale, makes them invaluable.

Concluding, at this stage GRACE derived bottom pressures fluctuations cannot yet be used to constrain low frequency variability of external transports observed at the MOVE site. However advances in processing and de-aliasing of the GRACE solutions, for which there is a large window of opportunity, might make this possible in the near future.

9 Conclusions and Outlook

9.1 Conclusions

Results from a pilot experiment providing estimates of deep zonally integrated meridional geostrophic volume transport fluctuations from moored end point measurements in the tropical West-Atlantic have been assessed and the applicability of this monitoring approach to provide estimates of the evolution of the MOC across 16°N has been discussed.

Technical system performance It was shown from scaling arguments, high resolution models, as well as observations that this technique has the potential to serve as an efficient tool to determine transport fluctuations integrated over large horizontal scales. One main emphasize of this study lay on the performance of the different components of the moored array.

The methodology of how to achieve optimal results from the in situ calibration of the MicroCAT temperature and conductivity as well as the MTD pressure sensors has been described. It could be shown from calibration casts acquired during the five mooring service cruises that the moored sensors exhibit a high degree of accuracy and remarkable long-term stability. Errors in temperature, conductivity and pressure can be reduced to ± 0.002°C, ± 0.002 mS/cm and ± 3 dbar after the linear trend removal. Furthermore the depth assignment of the sensors has to be carried out with care, and might require the use of a mooring simulation program to estimate the mooring curvature during strong events. Finally the sensors' depth is known within $\pm$ 3 m. The ensemble of uncertainties translates into an error of not more than 1.5 Sv of internal NADW transports (relative to the sea floor). This estimate relates to instantaneous measurements on sub-inertial time scales, whereas the errors in the time mean transport should be even smaller.

A direct comparison of measurements from two different types of bottom pressure recorders has shown that bottom pressure fluctuations can be measured within $\pm$ 0.002 dbar on time scales shorter than the individual deployment period, which corresponds to uncertainty in external transport fluctuations of roughly $\pm$ 2 Sv. However the long-term drift removal procedure as well as the necessity the subtract the mean from every (quasi-annual) deployment period removes parts the true oceanic annual cycle and essentially eliminates variability on time scales longer than the individual data segments, as could be seen from model simulations. Among the solutions to overcome these problems are an extension of of duration of the deployment periods as well the use of data segments overlapping sufficiently long in time such that leveling of one record with respect to the next can be carried out. This might allow for a recovery of fluctuations on time scales longer than length of the individual deployments. On very long time scales the sensors' drift may be constrained by extracting the evolution of the ocean mass signal from a combination of dynamic height and altimeter measurements. The boundary triangle transports in the NADW/AABW range can be detected within $\pm$ 0.3 Sv from direct current meter measurements.

Thus, two of the three observational components of the MOVE design, namely the measurements of internal velocities and western boundary triangle velocities seem to exhibit robust estimates of transport fluctuations. Accuracies in internal transports might even be increased by increasing the vertical sampling rate (i.e., using a larger number of MicroCATs and MTD logger per

mooring). However modifications in the deployment and processing scheme are required to enhance the system's performance in detecting low-frequency external transport variability. This is especially important when designing such a system for an application at high latitudes. It should be added that the importance of external relative to internal transport fluctuations decreases towards longer periods, such that the present limitations in detecting lower frequency external transport fluctuations are likely to become less important in long-term monitoring applications.

Velocity and transport observations The vertical water mass distribution (within the AAIW / NADW / AABW range) appears to be closely related to the vertical velocity distribution, with strongest vertical shear being observed at the transitions between the water masses. Rather surprisingly, the two maxima of southward flow are not only observed in the western but also in the eastern part of the MOVE section. The principal patterns of variability in the internal velocity resemble that of quasi-geostrophic modes and therefore are assumed to reflect a physically meaningful rather than only statistical description of the time variable vertical velocity distribution which is consistent different classes of motions such as baroclinic Rossby waves or certain patterns of MOC fluctuations. The first 3 modes account for more than 95% of the variance. Whereas internal fluctuations are dominated by periods of several months, external velocities display a rather large degree of variability on weekly time scales. Direct current measurements within the DWBC are dominated by topographically steered southeastward flow with velocities peaking at 50 cm/s.

Rather large variability in the internal, the external and the directly measured western boundary triangle transports in the 1200-5000 dbar range have been observed, with r.m.s. amplitudes of 6.0, 8.4 and 3.4 Sv, respectively. Variability in boundary triangle and internal transports partly compensate each other such that r.m.s. amplitude of the sum of both contributions is 4.6 Sv. Its inter-annual variability amounts to 2.4 Sv. Thus, systematic errors in these observations are likely to be significantly smaller than this value, which confirms the above error estimates. Unfortunately, due to the limitations described above no statement can be made regarding inter-annual fluctuations of external transports.

Also, from the rather steady transitions from one data segment to the next, a high degree of consistency between records of internal transports from consecutive deployment periods has been demonstrated. The same applies for western boundary triangle and external transports. Spectral analysis has shown that the energy distribution of internal and external transports displays completely different characteristics. Internal transports are dominated by periods > 100 days, whereas large parts of the energy in the external ones are confined to periods < 20 days. The 180° out-of-phase relationship between internal transports observed in the east and west section in the 70 - 250 day band leads to a significant reduction of variance in this band when integrated across the whole section. This behavior is mainly attributable to baroclinic Rossby waves - as theoretical arguments, current meter measurements and model results suggest - dominated by wavelengths O(500 km). Since Rossby waves are to be considered noise in this experiment, which focuses on MOC variability, the strategy of applying a zonal integration scale of 1000 km leads to a clear increase in signal-to-noise ratio in this band. The fact that the spectrum of internal transports (integrated across whole section) continues to increase towards longer periods may also be taken as an indication that the experiment setup allows for the detection of inter-annual variability. Adding the boundary triangle contribution leads to a small but significant decrease in variance over a broad period range which is thought to reflect the meandering of the DWBC.

External transports integrated across the east section lead those in the west by 45°-90° in the 7-14 day band. It is suggested that these fast motions are attributable to barotropic Rossby waves associated with rather long wavelengths of O(3000 km), which is consistent with theoretical

arguments (dispersion relationship) as well as model results. Since in this case the wavelengths is larger than the zonal integration scale, no noise reduction can be reached in this band. However this is not a major problem, since MOC fluctuations on time scales of less than a month are not of particular interest. However it is interesting to note these large scale signals can be detected clearly by the bottom pressure sensors. The author takes this as an indication of the quality and the widespread range of applicability of these measurements.

It should also be noted that coherences between external and internal transports can be regarded insignificant over the whole frequency band displayed. Therefore it seems to be justifiable to treat both contributions separately with the external transports being associated with barotropic motions. The deep compensation of the seasonal cycle and of inter-annual variability of meridional surface Ekman flow across the MOVE section is expected to be of O(0.3 Sv). Thus, it cannot explain the inter-annual deep transport changes of 2.4 Sv observed by the MOVE array. It is presently unclear to which degree these changes are associated with the evolution of the MOC. This is even more true since inter-annual fluctuations in external transport, which might not be negligible compared to the internal ones, could not be observed. A much longer time series would be needed to allow for statistically significant statements. Finally it has been shown on several occasions, that for an interpretation of zonally integrated transport variability the integration scale has to be taken into account.

Absolute Transports Four techniques to derive absolute velocities from the geostrophic velocity fluctuations have been presented. A southward transport of 14.9 $\pm$ 3.0 Sv within the NADW layer can be considered the best estimate, derived by applying the MOVE/GAGE current meter measurements as constraints. However there are two caveats: Since the direct measurements do not resolve the scales of the flow completely, especially in the upper NADW range close to the western boundary as well as in the AABW range close to the Mid-Atlantic ridge, the referencing could only be applied over certain depth ranges which differ between the east and west section. Secondly, no current meter based referencing could be applied after the recovery of the GAGE array in April 2002.

The second approach, choosing the AAIW/NADW interface as a level of no motion gave an estimate of 16.0 $\pm$ 3.5 Sv of southward NADW transport for the 4 year period from February 2000 - February 2004 (including the 4.0 Sv from the boundary triangle transport). Thus, it agrees with the "best" estimate within the error bars, however, both estimates are not based on the same time interval. In general a level of no motion does not exist in the ocean. Nonetheless, when averaged over sufficiently long horizontal and time scales, it may be justified to associate this interface with a level of minimal net flow (provided that its depth does not change substantially in time). This puts strong limitations on the applicability of this technique.

Also, LADCP sections have been used as constraints. However due to the large uncertainties this reference option has been discarded. Two main problems occurred: Some of the individual profiles displayed unrealistically large velocity shear associated with the lower order (large vertical scale) baroclinic modes, which did not compare with the geostrophic velocity shear. This effect, which is supposedly due to the low signal-to-noise ratio in the LADCP measurements, made the referencing depend to a large degree on the depth range over which it was applied and thus turned out to be highly arbitrary. A second major problem is that of aliasing: The requirement to resolve the horizontal scales of the flow makes it necessary to use a horizontal spacing of the profiles of not more than 50 km. The corresponding time it takes to cover the 1000 km wide section is not sufficient to sample the spacial structure of the high-frequency barotropic signals. In the ACCP-3 experiment, where only a 80 km wide section had to be covered, LADCP measurements provided robust constraints on the estimation of absolute transports.

The referencing technique using RAFOS floats suffered mainly from two problems, namely from

the too low horizontal resolution (of 100 km) and from the fact that the floats departed rather quickly from the MOVE section (especially in the DWBC), which made this approach rather sensitive to the averaging interval and the interpolation procedure. Therefore this referencing option has been discarded as well. Doubling the number of floats and choosing much deeper target depth (below the upper core of the DWBC) might have reduced the uncertainties of this approach drastically.

From the referencing techniques reasonable estimates for the mean NADW transport in the western trough of the Atlantic have been found. Contributions from the eastern trough are presumably rather small, as model results suggest. On the other hand, since MOVE/GAGE current meter array is not available any longer and the use of LADCP as well as float data has shown to result in large uncertainties, the only option that remains for future applications is the level of no motion. In case that MOVE will be modified such that the zonal integration scale is extended far into the eastern trough (as suggest by the author), errors associated with this approach might reduce.

Design studies of MOC Monitoring Model simulations imply that the transport fluctuations detected by MOVE in the western trough of the Atlantic are moderately representative for the MOC signal at 16°N on longer than seasonal time scales. This simulation however relates to accurately working monitoring system. Since in the actual observations seasonal and lower frequency external transport fluctuations are not well represented the true representativeness for MOC fluctuations will be even less. The simulations also suggest that an eastward shift of the easternmost mooring towards the base of the Cap Verde Islands would most certainly lead to a strong increase in the representativeness of the detected signal for fluctuations of the MOC and of the MOC-related heat transport, allowing for robust estimates even on seasonal and shorter time scales. In this context it is worth mentioning that typical inter-annual MOC fluctuations of 2 Sv and less, as estimated by many ocean models, will be difficult to detect by any monitoring array, considering that the measurement errors are of about the same order of magnitude on these time scales. However, these systems are likely to exhibit some skill in detecting lower frequency MOC fluctuations.

But even if one would be able to detect MOC fluctuations at 16°N accurately, only at inter-decadal time scales these may be regarded representative for the whole Atlantic as model results suggest. Thus only at these time scales monitoring at one latitude would be sufficient to describe the MOC variability in the Atlantic. At inter-annual and shorter time scales wind forcing at well as the equatorial buffer mechanism appear to reduce the meridional scale of coherent signals, such that at least two monitoring lines should be operated simultaneously in the North Atlantic.

Also, the end point measurement approach is not particularly susceptible to distinct mechanisms responsible for MOC fluctuations. In order to distinguish between different contributions additional monitoring elements, specifically designed to detect these, have to be added. But even if such a system would be operated continuously, it might take longer than a century until a possible anthropogenic weakening of the MOC may be de-masked, since model results suggest that the MOC exhibits rather strong inter-decadal fluctuations. Nonetheless, natural MOC variability is of significant scientific interest as well, since its magnitude on different time scales is presently still unknown due to the lack of adequate observations and since there is a meridional heat transport signal associated with it.

Space-borne Bottom Pressure Measurements Assuming that over oceanic areas mass redistributions are confined entirely to the ocean and atmosphere, estimates of bottom pressure fluctuations can be derived from GRACE monthly averaged solutions of the Earth's time variable gravity field. This opens the opportunity to compute monthly changes in external velocities

from these measurements on a global scale. Over continents these signals may be interpreted mainly in terms of water storage.

Initial tests suggest that continental hydrological signals begin to emerge from the background noise, if expansions are limited to degree and order 20, whereas oceanic signals, which are typically about one order of magnitude smaller, are still masked by noise represented as patterns of meridional stripes, caused by the hard cut-off. Applying a Gaussian filter with 1000 km half-width, helps to reduce this effect significantly.

A comparison between GRACE derived bottom pressures (applying this filter scheme) with in-situ measurements clearly shows that GRACE largely overestimates the variability at the ground-truth site (MOVE) . This is also true for the external transport fluctuations, although to a somewhat smaller degree.

The validation using in situ bottom pressure observations reveals that the barotropic ocean model used for non-tidal de-aliasing exhibits deficiencies at the high and low frequency limit (i.e., for periods smaller than one day and larger than 2 weeks). Higher than 6-hourly resolved atmospheric forcing fields (which are currently not available) as well as the use of a full ocean GCM instead of a barotropic model might help to overcome these problems. Validation results also suggest that both models used for tidal de-aliasing still exhibit significant errors. Thus, there is a large window of opportunity for substantial improvements in the de-aliasing procedure.

Nevertheless GRACE measurements already seem to exhibit some realism in recovering the annual bottom pressure cycle when averaged of the entire North Atlantic (using a Gaussian filter of 2500 km half width). It is expected that the GRACE measurements display most skill in detecting bottom pressures fluctuations at higher latitude due to the more favorable signal-to-noise ratio.

9.2 Outlook

In order to assess whether the MOC effectively decreases due to the steady increase in greenhouse gas forcing, sustained monitoring activities are obviously needed. The recently deployed U.K. RAPID array at 26.5°N will represent a major contribution to the continuity of these efforts.

On the other hand, the future of MOVE is rather uncertain. The funding interval ends in 2005. However, a proposal for a second renewal has just been submitted. It includes the eastward extension of the array into the eastern trough of the Atlantic to increase the signal-to-noise ratio. If funded, the simultaneously operating MOVE and GRACE systems are likely to contribute much more to the understanding of MOC variability than any of these systems could possibly do without the other. A decomposition of MOC fluctuations into local and meridionally coherent signals may be feasible.

However, continuous monitoring activities may not be regarded the field of responsibility of universities and other research facilities. This means that after such systems have demonstrated skill in recovering MOC fluctuations, the technology should be passed over to national or international authorities to ensure sustained measurements.

Several advances in measurement technology may improve the performance of transport monitoring arrays. A new generation of PIES has been developed by R. Watts (URI), which exhibits an acoustic data telemetry option. Thus, the instruments may reside on the sea floor for several years - which is highly desirable to recover low-frequency fluctuations in external transports - and at the same time the data may be transferred to a research vessel at desired intervals.

To suppress the long-term instrumental drift in bottom pressure sensors, a new measurement method is envisioned (personnel communication C. Hughes, POL): The magnitude of the drift rate is dependent on the absolute pressure. However, in this application the knowledge of absolute pressure is not required. Therefore, the idea is to carry out relative pressure measurements, such that only pressure fluctuations are felt by the sensor. This should decrease the drift rates drastically. Like MOVE, the satellite gravity mission GRACE may also be regarded as a pilot project, whose accuracy presently is not sufficient to provide estimates of external transport fluctuations. However missions to succeed GRACE are already envisioned with improved measurement technology. In case the GOCE gravity mission, which is scheduled for launch in 2006, meets the expectations to provide a highly precise description of the Earth's geoid, the current technical problems of referencing geostrophic velocities may soon be reduced.

One advantage of horizontally integrated velocities in contrast to point measurements is that they can be directly compared with numerical model results. Thus, one might consider to apply them as constraints in assimilation efforts such as ECCO to improve ocean state estimates.

Despite of all these possible advances in observations and models, it should not be forgotten that even for a highly precise future monitoring system of the MOC it might take many decades to demonstrate the existence of a robust trend in the MOC related to global warming, due to the possible existence of natural multi-decadal variability. Therefore, besides MOC fluctuations other indicators for a sustained climate shift should be observed.

Bibliography

Adkins, J. F., E. A. Boyle, L. Keigwin, and E. Cortijo, 1997: Variability of the North Atlantic thermohaline circulation during last interglacial period. *Nature*, **390**, 154–155.

Ali, A. H. and V. Zlotnicki, 2003: Quality of wind stress fields measured by the skill of a barotropic ocean model: Importance of stability of the marine atmospheric boundary layer. *Geophysical Research Letters*, **30**(3), 1129,doi:10.1029/2002GL016058.

Apel, J., 1995: *Principles of Ocean Physics*. Academic Press.

Baehr, J., J. Hirschi, J.-O. Beisman, and J. Marotzke, 2004: Monitoring the meridional overturning circulation in the North Atlantic: a model-based design study. *Journal of Marine Research*, **62**, 283–312.

Barnier, B., L. Siefridt, and P. Marchesiello, 1995: Thermal forcing for a global ocean circulation model using a three-year climatology of ECMWF analysis. *Journal of Marine Systems*, **6**, 363–380.

Beckmann, A. and R. Döscher, 1997: A method for improved representation of dense water spreading over topography in geopotential-coordinate models. *Journal of Physical Oceanography*, **27**, 581–591.

Beismann, J.-O., C. Böning, and D. Stammer, 2002: Interannual to decadal variability of the meridional overturning circulation of the Atlantic: A comparison of the response to atmospheric fluctuations in three ocean models. *Clivar Exchanges*, **7**, 34.

Berteaux, H., 1976: *Buoy Engineering*. John Wiley & Sons.

Böning, C., F. Bryan, W. Holland, and R. Döscher, 1996: Deep-water formation and meridional overturning in a high resolution model of the North Atlantic. *Journal of Physical Oceanography*, **26**, 1142–1164.

Böning, C. and A. Semtner, 2001: *High-resolution modelling of the thermohaline and wind-driven circulation. In: Ocean Circulation and Climate*. Academic Press.

Bower, A. and H. Hunt, 2000: Lagrangian observations in the Deep Western Boundary Current in the North Atlantic Ocean. Part I: Large-scale pathways and spreading rates. *Journal of Physical Oceanography*, **30**, 764–783.

Bryden, H. and S. Imawaki, 2001: *Ocean Heat Transport. In: Ocean Circulation and Climate*. Academic Press.

CERSAT, 2002: Quickscat scatterometer mean wind field product user manual. *CESAT / IFREMER technical report: Reference C2-MUT-W-03-IF*.

Chelton, D., R. deSzoeke, M. Schlax, K. El Naggar, and N. Siwertz, 1998: Geographical variability of the first baroclinic Rossby radius of deformation. *Journal of Physical Oceanography*, **28**, 433–460.

Chen, J., R. Wilson, and D. Chambers, 1998: Seasonal global water mass balance and mean sea-level variations. *Geophysical Research Letters*, **25**, 3555–3558.

Condi, F. and C. Wunsch, 2004: Measuring gravity field variability, the geoid, ocean bottom pressure fluctuations, and their dynamical implications. *Journal of Geophysical Research*, **109**, doi:10.1029/2002JC001727.

Curry, R. G., B. Dickson, and I. Yashyaev, 2003: A change in the freshwater balance of the Atlantic Ocean over the past four decades. *Nature*, **426**, 826–829.

Curry, R. G., M. S. McCartney, and T. M. Joyce, 1998: Oceanic transports of subpolar climate signals to mid-depth subtropical waters. *Nature*, **391**, 575–577.

Cushman-Roisin, B., 1994: *Introduction to Geophysical Fluid Dynamics*. Prentice Hall.

Davis, R. and W. Zenk, 2001: *Subsurface Lagrangian observations in the 1990's. In:Ocean Circulation and Climate*. Acadamic Press.

Defant, A., 1941: Quantitative Untersuchungen zur Statik und Dynamik des Atlanitschen Ozeans. Die absolute Topographie des des physikalischen Meeresniveaus und der Druckflächen sowie die Wasserbewegungen im Raum des Atlantischen Ozeans. *Wissenschaftliche Ergebnisse der Deutschen Atlantischen Expedition auf dem Forschungs- und Vermessungsschiff METEOR 1925-1927*, **6**, 191–260.

Delworth, T., S. Manabe, and R. J. Stouffer, 1993: Interdecadal variations of the thermohaline circulation in a coupled ocean-atmosphere model. *Journal of Climate*, **6**, 1993–2011.

Dickey, J., 1993: Atmospheric exitation of the earth's rotation: Progress and prospects via space geodesy. *Contibutions to Space Geodesy and Geodynamics: Earth Dynamics and Geodynamics*, **24**, 55–70.

Dickson, B., I. Yashyayev, J. Meincke, B. Turrell, and S. Dye, 2002: Rapid freshening of the deep North Atlantic Ocean over the past four decades. *Nature*, **416**, 832–837.

Döll, P. and B. Lehner, 2003: A global hydrological model for deriving water availability indicators: model tuning and validation. *Journal of Hydrology*, **270**, 105–134.

Dong, B.-W. and R. T. Sutton, 2001: The dominant mechanisms of variability in the Atlantic Ocean heat transport in a coupled ocean-atmosphere GCM. *Geophysical Research Letters*, **28**, 2445–2448.

Dong, B.-W. and R. T. Sutton, 2002: Adjustment of the coupled ocean atmosphere system to a sudden change in the thermohaline circulation. *Geophysical Research Letters*, **29**, 18.

Döös, K. and Webb, D.J., 1994: The Deacon Cell and other meridional cells of the Southern Ocean. *Journal of Physical Oceanography*, **24**, 429–442.

Döscher, R., C. Böning, and P. Herrmann, 1994: Response of circulation and heat transport in the North Atlantic to changes in the thermohaline circulation in northern latitudes: A model study. *Journal of Physical Oceanography*, **24**, 2306–2320.

Eanes, P., 2002: The CSR 4.0 global ocean tide model. *ftp://www.csr.utexas.edu/pub/tide*.

Eden, C. and J. Willebrand, 2001: Mechanism of interannual to decadal variability of the North Atlantic circulation. *Journal of Climate*, **14**, 2266–2280.

Egbert, G. and R. Ray, 2003a: Semi-diurnal and diurnal tidal dissipation from TOPEX/Poseidon altimetry. *Geophysical Research Letters*, **30**, 1907.

Egbert, G. and R. D. Ray, 2003b: Deviation of longperiod tides from equilibrium: Kinematics and geostrophy. *Journal of Physical Oceanography*, **33**, 822–839.

Emery, W., W. Lee, and L. Magaad, 1984: Geographic and seasonal distribution of BV Frequency and Rossby Radii in the North Pacific and North Atlantic. *Journal of Physical Oceanography*, **14**, 294–317.

Emery, W. and R. Thomson, 1998: *Data Analysis Methods in Physical Oceanography*. Elsevier.

Eubanks, T., 1993: Variations of the orientation of the Earth. *Contibutions to Space Geodesy and Geodynamics: Earth Dynamics and Geodynamics*, **24**, 1–54.

Farrell, W., 1972: Deformation of the Earth by surface loads. *Reviews of Geophysics*, **10**, 761–797.

Fidler, J., 2003: *Mechanismen der interannualen Variabilität im westlichen Randstromsystem des subtropischen Nordatlantiks – Diplomarbeit*. Institut für Meereskunde, Kiel.

Filloux, J. H., 1980: Pressure fluctuations on the open ocean floor over a broad frequency range: New program and early results. *Journal of Physical Oceanography*, **12**, 1959–1971.

Fine, R. N. and R. L. Molinari, 1988: A continuous deep western boundary current between Abaco (26.5°N) and Barbados (13°N). *Deep Sea Research*, **35**, 1441–1450.

Fischer, J. and F. Schott, 1997: Seasonal transport variability of the deep western boundary current in the equatorial Atlantic. *Journal of Geophysical Research*, **102**, 27751–27769.

Flechtner, F., 2003: AOD1B product description document. *GRACE Product Documentation JPL*, pp. 1–33.

Fu, L., 2001: *Ocean circulation and variability from satellite altimetry. In: Ocean Circulation and Climate*. Academic Press.

Fu, L. L. and G. Pihos, 1994: Determining the response of sea level to atmospheric pressure forcing using TOPEX/POSEIDON data. *Journal of Geophysical Research*, **99**, 24633–24642.

Ganachaud, A. and C. Wunsch, 2000: Improved estimates of global ocean circulation, heat transport and mixing from hydrographic data. *Nature*, **408**, 453–456.

Ganopolski, A. and S. Rahmsdorf, 2001: Rapid changes of glacial climate simulated in a coupled climate model. *Nature*, **409**, 153–158.

Ganopolski, A., S. Rahmsdorf, V. Petoukhov, and M. Claussen, 1998: Simulation of modern and glacial climates with a coupled global model of intermediate complexity. *Nature*, **391**, 351–356.

Gaspar, P. and R. Ponte, 1997: Relation between sea level and barometric pressure determined from altimeter data and model simulations. *Journal of Geophysical Research*, **102**, 961–971.

Gent, P., 2001: Will the North Atlantic Ocean thermohaline circulation weaken during the 21st century? *Geophsical Research Letters*, **28**, 1023–1026.

Gent, P. and J. McWilliams, 1990: Isopycnal mixing in ocean circulation models. *Journal of Physical Oceanography*, **20**, 150–155.

Glicksen, D. A., D. M. Fratantoni, C. M. Wooding, and P. L. Richardsen, 2000: North Brazil current rings experiment: Surface drifter data report november 1988 - june 2000. *Woods Hole Institution Technical Report*, **10**, 1–121.

Gnanadesikan, A., 1999: A simple predictive model for the structure of the oceanic pycnocline. *Science*, **283**, 2077–2079.

Goosse, H. and T. Fichefet, 1999: Importance of ice-ocean interactions for the global ocean circulation: a model study. *Journal of Geophsical Research*, **104**, 23337–23355.

Greatbatch, R. and J. Lu, 2003: Reconciling the Stommel box model with the Stommel-Aarons model: A possible role for southern hemisphere wind forcing. *Journal of Physical Oceanography*, **33**, 1618–1632.

GRIP, 1993: Climate instability during the last interglacial period in the GRIP ice core. *Nature*, **364**, 203–207.

Häkkinen, S. and P. Rhines, 2004: Decline of subpolar North Atlantic circulation during the 1990s. *Science*, **304**, 555–559.

Han, S.-C., C. Jekeli, and C. Shum, 2004: Time-variable aliasing effect of ocean tides, atmosphere and continental water mass on monthly mean GRACE gravity field. *Journal of Geophysical Research*, **109**, B04403,doi:10.1029/2003JB002501.

Haney, R., 1971: Surface thermal boundary condition for ocean circulation models. *Journal of Physical Oceanography*, **1**, 79–93.

Helmbrecht, L., 2001: *Entwicklung einer Verankerungssimulation als Designhilfe und zur Verbesserung der Datenanalyse – Diplomarbeit*. Institut für Meereskunde, Kiel.

Hirschi, J., J. Baehr, and J. Marotzke, 2003: A monitoring design for the Atlantic meridional overturning circulation. *Geophysical Research Letters*, **30**.

Hogg, N., 2001: *Quantification of the deep circulation. In: Siedler G, Church, J and Gould, J (eds) Ocean Circulation and Climate*. Academic Press.

Huang, X., 1999: Mixing and energetics of the thermohaline circulation. *Journal of Physical Oceanography*, **29**, 727–746.

Hughes, C. W. and M. J. Smithson, 1996: Bottom pressure correlations in the South Atlantic. *Geophysical Research Letters*, **23**(17), 2243–2246.

IPCC, 2001: *Climate Change 2001: The scientific basis. Contributions of Working Group I to the Third Assessment Report of the Intergovernmental Panel on Climate Change*. Cambridge University Press.

Jayne, S. R. and J. Marotzke, 1999: A destabilizing thermohaline circulation-atmosphere-sea ice feedback. *Journal of Climate*, **12**, 642–651.

Jayne, S. R. and J. Marotzke, 2001: The dynamics of ocean heat transport variability. *Reviews of Geophysics*, **39**, 385–411.

Jekeli, C., 1981: *Alternative methods to smooth the Earth's gravity field*, volume 327. Ohio State University Press, Columbus.

Johns, W., D. Fratantoni, and R. Zantopp, 1993: Deep western boundary current variability off northwestern Brazil. *Deep Sea Research I*, **40**, 293–310.

Johns, W. E., T. Kanzow, and R. Zantopp, 2004: Estimating ocean transports with dynamic height moorings: An application in the Atlantic deep western boundary current. *submitted to Deep Sea Research*.

Johnson, H. L. and D. P. Marshall, 2002: A theory for the surface Atlantic response to thermohaline variability. *Journal of Physical Oceanography*, **32**, 1121–1132.

Johnson, H. L. and D. P. Marshall, 2004: Global teleconnections of meridional overturning circulation anomalies. *Journal of Physical Oceanography*, **34**, 1702–1722.

Johnson, S. J., H. B. Clause, W. Dansgaard, K. Fuhrer, N. Gundestrup, C. H. Hammer, P. Iversen, J. Jouzel, B. Stauffer, and J. P. Steffensen, 1992: Irregular glacial interstadial recorded in a new greenland ice core. *Nature*, **311**, 311–313.

Kalnay, E. and et al, 1996: The NCEP/NCAR40-year re-analysis project. *Bull. Amer. Meteor. Soc.*, **17**, 437–471.

Kanzow, T., 2000: *Integrale Erfassung langperiodischer Transporte: Simulation und Optimierung eines verankerten Systems – Diplomarbeit*. Institut für Meereskunde, Kiel.

Kawase, M., 1987: Establishment of deep ocean circulation driven by deep-water production. *Journal of Physical Oceanography*, **17**, 2294–2317.

Kessler, W. and J. McCreary, 1993: The annual wind-driven Rossby wave in the subthermocline equatorial pacific. *Journal of Physical Oceanography*, **23**, 1192–1207.

Kieke, D., M. Rhein, L. Stramma, W. Smethie, D. Lebel, and W. Zenk, submitted in 2004: Changes in the CFC inventories and formation rates of Upper Labrador Sea Water, 1997-2001. *Journal of Physical Oceanography, submitted*.

Klein, B., R. Molinari, T. Müller, and G. Siedler, 1995: A transatlantic section at 14.5°N: Meridional volume and heat fluxes. *Journal of Marine Research*, **53**, 929–957.

Knudsen, P., 2003: Ocean tides in the GRACE monthly averaged fields. *Space Science Reviews*, **108**, 261–270.

Koltermann, T., A. V. Sokov, V. P. Tereschenkov, S. A. Dobroliubov, K. Lorbacher, and A. Sy, 1999: Decadal changes in the thermohaline circulation of the North Atlantic. *Deep Sea Research Part II*, **46**, 109–138.

Kraus, E. and J. Turner, 1967: A one-dimensional model of the seasonal thermocline I. A laboratory experiment and its interpretation. *Tellus*, **19**, 88–97.

Lankhorst, M., 2003: *Klassifizierung charakteristischer Eigenschaften von Float-Trajektorien in unterschiedlichen dynamischen Regionen – Diplomarbeit*. Institut für Meereskunde, Kiel.

Large, W., J. McWilliams, and S. Doney, 1994: Oceanic vertical mixing: A review and a model with nonlocal boundary layer parameterization. *Reviews of Geophysics*, **32**, 363–403.

Larsen, J. and T. Sanfort, 1985: Florida Current volume transports from voltage measurements. *Science*, **227**, 302–304.

Latif, M., E. Roeckner, M. Botzet, M. Esch, S. Haagemann, J. Jungclaus, S. Legutke, S. Marsland, U. Mikolajewicz, and J. Mitchell, 2004: Reconstructing, monitoring and predicting decadal-scale changes in the north atlantic thermohaline with sea surface temperature. *Journal of Climate*, **17**, 1605–1614.

Latif, M., E. Roeckner, U. Mikolajewicz, and R. Voss, 2000: Tropical stabilization of the thermohaline circulation in a greenhouse warming scenario. *Journal of Climate*, **13**, 1809–1813.

Lee, T. N., W. E. Johns, R. J. Zantopp, and E. R. Fillenbaum, 1996: Moored observations of western boundary current variability and thermohaline circulation at 26.5 °N in the subtropical North Atlantic. *Journal of Physical Oceanography*, **26**, 962–983.

LeProvost, C., 2002: Fes2002- A new version of the FES tidal solution series. *Abstract volume of: Jason-1 Science Working Team Meeting, Biarritz, France*.

Levitus, S. and T. Boyer, 1994: Temperature: Volume4. World Ocean Atlas 1994, noaa atlas nesdis. *U.S. Dep. of Comm., Washington, D.C.*.

Lohmann, K., 1999: *Gezeitenkorrektur von schiffsgestützten Strömungsmessungen – Diplomarbeit*. Institut für Meereskunde.

Luther, D. S. and A. D. Chave, 1993: Observing integrating variables in the ocean. *Proc. 7th 'Aha Huliko'a Hawaiian Winter Workshop on Statistical Methods in Physical Oceanography*, **26**, 103–128.

Lux, M., H. Mercier, and M. Arhan, 2001: Interhemispheric exchange of mass and heat in the Atlantic ocean in January - March 1993. *Deep Sea Research*, **48**, 605–638.

Manabe, S. and R. J. Stouffer, 1994: Multiple century response of a coupled ocean-atmosphere model to an increase of atmospheric carbon dioxide. *Journal of Climate*, **7**, 5–23.

Marotzke, J., 1996: *Thermohaline Feedbacks. In: Anderson DLT, Willebrand J (eds) Decadal Climate Variability and Predictibility. NATO advanced Science Institutes Series I: Global Environmental Change 44*. Springer-Verlag.

Marotzke, J., R. Giering, Q. Zhang, D. Stammer, C. Hill, and T. Lee, 1999: Construction of the adjoint MIT ocean general circulation model and application to Atlantic heat transport sensitivity. *Journal of Geophysical Research*, **104**, 29529–29548.

Marotzke, J. and J. Scott, 1999: Convective mixing and the thermohaline circulation. *Journal of Physical Oceanography*, **29**, 2962–2970.

Marshall, J., A. Adcroft, C. Hill, and C. Heisey, 1997: A finite-volume, incompressible Navier-Stokes model for studies of the ocean on parallel computers. *J. Geophys.*, pp. 5753–5766.

Mauritzen, C., K. L. Polzin, M. S. McCartney, R. C. Millard, and D. E. West-Mack, 2002: Evidence in hydrography and density fine structure for enhanced vertical mixing over the Mid-Atlantic Ridge in the western Atlantic. *Journal of Geophysical Research*, **107**(10), 11 1–19.

McCartney, M., 1993: Crossing of the equator by the deep western boundary current in the Western Atlantic Ocean. *Journal of Physical Oceanography*, **23**, 1953–1974.

Meinen, C. S. and D. R. Watts, 1998: Calibrating inverted echosounders equipped with pressure sensors. *Journal of Atmospheric and Oceanic Technology*, **15**, 1339–1345.

Meredith, M. P., J. M. Vassie, K. J. Heywood, and R. Spencer, 1996: On the temporal variability of the transport through Drake Passage. *Journal of Geophysical Research*, **110**, 22485–22494.

Molinari, R. L., R. A. Fine, D. W. Wilson, R. G. Curry, J. Abell, and M. S. McCartney, 1998: The arrival of recently formed Labrador Sea Water in the deep western boundary current at 26.5°N. *Geopysical Research Letters*, **25**(13), 2249–2252.

Müller, T. and G. Siedler, 1992: Multi-year current time series in the North Atlantic Ocean. *Journal of Marine Research*, **50**, 63–98.

Munk, W., 1966: Abyssal recipes. *Deep-Sea Research*, **13**, 707–730.

Munk, W. and C. Wunsch, 1966: Abyssal recipes II. *Deep-Sea Research*, **45**, 1977–2010.

Opsteegh, J., R. Haarsma, F. Selten, and A. Kattenberg, 1998: Ecbilt: A dynamic alternative to mixed boundary conditions in ocean models. *Tellus*, **50**, 348–367.

Osborn, T., 1980: Estimates of the local rate of diffusion from dissipation measurements. *Journal of Physical Oceanography*, **10**, 83–89.

Pacanowski, R., 1995: MOM 2 documentation, user's guide and reference manual. *GFDL Ocean Group Technical Report*, **3**.

Paparella, F. and W. Young, 2002: Horizontal convection is non-turbulent. *Journal of Fluid Mechanics*, **466**, 205–214.

Parke, M., R. H. Steward, D. Farless, and D. Cartwright, 1987: On the choice of orbits for an altimetric satellite to study ocean circulation and tides. *Journal of Geophysical Research*, **92**, 1693–1707.

Pasquero, C. and E. Tziperman, 2004: Effects of a wind-driven gyre on thermohaline circulation variability. *Journal of Physical Oceanography*, **34**, 805–816.

Paul, A. and M. Schulz, 2002: *Holocene Climate Variability on Centennial-to-Millennial Time Scales: 2. Internal and Forced Oscillations as Possible Causes. In: Climate Development and History of the North Atlantic Realm*. Springer-Verlag.

Pawlowicz, R., B. Beardsley, and S. Lentz, 2002: Harmonic analysis including error estimates in MATLAB using T_TIDE. *Computers and Geosciences*, **28**, 929–937.

Pedlosky, J., 1979: *Geophysical fluid dynamics*. Springer-Verlag.

Pickard, R. and W. Smethie, 1998: Temperal evolution of the Deep Western Boundary Current where it enters it the sub-tropical domain. *Deep-Sea Research*, **45**, 1053–1083.

Polzin, K. L., J. M. Toole, J. R. Ledwell, and R. W. Schmitt, 1997: Spacial variability of turbulent mixing in the abyssal ocean. *Journal of Physical Oceanography*, **276**, 93–96.

Pond, S. and G. L. Pickard, 1978: *Introductory Dynamic Oceanography*. Pergamon Press.

Ponte, R. M. and P. Gaspar, 1994: Regional analysis of the inverted barometer effect over the global ocean using TOPEX/POSEIDON data and model results. *Journal of Physical Oceanography*, **24**, 1966–1977.

Ponte, R. M. and R. Ray, 2002: Atmospheric pressure correction in geodesy and oceanography: A strategy of handling tides. *Geophysical Research Letters*, **29**, 2153, doi: 10.1029GL016340.

Ponte, R. M. and R. D. Rosen, 1994: Oceanic angular momentum and torques in a general circulation model. *Journal of Physical Oceanography*, **24**, 1966–1977.

Prange, M., G. Lohmann, V. Romanova, and M. Butzin, 2004: Modelling tempo-spatial signatures of Heinrich events: influence of the climatic background state. *Quaternary Science Reviews*, **23**, 521–527.

Rahmstorf, S., 1996: On the freshwater forcing and transport of the Atlantic thermohaline circulation. *Climate Dynamics*, **8**, 799–811.

Rahmstorf, S. and J. Willebrand, 1995: The role of temperature feedback in stabilizing the thermohaline circulation. *Journal of Physical Oceanography*, **25**, 787–805.

Reigber, C., R. Schmidt, F. Flechtner, R. König, U. Meyer, K.-H. Neumayer, P. Schwintzer, and S. Zhu, 2004: An Earth gravity field model complete to degree and order 150 from GRACE: EIGEN-GRACE02S. *submitted to Journal of Geodynamics*.

Rhein, M., L. Stramma, and U. Send, 1995: The Atlantic deep western boundary current: Water masses and transports near the equator. *Journal of Geophysical Research*, **100**, 2441–2457.

Rhein, M., M. Walter, C. Mertens, R. Steinfeld, and D. Kieke, 2004: The circulation of North Atlantic Deep Water at 16°N, 2000-2003. *submitted to Geophysical Research Letters*.

Rossby, T., 1969: On monitoring depth variations of the main thermocline acoustically. *Journal of Geophysical Research*, **74**, 5542–5546.

Sandström, J., 1908: Dynamische Versuche mit Meerwasser. *Ann. Hydrogr. Martimen Meteorol.*, **36**, 6–23.

Saunders, P. M., K.-H. Mahrt, and R. T. Williams, 1991: Standards and laboratory calibration. *WHP Operations and Methods*, pp. 1–11.

Schmidt, H., 2004: *Anwendung von Satellitenaltimetrie zur Verbessung von integralen in situ Transportmessungen – Diplomarbeit*. Institut für Meereskunde.

Schmidt, R., P. Schwinzer, F. Flechtner, C. Reigber, A. Güntner, P. Döll, G. Ramillien, A. Cazenave, S. Petrovic, H. Jochmann, and J. Wünsch, 2004: GRACE observations of changes in continental water storage. *submitted to Global and Planetary Change*.

Schmitz, W., 1995: On the interbasin-scale thermohaline circulation. *Reviews of Geophysics*, **33**, 151–173.

Schott, F., J. Fischer, J. Reppin, and U. Send, 1993: On the mean and seasonal currents and transports at the western boundary of the equatorial Atlantic. *Journal of Geophysical Research*, **98**, 14353–14368.

Schott, F., J. McCreary, and G. Johnson, 2004a: *Shallow overturning circulations of the tropical-subtropical oceans*. American Geophysical Union , (in press).

Schott, F., R. Zantopp, L. Stramma, M. Dengler, J. Fischer, and M. Wibaux, 2004b: Circulation and deep-water export at the western exit of the subpolar North Atlantic. *Journal of Physical Oceanography*, **34**, 817–843.

SeaBird-Electronics, 2002: Compressibility compensation of sea-bird conductivity sensors. *Application Note*, **10**, 1–2.

Send, U., T. Kanzow, W. Zenk, and M. Rhein, 2002: Monitoring the Atlantic meridional overturning circulation at 16°N. *CLIVAR exchanges*, **7**, 1–4.

Smith, S. D., 1998: Coefficients for sea surface wind stress, heat flux and wind profiles as a function of wind speed and temperature. *Journal of Geophysical Research*, **93**, 15467–15472.

Song, Y. T. and V. Zlotniki, 2004: Ocean bottom pressure waves predicted in the tropical Pacific. *Geophysical Research Letters*, **31**, L05306,doi:10.1029/2003GL018980.

Stammer, D., C. Wunsch, R. Giering, C. Eckert, P. Heimbach, J. Marotzke, A. Adcroft, C. N. Hill, and J. Marshall, 2002: The global ocean circulation 1992-1997, estimated from ocean observations and a general circulation model. *Journal of Geophysical Research*, **107**, doi:10.1029/2001JC000888.

Stammer, D., C. Wunsch, R. Giering, C. Eckert, P. Heimbach, J. Marotzke, A. Adcroft, C. N. Hill, and J. Marshall, 2003: Volume, heat and freshwater transports of the global ocean circulation 1993-2000, estimated from a general circulation model constrained by World Ocean Circulation Experiment (WOCE) data. *Journal of Geophysical Research*, **108**, doi:10.1029/2001JC001115.

Stammer, D., C. Wunsch, and R. Ponte, 2000: De-aliasing of global high frequency barotropic motions in altimeter observations. *Geophysical Research Letters*, **27**, 1175–1178.

Steinfeldt, R. and M. Rhein, 2004: Spreading velocities and dilution of North Atlantic Deep Water in the tropical Atlantic based on CFC time series. *Journal of Geophysical Research*, **109**, C03046.

Stevens, D., 1990: On open boundary conditions for three dimensional primitive equation ocean circulation models. *Geophysical and Astrophysical Fluid Dynamics*, **51**, 103–133.

Stommel, H., 1961: Thermohaline convection with two stable regimes. *Tellus*, **13**, 224–230.

Stommel, H. and A. B. Aarons, 1960: On the abyssal circulation of the world ocean: 1. Stationary planetary flow patterns on a sphere. *Deep Sea Research*, **6**, 140–154.

Straub, D., 1996: An inconsistency between two classical models of the ocean buoyancy driven circulation. *Tellus*, **48**, 477–481.

Tapley, B. and C. Reigber, 2001: The GRACE mission: Status and future plans. *EOS Trans. AGU*, **82**(47), Abstract G41C–02.

Thomson, D. J., 1982: Spectral estimation and harmonic analysis. *Proc. IEEE*, **70**, 1055–1096.

Thorpe, R., J. Gregory, T. Johns, R. Woods, and J. Mitchell, 2001: Mechanisms determining the Atlantic thermohaline circulation response to greenhouse gas forcing in a non-flux-adjusted climate model. *Journal of Climate*, **14**, 3102–3116.

Tierney, C., J. Wahr, F. Bryan, and V. Zlotnicki, 2000: Short-period oceanic circulation: implications for satellite altimetry. *Geophys. Res. Lett.*, **27**, 1255–1258.

Toggweiler, J. and B. Samuels, 1995: Effect of Drake Passage on the global thermohaline circulation. *Deep-Sea Research*, **42**, 477–500.

Toggweiler, J. and B. Samuels, 1998: On the ocean's large scale circulation in the limit of no vertical mixing. *Journal of Physical Oceanography*, **28**, 1832–1852.

Trenberth, K. and J. Caron, 2001: Estimates of meridional atmosphere and ocean heat transports. *Journal of Climate*, **14**, 3433–3443.

Tziperman, E., 2000: Proximity of the present-day thermohaline circulation to an instability threshold. *Journal of Physical Oceanography*, **30**, 90–104.

Vellinga, M. and R. Wood, 2002: Global climatic impacts of a collapse of the Atlantic thermohaline circulation. *Climatic Change*, **54**, 251–267.

Visbeck, M., 2002: Deep velocity profiling using lowered acoustic doppler current profiler: Bottom track and inverse solutions. *Journal of Atmospheric and Oceanic Technology*, **19**, 794–807.

Wahr, J., S. Jayne, and F. Bryan, 2002: A method of inferring changes in deep ocean currents from satellite measurements of time-variable gravity. *Journal of Geophysical Research*, **107**, 3218,doi:10.1029/2001JC001274.

Wahr, J., M. Molenaar, and F. Bryan, 1998: Time variability of the earth's gravity field: Hydrological and oceanic effects and their possible detection using GRACE. *Journal of Geophysical Research*, **103**, 30205–30229.

Wahr, J., S. Swenson, V. Zlotniki, and I. Velicogna, 2004: Time variable gravity from GRACE. *Geophysical Research Letters*, **31**, L11501, doi:10.1029/2004GL019779.

Wallace, J. and D. Gutzler, 1981: Teleconnections in the geopotential height field during the Northern Hemisphere Winter. *Monthly Weather Review*, **109**, 784–812.

Watts, D. and H. Rossby, 1977: Measuring dynamic heights with inverted echo sounders: results from mode. *Journal of Physical Oceanography*, **7**, 345–358.

Watts, D. R. and H. Kontoyiannis, 1990: Deep-ocean bottom pressure measurement: Drift removal and performance. *Journal of Atmospheric and Oceanic Technology*, **7**, 296–306.

Weaver, A. J., J. Marotzke, P. F. Cummins, and E. Sarachik, 1993: Stability and variability of the thermohaline circulation. *Journal of Physical Oceanogaphy*, **23**, 39–60.

Webb, D. and N. Suginohara, 2001a: *The interior circulation of the ocean. In: Ocean Circulation and Climate*. Academic Press.

Webb, D. and N. Suginohara, 2001b: Vertical mixing in the ocean. *Nature*, **409**, 37.

Wenzel, M., F. Flechtner, R. Schmidt, C. Reigber, V. Seufer, B. Fritsch, and J. Schröter, 2004: Verification of an ocean general circulation model with time varying GRACE geoid data. *Poster presented at the Joint Champ/Grace Science Meeting, Potsdam, July 6-8*.

Whitworth, T., 1983: Monitoring the transport of the Antarctic circumpolar current at Drake Passage. *Journal of Physical Oceanography*, **13**, 2045–2057.

Whitworth, T. and R. G. Peterson, 1985: The volume transport of the Antarctic circumpolar current from bottom pressure measurements. *Journal of Physical Oceanography*, **15**, 810–816.

Willebrand, J., 1993: *Forcing the ocean with heat and freshwater fluxes. In: Raschke E, Jacob D (eds) Energy and Water Cycles in the Climate System. NATO advanced Science Institutes Series I: Global Environmental Change 5*. Springer-Verlag.

Willebrand, J., S. G. H. Philander, and R. C. Pacanowski, 1980: The oceanic response to large-scale atmospheric disturbances. *Journal of Physical Oceanography*, **10**, 411–429.

Wunsch, C., 1997: The vertical partition of oceanic horizontal kinetic energy. *Journal of Physical Oceanography*, **27**, 1770–1794.

Wunsch, C., 2002: What is the thermohaline circulation? *Science*, **298**, 1179–1181.

Wunsch, C. and R. Ferrari, 2004: Vertical mixing, energy and the general circulation of the oceans. *Annual Reviews of Fluid Mechanics*, **36**, 281–314.

Wunsch, C. and D. Stammer, 1997: Atmospheric loading and the oceanic 'inverted barometer' effect. *Reviews of Geophysics*, **35**, 79–107.

Yang, J., 1999: A linkage between decadal climate variations in the Labrador Sea and the tropical Atlantic ocean. *Geophysical research letters*, **26**, 1023–1026.

A Models

A.1 FLAME

Model description In this study output from the 1/12° and 1/3° (horizontal resolution) versions of the geopotential-coordinate ocean general circulation model FLAME (Family of Linked Atlantic Model Experiments) has been used (e.g., Eden and Willebrand, 2001). FLAME is based on the well-known GFDL-MOM code (Pacanowski, 1995). The 1/3° and 1/12° versions can roughly be characterized "eddy-permitting" and "eddy-resolving", respectively. The model comprises 45 levels with a vertical spacing ranging from 10 m near the surface to 250 m in the deep ocean. The maximum depth is 5500 m. The horizontal (latitude x longitude) grid is organized as follows in the two versions: $\frac{1}{3}^\circ$ x $\frac{1}{3}^\circ$ $\cos\theta$ and $\frac{1}{12}^\circ$ x $\frac{1}{12}^\circ$ $\cos\theta$, with θ denoting geographical latitude. The model region extends from 70°N to 70°S.

Mixed layer processes are parameterized applying a "Kraus-Turner" model (Kraus and Turner, 1967). FLAME makes use of the "rigid-lid" surface boundary and the "no slip" coastal boundary condition in the equation of motion. Open boundaries are treated according to Stevens (1990). Tracers are mixed along isopycnals. Additionally in the 1/3° version, eddy-induced advection of tracers is parameterized after Gent and McWilliams (1990). The bottom boundary layer scheme of Beckmann and Döscher (1997) for improved spreading characteristics of dense overflows has been applied.

Forcing For the heat flux forcing the formulation of Haney (1971) has been used: It consists of a combination of prescribed heat flux plus a relaxation to climatological SST, given by (Barnier et al., 1995) based on an analysis of ECMWF data. Sea surface salinity (SSS) is restored towards the climatology of Levitus and Boyer (1994). In the 6-year long model run of the 1/12 °version used in this study a monthly averaged climatological forcing has been applied. Output from two different experiments of the 1/3° version have been analyzed, the so-called CONTROL and HEAT run. In the CONTROL configuration, which covers the years 1958-2000, monthly anomalies of heat flux and wind stress from NCEP/NCAR reanalysis data (Kalnay and et al, 1996) have been added to the climatology. Instead for HEAT, which also covers the years 1958-2000, the same heat flux anomalies have been applied but climatological winds have been used. A comparison of output from those two experiments partly allows for the isolation of the effects of inter-annual buoyancy and wind forcing.

A.2 ECCO

Model description The ECCO (Estimating the Circulation and Climate of the Ocean) estimates (Stammer et al., 2002, 2003) are based on the Massachusetts Institute of Technology (MIT) ocean general circulation model (Marshall et al., 1997) and its adjoint (Marotzke et al., 1999). It applies a hydrostatic primitive equation formulation with an implicit free surface, making use of free-slip bottom and no-slip side wall boundary conditions. Mixed layer processes are parameterized using the "KPP" model after Large et al. (1994). In the ocean interior convective

adjustment is applied to eliminate static instabilities. The model's grid comprises a horizontal resolution of 2° x 2°and 22 layers in the vertical, with the modeled region extending from 80°N to 80°S.

Forcing The model is constrained by satellite altimeter data from the TOPEX/POSEIDON and ERS-1/2 missions, the Levitus and Boyer (1994) full water column hydrographic climatology, monthly mean surface temperature fields as well as the estimated air-sea fluxes of momentum, freshwater and heat (refer to Stammer et al. (2002) for details). It is assumed that model errors are entirely caused by uncertainties in the initial conditions from the Levitus and Boyer (1994) climatology and the first guess forcing fields from the NCEP/NCAR reanalysis (Kalnay and et al, 1996). The model output used in this study represents the last iteration of the freely running forward model, driven by the optimized set of forcing fields. That means that in contrast to sequential data assimilation techniques such as the so-called Kalman filter, this method provides a dynamically consistent solution.

A.3 ECBilt-Clio

Model description The ECBILT-CLIO global climate model comprises an oceanic, an atmospheric and a sea ice component coupled with each other. The 3-layer adiabatic quasi-geostrophic atmospheric model (ECBILT) exhibits a horizontal resolution of approximately 5.6° x 5.6°. It uses parameterizations for the hydrological cycle (Opsteegh et al., 1998). The oceanic component CLIO (Goosse and Fichefet, 1999) consists of a primitive equation free surface general circulation model. It is coupled to a thermodynamic-dynamic sea ice model. CLIO is evaluated on a 3°x 3°grid with 20 levels in the vertical and has a realistic topography. A redistribution of air-sea freshwater fluxes is required. CLIO includes mixing along isopycnals and the effect of meso-scale eddies on tracer advection is parameterized according to Gent and McWilliams (1990). The coupling of the 3 components involves exchange of momentum, heat and freshwater.

Forcing and model setup The model is forced by solar insolation at the top of the atmosphere. The experiment used in this study is based on a pre-industrial climate setup, meaning that representative parameters for orbital forcing (eccentricity, etc.) as well as greenhouse gas concentrations (CO_2, methane, etc.) and land albedo have been chosen.

B Scatterometer Wind Stress

Scatterometer Wind Stress Ekman transports have been computed using data from the NASA Quick Scatterometer (QuickSCAT) satellite mission. Most of the subsequent information is issued from the Quickscat user manual from CERSAT (Centre ERS d'Archivage et de Traitement; CERSAT (2002)). About 14 orbits per day are accomplished by the satellite in roughly 800 km above the Earth. QickSCAT covers 90% of the Earth's surface per day. The Sea Winds instrument on QuickSCAT is an active microwave radar which measures the power of the electromagnetic backscatter from the sea surface. Small waves and ripples generated by wind stress modify the radar cross section and hence the amplitude of the backscattered power. The determination of wind speed and magnitude is based on empirical algorithms, derived from experiments and theoretical analysis.

In this study wind stress products from CERSAT are used (CERSAT, 2002). These are daily averaged wind stress fields interpolated on a 0.5° x 0.5° horizontal grid using an objective analysis scheme. Wind stress τ is estimated from scatterometer winds using the bulk formulation

$$\tau = (\tau_x, \tau_y) = \rho_{air} C_D W(u, v) \tag{B.1}$$

with W, u, v, ρ_{air} and C_D denoting wind speed, its zonal and meridional component, surface air density and the drag coefficient. The formulation of Smith (1998) is used for estimating C_D.

Meridional Ekman volume transports M_{ek} have been computed from zonal integration of τ_x applying the widely used relationship:

$$M_{ek} = -\int \frac{\tau_x(x)}{\rho f} \mathrm{d}x \tag{B.2}$$

C GRACE

Month	Year	GFZ	UTCSR
April/May	2002	x	x
August	2002	x	x
November	2002	x	x
February	2003	-	x
March	2003	x	x
April	2003	x	x
May	2003	x	x
July	2003	x	x
August	2003	x	x
September	2003	-	x
October	2003	x	x
November	2003	x	x

Table C.1: *Monthly averaged GRACE gravity field products available from GFZ and UTCSR processing centers. Direct comparisons between GFZ and UTCSR fields can be carried out from 9 monthly solutions.*

De-aliasing In the de-aliasing process time varying gravitational phenomena such as Earth, atmosphere and ocean tides or long-wavelength post-glacial rebound are accounted for. Also, non-tidal short-term atmospheric and oceanic mass variations are eliminated using a barotropic ocean model provided by the Jet Propulsion Laboratory (JPL). It was originally coded by Pacanowski, and subsequently modified by Ponte, Hirose and more recently by Ali and Zlotnicki (2003). In the following it is referred to as "PPHA".

The model is forced by 6-hourly meteorological fields from the European Center of Medium-range Weather Forecast (ECMWF) having a horizontal resolution of 0.5°. PPHA computes the component of oceanic mass redistribution ("barotropic sea level") due to wind stress and atmospheric pressure for an area between 65N and 75S. It lacks baroclinic dynamics and surface buoyancy forcing which are commonly believed to have little effect on time scales up to one month (Tierney et al., 2000). Ocean bottom pressure is then derived by adding vertical integrated ECMWF atmospheric pressure (Flechtner, 2003).

Apart from the non-tidal ocean and atmosphere contribution also ocean tides have to be accounted for during generation of gravity field partials. Two different ocean tide models are currently applied, at GFZ the FES2002 (LeProvost, 2002) and at UTCSR the CSR4.0 model (Eanes, 2002). Whereas FES2002 uses a combined hydrodynamic and data assimilation approach, CSR4.0 represents an empirical model based on satellite altimetry.

PPHA bottom pressure as well as ECMWF sea level pressure (SLP) are available in a time and horizontal resolution of 6-hourly and 0.5° x 0.5° for the period from January 2002 until December 2003. FES2002 and CSR4.0 ocean tide amplitudes and phases were transformed into spherical harmonic coefficients up to degree and order 50 representing with a time resolution of one hour for the time span April to December 2002.

D Glossary

Acronym	Meaning
ACCP	Atlantic Climate Change Program
AABW	Antarctic Bottom Water
DWBC	Deep Western Boundary Current
ECCO	Estimating the Circulation and Climate of the Ocean
ECMWF	European Center for Medium-Range Weather Forecasts
FLAME	Family of Linked Atlantic Model Experiments
GAGE	Guiana Abyssal Gyre Experiment
GCM	General Circulation Model
GOCE	Gravity Field and Steady-State Ocean Circulation Explorer
GRACE	Gravity Recovery and Climate Experiment
lADCP	lowered Acoustic Doppler Current Profiler
lNADW	lower North Atlantic Deep Water
LSW	Labrador Sea Water
MAR	Mid-Atlantic Ridge
MicroCAT	Micro Conductivity and Temperature sensor
MIT	Massachusetts Institute of Technology
MOVE	Meridional Overturning Variability Experiment
NADW	North Atlantic Deep Water
NAO	North Atlantic Oscillation
NCEP	National Centers for Environmental Prediction
oNADW	overflow North Atlantic Deep Water
OGCM	Oceanic General Circulation Model
PIES	Pressure Sensor and Inverted Echosounder
POL	Proudman Oceanographic Laboratory
PPHA	barotropic ocean model used for de-aliasing of GRACE measurements
RAFOS	type of float, reverse of SOFAR (sound fixing and ranging)
vmADCP	vessel-mounted Acoustic Doppler Current Profiler
SLP	sea level pressure
suNADW	shallow upper North Atlantic Deep Water
SSH	Sea Surface Height
SSS	Sea Surface Salinity
SST	Sea Surface Temperature
URI	University of Rhode Island
WHOI	Woods Hole Institution of Oceanography